Ph.D-thesis

EXP-potential and Quasi-universality
A study

Andreas Kvist Bacher,

September 28, 2018

supervisor: Jeppe Dyre
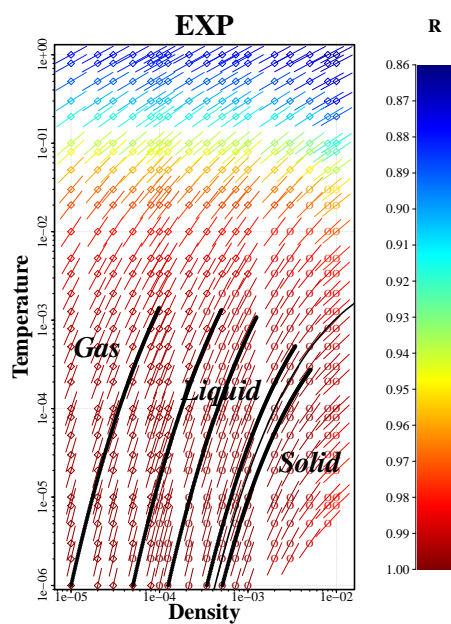
Danish National Research Foundation Centre *Glass and Time*,
IMFUFA, Department of Science and Environment,

Roskilde University, Denmark

This thesis has been submitted to the Doctoral School of Science and Environment

Abstract

This work investigates the exponential pair potential (EXP-potential) in a part of its density-temperature phase diagram spanning six decades of temperatures: from 10^{-6} to 1 and three decades of densities: from 10^{-5} to 0.01. The EXP potential is purely repulsive and cannot uphold a liquid-gas interface, but a narrow fluid-solid coexistence region is found. The main focus of the research has been the fluid phase. In this phase strong correlations between the fluctuations in the potential energy and in the virial is found. The strong correlations are found to persist far into the dilute fluid. The properties of the EXP-potential is investigated with respect to structure, dynamics, thermodynamics and with respect to the isomorph theory.

The investigation of the fluid phase revealed the existence of two distinct regions: A gas phase and a liquid phase. The transition between the phases is smooth. A structural signature to distinguish gas from liquid was defined as the existence of a first minimum in radial distribution function. The signature is ambiguous as it is dependant on the numerical protocols used. It nevertheless serves the purpose of separating the two identified phases. The gas phase has different domains in relation to the isomorph theory, since there is a cold dilute and strongly correlating gas, and hot gas that does not have strong correlations.

The strongly correlating gas was found to be of great interest as it is characterized by being very dilute and controlled by single pair interaction. This simplicity allows for prediction based on kinetic theory of: the state point dependence of the reduced diffusion coefficient, the change in reduced excess isochoric specific heat capacity along isomorphs, the temperature dependent correlation coefficient (R), and the density scaling exponent (γ). The predictions agrees with simulation results.

The EXP system is found to conform well with hidden scale invariance throughout most of the explored phase diagram. The correlation is found to depend almost entirely on temperature and stays well above 0.9 for temperatures lower than 0.2. Density dependence of the correlation is only at the highest densities. Due to the strong correlations EXP system is found to have isomorphs in the low temperatures. Five isomorphs, each traced by three different techniques were investigaated. The different techniques are: The small step method tracing the "true" isomorphs, the direct isomorph check (DIC) allowing for larger density and temperature jumps, and the $h_p(\rho)$ method yielding a functional form of the isomorph. The different methods are compared and its found that the DIC method works well even for very long density jumps if the system is in the condensed region. The analytical $h_p(\rho)$ method is tested for different choices of p ($p \in \{0, 1, 2\}$). In the condensed phase $p = 2$ is found to give more accurate results, and that as the system becomes increasingly dilute system, p tends to zero in the gas phase. By a combination of kinetic theory and isomorph theory an

expression to predict the optimal p for that state point, from single simulation at the state point is derived and seen to agree well with the isomorph observation.

The thesis conclude with a chapter describing how the EXP-potential might provide a definition and explanation of quasi-universality and a demonstration hereof by mapping four Lennard-Jones state points to the EXP-potential, using foremost the reduced diffusion constant and "fine tuning" by the density scaling exponent. The quasi-universality predicts systems with matching dynamics also have matching structure. Structure is compared by the radial distribution function and a very good collapse is found.

The EXP-potential was simulated using Roskilde University Molecular Dynamic (RUMD) open-source software on NVIDIA graphic-cards in the Roskilde University HPC center.

Resumé

Dette Ph.D. arbejde undersøger det eksponentielle par potentiale (EXP-potentialet) i en del af dets densitet-temperatur fasediagram. Temperaturene fordeler sig over seks dekader fra 10^{-6} til 1, og densiteterne over tre fra 10^{-5} til 0.01. EXP-potentialet er udelukkende frastødende hvilket betyder at en væske-gas overflade. Potentialet har et koeksistens område mellem fluid og faststof. Hovedfokus i dette arbejde har været fluidfasen hvor der er fundet stærke korrelationer mellem fluktuationerne i den potentielle energi og virialet. Disse stærke korrelationer findes også i den tynde fluid.

Strukturen, dynamikken, og termodynamikken for systemer beskrevet ved EXP-potentialet er undersøgt. Det er tillige systemernes egenskaber i relation til isomorfteorien. Undersøgelsen har afsløret at fluidfasen kan opdeles i to adskilte område: En gasfase og en væskefase. Overgangen mellem de to faser glidende. Derfor er en strukturel fasemarkør: eksistensen af et første minimum i den radielle fordelingsfunktion, defineret for at adskille faserne. Denne markør er ikke entydigt defineret, da den afhænger af den numeriske protokol der bliver anvendt. Markøren er dog alligevel formålstjenlig til at adskille gasfasen og væskefasen.

Gasfasen kan opdeles i to områder med relevans for isomorfteorien: en kold og tynd gas som er stærkt korrelerende, og en varm gas der ikke er. Fysikken i den kolde gas er simple i det den er domineret af enkel par interaktioner. Denne simplicitet medfører at teoribaserede forudsigelser for: den reducerede diffusionen, ændringen i den reducerede excess isochore specifikke varmekapacitet langs isomorferne, den temperaturafhængige korrelationskoefficient (R) og den temperaturafhængige densitetsskalerings eksponent (γ). Forudsigelserne vises at stemme godt med simuleringsresultaterne.

EXP-potentialet vises at opfylde isomorfkriteriet (ligning 3.1) i det meste af det afdækkede fasediagram. Korrelationerne vises stort set kun at afhænge af temperaturen, undtagen ved de højeste densiteter hvor et svagt fald observeres. De stærke korrelationerne ved lave temperature betyder at EXP-potentialet har isomorfer her. Fem sådanne er bestemt ved tre forskellige teknikker: En metode hvor isomorfen spores ved i små skridt at følge linjer med konstant excess entropi. Den anden metode det direkte isomorfcheck (DIC) udnytter isomorfkriteriet til at lave meget større spring i densitet og temperatur. Ved den sidste metode findes et funktionsudtryk for isomorfen udfra en simulering i et enkelt tilstandspunkt. Denne metode kaldes $h_p(\rho)$ metoden. Her kan antage forskellige værdier $p \in \{0, 1, 2\}$. I det kondenserede system passer $p = 2$, men som systemet bliver mindre og mindre tæt, må lavere værdier af p anvendes. $p = 0$ giver den bedste approksimation i gasfasen. Slutteligt kombineres gasfase-teorien med $h_p(\rho)$ og en metode til bestemmelse af den optimale p værdi vises at stemme godt med observationerne fra de dannede isomorfer. Afhandlingen afsluttes med et kapitel hvori det beskrives hvordan EXP-potentialet kan bruges til at

definere og forklare kvasi-universalitet. Kapitlet afsluttes med en demonstration af dette: Den reducerede diffusionskonstant for fire Lennard-Jones tilstandspunkter bestemmes. Til hvert af disse findes et en isomorf i EXP-potentialet med den samme reducerede dynamik (diffusionskonstant). Nu sammenlignes strukturen af Lennard-Jones tilstandspunkterne og punkter fra de respektive EXP isomorfer. Det ses strukturen er ens når dynamikken er ens, hvilket er en indikator for kvasi-universalitet. Ved at matche ikke kun diffusionskonstanten, men også densitetsskalerings eksponenten kan kollapset i struktur gøres endnu bedre.

Simuleringerne af EXP-potentialet blev lavet med programmet Roskilde University Molecular Dynamic (RUMD) open-source software på NVIDIA grafikkort i Roskilde Universitets HPC center.

Preface

The doctoral thesis describes some of the work done by the author since the initiation in August 2014. During this period the author spend three good years in the *Glass and Time group* at Roskilde University, one year in the United States of America visiting first Professor Pablo G. Debenedetti and his group at Princeton University for six month learning about the many different aspect of research in disordered systems. Hereafter the author visited Professor Corey S. O'Hern and his group at Yale University spending half a year studying jamming of disks with friction. Both experiences has in many different ways rewardingly contributed to the research experience of the author, even if its not directly reflected in the present thesis. In addition hereto the research has been halted six month due to paternity leave.

Acknowledgements

I have been very fortunate in being surrounded by wonderful people during my time on this project. I would like first to thank Jeppe for believing in me all along, for all his guidance and help, all his kind words when kind words are needed. Thank you Jeppe! I deeply appriciate the help from Johanne and Lorenzo in proofreading this thesis. I much appriciate the ever helpfull within the simulations group: Thank you Lorenzo, Ulf, Thomas, Nick, Claire, Jesper, Andreas, Laura and Heine.
I have enjoyed the friendly environment in IMFUFA in general and within the Glass and Time group in particular. I appreciate the willingness to always help.
A very special thanks goes to my wife and our children.

Papers

The author has contributed to five papers, but only three of these is attached to the thesis. The five papers are listed below:

Paper I *The mother of all pair potentials*
A. K. Bacher, and J. C. Dyre,
Colloid and Polymer Science, **292**, 1971, 2014. Online

Paper II *Explaining why simple liquids are quasi-universal*
A. K. Bacher, T. B. Schrøder, and J. C. Dyre,
Nature Communications, **5**, 5424, 2014. Online

Paper III *RUMD: A general purpose molecular dynamics package optimized to utilize GPU hardware down to a few thousand particles*
N. P. Bailey, T. S. Ingebrigtsen, J. S. Hansen, A. A. Veldhorst,
L. Bøhling, C. A. Lemarchand, A. E. Olsen, A. K. Bacher,
L. Costigliola, U. R. Pedersen, H. Larsen, J. C. Dyre
SciPost Phys., **3**, 6, 038, 2017. Online

Paper IV *The EXP pair-potential system. I. Fluid phase isotherms, isochores, and quasiuniversality*
A. K. Bacher, T. B. Schrøder, and J. C. Dyre,
The Journal of Chemical Physics, **149**, 114501, 2018. Online

Paper V *The EXP pair-potential system. II. Fluid phase isomorphs*
A. K. Bacher, T. B. Schrøder, and J. C. Dyre,
The Journal of Chemical Physics, **149**, 114502, 2018. Online

Paper I has been left out of this work, as its content is covered also in Paper II, IV and V. Paper III has been leftout due to the auther of this thesis is not amoung the main cotributers of the paper.

Contents

Bibliography **161**

Chapter 1

Introduction

The broad scope of this project is to investigate the properties of matter - understood as the different phases that matter can be found in: a gas like the air we breath, a liquid like the seas we sail, a solid like the rock on which we stand and build our world. But also the glasses made from the fires inside the earth, the plasmas of the lightning and the granular sensation of the sand in the beach. Not all states of matter can be covered in the time span of this project, so focus is greatly needed. First the plasmas will be disregarded as exotic, fundamental and important they might be. The glasses are interesting as a probe for understanding condensed matter, as minute differences in i.e. temperature can have profound effect on the properties of these systems- they allow us to put predictions of our understanding to the test. It is from the studies of the glassy state in the *Glass and Time group* at Roskilde University, that the foundations of research in this project comes. Even so the glassy state will not be the topic of the investigations. The same goes for the granular materials that play an ever important role in our life on earth. The state of matter researched in this project is thus the gas, liquid, and crystal phase. The phases are separated by phase transitions are known from our everyday life when boiling water to cook or making and using ice cubes. We experience the phase transition as something happening as temperature (T) is changed. This is a naïve one parameter understanding of thermodynamics, but when going to mountains we find that the eggs we boiled did not cook as expected and we discover the pressure (p) also affects the properties of the water - here to lower the boiling temperature of the water. We hereby arrive at the conclusion that the properties of a system depends on two parameters. In the example temperature and pressure. Thus a thermodynamic phase diagram must have two independent variables. A generic example can be seen in Fig. 1.1(*left*) where the dashed line marked p_B correspondence to the everyday experience: At a given pressure, cool a liquid (l), and it will crystallize; heat a liquid, and it will boil. The condition for this behaviour is that the pressure
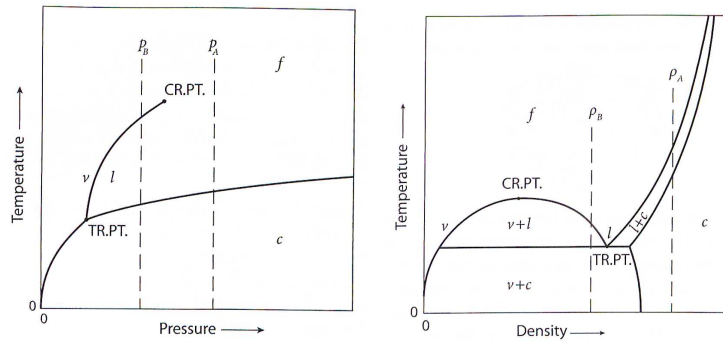
Figure 1.1: *Left:* Generic pressure-temperature phase diagram. The different phases are marked by letters: (l) liquid, (c) crystal, (v) vapor and (f) fluid. The triple point is marked by TR.PT., and the critical point by CR.PT. Two isobars are marked by dashed lines. *Right:* Generic density-temperature phase diagram. Phases and triple- and critical points are marked in the same way as in left figure. ($v + c$) indicates the vapor-crystal coexisistence region, ($v + l$) the vapor-liquid coexisistence region, and ($l + c$) the liquid-crystal coexixtence region. Two isochores is marked by dashed lines. Both figures are from Stillinger [1].

is higher than the pressure at the triple point - marked by TR.PT. in the figure, but lower than that of the critical point - marked by CR.PT. The dashed line marked p_A is at pressure above the critical point pressure, and therefore it has no phase transition from liquid to gas - it has no boiling point and the gas-liquid phase, and is in a fluid phase. Note that the phase transition lines are sharp transitions. By further investigations we discover that also density can be used as a control parameter, and another way of examining the same system, is by controlling not the pressure, but the density (ρ) of the system. A (ρ, T) phase diagram for the same generic system is see in Fig. 1.1(*right*). This kind of phase diagram is particular useful in computer simulations. Note how phase transitions happens by crossing coexistence region. The two phase diagrams presented above are termed generic as they represent the behaviour of most systems. However not all, as water has an anomalous behaviour, it has a negative thermal expansion in liquid phase, and the phase transition line between crystal and liquid is non-monotonous[2]. This is not unique for water but also applies for i.e. silicon[3].

Computer simulations can be helpful tool in theory development as it aides understanding of the fundamental properties of matter, as even the microscopic movements and interactions are accessible in computer simulations. In experiments the microscopic knowledge is hard to get to, and must often be inferred from macroscopic data. The generic phase dia-

gram of Fig. 1.1 could be the phase diagram of the Lennard-Jones[4, 5] model system, where the interactions between particles are given by $v(r) = 4\varepsilon \left[\left(\frac{\sigma}{r} \right)^{-12} - \left(\frac{\sigma}{r} \right)^{-6} \right]$. In this expression v is the potential energy associated with two particles separated by a distance (r), ε is an energy parameter, and σ a length. The potential is characterized by harsh repulsion as two particles come very close, and an attraction as particles are further apart. When the particles are at distance $2^{1/6}\sigma$ from each other, they are in the potential energy minimum.

The Lennard-Jones potential is often use as the generic model of matter: it is simple in its mathematical form, it features all the relevant phases and fast to evaluate in a computer[6]. This simple rule of interaction is thus sufficient to produce phase diagrams that looks similar to that of real liquids - especially mono-atomic noble gases like argon.

As fascinating and important water is as a case, it is not an exemplary case. The aim of this project is to generalize by simplification, and understand simple systems like the Lennard-Jones system. A class of system knowns as *the class of simple liquids*[7, 8].

The topic of this thesis is to study another simple liquid: the EXP pair potential system. The EXP pair potential is a purely repulsive potential between pairs of particles described by a simple decaying exponential function: $v_{EXP}(r, \varepsilon, \sigma) = \varepsilon e^{-r/\sigma}$, where again v is the pair potential energy, r is the separation between two particles, ε an energy parameter, and σ a length parameter. The EXP pair potential has been used as a part of other models of matter: In 1931 Max Born and Joseph E. Mayer[9] argued to replace the inverse power law previous used to model the repulsion between particles[4, 5] with an exponential term of the same form as the EXP pair potential. The argument they used was that the repulsion comes from the overlap of the wavefunctions of the electrons, and the decay of the bound-state wavefunctions follows a decaying exponential function[10]. The attractions were maintained as the r^{-6} dependence of the London forces[11]. The potential of Born and Meyer is often refereed to as the Buckingham potential[12]. Other potentials that include an exponential term are: the Morse potential[13], where the exponential is both at the repulsive and attractive term, the Yukawa potential[14, 15], also called screened Coulomb potential, where a Coulomb interaction is multiplied by an exponential, and the embedded-atom models of metals[16], where an exponential is part of the core-core repulsion used. The exponential repulsion has also been used in experimental settings e.g. by Abrahamson [10] where parameter values for the exponential function to fit atoms with a atomic numbers from $Z = 2$ to $Z = 105$ are listed. Recently the EXP-potential were used in relation to unjamming, where a binary mixture of particles interacting with EXP-potentials were studied[17]. Nonetheless the EXP system has not been studied much in its own right.

The EXP system is appealing to investigate due to its simple mathematical form and because the EXP can be written as a sum of inverse power laws. The inverse power law (IPL) system has been investigated for many different values of n[18] and has been found to be usable in a wide range of applications, and a stepping stone for further understanding of simple liquids. At first glance, it may seem odd to investigate potentials with no attractions as the attractions stabilize the system. No attractions between the particles, also means that a liquid-gas interface cannot be upheld and therefore neither have a triple point, a critical point, nor a first order thermodynamic phase transition. Part of this issue is overcome in computer simulations, as the model system is always contained either in a box, or by being infinite by the use of periodic boundary conditions. This containment means that particles must stay close and they can have both a solid and a fluid phase. When the density is high the physics of systems with attractive forces is nonetheless dominated by the repulsion[19]. As will be demonstrated in this work, the fluid phase of the EXP system can be split into a liquid phase and a gas phase - in the sense that the properties of the system correspond to typical liquid and gas behaviour, respectively.

The short answer to why leave out the attractive term is to simplify. To get the simplest possible system still able to reproduce experimentally observed behaviour. The finding that many systems has similar properties with regards to structure and dynamicsrelates to the concept of "simple liquid". Simple is not understood as the mathematical simplicity of the potential function in simulations, or the physical simplicity of the noble gasses like argon. Simple relates to behaviourof the system in different state points in (parts) of the phase diagram. The IPL systems belong to this class of simple liquids, where IPL systems with different exponents have similar structure and dynamics[18, 20–22]. Another simple system is the hard-sphere system that consists of infinite hard spheres interacting in perfectly elastic collisions only and can be viewed as a limit system of the IPL systems when the exponent goes to infinity. This system has the advantage that it can be well explained analytically, and that it depends on the density solely. The hard-sphere system can be used as a reference system for comparison across other systems: If two systems can be mapped to the same hard-sphere system, then they will have approximately the same structure and dynamics[23]. The mapping involved is by identification of an appropriate radius of the hard-spheres [24]. Unfortunately, it is an open question how to determine the proper hard-sphere radius, but the concept of a single parameter system is appealing, and suggests a characteristic of a simple liquid: That it is controlled by a single parameter in (parts of) its thermodynamic phase diagram[7, 25]. The hard-sphere approach has another short coming in the lack of method for predicting what systems that belongs to the class of simple liquids[25].

1.1 Reading guide

The work presented in this thesis all relates to an exploration of the EXP-potential. Many of the findings was recently published in two of the accompanying papers. As the reader will learn, many figures and findings is repetitions from the papers. Throughout the thesis a marking system for the figure is used:

($*$) marks a reproduction from one of the two papers.

(M) marks a modified reproduced figure. In many cases modification implies that additional data added to the figure.

(N) marks a figure not in the papers.

The thesis is structured to first provide some background relating to molecular dynamic simulations, and the conceptual frameworkof the isomorph theory.

The study of the EXP-potential is in the second part. The structure follows to some extent the papers: first a chapter providing an overview of properties of the system and the known parts of its phase diagram (Chapter 4) corresponding to Bacher et al. [26], then a chapter describing the isomorphs of the system (Chapter 5) corresponding to Bacher et al. [27].

Chapter 4 begins with an overview of the phases of the EXP-system, before giving the a description of the simulation details. It is the aim to equip the reader with all the relevant knowledge to do further research using the potential. Afterwards the findings of the correlation coefficient (R), the density scaling exponent (γ), the structure (radial distribution function) and dynamics (mean-square displacements and diffusion), and the thermodynamics ($\tilde{U}$, $\tilde{W}$, $\tilde{p}$ and $\tilde{c}_V^{\text{ex}}$) reported in the phase diagram, along isotherms and along isochores. The chapter concludes with a section on the gas phase where prediction for the correlation coefficient R and the density scaling parameter are derived.

Chapter 5 explores five isomorphs in the phase diagram of the EXP-potential - two of which not previously reported. The structure and dynamics, as well as the reduced excess isochoric heat capacity, is investigated for isomorph invariance. Different methods for finding the isomorph is compared - including a technique not in the papers: The $h_p(\rho)$-approximate isomorphs.

The final chapter on the EXP-system in the thesis shows how the EXP system can be used on the way to understanding quasi universality. A few examples on using the EXP-system as a reference system is given. The content of this chapter is also presented in Bacher et al. [26].

Chapter 2

Molecular dynamics, GPU and RUMD

This chapter gives a background on the principles of molecular dynamics: an introduction to the use of periodic boundary conditions, cutoffs and thermostat. The differences between CPU and GPU computing in relation to molecular simulations is briefly discussed. The chapter concludes with a brief introduction to RUMD.

In molecular dynamics (MD) a computer is used to calculate the time evolution of the Hamiltonian (Eq. (2.4)) of system of particles confined in a box of some size, but often periodic boundary conditions is used. Periodic boundary conditions allows simulation of bulk properties even for systems with only on order 1000 particless[28]. The periodic boundary conditions means that a particle leaving the box to the right will be replaced by another identical particle entering from the left with the exact same momentum. Moreover will interactions between particles cross the boundary of the cell as well. Another way of understanding the periodicity is to consider the box surrounded by identical boxes all around; as seen in Fig. 2.1. The particles in these boxes is often referred to as image particles, since they must behave exactly like the original particle. In order to make sure a particle is not interacting twice with the same particle (or another particle and one of that particle's images) is to require interactions with particles outside a specified radius to be zero. The distance at which the interactions is set to zero is called the cutoff distance. The cutoff must be less than half the width of the shortest box-side length.

The cutoff can be done in various way: The potential energy function of interacting particles ($v(r)$) can be truncated, it can be truncated and shifted, in what is called a shifted potential cutoff[6], or the forces can be
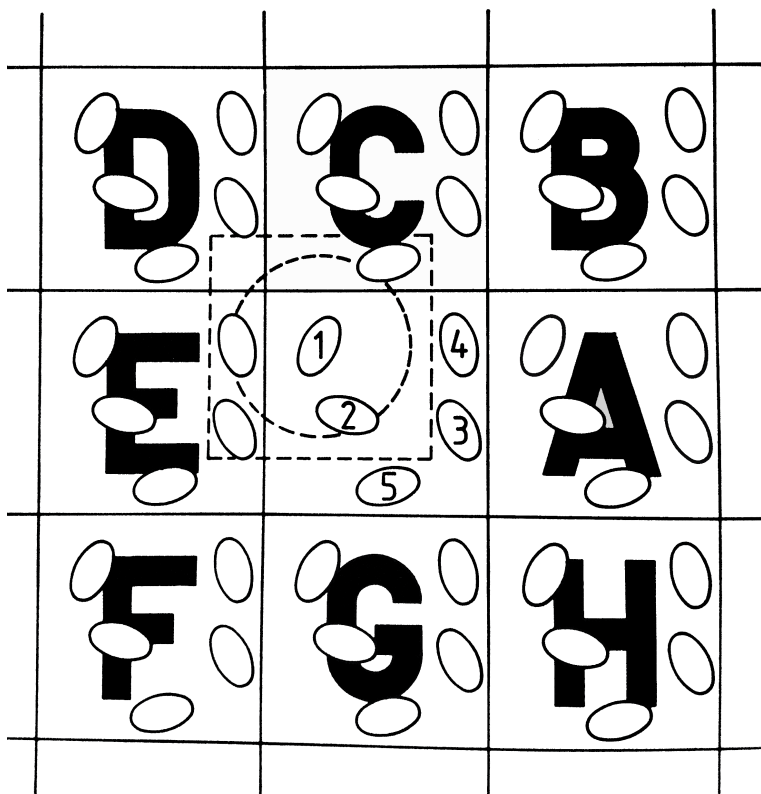
Figure 2.1: The figure illustrates a simulation box (center) with five particles and periodic boundary conditions. The periodic boundary conditions can be thought of, as having the system surrounded by exact copies on all sides (boxes A, B, C, D, E, F, G and H). The dashed square shows the simulation box centered at particle one, while the dashed circle illustrates the cutoff distance. If the diameter of circle becomes larger than the side length of the box, particle one might interact twice with the same particle. Figure from Allen and Tildesley [29]

truncated and shifted - called a shifted force cutoff[30]. The truncation at cutoff distance r_c without shifting is given by:

$$v(r) = \begin{cases} v(r) & \text{for } r \leq r_c \\ 0 & \text{else} \end{cases} \qquad (2.1)$$

and leaves the potential energy function discontinuous in the cutoff. This discontinuity is avoided in the shifted potential cutoff, as the value of the potential at the cutoff distance, is subtracted the potential energy function:

$$v(r) = \begin{cases} v(r) - v(r_c) & \text{for } r \leq r_c \\ 0 & \text{else} \end{cases} . \qquad (2.2)$$

The resulting function is guaranteed to be continuous but not differentiable, and as a consequence the force might be discontinuous. The shifted force cutoff resolve this by shifting the force function to be continuous at the cutoff distance - corresponding to adding a linear term to the potential energy function:

$$
v(r) = \begin{cases} v(r) - (r - r_c) \left. \frac{dv}{dr} \right|_{r=r_c} - v(r_c) & \text{for } r \leq r_c \\ 0 & \text{else} \end{cases} . \qquad (2.3)
$$

The shifted force cutoff has the advantage of reducing the needed cutoff distance and reducing simulation time[30].

The time evolution of a system of particles is found from the state of the system as described by its Hamiltonian of the following form:

$$
H(\mathbf{R}, \mathbf{P}) = K(\mathbf{P}) + U(\mathbf{R}) = \sum \frac{\mathbf{P}^2}{2m} + U(\mathbf{R}), \qquad (2.4)
$$

where $\mathbf{R}$ is the (often) $3N$-dimensional position vector of the particles in the system and $\mathbf{P}$ the momentum vector (with p_i being the momentum of particle i of mass m_i). K and U is the kinetic respectively potential energy of the entire system. Different simulation techniques can add additional terms to the Hamiltonian - one such example is the interface pinning (more in Section 5.4). To know the system is thus to know its starting configuration (positions), the momentas of the particles, and the potential energy function. The potential energy of the system is a sum over the potential energy of each particle, which is by itself a sum of the potential energy with respect to an external field, and a summation over the potential energy of each of that particles interaction with other particles. The interactions between the particles can be separated into contributions from an external field, from pair interactions, from triplet interactions, and so forth. In this work only pair potentials are considered.

From the Hamiltonian of the system, the velocity ($\dot{\mathbf{r}}_i$) of - and forces ($\mathbf{f}_i$) on - each particle can be determined:

$$
\dot{\mathbf{r}}_i = \frac{\partial H(\mathbf{R}, \mathbf{P})}{\partial \mathbf{p}_i} = \frac{\mathbf{p}_i}{m_i} \qquad (2.5)
$$

$$
\mathbf{f}_i = \dot{\mathbf{p}}_i = -\frac{\partial H(\mathbf{R}, \mathbf{P})}{\partial \mathbf{r}_i} = -\nabla_i U(\mathbf{R}). \qquad (2.6)
$$

To follow the time evolution of the system, knowledge of the time evolution of these equations must be obtained. This can be done numerically on a computer if the equations of motion is discretized in small time steps Δt.

There are different protocols for evolving the motions of equations. The discretization used in this work is the leapfrog algorithm - a further modification of the Verlet algorithm. The offset is thus the Verlet algorithm[31, 32],

where the position of a particle at the next time step $(t + \Delta t)$ is determined from Taylor expansions of $r(t)$ around t forward and backwards in time[6]:

$$\mathbf{r}_i(t + \Delta t) = \mathbf{r}_i(t) + \dot{\mathbf{r}}_i(t)\Delta t + \frac{1}{2}\ddot{\mathbf{r}}_i(t)(\Delta t)^2 + \frac{1}{3!}\dddot{\mathbf{r}}_i(t)(\Delta t)^3 + \mathcal{O}(\Delta t)^4 \quad (2.7)$$

$$\mathbf{r}_i(t - \Delta t) = \mathbf{r}_i(t) - \dot{\mathbf{r}}_i(t)\Delta t + \frac{1}{2}\ddot{\mathbf{r}}_i(t)(\Delta t)^2 - \frac{1}{3!}\dddot{\mathbf{r}}_i(t)(\Delta t)^3 + \mathcal{O}(\Delta t)^4 \quad (2.8)$$

By addition of Eqs. (2.7) and (2.8), the positions at the next time step $(t + \Delta t)$ can be determined from the positions at the current time (t), and the positions in the previous time step $(t - \Delta t)$:

$$\mathbf{r}_i(t + \Delta t) = 2\mathbf{r}_i(t) - \mathbf{r}_i(t - \Delta t) + \frac{1}{m_i}\mathbf{f}_i(t)\,(\Delta t)^2 + 2\mathcal{O}(\Delta t)^4. \quad (2.9)$$

An expression for the velocities can be determined by a subtraction of Eqs. (2.7) and (2.8):

$$\dot{\mathbf{r}}_i(t) = \frac{\mathbf{r}_i(t + \Delta t) - \mathbf{r}_i(t - \Delta t)}{2\Delta t} + \mathcal{O}(\Delta t)^2 \quad (2.10)$$

As can be seen form Eq. (2.9), the error term of the positions is dependent on the time step size to the power of four, while it for velocities is the power of two. However, the error on the velocities does not affect the trajectories of the system, as the velocity does not enter Eq. (2.9). One disadvantages of the Verlet algorithm is the need for knowing not only the present particle configuration, but also that of the system one time step previously. This is overcome in a modification of the algorithm called the *velocity Verlet* algorithm. Here the velocities are calculated at each time step, and the knowledge hereof used to find the positions of the next time step by Eq. (2.7) truncated after the second order term. The change in velocities of the particles in the time interval t to $t + \Delta t$ can be determined in different ways: from the average acceleration: $\frac{\ddot{\mathbf{r}}_i(t+\Delta t)+\ddot{\mathbf{r}}_i(t)}{2}\Delta t$ and directly from the velocities: $\dot{\mathbf{r}}_i(t + \Delta t) - \dot{\mathbf{r}}_i(t + \Delta t)$. Equating and solving for the velocities at $t + \Delta t$ gives:

$$\dot{\mathbf{r}}_i(t + \Delta t) = \dot{\mathbf{r}}_i(t) + \frac{1}{2}\left(\ddot{\mathbf{r}}_i(t + \Delta t) + \ddot{\mathbf{r}}_i(t)\right) \quad (2.11)$$

Another advantage of the velocity Verlet is that the velocities are determined without subtraction of numbers[33] of almost the same size, as is the case with the displacements of particles in two (possibly) almost matching configurations in Eq. (2.10).

Another modification of the Verlet algoritme is the leapfrog, where the calculations of the velocities and positions are separated by half a time step. The advantage of this separation is that an expression to update the positions can be derived from the central difference over one time step: half

a time step before t and half a time step after t. Consider the velocities at time t to be determined in this way:

$$\dot{\mathbf{r}}_i(t_1) = \frac{\mathbf{r}_i(t_1 + \Delta t/2) - \mathbf{r}_i(t_1 - \Delta t/2)}{\Delta t} \,. \qquad (2.12)$$

Rewriting this to get an expression for the new positions

$$\mathbf{r}_i(t_1 + \Delta t/2) = \mathbf{r}_i(t_1 - \Delta t/2) + \dot{\mathbf{r}}_i(t_1)\,\Delta t \,. \qquad (2.13)$$

In the same can the velocities be update: The central difference of the velocities gives the acceleration:

$$\ddot{\mathbf{r}}_i(t_0) = \frac{\dot{\mathbf{r}}_i(t_0 + \Delta t/2) - \dot{\mathbf{r}}_i(t_0 - \Delta t/2)}{\Delta t} \qquad (2.14)$$

which by rearrangement expresses the updated velocities

$$\dot{\mathbf{r}}_i(t_0 + \Delta t/2) = \dot{\mathbf{r}}_i(t_0 - \Delta t/2) + \ddot{\mathbf{r}}_i(t_0)\,\Delta t \,. \qquad (2.15)$$

Equations (2.13) and (2.15) together form the Leapfrog algorithm if evaluated with half a time step separation ($t = t_0 = t_1 - \Delta t$). With this algorithm taking the square of the time step is avoided, but when evaluating the energies it must be taking into account that the velocities and positions are separated in time. This can be done by assuming the velocities at time t to be the average of the velocities at time $t - \Delta t/2$ and $t + \Delta t/2$.

The above mentioned algorithms is all simulating the microcanonical ensemble in an NVE simulation (keeping the number of particles N, the volume V, and the total energy E fixed). The energy is conserved as there is no other mechanism for allowing the energy to change - except for possibly a slow drift due to the finite machine precision. A thermostat is a device (here an algorithm) to control the temperature of a system by coupling the system with a heat bath. The use of a thermostat enables canonical ensemble simulation (where temperature (T) is fixed instead of energy). The vast part of the simulations reported in this work is canonical ensemble simulations (NVT-simulations). Thermostating was developed in the beginning of the 1980s as a method to keep the temperature of the system constant[28]. This can be accomplished in many different ways including simple rescaling of temperatures at regular time intervals and stochastic forces interacting with random particles chosen from appropriate Boltzmann distributions[34]. Many thermostats can reproduce the time independent quantities in the canonical ensemble, but cannot reproduce the correct dynamics[28]. The Nosé-Hoover thermostat - first presented in Nosé [35, 36], and reformulated and further developed in Hoover [37] - is a choice of thermostat that correctly reproduces the canonical dynamics. It introduces a time-reversible, deterministic and smooth (differentiable) variable in the force equation:

$$\mathbf{f}_i = m_i \ddot{\mathbf{r}}_i - \zeta \dot{\mathbf{p}}_i \,, \qquad (2.16)$$

where ζ is thermostat state providing "friction". The friction thus depends on both the thermostat state and the velocity of particle i. The state of the thermostat is changed in accordance with

$$\dot{\zeta} = \frac{\frac{K_t}{K_0} - 1}{\tau_0^2} \, , \tag{2.17}$$

where K_t is the kinetic energy of the system, $K_0 \equiv \lim_{t \to \infty}(\langle K_t \rangle) = DNk_BT_0/2$ is the thermodynamic kinetic energy at the target temperature T_0 and D is the dimensionality (usually 3) of the system, and τ_0 is the characteristic time of the thermostat[38]. This definition gives $\dot{\zeta} = 0$ when the temperature of the system T is equal to the target temperature. If $T > T_0$, $K_t > K_0$, and $\dot{\zeta} > 0$ so ζ increases and the particles are slowed more, and vise versa. Note that if ζ is fixed to zero, the micro canonical ensemble is recovered.

Two other ensembles used briefly in this work, are the constant particle-pressure-temperature (NPT) ensemble (realized by adding another term scaling distances to change the pressure as described in Martyna et al. [39]), and the constant particle-volume-potential energy (NVU) ensemble. The former is used as part of the work to establish melting and freezing lines by interface pinning in Section 5.4, while the latter is used in a theoretical argument in Chapter 6.

The NVU-ensemble[40–42] is sampling geodesics on the constant-potential-energy hypersurface $\Omega \equiv \{\mathbf{R}|U(\mathbf{R}) = \langle\mathbf{R}\rangle\}$. In case of a three dimensional system, consisting of N spherical particles, Ω is an $3N - 1$ dimensional hypersurface. Evolution of a system in the NVU-dynamics is done with a numerical algorithm resembling the Verlet algorithm described above. The resemblance becomes evident by defining the NVU time step length by $\Delta t_{i,NVU} \equiv \sqrt{-2\frac{\mathbf{F}_i \cdot (\mathbf{R}_i - \mathbf{R}_{i-1})}{\mathbf{F}_i^2} m}$[41]. The definition is subscripted by i as it is non-constant quantity. The algorithm can be improved in different ways to ensure equal time step lengths, and minimize energy- and entropic drift[40]. The NVU dynamic gives equivalent results as well NVE- and NVT-dynamics, as two stochastic dynamics[41].

GPU computing

Molecular dynamics are algorithms used to time evolve systems of interacting particles. The algorithms are implemented in a computer program and the computations of the code are done by the computers processing unit. Today many computers contain two different processing units: the central processing unit (CPU), and the graphics processing unit (GPU). Today both can be programmed to run MDs programs - see for instance Anderson et al. [43]. The main difference between the two processing units is that where the CPU typically has a few versatile cores (independent processing units) with a large amount of memory, the GPU have several thousand quite specialized cores with a limited memory. Since each core is able to preform only

one calculation at a time, more cores means more simultaneous calculations - a feature desirable for the MD algorithms, where neighbor list updates, force calculations and time step integration can be preformed simultaneously (parallelized)[43]. While the early GPUs where highly specialized to calculate the color of pixels, development the last ten years now allows for a more versatile use. A development taking speed with the development of CUDA. CUDA is an extension to programming language like C++, making the GPUs programmable and thus opening a door to general use of the computational power within.

RUMD

The molecular dynamics program used in most of this work, is the Roskilde University Molecular Dynamics package (RUMD)[44, 45]. RUMD is written in C++ with the CUDA extension to run on a single NVIDIA graphic card. The user interface is python. The main feature of RUMD compared to other GPU MD codes is that RUMD is optimized for small system sizes (up to a few thousand particles). A comparison with a widely used MD code LAMMPS can be seen in Fig. 2.2. Here three GPU versions, and CPU version is compared to rumd. All GPU codes is approximately equally fast for large system, while rumd is superior in small systems sizes. The reason that rumd is faster has to to do with different strategies for distributing the calculations to take advantage of the many cores of the GPU.

The usual strategy for implementing e.g. the force calculation is to calculate the force on each particle at a time, i.e. allocate one threat per particle, where a thread is a small segment of a process. In this example the process is the force calculation on all particles and the thread is the force calculation on one particle. This scheme works well for large system, where the number of particles, and therefore number of threads surpasses the number of cores by some amount (which should be large enough to hide latency due to memory access). However, when simulating systems with a smaller number of particles, the force calculations per particle should be split up in multiple threads in order to keep the number of threads sufficiently high to hide the latency. RUMD chooses what strategies to use by a script called the autotuner[44].
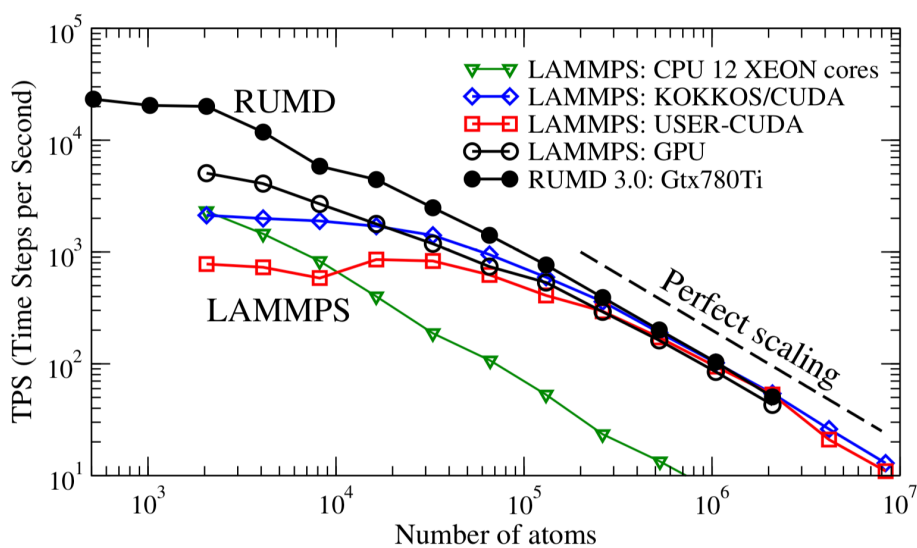
Figure 2.2: Benchmarking RUMD to LAMMPS[46, 47] by a melting FCC crystal simulated at constant energy. The figure plots number of calculated time step per second as function of system size. Perfect scaling (slope -1) is seen at large system sizes, where the number of particles vastly supersedes the number of cores on a GPU. At small system sizes RUMD outperforms LAMMPS. Figure from Bailey et al. [44].

Chapter 3

Hidden scale invariance

This chapter summarizes the isomorph theory, starting with discussing reduced units, as the hidden scale invariance of the isomorph theory is realised in the macroscopic reduced units. This is followed by a general presentation of the isomorph theory explaining how the hidden scale invariance and isomorph condition implies invariance of structure and dynamics along the configurational adiabats.

3.1 Reduced units

When dealing with a physical system there is not one single way of choosing what unit system to make use of - the most useful unit system in the kitchen might well be different from what is useful when building bridges or observing the universe. All unit systems how different they might be, must have some fundamental quantities (base units) in terms of which, everything else can be expressed. The SI-system has seven fundamental quantities, but in what follows only three is needed: length, energy and mass. It is often desirable to use "reduced units" - ie. to express quantities in terms of some characteristic measures in whatever system is being under investigation. When working with models in computer simulations the different parameters of the model offers such a reduced unit system: for molecular dynamics simulations with pair potentials, the potential pair energy $(v(r))$ as a function of the separation between the particles (r) is given by $\varepsilon \Phi(r/\sigma)$, where σ is a characteristic length and ε an energy. Mass can be scaled by the average mass $(\langle m \rangle)$ of the constituent particles. Time can now be expressed in units of $t_0 = \sigma \sqrt{\frac{m_0}{\varepsilon}}$. This unit system is often used and referred to as Lennard-Jones units or *microscopic reduced units*. It has the advantage of being completely determined from the parameters of the model, and thus

state point independent. This can be very useful when interest is in the specific model, but it suffers somewhat from being inaccessible in experiments. An alternative reduced unit system comes from the thermodynamical state point of the system: length from density stated as $l_0 = \rho^{-1/3}$, and energy from temperature stated as $E_0 = k_B T$. The mass is still measured by the average mass of the particles in the system. In this *macroscopic reduced unit*[48] system, time is measured in $t_0 = \rho^{-1/3}\sqrt{\frac{m_0}{k_B T}}$. This system has the advantage of being model independent and accessible in experiments. Moreover, as discovered by Rosenfeld this reduced unit system is the right for excess entropy scaling[48, 49] . In the framework provided here, the choice of the macroscopic reduced unit system can be justified from arguments related to the invariance of structure and dynamics in some systems: the structure can be quantified by the radial distribution function $g(r)$, but as this trivially scales with density as $\rho^{-1/3}$. With $l_0 = \rho^{-1/3}$ the trivial scaling is given. Likewise, the same dynamics require the mean-square displacements to be the same - especially at t_0, where $\langle v^2 \rangle \propto k_B T$. By choosing to scale energies by $E_0 = k_B T$ the trivial scaling is given.

In this work mostly the macroscopic reduced units will be used, and hence "reduced unit" will refer to macroscopic reduced units. If another unit system is used this will be clear from the text. One example of this is what is termed the EXP unit system, where $\varepsilon = \sigma = 1$. Throughout most of the thesis Boltzmann's constant will be equal to one.

3.2   Isomorph theory

The isomorph theory has been developing since 2008[50, 51] where among others the first two papers[52, 53] in a series of five[52–56] describing the theory, were published. At this time it was noticed that if a system has strong correlations (Pearson correlation coefficient larger than 0.9) between the fluctuations of the potential energies and the virial, then the potential can be approximated by an effective inverse power law (IPL) potential. A consequence of the strong correlations is emphasized in relation to viscous liquids, where the knowledge of one of the eight frequency-dependent thermoviscoelastic response functions implies knowledge of all[53] and that density scaling (scaling along lines with constant ρ^γ/T) could be applied with the slope of the correlation as the density scaling parameter γ. In 2009 followed paper three[54] and four[55] introducing the terms "isomorph" and "hidden scale invariance". An isomorph is a line in the phase diagram of the system along which the stucture and dynamics of the system in reduced units is invariant. Since the reduced excess entropy (the total entropy subtracted the entropy of the ideal gas at the given state point) also is invariant on the isomorphs they are also configurational adiabats. Note that not all configurational adiabats are isomorphs - it only applies in the presence of

strong correlations. Together these first four papers were the foundation of the framework of the isomorph theory as summarized in Ingebrigtsen et al. [7], until the thewory was generalized in the 2014 paper of Schrøder and Dyre [57]. In Schrøder and Dyre [57] it was shown that the theory up until then was a first-order approximation. As a consequence of the generalization the excess specific heat (C_V^{ex}) is allowed to change along the isomorphs, and the density scaling exponent to change with temperature.

The offset of the theory in the new formulation is that for Euler homogeneous pair-potentials ($v(\lambda r) = \lambda^\alpha v(r)$, $\lambda \in \mathbb{R}^+$) an inequality of the potential energies of two different configurations ($\mathbf{R}_a$ and $\mathbf{R}_b$) holds after rescaling the configurations to a new density ($\rho_{scale} = \lambda^{-3}\rho$):

$$U(\mathbf{R}_a) < U(\mathbf{R}_b) \Rightarrow U(\lambda\mathbf{R}_a) < U(\lambda\mathbf{R}_b). \qquad (3.1)$$

The condition above (Eq. (3.1)) is named *the isomorph condition* or *the hidden scale invariance.* Assuming the relation holds for a range of densities, scaling forth and back allows the $\Rightarrow$ to be replaced by a $\Leftrightarrow$, and thus the inequality can be replaced by an equality:

$$U(\mathbf{R}_a) = U(\mathbf{R}_b) \Leftrightarrow U(\lambda\mathbf{R}_a) = U(\lambda\mathbf{R}_b). \qquad (3.2)$$

Taking the derivative of the right hand expression gives that if the potential energies of two configurations are the same, then the virials are too - letting the microscopic virial be defined as $W(\mathbf{R}) \equiv -1/3\,\mathbf{R} \cdot \nabla U(\mathbf{R})$[58] :

$$\frac{\partial U(\lambda\mathbf{R}_a)}{\partial \lambda} = \frac{\partial U(\lambda\mathbf{R}_a)}{\partial \lambda}$$
$$\mathbf{R}_a\,\nabla U(\lambda\mathbf{R}_a) = \mathbf{R}_b\,\nabla U(\lambda\mathbf{R}_b)$$
$$W(\mathbf{R}_a) = W(\mathbf{R}_b). \qquad (3.3)$$

It follows that Euler homogeneous systems have perfect correlation between the fluctuations in U and W, and that for systems with strong correlations between U and W the isomorph condition in Eq. (3.1) is fulfilled to a good approximation. A direct test and illustration of the isomorph condition can be seen in Fig. 4.3 where 20 statistically independent configurations from equilibrium simulations have been rescaled to different densities.

The Hamiltonian of the system can be separated into an ideal gas contribution and a configuratinal contribution - an excess part. Likewise, the partition function and the entropy can. The excess entropy (S_{ex}) is the entropy of the system subtracted the entropy of an ideal gas at same state point. Since the ideal gas maximizes the entropy at a given state point, the excess entropy is always negative. Define a microscopic excess entropy as the thermodynamic equilibrium excess entropy of the state point with a given density and average potential energy[58]:

$$S_{ex}(\mathbf{R}) \equiv S_{ex}(\rho, U)|_{U=U(\mathbf{R})}. \qquad (3.4)$$

This relation is bijective as $T \equiv \left(\frac{\partial U}{\partial S_{\text{ex}}}\right)_\rho > 0$, and can therefore be inverted to express the potential energy as a function of excess entropy:

$$U(\mathbf{R}) = U(\rho, S_{\text{ex}}(\mathbf{R})). \tag{3.5}$$

Consider now two configuration at different densities ρ_1 and ρ_2 fulfilling the hidden scale invariance: $\mathbf{R}_1$ and $\mathbf{R}_2 = \lambda\mathbf{R}_1$. It can be shown[8, 57] that they have the same excess entropy: $S_{\text{ex}}(\mathbf{R}) = S_{\text{ex}}(\lambda\mathbf{R})$. Setting $\lambda = (\rho_1/\rho_2)^{1/3}$ it is clear that the excess entropy only depends on the reduced configuration $S_{\text{ex}}(\tilde{\mathbf{R}})$ and for the equilibrium potential energy at a given density and excess entropy:

$$U(\mathbf{R}) = U(\rho, S_{\text{ex}}(\tilde{\mathbf{R}})) \tag{3.6}$$

Equation (3.6) implies invariant structure and dynamic between points in phase space fulfilling hidden scale invariance. To show the invariance of the dynamics consider the forces of the system:

$$\frac{d^2}{dt^2}\mathbf{R} = \mathbf{F} = -\nabla U. \tag{3.7}$$

To find the reduced version, note that $\tilde{\nabla} = \rho^{-1/3}\nabla$ to get by Eq. (3.6)

$$\mathbf{F} = -\rho^{1/3}\tilde{\nabla}U(\rho, S_{\text{ex}}(\tilde{\mathbf{R}}))$$
$$= -\left(\frac{\partial U}{\partial S_{\text{ex}}}\right)_\rho \rho^{1/3}\tilde{\nabla}S_{\text{ex}}(\tilde{\mathbf{R}}). \tag{3.8}$$

Since the reduced force is $\tilde{\mathbf{F}} \equiv \frac{\rho^{-1/3}}{T}\mathbf{F}$ and $\left(\frac{\partial U}{\partial S_{\text{ex}}}\right)_\rho = T$, the reduced force can be expressed as

$$\tilde{\mathbf{F}} = -\tilde{\nabla}S_{\text{ex}}(\tilde{\mathbf{R}}) \tag{3.9}$$

which implies that the reduced dynamics and therefore also the reduced structure are invariant along the points fulfilling the hidden scale invariance. Such a set of points is what constitutes an isomorph.

3.2.1   Correlations

From Eq. (3.3) it is clear that the virial follow the potential energies in conforming with the hidden scale invariance. It can therefore as will be shown in the following, be written as a function of density and potential energy. Starting from the definition of the virial ($W(\mathbf{R}) \equiv -1/3\,\mathbf{R}\cdot\nabla U(\mathbf{R})$), and rewriting in following way: $W(\mathbf{R}) = \left.\frac{\partial U(\mathbf{R})}{\partial \ln \rho}\right|_{\tilde{\mathbf{R}}}$. From Eq. (3.6) the potential energy can be rewritten to get:

$$W(\mathbf{R}) = \left.\frac{\partial U(\rho, S_{\text{ex}})}{\partial \ln \rho}\cdot\right|_{S_{\text{ex}}=S_{\text{ex}}(\tilde{\mathbf{R}})} \tag{3.10}$$

This allows the virial to be written in the same way as the potential energy in Eq. (3.6):

$$W(\mathbf{R}) = W(\rho, S_{\text{ex}}(\tilde{\mathbf{R}})) \,. \tag{3.11}$$

Since the excess entropy is a function of the potential energy $S_{\text{ex}}(\tilde{\mathbf{R}}) = S(\rho, U(\mathbf{R}))$, so is the virial: $W(\rho, U(\tilde{\mathbf{R}}))$. This implies perfect correlation between the virial and the potential energy at fixed density for any physical relevant configuration. For systems with non-perfect correlations the hidden scale invariance only holds to some extend. How well depends on the strength of the correlations. The degree of correlation can be determined from the Pearson correlation of the fluctuations in the potential and the virial:

$$R(\rho, T) = \frac{\langle \Delta W \, \Delta U \rangle}{\sqrt{\langle (\Delta U)^2 \rangle \langle (\Delta W)^2 \rangle}} \,. \tag{3.12}$$

Figure 3.1 shows the time evolution of U and W for a strongly correlating
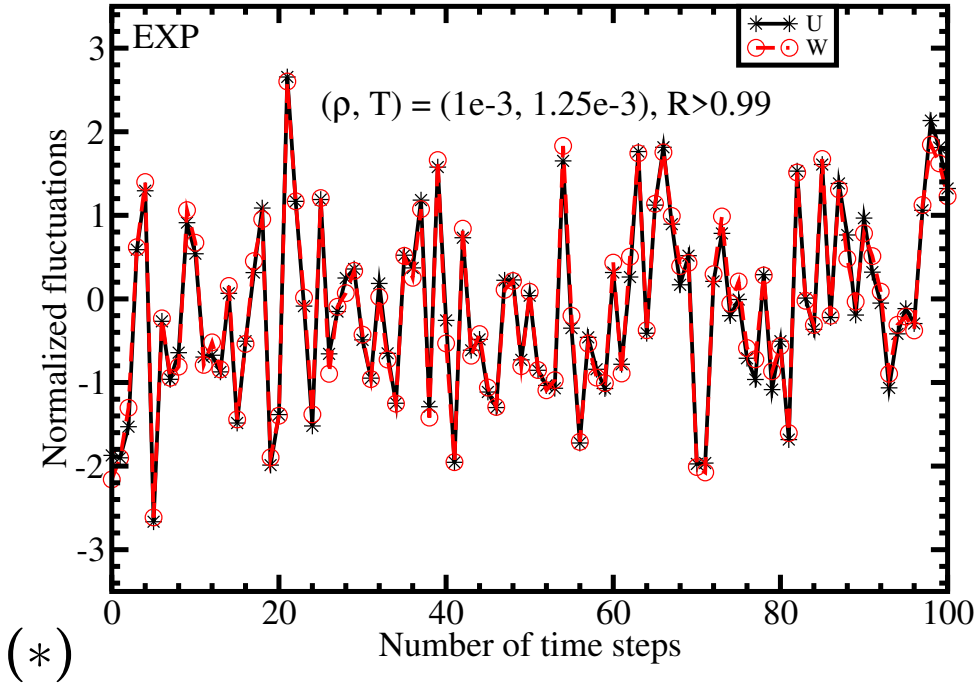
Figure 3.1: Normalized fluctuations of virial (red) and potential energy (black) at the state point $(\rho, T) = (10^{-3}, 1.25 \cdot 10^{-3})$. The correlations are strong ($R = 0.9916$), showing that the EXP pair potential system is R-simple at this state point.

state point. The fluctuations has been normalized and are seen to be almost completely collapsing. The normalization can be done since good correlation implies almost proportional fluctuations $\Delta U \approx \gamma \Delta W$. Rewriting this can give different expressions for the density scaling exponent as discussed in

Gnan et al. [55]. One of the possibilities is

$$\gamma = \frac{\langle \Delta W \Delta U \rangle}{\langle (\Delta U)^2 \rangle} \,. \tag{3.13}$$

In the next section it will be shown that this choice is equivalent with the slope of the configurational adiabats.

3.2.2   Density scaling exponents

The density scaling exponent is the slope of the configurational adiabats - the slope of the isomorphs if the system is strongly correlating - in the $(\log(\rho), \log(T))$-phase diagram:

$$\gamma(\rho, T) = \left(\frac{\partial \ln(T)}{\partial \ln(\rho)} \right)_{S_{\mathrm{ex}}} \,. \tag{3.14}$$

Since the isomorphs is configurational adibats dS_{ex} must be zero giving:

$$\left(\frac{\partial S_{\mathrm{ex}}}{\partial T} \right)_V dT + \left(\frac{\partial S_{\mathrm{ex}}}{\partial V} \right)_T dV = 0 \,. \tag{3.15}$$

By the Maxwell relation and $P_{\mathrm{ex}} = W/V$ this can be rewritten as

$$\left(\frac{\partial S_{\mathrm{ex}}}{\partial T} \right)_V T d \ln(T) - \left(\frac{\partial W}{\partial T} \right)_V d \ln(\rho) = 0 \,, \tag{3.16}$$

combining with $dU = TdS - PdV$ to get

$$\left(\frac{\partial U}{\partial T} \right)_V d \ln(T) - \left(\frac{\partial W}{\partial T} \right)_V d \ln(\rho) = 0 \,. \tag{3.17}$$

The thermodynamical derivatives can be connected to the fluctuations by $\left(\frac{\partial A}{\partial \beta} \right)_V = -\langle \Delta A \Delta U \rangle$[52], which gives:

$$\left(\frac{\partial W}{\partial T} \right)_V = -\langle \Delta W \Delta U \rangle \tag{3.18}$$

$$\left(\frac{\partial U}{\partial T} \right)_V = -\langle (\Delta U)^2 \rangle \,. \tag{3.19}$$

Combined this gives that the density scaling exponent determined form the fluctuations is the same as the density scaling exponent expressed by the slope of the configurational adiabats in log-log phase diagram:

$$\left(\frac{\partial \ln(T)}{\partial \ln(\rho)} \right)_{S_{\mathrm{ex}}} = \frac{\langle \Delta W \Delta U \rangle}{\langle (\Delta U)^2 \rangle} \,. \tag{3.20}$$

The isomorph theory is in its nature an approximate theory as only IPL-systems has perfect correlation. Testing the theory is illusive due to its approximate nature: what observables are contradicting the theory, and what are expected deviations due to non-perfect correlations? Nonetheless is it the succeeds the theory to provide a coherent framework for understanding the properties of simple liquids and excess entropy scaling.

This concludes the introductory part and sets the scene for the study of the EXP-potential in the next.

Part I

The EXP-potential

Chapter 4

Phase diagram of EXP

In this chapter begins with an overview of the phases of the EXP-system, before giving the a description of the simulation details. It is the aim to equip the reader with all the relevant knowledge to do further research using the potential. Afterwards the findings of the correlation coefficient (R), the density scaling exponent (γ), the structure (radial distribution function) and dynamics (mean-square displacements and diffusion), and the thermodynamics ($\tilde{U}$, $\tilde{W}$, $\tilde{p}$ and $\tilde{c}_V^{\text{ex}}$) reported in the phase diagram, along isotherms and along isochores. The chapter concludes with a section on the gas phase where prediction for the correlation coefficient R and the density scaling parameter are derived.

The simplicity of the EXP pair potential is appealing: two parameters corresponding to the thermodynamic control variables, namely density and temperature. An exploration of the (ρ, T) phase diagram of one EXP system is thus sufficient as any other EXP system can be achieved by a simple rescaling. The state point reported is in the EXP unit system with density in units of $1/\sigma^3$ and temperature in units of ε/k_B. All other quantities is reported in macroscopic reduced units. In this system the potential energy barrier at zero separation distance is one and thus if temperature is on that order, particles will often have enough energy to pass through one another. If temperature is raised higher the system is expected to approach an ideal gas. In this study temperatures spanning six decades - from 10^{-6} to 1 - and densities spanning three decades - from 10^{-5} to 10^{-2} - is examined. The state points investigated can be seen in Fig. 4.1. Here additionally the freezing line is drawn [1] is drawn. All densities and temperatures can be seen in Chapter 7

---

[1] the freezing line is approximated by a $h_2(\rho)$-approximate isomorph fitted by eye to match what is known about the position of the freezing and melting curve (see Section 5.4)

(*)
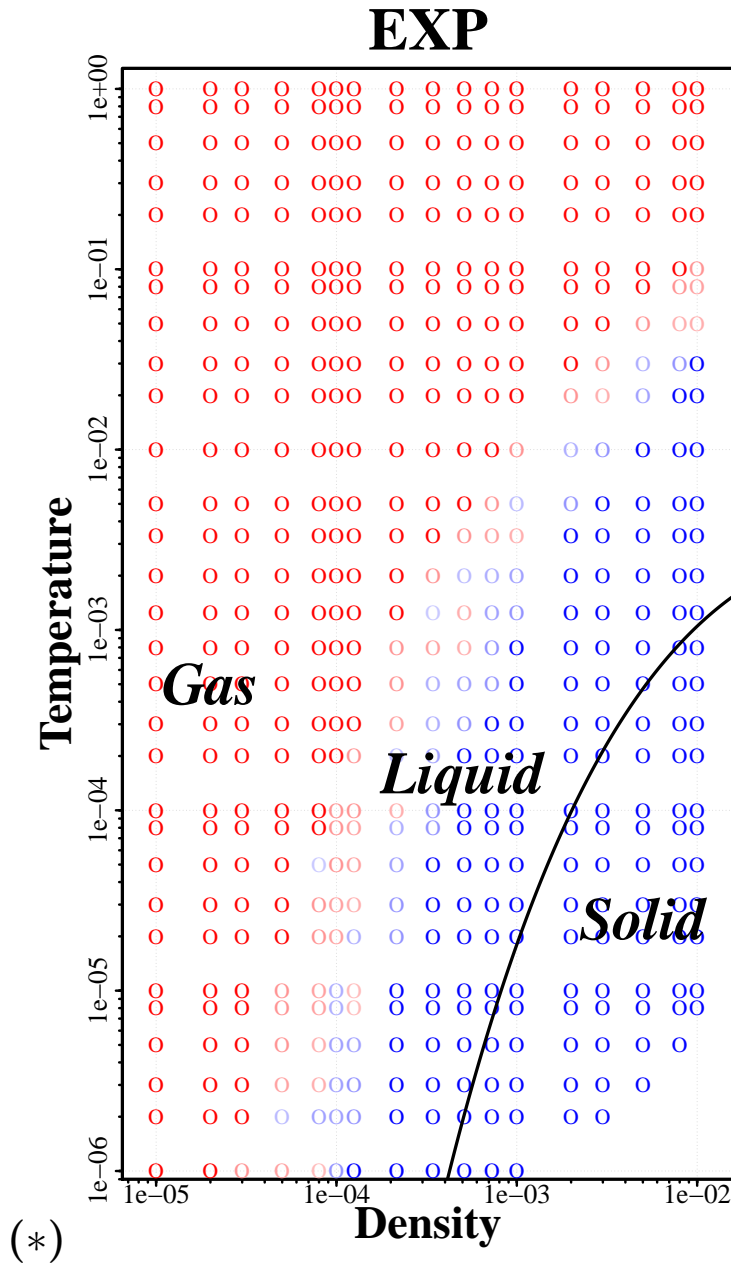
Figure 4.1: Log-log density-temperature phase diagram of the EXP system given by the numerically investgated state points. Gas-phase state points are shoven in red, liquid and solid condensed-phase state points are shown in blue. Due to the EXP pair potential being purely repulsive no gas-liquid phase transition and no gas-liquid coexistence region exists. Instead the gas and liquid phases change gradually into one another. Liquid state points are distinguished pragmatically from those of the gas phase by having a first minimum in the pair-distribution function. The solid-liquid coexistence region is covered by the black line, which is the approximate melting-line isomorph calculated by the $h_2(\rho)$ method with $\Lambda = 1.045$ (See Section 5.4).

The EXP system has as other purely repulsive systems a fluid phase with a domain, where the structure and dynamic behave like a liquid in having multiple peaks in the radial distribution function, a nearest neighbour-distance on the order of one, and, hence, a transition to diffusive motion occurring when the mean-square displacement is on that order, and that it can be crystallized into a solid - probably in a bcc or fcc configuration depending on the state point. As previously mentioned, systems with no attractive forces cannot support a liquid-gas interface, and there can be no critical point and no liquid-gas first order thermodynamic phase transition. Naturally this applies likewise for the EXP system. In the explored region at the higher temperatures, and in the low density-low temperature part of the phase diagram, the system behaves like a gas - the physics being dominated by the single pair interaction (see Fig. 4.1). In this interacting gas-region predictions are derived for the behavior of the system based on Enskog theory. Since a sharp phase transition is present between gas and liquid, a structural signature is given to distinguish between the two phases. The transition between the phases is smooth as indicated in Fig. 4.1.

4.1 Simulating the EXP system

The EXP system was simulated using Roskilde University Molecular Dynamics (RUMD) open-source software[44] on NVIDIA graphic-cards of different generations in the Roskilde University HPC center. The density-temperature phase diagram of the system was explored by keeping temperature and density at unity ($T = \rho = 1$) in the NVT-simulations, and then exploring phase space by changing the parameters ε and σ - thus taking advantage of the one-to-one relations between temperature and the energy parameter, and density and the length parameter. The reduced unit time-step was kept constant at $\Delta \tilde{t} = 0.0025$ in most of the phase diagram - except for state points at $T = 10^{-6}$ with $\rho > 2 \cdot 10^{-4}$ where $\Delta \tilde{t} = 0.002$. The integrator was a leap-frog algorithm, and the temperature was controlled by a Nose-Hoover thermostat with a characteristic reduced time of 0.2 - the default value in RUMD, which was found to work well. An initial configuration with 1000 particles was used. The particles was thought to be in a simple cubic configuration, but careful investigation latter revealed every second layer in the z-direction to be shifted half a unit cell in x- and in y-direction. This was due to an error in a early version of RUMD. The initial configuration was a "stretched bcc" with unit cell dimensions $L \times L \times 2L$. In Bacher et al. [26, 27] this is reported as a single cubic crystal. This is probably insignificant as the system is equilibrated before data collection. The 1000 particle stretched bcc configuration was used in most state points. State points in the temperature range $1.5 \cdot 10^{-6}$ to $1.5 \cdot 10^{-3}$ and density larger than $1.5 \cdot 10^{-3}$ had initially a body centred cubic configuration with
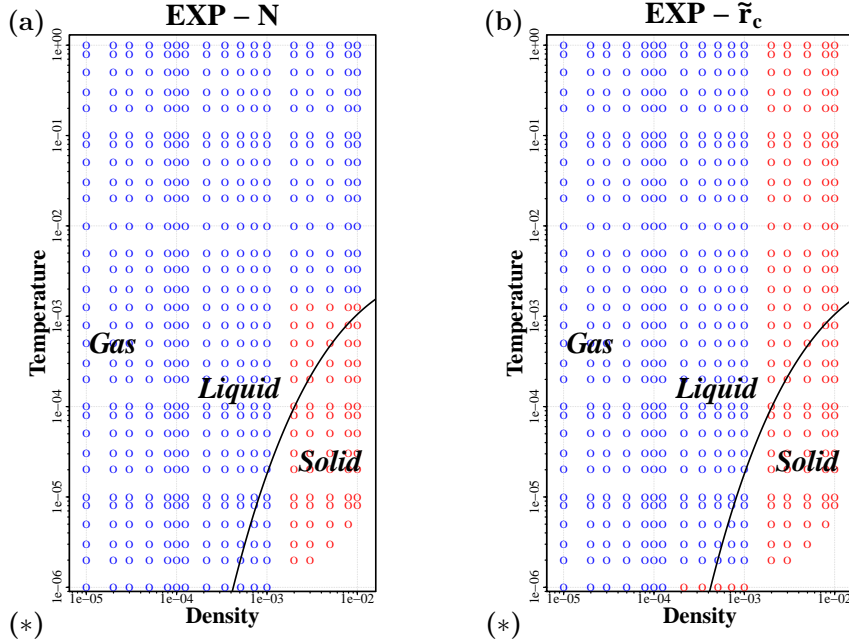
Figure 4.2: (a) Number of particles N simulated at different state points where blue indicates 1000 particles and red 2000. (b) Shifted-force cutoff distances r_c in reduced units, $\tilde{r}_c \equiv r_c \rho^{1/3}$, where blue indicates $\tilde{r}_c = 2$ and red $\tilde{r}_c = 4$.

$N = 2000$ (see Fig. 4.2(a)). The initial configuration was equilibrated at the desired state point for 10^7 time steps ensuring a reduced mean-square displacement of at least 1000 and a decay of the self-part of the intermediate scatter function to less than $1/e$ for fluid state points. The number of time steps in the data collection was also 10^7, except for state points at $T = 10^{-6}$ and $\rho > 2 \cdot 10^{-4}$ where it was doubled to $2 \cdot 10^7$ time steps.

A Shifted Force cutoff[30, 59] was used with a constant reduced unit cutoff distance ($\tilde{r}_c \equiv r_c \rho^{\frac{1}{3}}$) of two or four - blue points and red points, respectively, on Fig. 4.2(b). By using reduced unit cutoff the cutoff scales with density and thus increases when density decreases and vice-versa. Which is part of the reason for the need for larger cutoff in the highest densities. Had a reduced unit cutoff not been used, the cutoff would need to be changed more often. The cutoff distance was also increased in the low temperature, high density region of phase diagram, because interaction strengths remain considerably high at $\tilde{r} = 2\rho^{\frac{1}{3}}$ due to the slow decline of the potential. The choice of a Shifted Force cutoff aids to keep the cutoff as short as possible[30] The Shifted-force cutoff was chosen, as it allows for a shorter cutoff distance compared to Shifted-potential cut off. RUMD is written in single precision, which can be a problem in some cases[44]. Therefore a customized version with double precisions was use to validate simulation results in selected state

points. Good agreement was found and it was concluded that single precision works well in most of the explored phase diagram. Only in the high density, low temperature part, did single precision become insufficient. As this is deep in the crystalline phase, the phase points are left out.

The above mentioned simulation details explain how to simulate the potential in the reported region. Moving outside this region one need to take some precautions: If the density is decreased to even lower values, the force and potential decreases to values below $2^{-126} = 1.1755 \cdot 10^{-38}$ at a critical value (r_{critical}) before the cutoff - and thus rounded to zero due to the single precision of RUMD. The critical value at density 10^{-5} is 2 or below ($r_{\text{critical}} < 2$) for temperatures at 0.0041 or above ($T > 0.0041$). The temperature dependence is fairly week, so at temperature 1 the critical distance is $r_{\text{critical}} = 1.88$. This is a concern, but from kinetic gas theory (Section 4.6) the typical interaction distance or effective particle radius (r_0) of the EXP system can be determined from $r_0 = -\rho^{\frac{1}{3}} \ln(T)$. Taking the ratio gives $r_{\text{critical}} = -\ln(2^{-126}) \cdot r_0 \approx 87 r_0$.

This issue does not only affect the EXP potential, but as described in Chapter 2 also the linear term added to the potential in the shifted force cutoff is affected by (r_{critical}), since it dependence on the value of the potential energy at the cutoff distance. This means that if $r_{\text{critical}} < r_{cut}$, then the linear term will be zero. If care is not taken in the implementation of the potential and in the calculations of the force and potential energy it can happen earlier. In the most straightforward implementation, the linear term will be rounded to zero when $T > 0.0041$ at $\rho = 10^{-5}$. The effect will probably be minute, as the linear term is very small compared to the potential energy at the typical interaction distance - an order 10^{-35} lower. The discontinuity will likewise be unimportant as this is where the potential decreases to zero in machine precision as described above.

Based on the above, we conclude that single precision is sufficient in the reported state points and speculate that it can be used in even lower densities if one consider the above mentioned points.Simulating state points at $T < 10^{-6}$ should not be a problem, as long as the system remains in the fluid state. If density is increased into the crystal, the numerical values of the potential energies (and the forces) of the interactions at the typical nearest neighbour distance will increase dramatically due to the closeness of the particles. This will give rise to large numbers, which by itself is handled by the floating numbers, but the change of the potential energies - and thereby forces - is controlled by the kinetic energy. And as the temperature is low, the fluctuations in the potential energy is likewise small. Large numbers with small fluctuations pose a challenge to the use of single precision floating numbers.

4.2   Correlation

The signature of a system obeying the isomorph theory is, that it has a Pearson correlation coefficient of the flutuations of the potential energy and virial (R) larger that 0.9. The higher the value of R, the better the agreement with isomorph condition (Eq. (3.1)) is expected. In Fig. 3.1 the normalized fluctuations of the potential energy and the virial in 100 time steps in a dilute liquid state point close to the liquid-gas transition is plotted. As seen the fluctuations correlate very well - also expressed in the value of the Pearson correlation coefficient being larger than 0.99.

$(*)$
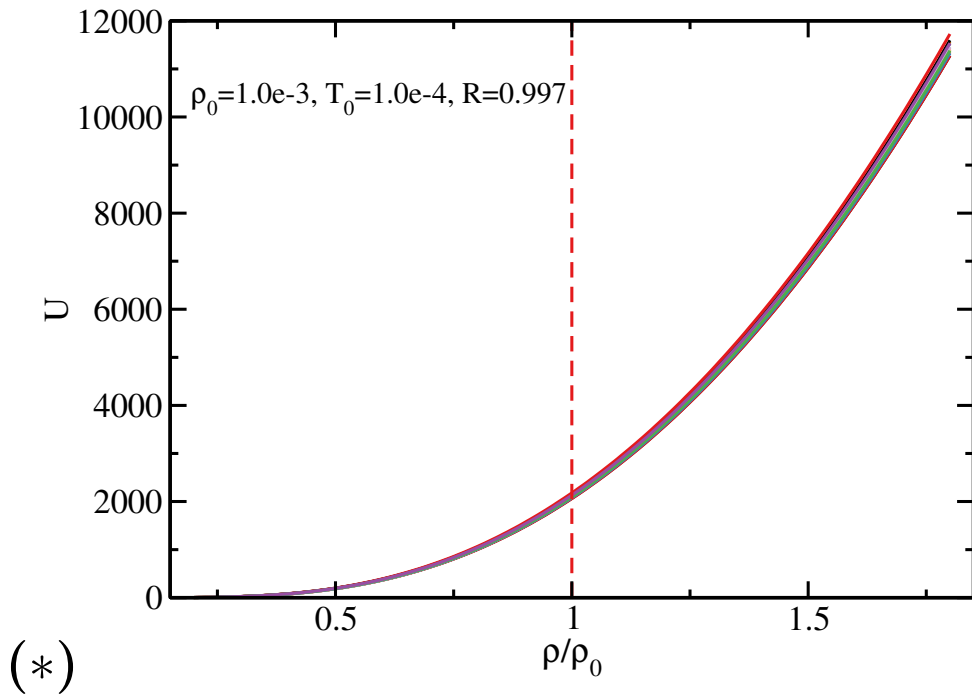
Figure 4.3:   Checking Eq. (3.1) for the EXP pair-potential systems. Potential energies of statistically independent configurations from an equilibrium simulation of a system with 1000 particles at density $\rho = 10^{-3}$ and temperature $T = 10^{-4}$ subsequently scaled uniformly to different densities.

In the updated version of the isomorph theory[57] the condition for a system being isomorphic was condensed in Eq. (3.1). Figures 4.3 and 4.4 demonstrates that the EXP system to a good approximation obeys Eq. (3.1) in part of its phase diagram and in Fig. 4.6 correlation between the potential energies of unscaled and scaled configurations is observed in agreement with expectations from Eq. (3.1) and confirming the system have hidden scale invariance.

In Figs. 4.3 and 4.4(a) 20 statistically independent configuration from a simulation at density $\rho = 10^{-3}$ and temperature $T = 10^{-4}$ are selected and

rescaled to densities from $0.2 \cdot 10^3$ to $1.8 \cdot 10^3$, and the potential energies of the rescaled configuration are determined. In Fig. 4.3 the potential energies of the configurations are plotted and in Fig. 4.4(a) the average potential energy is subtracted each configuration allowing for better inspection of crossings. Only a few crossing are observed, meaning that the system to a good approximation obeys the hidden scale invariance condition (Eq. (3.1)). A system in complete agreement with the hidden scale invariance condition has no crossings. Panel (b) and (c) is the same as in (a), but at different temperatures: in (b) the temperature is increased to $T = 10^{-2}$ leading to a state point with lower R-value, more crossings, and thus less compliance with the hidden scale invariance. In (c) temperature is decreased to $T = 10^{-6}$ giving a state point with higher R-value, fewer crossings, and better compliance with the hidden scale invariance. In Fig. 4.5 the same data is presented scaled by the variance. Inspections of crossings is clearly seen.

The Pearson correlation coefficient remains the practical signature of compliance with the hidden scale invariance, as it is computationally more accessible. In Fig. 4.7(b) the correlation coefficient of 499 state points[2] is reported in a log-log density-temperature phase diagram, while (a) shows a color plot with interpolation of the correlation between the simulated state points. The figure shows that the correlation is mostly dependant on the temperature - only in the highest densities does correlation appears to deteriorate with increasing density (also clearly seen along the isotherms in Fig. 4.9(b)).

---

[2]12 of them is hidden by the legend
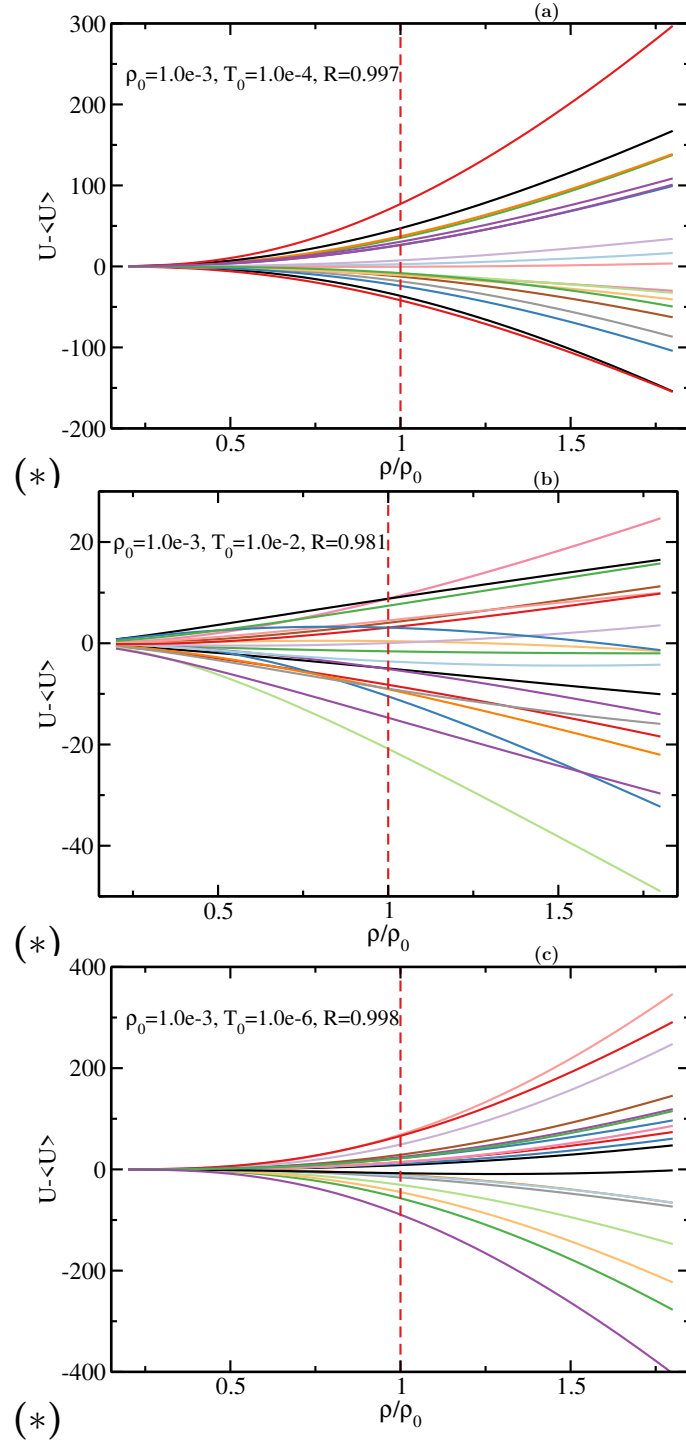
Figure 4.4: (a) Same data as in Fig. 4.3 with the average potential energy subtracted, making it easier to compare to the prediction of Eq. (3.1) that no crossings take place, i.e., that the ordering of configurations according to their potential energies is maintained upon scaling. This is seen to apply to a good approximation. (b) Same as in (a) for configurations taken from an equilibrium simulations at $\rho = 10^{-3}$ and $T = 10^{-2}$. There are now more crossings, meaning that eq:hs is obeyed to a smaller degree. (c) Same as in (a) for configurations taken from an equilibrium simulations at $\rho = 10^{-3}$ and $T = 10^{-6}$. Close inspection reveals that there are here fewer crossings, which means that Eq. (3.1) is obeyed to a higher degree.
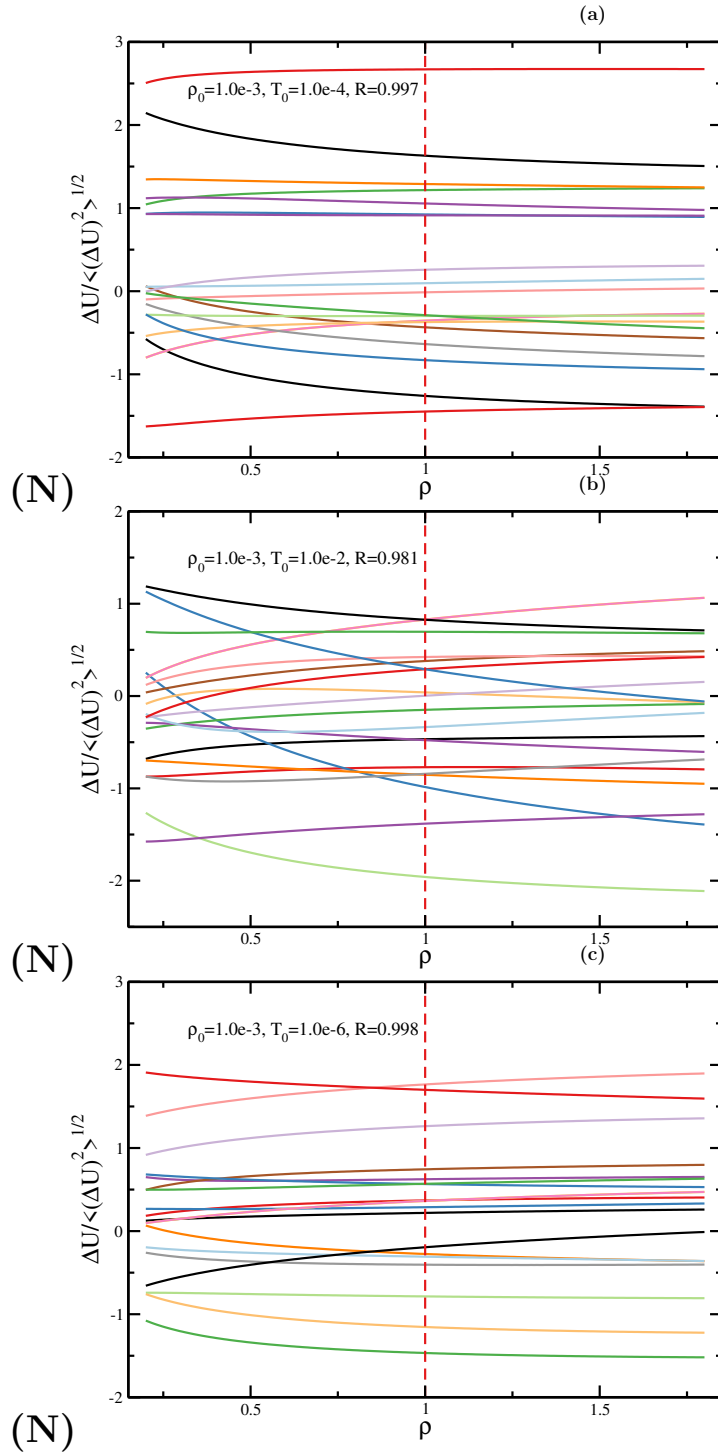
Figure 4.5: Same data as in Fig. 4.4 scaled by the variance as done in Schrøder and Dyre [57] to allow a closer inspection. The conclusions from Fig. 4.4 is conformed.
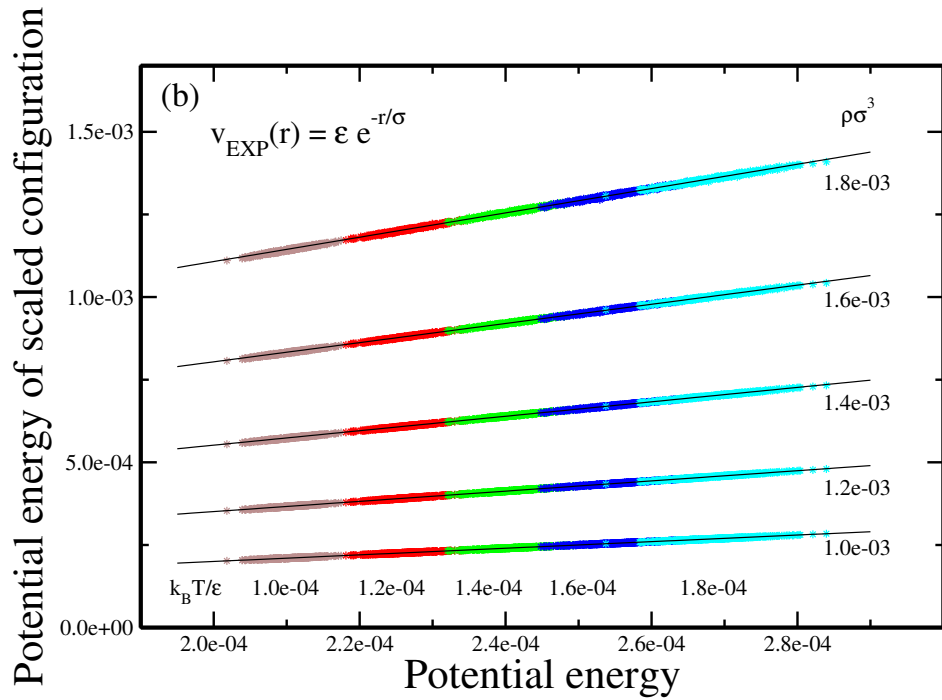
Figure 4.6: Potential energies and scaled potential energies of configurations from five state points on the $1 \cdot 10^{-3}$-isochore, with temperatures between $1.0 \cdot 10^{-4}$ and $1.8 \cdot 10^{-4}$ (bottom scatter plots), scaled to four densities between $1.2 \cdot 10^{-3}$ and $1.8 \cdot 10^{-3}$ as indicated. There is a strong correlation between the scaled and non-scaled potential energies, which as shown in Section 5.2 to be a prediction of Eq. (3.1). The lines are best fit to the green points [reproduced from Bacher et al. [25]].
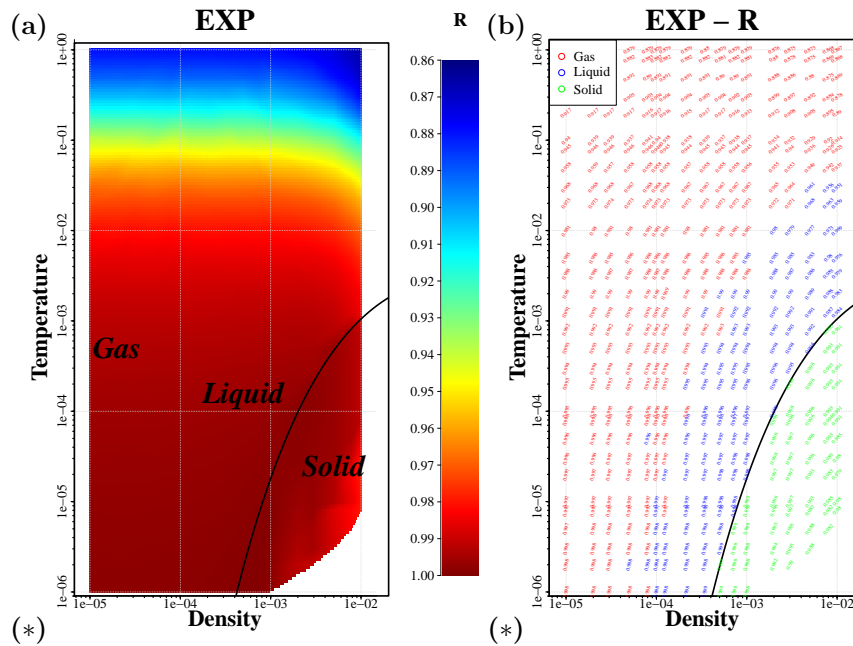
Figure 4.7: (a) Log-log density-temperature phase diagram of the EXP system with the color coding giving the virial potential-energy correlation coefficient R. Strong correlations is present at most state points, showing that the EXP system has hidden scale invarinance in the low-temperature part of its phase diagram. Except for the highest densities, the correlation coefficient depends on the temperature. The full black line is the melting line isomorph, the thickness of which corresponds roughly to the solid-liquid coexistence region (see Section 5.4). (b) The values of R at the different state points. At each state point the value of R is written with a slope marking the direction of the isomorph through the state point in question; red indicates gas, blue liquid, and green solid phase state points.

4.3   Density scaling exponent

In 4.3 the density scaling exponent was defined as

$$\gamma \equiv \left(\frac{\partial \ln T}{\partial \ln \rho} \right)_{S_{\mathrm{ex}}} \tag{4.1}$$

and was shown to be easily determined in NVT-simulations by

$$\gamma = \frac{\langle \Delta U \Delta W \rangle}{\langle (\Delta U)^2 \rangle} \,. \tag{4.2}$$

The density scaling exponent expresses the slope of lines of constant excess entropy in the log-log density-temperature phase diagram - and thus also the isomorphs, because the constant S_{ex}-lines are the isomorphs as the excess entropy is an isomorph invariant quantity when $R > 0.9$.

The density scaling exponent appears in experimental observation of many quantities as they are invariant along lines of constant $\frac{\rho^{\gamma}}{T}$. Often γ is treated as a constant, due to limited range of densities accessible in experiments. In computer simulations density of many orders of magnitude is accessible. Here is usually found that the density scaling parameter varies. Within the framework of the isomorph theory, the variation of γ with density is well explained[8].

As seen in Fig. 4.8 the EXP system also exhibits a density dependent γ, but only in the low temperature, high density region, where the system is close to the freezing line. Likewise from Fig. 4.8 a region where γ is constant along the isochores is observed: In the low densities γ is almost constant across densities spanning 1-2 decades. Instead a temperature dependence is present in this region. These two domains - for which approximate analytical predictions for the density scaling exponent can be constructed - are separated by a smooth transition region.

In the dense region, where the system is in a crystalline or a dense liquid state, the physics is dominated by strong interactions with many nearest neighbours. In Bailey et al. [53] the Lennard-Jones (LJ) pair-potential liquid was considered and it was found to be well approximated by an "extended inverse power law" (eIPL) potential. The eIPL potential is given by an inverse power law (Ar^{-n}) added with a linear term $(B + Cr)$. In a fixed volume simulation, the linear term contribution to the total potential energy and the virial stay more or less constant for small particle displacement - as some inter-particle distances decreases when other increases. Consequently, it does not contribute significantly to the fluctuations in these quantities[53], and the fluctuations are mostly controlled by the inverse power law term. Inverse power law systems have perfect correlation and the density scaling exponent is determined by $\frac{n}{3}$, with n being the exponent of the IPL. Methods for determining the local effective power-law exponent in the eIPL that best
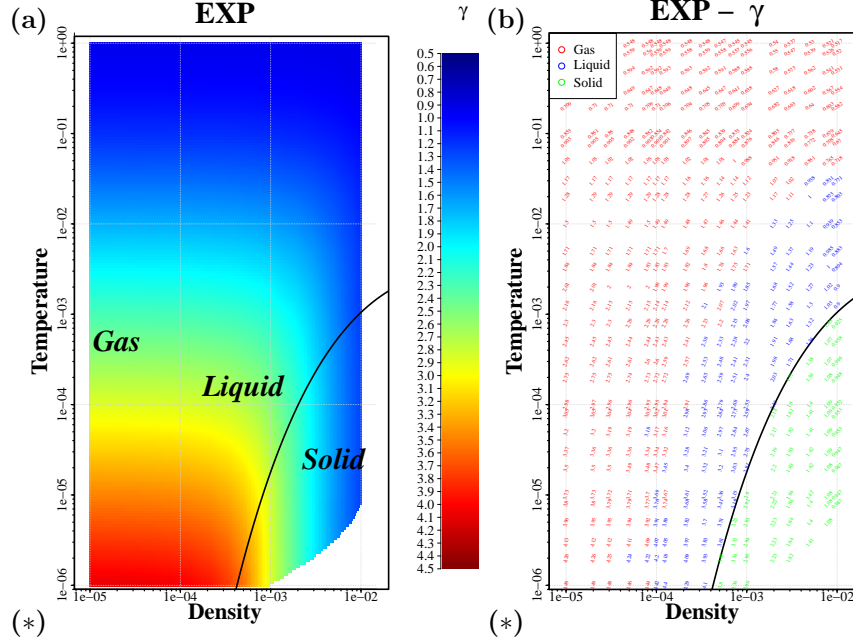
Figure 4.8: Temperature and density variation of the density-scaling exponent γ. (a) shows the density-scaling exponent in a continuous color plot. This figure visualizes the fact that γ at low densities is mainly temperature dependent, whereas it at high densities and low temperatures (i.e., in the condensed liquid and solid phases) is mainly density dependent. (b) reports the numerical values of γ at the different state points. The colors indicate the three phases. The full black line is the approximate melting-line isomorph, covering the entire liquid-solid coexistence region (see Section 5.4).

matches a system in a given state point is discussed in Bailey et al. [53], and it is showed that the local effective power-law exponent can be found by the following relation

$$n_p(r) \;=\; -p \;-\; r\frac{v^{(p+1)}(r)}{v^{(p)}(r)}\,, \tag{4.3}$$

where $p \in \mathbb{Z}^+$ and $v^{(p)}(r)$ is the pth derivative of $v(r)$. Note that for IPL systems this gives the exponent of the system independent of p. For non-IPL system an approximate state point dependent γ can be estimated by utilizing the fact that IPL system's has perfect correlation with $\gamma = \frac{n}{3}$. Thus using the n_p-approximate IPL exponent gives

$$\gamma \;\cong\; \left.\frac{n_p(r)}{3}\right|_r \tag{4.4}$$

evaluated in some characteristic distance. The characteristic distance varies with the state point, but how it varies depends on the physics controlling the interaction.

Evaluating $p = 2$ in the typical nearest neighbour distance was found to work well for the Lennard-Jones system in the condensed phase[53]and lets the square of an effective reduced "Einstein" frequency of a single particle pair be isomorph invariant[60]. Different values of p have been used in different settings: In Stillinger [61] the logarithmic derivative - corresponding to $p = 0$ - is used to estimate an effective exponent for the Gaussian core system. In Khrapak et al. [62] n_1 evaluated at mean interparticle distance is used around the melting curve.

Hence, there is a difference between the dilute and gaseous region, and the dense and crystalline region. This will be an object for further exploration in the following. As will be seen, the properties of the dense and crystalline region are clearly seen along the isotherms, while the properties of the dilute and gaseous region are clear along the isochores. This separation into regimes is also observed for other systems[63] and in experiments[64].

Isotherms

In the dense liquid and crystal using the n_2, and evaluating it in the approximately nearest neighbor distance when $\Lambda \cong 1$ in $r = \Lambda \rho^{-1/3}$, gives the following estimate for the density-scaling exponent:

$$\gamma(\rho) \cong -\frac{2}{3} + \frac{1}{3}\Lambda \rho^{-1/3} \tag{4.5}$$

In Fig. 4.9(a) Eq. (4.5) is evaluated in $\Lambda = 1.075$ giving the black dashed line. The value of Λ is in agreement with values of γ found in the crystalline phase not far from the melting line. From Fig. 4.9(b) it is clear that the correlation coefficient almost entirely depends on the temperature - only in the highest density is a small density dependence observed. This density dependent decorrelation is expected, since when the density scaling exponent decreases towards zero so must the correlation. If the n_2-assumption evaluated at $\Lambda \cong 1$ holds for even larger densities, the density exponent of the EXP system will be zero at densities around 0.125 and thus also the correlation. The density scaling exponent will even be negative if the n_2 prediction hold to even higher densities. This would signify re-entrant melting - a phenomenon also observed in the Gaussian core model[**?**]. At density 10^{-2} the approximate IPL exponent (n) is around 2.6, which is consistent with where the IPL systems become thermodynamical unstable unless a background screening potential is introduced[62]

Isochores

A crude estimate for the state point dependence of γ in the dilute phase can be obtained from generalizing the findings from [60] by replacing "the typical nearest neighbour distance" with "the typical interaction distance".

The typical interaction distance in the dilute phase can be obtained from equalizing the potential energy of the pair interactions to $k_B T$ given by the temperature as also done in Stillinger [61]. Following this route the density scaling exponent can be estimated by the following relation as will be shown in Section 5.3

$$\gamma\left(T\right) \cong -\frac{p}{3} - \frac{1}{3}\ln(T).$$ (4.6)

This linear dependence in $\ln(T)$ holds well in the gas-phase as seen in Fig. 4.10(a), where the black dashed line is almost a straight line with slope $1/3$ at low temperatures. In the high temperatures the black dashed line is no longer approximately straight. The expression for the line will be derived in Section 4.6.
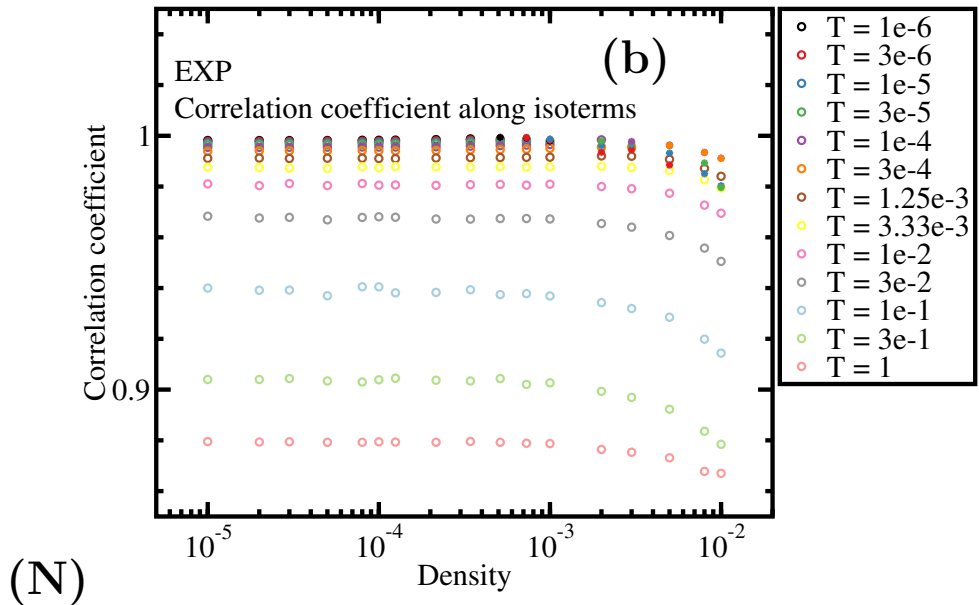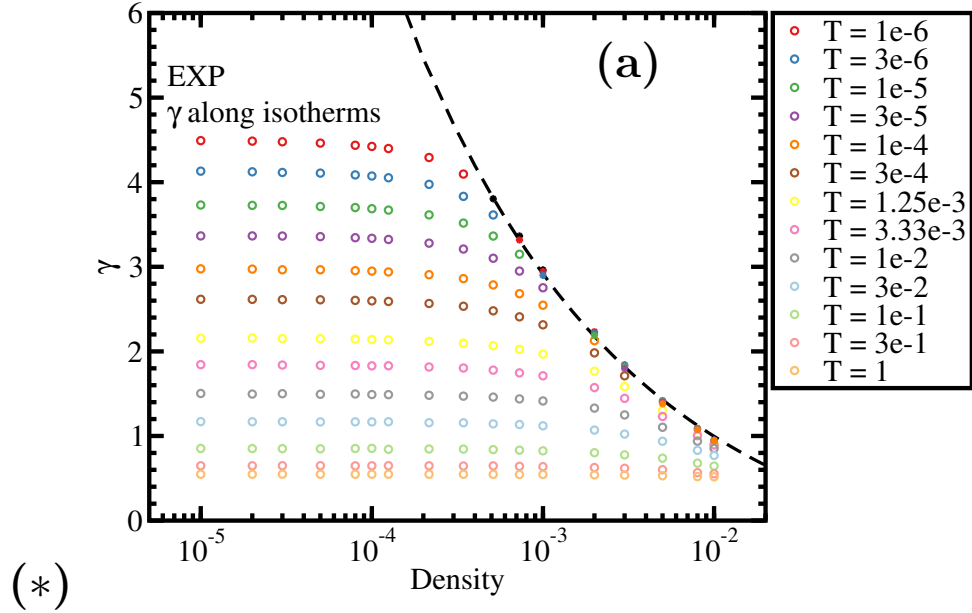
Figure 4.9: *Left:* γ along isotherms. At low densities γ is seen to be temperature dependant, while being density dependant in the dense fluid and solid. The density dependence is well described by $\gamma = {}^{n^{(2)}(\Lambda)}\!/\!{}_3$[53] evaluated at $\Lambda = 1.075$. *Right:* Correlation between potential energy and virial is almost only dependant on temperature. State points from the fluid part of figure 4.1 has open symbol, while stars corresponds to crystal state points.
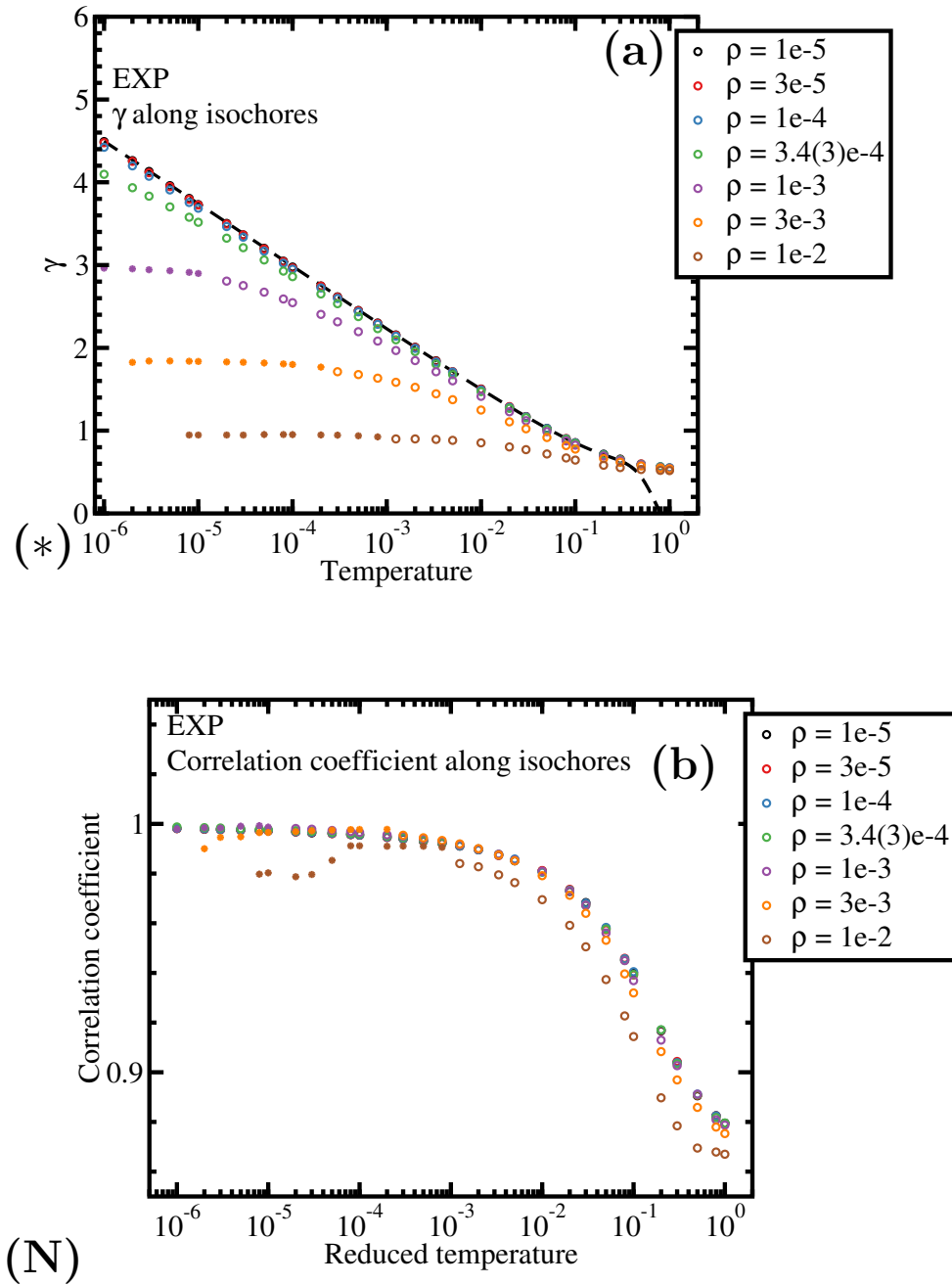
Figure 4.10: *Left:* γ along isochores. At the low temperatures, along the high density isochores γ is seen to be a function of density, while it in the low densities is temperature dependant following the black dashed line - a prediction for the temperature dependant γ in the gas phase (see more in Section 4.6). At the low temperatures the line is well approximated by the prediction of Eq. (4.6). Deviation from the prediction is observed for all densities at high temperature. *Right:* Correlation between potential energy and virial is almost only dependant on temperature: As temperature increases correlation drops, to become lower that 0.9 around the same temperature as γ deviates from the prediction. Fluid: Open symbols, Crystal: Stars. *Note:* Simulations in the crystalline phase is recrystallized. As a consequence the crystals are imperfect and have many defects. Non-equilibrium simulation lead to uncertainties in the estimation of R and γ.

4.4   Structure and dynamics

The structure of the EXP-system in the simulated region can be quantified
by the maximum height of the first peak in the radial distribution function
as shown in Fig. 4.11 and the dynamics by the reduced diffusion constant
($\tilde{D}$). For both the structure (Fig. 4.11) and the dynamics (Fig. 4.12) five
isomorphs have been drawn for comparison with this prediction. The iso-
morphs will be discussed in details in chapter 5.

In Fig. 4.11 small deviations are seen between the isomorphs and the
white contour lines. This deviation is well known, when structure is probed
by the first peak.   The deviation can be understood by considering the
invariant structural quantity to be the area of the peak (the number of
nearest neighbours) combined with fact that γ changes along the isomorph
line (shown on Fig. 5.7): the steepness of the initial departure of the radial
distribution from zero) depends on γ, and thus the height must decrease to
preserve the area under the first peak. This is because the radial distribution
function at small distances can be described by the Boltzmann distribution
$g(r) \sim \exp{(-v(r)/k_B T)}$[6], and the higher the γ-value, the harder the poten-
tial, the steeper the rise of the radial distribution function. This is related to
the pair potential not being isomorph invariant. The deep crystalline region
of the EXP-system is not included in Fig. 4.23, but the maximum continue
to increase as temperature is lowered and density increased. The maximum
value obtained in the simulations was almost 28. Figure 4.11 also reveals a
large region of phase space with very little structure. At the highest tem-
peratures the "peak" is noise in the calculated pair distribution function,
because the system is in a state where the average kinetic energy is on the
order of the zero-distance potential energy barrier and thereby allowing the
particles to pass through one another.

The dynamic as quantified by the reduced unit diffusion coefficient is seen
to follow the isomorphs well, which is a clear sign of its isomorphic invariance
- The excess entropy scaling of the diffusion has been discussed[63, 65, 66]
since the findings of Rosenfeld [48] . The diffusion coefficient is calculated
from the diffusive part of the mean-square displacement - a method giving
good result in the liquid phase, but should be used with caution in both
the solid and gas, as it becomes inaccurate in the crystal due to lack of
diffusion, and long simulations are needed in the gas phase in order to reach
the diffusive state. According to kinetic theory the diffusion coefficient in
the gas phase is proportional to the product of mean-free path and the
thermal velocity ($D \propto l\,v$). The thermal velocity is proportional to l_0/t_0,
as $l_0 = \rho^{-1/3}$, and $t_0 = \rho^{-1/3}\sqrt{m/k_B T}$ giving $\frac{l_0}{t_0} \propto \sqrt{k_B T/m} \propto v$ and the
mean-free path (μ) inversely proportional to $\rho\, r_0^2$, as the distance travel by a
particle is l_0, the volume swept in the same motion is proportional to $r_0^2 l_0$,
and the number of particles encountered is given by multiplying volume with

density - thus $\mu \propto \frac{l_0}{r_0^2 l_0 \rho} = \frac{1}{r_0^2 \rho}$, where r_0 is the effective radius of a particle. r_0 can be estimated from: $v(r_c) = k_b T$ giving $\frac{r_0}{\sigma} = \ln\left(\frac{\varepsilon}{k_B T}\right)$ and in the EXP-unit system $r_0 = -\ln(T)$. This leads to

$$D \propto \frac{l_0}{t_0\, \rho\, \ln^2(T)} \tag{4.7}$$

The reduced diffusion is defined as $\tilde{D} \equiv {}^D/{}_{D_0}$, where $D_0 = \frac{l_0^2}{t_0}$ hence the reduced diffusion can be expressed as

$$\tilde{D} = \frac{3}{8\sqrt{\pi}} \frac{\rho^{-\frac{2}{3}}}{\ln^2(T)} \tag{4.8}$$

where the constant is determined from Enskog kinetic theory[67, 68]. This equation is based on the assumption that the mean-free path is given by an effective radius, and that this can be obtained from the kinetic energy. As density is increased at low temperatures, the system densifies and the mean-free path approaches the average inter-particle distance. At this point Eq. (4.8) is no longer expected to hold.

In the following the structure and dynamics will be analysed along first the isotherms, then by the isochores.
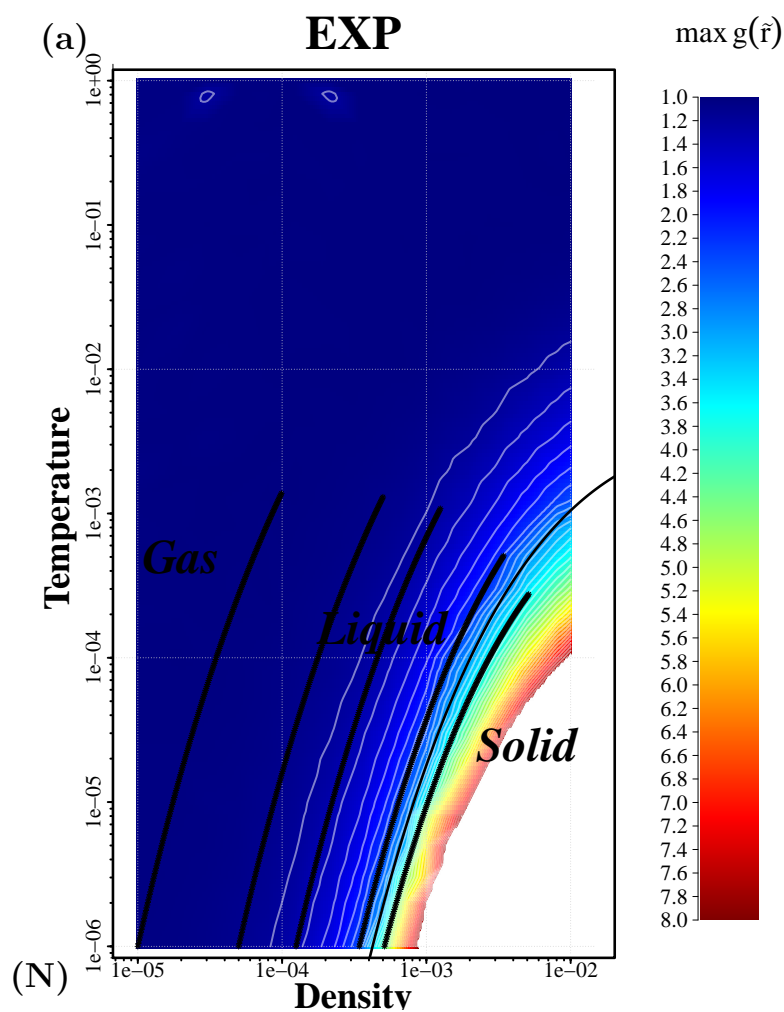
Figure 4.11: The structure quantified by the maximum value of the radial distribution function. The structure is an isomorph invariant, but as comparing the white contour lines to the isomorphs shows deviation in the first peak. This can be explained by the variations in γ along the isomorphs (see Section 4.4).
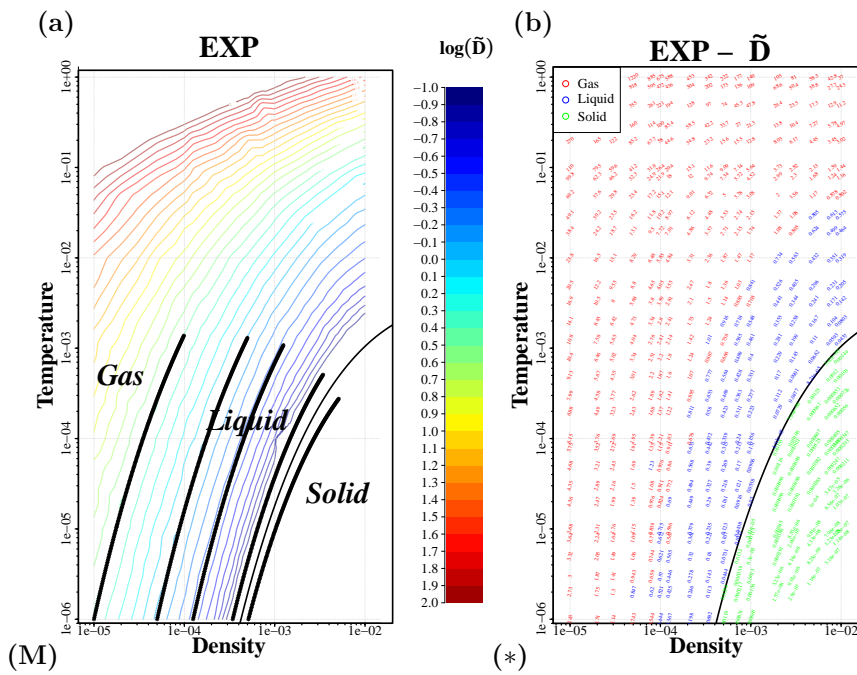
Figure 4.12: Temperature and density variation of the reduced diffusion coefficient determined from the diffusive part of the mean square displacement. (a) shows the contour lines of constant $\tilde{D}$. Comparing with isomorphs (black dots) illustrates the isomorph invariance of the reduced dynamics. (b) The numerical values in each of the simulated state points with a slope indicating the direction of the isomorph. Red indicates gas, blue liquid, and green solid state points.

4.4.1 Isotherms

In this section structure and dynamics for selected densities along the following four selected isotherms will be discussed: $T = 1$, $T = 10^{-2}$, $T = 10^{-4}$ and $T = 10^{-6}$.

Figure 4.13 shows the radial distribution function along the four isotherms. In the highest temperature (Fig. 4.13(a)) we see very little structure as the system is in gas phase for all densities. As distances are reduced to short distances, a decline shows the repulsion of the particles. The distance of repulsion is decreasing with density due to the reduced units (r scales with σ). Decreasing temperature Fig. 4.14(b), the system begins to show some structure and liquifies when compressed. At the two lowest isotherms (Fig. 4.14(c) and Fig. 4.14(d)) we see all three phases of the system as density is increased.

In the short time ballistic regime, a nice collapse due to use of reduced units is observed. In this region motion is characterized by the particles being in free flight: $\langle (\Delta r(t))^2 \rangle = (\langle \mathbf{v} \rangle t)^2$. The reduced mean square displacement is then found by division with l_0^2 giving

$$\langle (\Delta \tilde{r}(t))^2 \rangle = \rho^{2/3} \langle \mathbf{v} \rangle^2 \, t^2 \, . \tag{4.9}$$

The average velocity squared is by the equipartition theoremdetermined from the temperature as $3 k_B T / m$. Remember that $t_0 = \rho^{-1/3} \sqrt{m/k_B T}$ to get

$$\langle (\Delta \tilde{r}(t))^2 \rangle = 3 \tilde{t} \, . \tag{4.10}$$

That the reduced unit mean-square displacement is proportional to the reduced time in diffusive regime is seen reducing both sides of the Einstein relation to: $\langle (\Delta \tilde{r}(t))^2 \rangle = 6 \tilde{D} \tilde{t}$. The different phases is seen in the mean-square displacement: In the gas phase the large inter-particle distance gives rise to a free flight above order of unity and the ballistic regime is dominant for a long time. In the liquid phase where the inter-particle separation is of order unity, the diffusive regime will take over when the mean-square displacements is on that order. In the crystal phase only cage rattling is possibleresulting in the mean-square displacement reaching a plateau. In Fig. 4.14(d) the crystal shows an additional increase after some time. This is a signature of the defect crystal.

In Fig. 4.15 the reduced diffusion coefficient calculated from the diffusive part of the mean-square displacement is plotted. From Eq. (4.8) the reduced diffusion coefficient along the isotherms is expected to behave as $\tilde{D}(\rho) \propto \rho^{-\frac{2}{3}}$ in the dilute state points. The black dashed line in Fig. 4.15 has slope $-\frac{2}{3}$. Good agreement with theory is noted for most densities, when temperature is above $T = 10^{-3}$. As temperature decreases so must density in order for Eq. (4.8) to remain valid. At higher density and lower temperatures, where Eq. (4.8) is no longer accurate, there is an increased slow down of diffusion

due to first the proximity of the particles. The diffusion is no longer controlled by single particle pair interactions, but rather by a complex potential energy surface leading to the particles becoming increasingly trapped. The diffusion coefficient is only shown for the non-crystal state points as the crystal diffusion is due to defects.
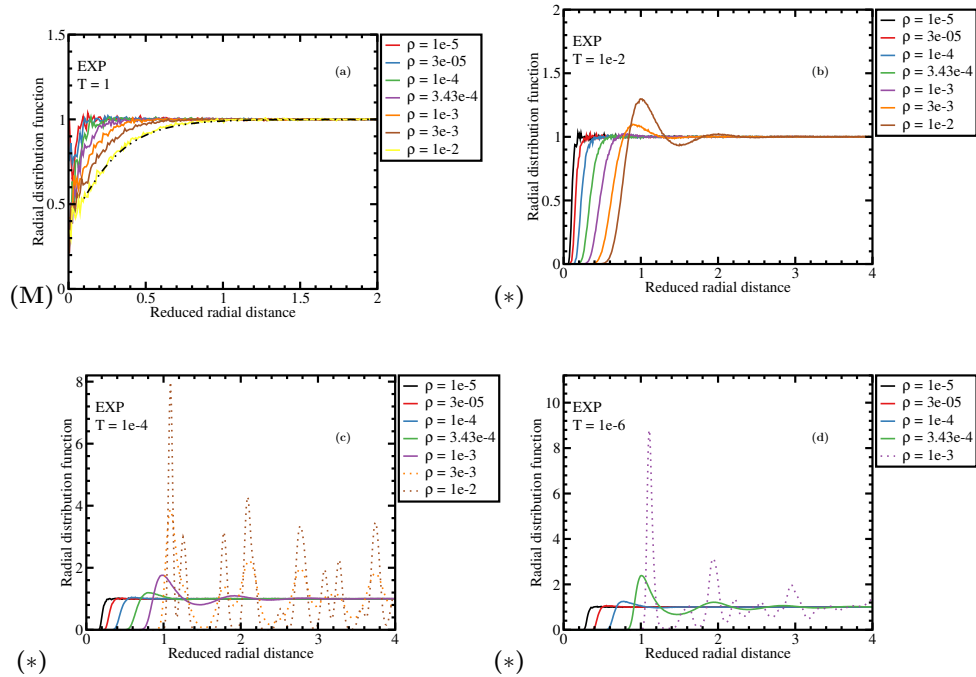
Figure 4.13: Radial distribution function for selected state points along four different isotherms: $T = 1$, $T = 1 \cdot 10^{-2}$, $T = 1 \cdot 10^{-4}$, and $T = 1 \cdot 10^{-6}$. State points in the fluid phase in figure Fig. 4.1 has full lines, while solid state points have dotted lines. *(a)* $T = 1$ corresponds to the average kinetic energy being on the same order as the potential energy barrier at zero separation. The system remains in a gas-like structure in the investigated density range. The black dashed line is the Boltzmann distribution of the potential energies $(e^{-\beta v(r)})$ for the state point $(\rho, T) = (0.01, 1)$ (yellow curve). A very nice agreement is observed. *(b)* The kinetic energy is low enough to observe liquid-like structure in the most dense part. *(c) and (d)* The system have all three phases along these each of these isotherms.
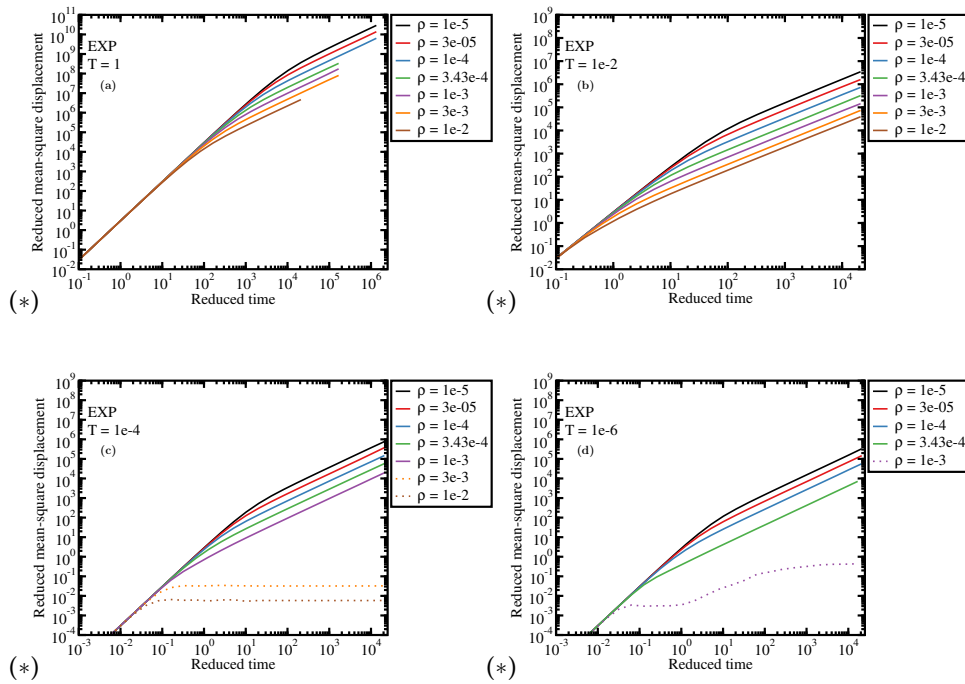
Figure 4.14: Mean square displacement for selected state points along the same four isoterms: $T = 1$, $T = 1 \cdot 10^{-2}$, $T = 1 \cdot 10^{-4}$, and $T = 1 \cdot 10^{-6}$. Balstic regime collaps is due to use of reduced units. The gas phase is characterized by long mean free path. The liquid by diffisive motion when mean-square displacement is on the order of one. The particles in a perfect crystal cannot difuse, so the mean-square displacement plateaus, but movement takes place due to defects in the crystal. Fluid state points is indicated by full lines, while solid state points have dotted lines.
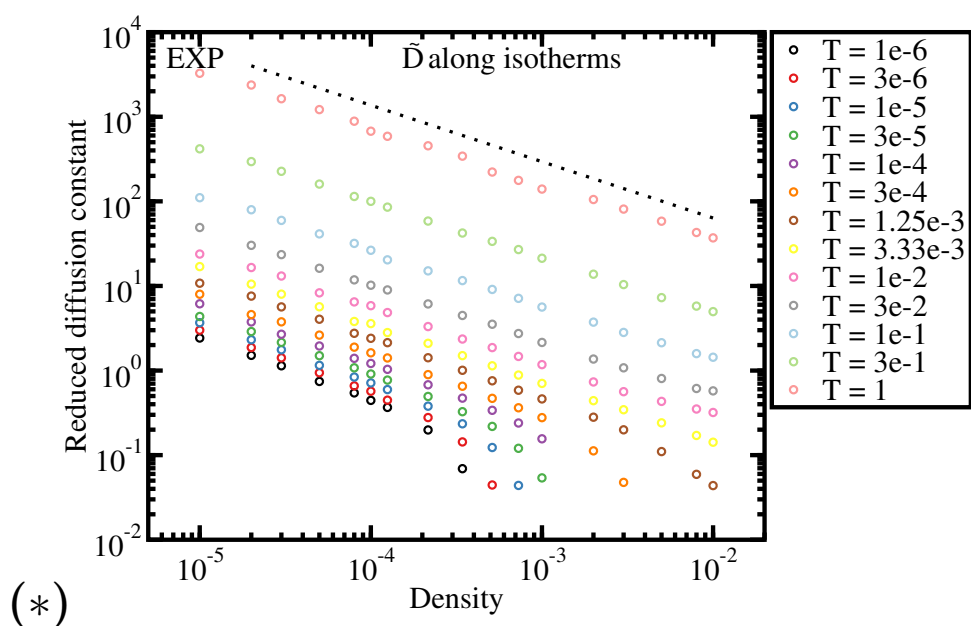
Figure 4.15: Diffusion coefficient along two isoterms pr decade (all densities from Fig. 4.1). The diffusion coefficient was determined from the non-ballistic part of the mean squre displacement. The black dotted line is the gas phase prediction of Eq. (4.8). Only state points from the fluid phase of figure 4.1 are plotted.
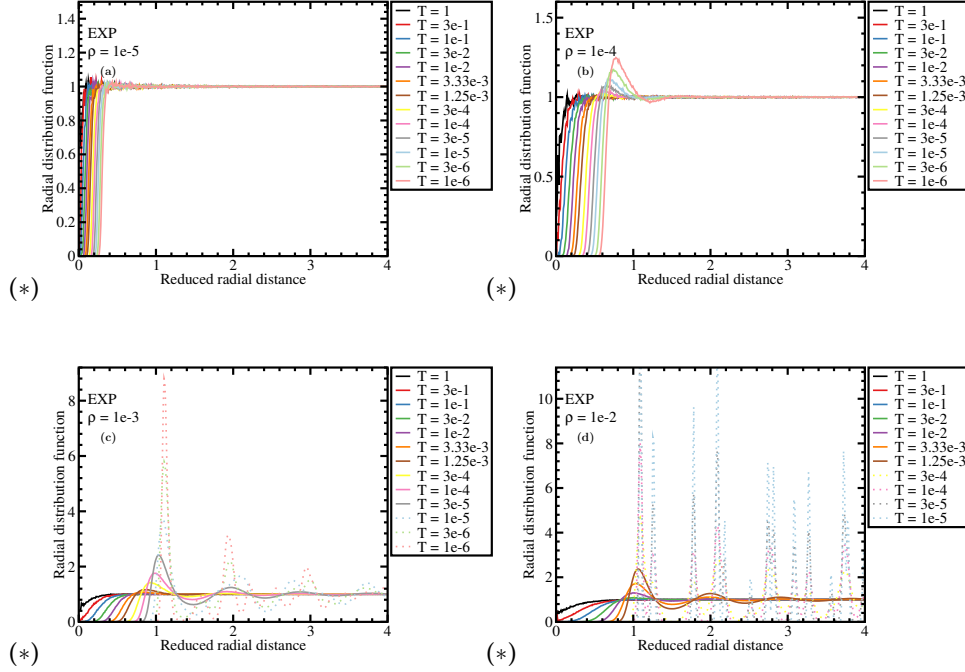
Figure 4.16: Radial distribution function for selected state points along four different isochores: $T = 1 \cdot 10^{-5}$, $T = 1 \cdot 10^{-4}$, $T = 1 \cdot 10^{-3}$, and $T = 1 \cdot 10^{-2}$. State points in the fluid phase in figure 4.1 has full lines, while solid state points have dotted lines. In the lowest density very little structure is present and the system is gas-like - even at the lowest temperature. As density is increased liquid-like structure appears in lowest temperature, and from $\rho = \cdot 10^{-3}$ also crystal structure is observed.

4.4.2 Isochores

Along the isochores the radial distribution function (Fig. 4.16) reveals that the systems remains in the gas phase at all simulated temperatures at the lowest density isochore ($\rho = 10^{-5}$). Increasing density ten times gives a liquid structure at the lowest temperatures, while further increase (to $\rho = 10^{-3}$ and $\rho = 10^{-2}$) leads to crystallization in the lowest temperatures.

As with the mean-square displacement along the isotherms, the mean-square displacements along the isochores (Fig. 4.17) reveal the different phases: Gas phase with a long ballistic part, liquid with a quick transition to the diffusive part due to the proximity of the other particles, and the solid with the plateau.

The reduced diffusion coefficient along the isochores can be see in Fig. 4.18. Equation (4.8) likewise gives an expected behavior, as can be seen as a black dashed line in Fig. 4.18(a) and a black dotted line in Fig. 4.18(b). Good
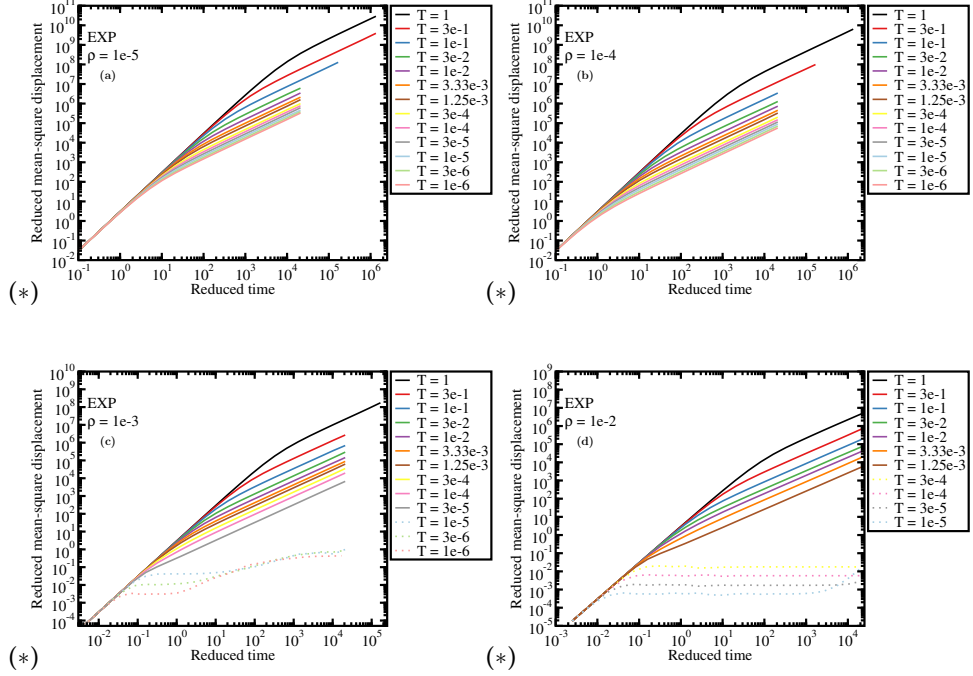
Figure 4.17: Mean square displacement for selected state points along the same four isochores: $\rho = 1 \cdot 10^{-5}$, $\rho = 1 \cdot 10^{-4}$, $\rho = 1 \cdot 10^{-3}$, and $\rho = 1 \cdot 10^{-2}$.

compliance with the prediction is observed in large part of the state points. As density increases and temperature drops, the system densifies and again the restriction of the kinetic theory are seen, but another limitation to the prediction is seen at the highest temperatures: From Eq. (4.8) a unphysical divergence in the diffusion constant at $T = 1$ is expected. In Fig. 4.18(b) the divergence between prediction and simulation data is clearly seen at $-\ln^{-2}(T) \approx 20$ corresponding to $T = 0.8$, where at all densities the diffusion is much slower than predicted by Eq. (4.8).

In Figure 4.18 the radii of the particles r_0 were defined by $v(r) = k_B T$. If instead the effective radii is calculated from equating the potential energy to the kinetic energy $v(r) = 3/2 k_B T$, the divergence of the diffusion is found at $T = 2/3$. The new prediction is seen in Fig. 4.19 as a black dotted line - the dashed line being the same as in Fig. 4.18. Comparing the two lines they both depart from simulation results, as temperature becomes high, and as the the dotted line has a divergence sooner $T = \frac{2}{3}$ compared to $T = 1$, the departure happens sooner in this case. Before the departure, the dotted line might seems to provide the best fit to simulation data.
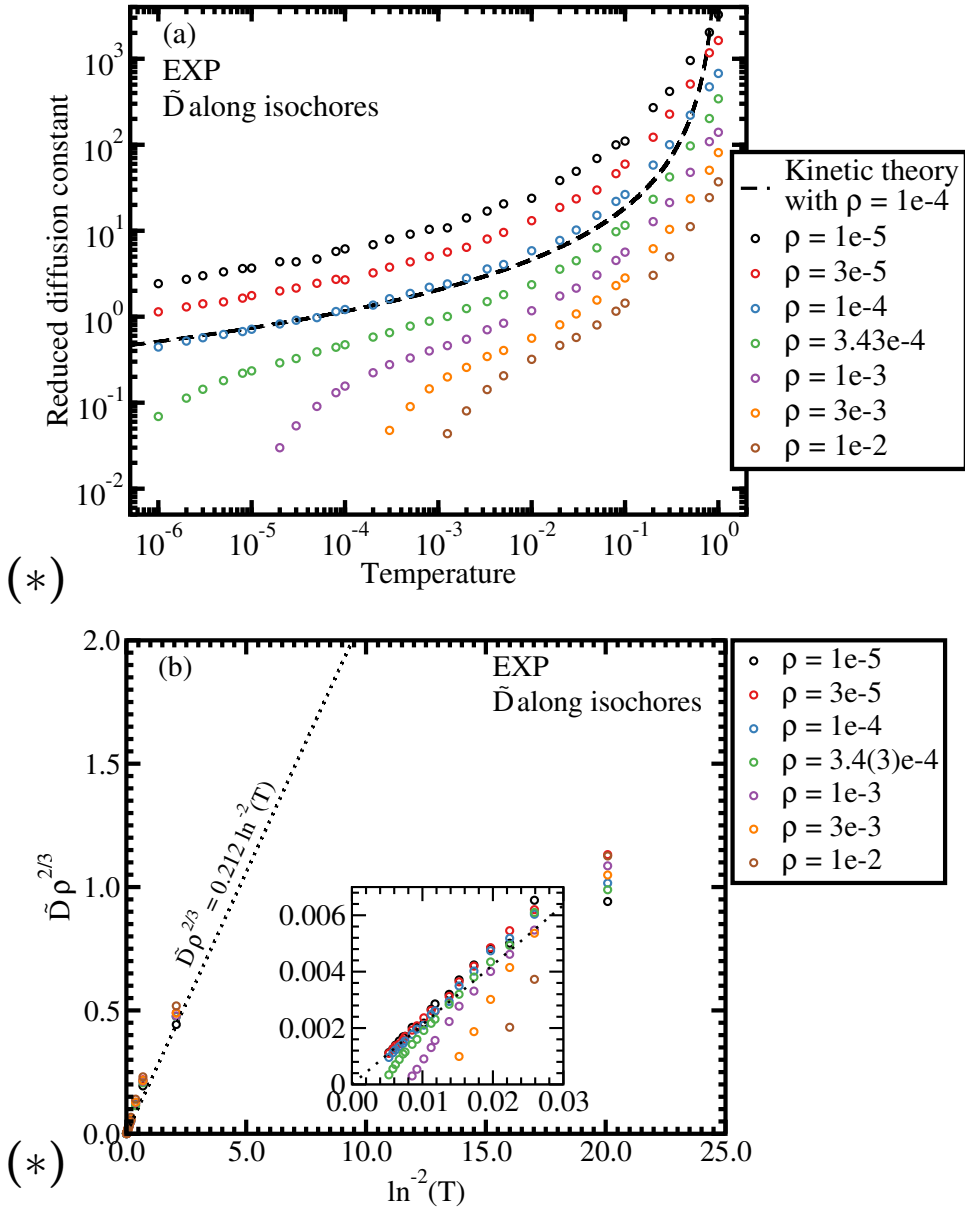
Figure 4.18: Diffusion coefficient along two isochores pr decade (all fluid temperatures from Fig. 4.1. The diffusion coefficient was determined from the non-ballistic part of the mean squre displacement. *Left:* Black dashed line is generated by kinetic (Enskog) theory (Eq. (4.8)). *Right:* Plotting $\rho^{\frac{2}{3}}\tilde{D}$ against $\frac{1}{\ln^2 T}$ to examine the extend of compliance with Enskog theory (dotted line). Inset focus' on the high temperatures where the prediction works well for the low densities.
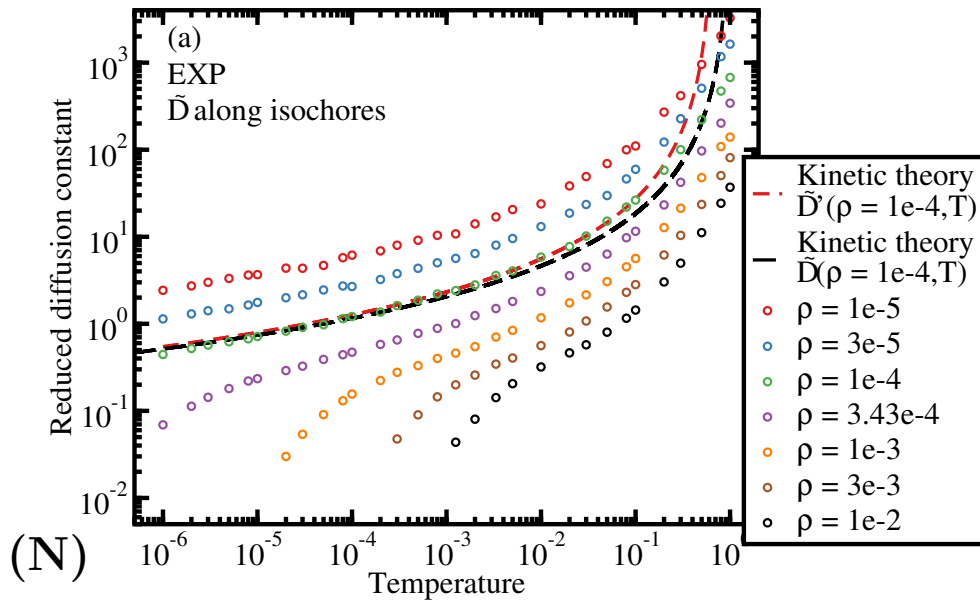
Figure 4.19: Diffusion coefficient along two isochores pr decade (all fluid temperatures from figure 4.1. The diffusion coefficient was determined from the non-ballistic part of the mean squre displacement. Black and red dashed lines are generated by kinetic (Enskog) theory by determining the particle size r_c. The black line is obtained by solving $v_{EXP}(r_c) = k_B T$, while the red line is obtained by solving $v_{EXP}(r_c) = \frac{3}{2} k_B T$. Both lines is plotted with $\rho = 10^{-4}$.

4.5 Thermodynamics

In this section the thermodynamic properties of the EXP-potential is presented by the $\tilde{W}$, $\tilde{U}$, $\tilde{p}$ and $c_V{}^{\text{ex}}$.

Figure 4.20 shows the logarithm of the average reduced unit pressure: $\langle \tilde{p} \rangle \equiv \frac{\langle p \rangle}{(\rho k_B T)}$. As expected the pressure is on order of unity in the gas - corresponding to an ideal gas as $\langle \tilde{p} \rangle = 1 \Leftrightarrow \langle p \rangle = \rho k_B T$. As the system becomes denser, the average reduced unit pressure increases due to the repulsion between the particles. The pressure contribution that is not the ideal gas contribution is the excess pressure or the virial.

From Fig. 4.21 the average reduced virial per particle is seen to increase from a very low value in gas phase, to being the dominant contributor to the pressure in the dense liquid and solid phases.

As the virial is related to the potential energy by the potential energy is dominant in the dense systems, while the kinetic energy is dominating the dilute system. Figure 4.22 shows the reduced average potential energy per particle and the transition from a kinetic region to a potential region is seen - the average kinetic energy per particle is 1 (or $\frac{3}{2}$).
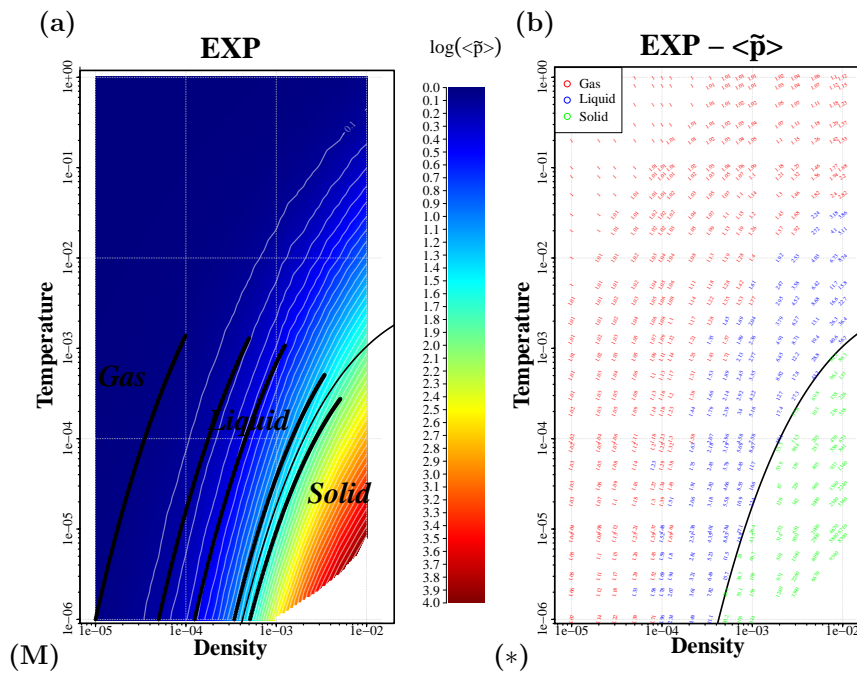
Figure 4.20: Log-log density-temperature phase diagram of the EXP system showing the average reduced pressure. The color coding is based on a linear interpolation of the logarithm of the average of the reduced pressure in the simulated state points. White contour lines and the small-step isomorphs show that reduced pressure is changing along isomorphs.
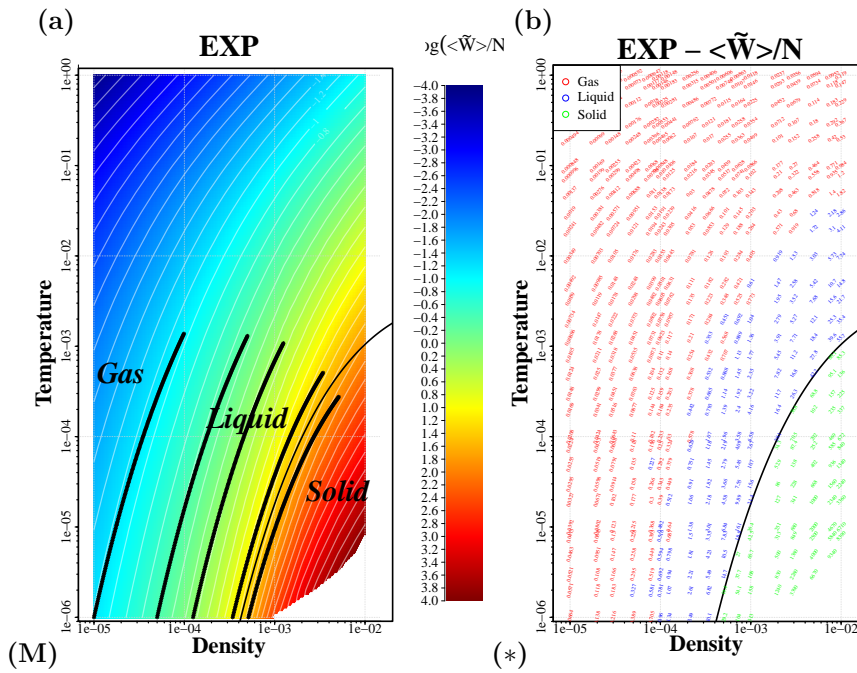
Figure 4.21: Temperature and density variation of the reduced per particle average virial. (a) shows the logarithm of the reduced per particle virial in a continuous color plot. White lines are contour lines, and five of isomorphs are plotted for comparison. (b) gives the numerical values in each of the simulated state points with a slope indicating the direction of the isomorph. Red indicates gas, blue liquid, and green solid state points.
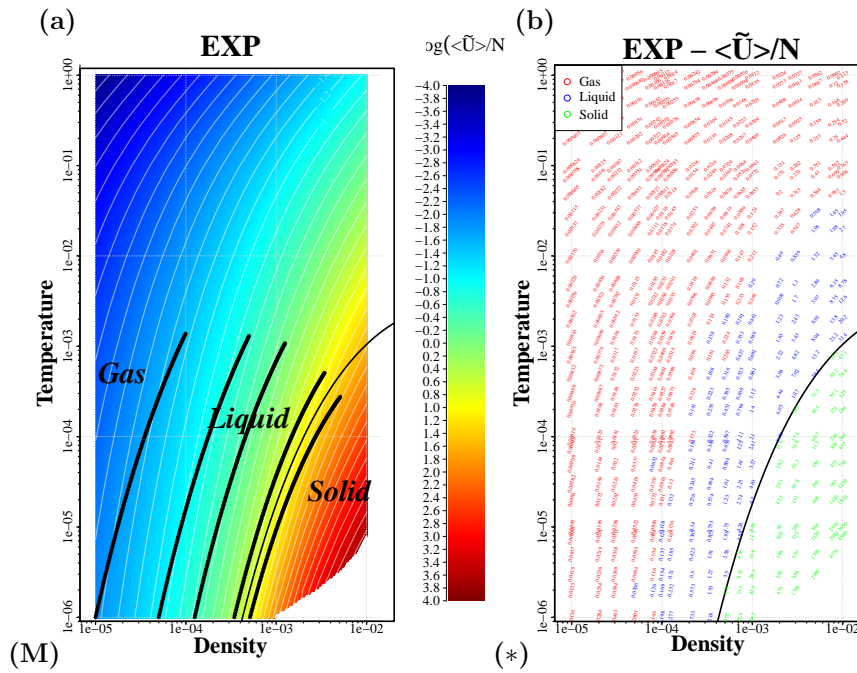
Figure 4.22: Temperature and density variation of the reduced per particle average potential energy. (a) shows the logarithm of the reduced per particle potential energy in a continuous color plot. White lines are contour lines, and five isomorphs are plotted for comparison. (b) gives the numerical values in each of the simulated state points with a slope indicating the direction of the isomorph. Red indicates gas, blue liquid, and green solid state points.
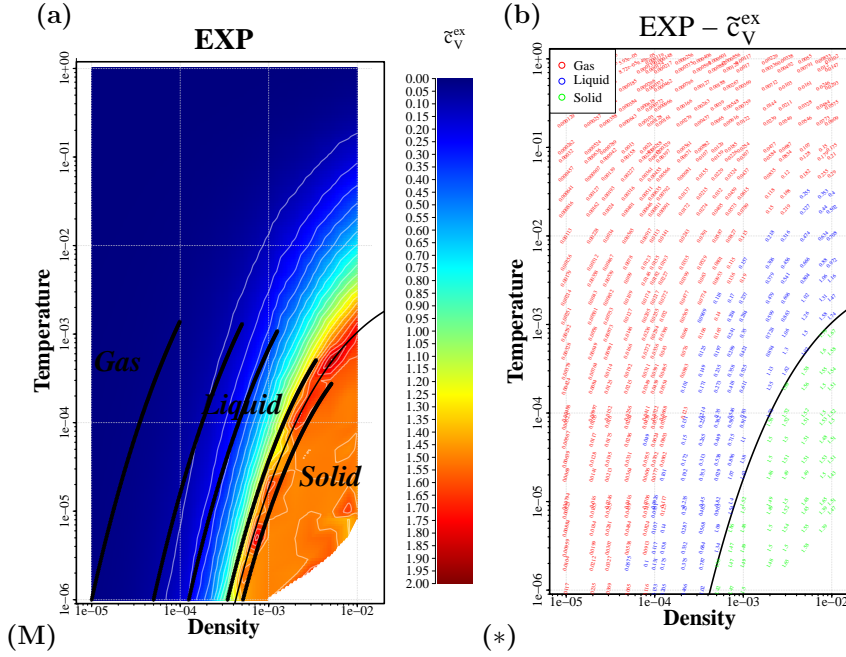
Figure 4.23: Log-log density-temperature phase diagram of the EXP system showing the reduced isochoric exess heat capacity. The color coding is based on a linear interpolation of the logarithm of the heat capacity in the simulated state points. The first version of the isomorph theory[52–55] assumed this quantity to be an isomorph invariant. The white contour lines and the small-step isomorphs shows this is not the case - as allowed by the second version of the theory[57].

4.5.1 Specific heat

The reduced isochoric excess specific heat capacity per particle $c_V{}^{\text{ex}}$ is defined as $\frac{c_V}{k_B} - \frac{3}{2}$, where the latter term is the ideal gas contribution. In this work the excess specific heat is determined by the fluctuations in the potential energy of the system, using the fluctuation-dissipation theorem: $C_V{}^{\text{ex}} = \frac{\langle (\Delta U)^2 \rangle}{k_B T^2}$.

The reduced isochoric excess specific heat capacity was predicted by the first version of the isomorph theory[55] to be an isomorph invariant, but it was realized only to be correct as a first order approximation[57]. In Fig. 4.23 the white contour lines and the black isomorphs is seen not to be exactly parallel - reflecting the fact that the reduced isochoric excess specific heat capacity is not an isomorph invariant.

Following the isotherms in Fig. 4.24 shows that the reduced isochoric excess specific heat capacity increases on compression until the value $\frac{3}{2}$ is reached - marked by the black dashed line. This is the prediction for a harmonic crystal. The solid phase in Fig. 4.23 is seen to have values just around
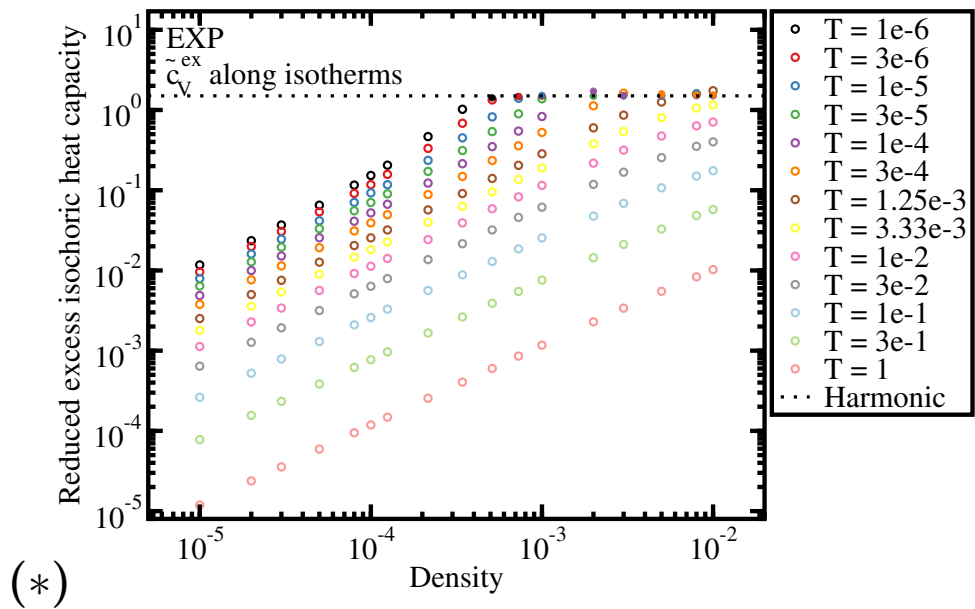
Figure 4.24: Isochoric excess heat capacity along isoterms determined from the fluctuations of the potential energy. State points from the fluid part of Fig. 4.1 have open symbols, while stars corresponds to crystal state points.

1.5 - the apparent regions marked in the solid is due to the uncertainties in the determination of the specific heat. The high temperature isotherms remains in a gas phase and thus have considerably lower reduced isochoric excess specific heat capacity due to the weaker interactions.
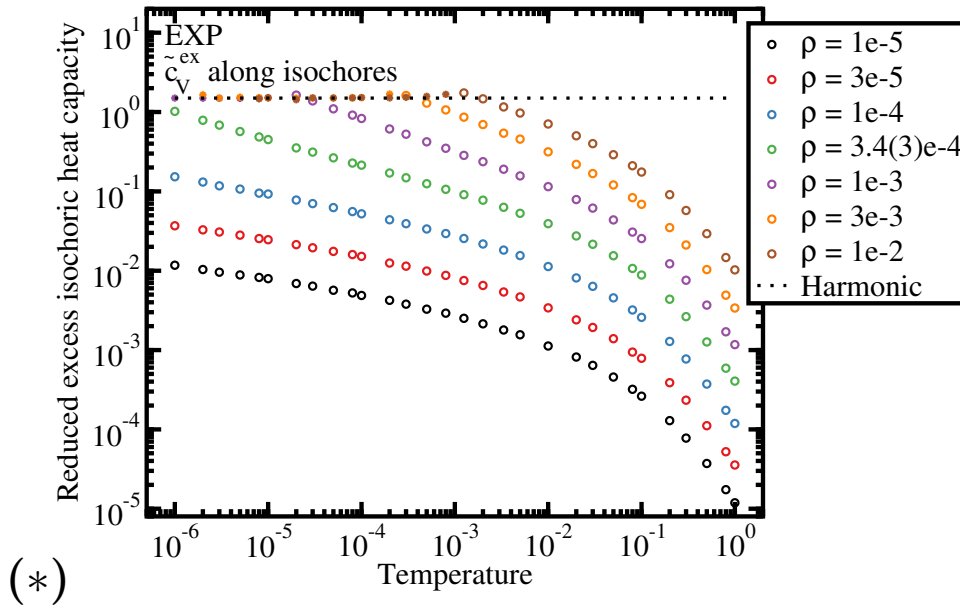
Figure 4.25: Isochoric excess heat capacity along two isochores pr decade (all temperatures from Fig. 4.1). Determined from the fluctuations of the potential energy. State points from the fluid part of figure 4.1 have open symbols, while stars corresponds to crystal state points.

Following the isochores in Fig. 4.25 again a transition is seen. At high enough densities in the systems low temperature part, c_V^{ex} is around the harmonic crystal $\frac{3}{2}$-value. As temperature is increased a significant drop in c_V^{ex} is seen. At the lowest densities the system remains in the gas phase and c_V^{ex} is far from the value of the harmonic crystal.

4.6 Gas

In this section the gas phase will be defined and discussed. As mentioned before the EXP system has only one first order thermodynamic phase transition separating a solid and a fluid. Since there is no attractive forces, there is nothing to support a liquid-gas interface, so there cannot be liquid-gas transition, and nor critical or triple points. Even so it is still meaningful to

separate the fluid phase in a gas phase and a liquid phase, separated by a broad transition region (marked on Fig. 4.1). If the transition between gas and liquid is ambiguous, then the transition region it self is ill-defined. It serves only as a reminder of the ambiguousness of transition it self. The separation into gas and liquid is motivated by the observation of regions of phase space where the state points structur, dynamic and thermodynamic conforms well with gas behavior, and regions where the behavior conforms well with liquid systems. More over the separation of the fluid phase in two regions is refound in the behavior of the density scaling exponent and the isomorphs.

4.6.1   Defining the gas

In the region where the system has the characteristics of liquid, the local structure has a well defined first peak, and a transition from ballistic to diffusive behavior on time scales of order one, while in the region where the system has the characteristics of a gas, the pressure is dominated by the ideal gas contribution, the system has a very low degree of structure, and the dynamics is characterized by a very long ballistic part of the mean square displacement and a high diffusion constant. The separation of a liquid- and gas phases is also found in the density scaling exponent as discussed in Section 4.3. Thus there is a need to define a criterion for the transition. In this work a structural signature was chosen: *A gas is a state point with no identifiable local minimum after the first peak in the radial distribution function.* This signature works well in splitting what is clearly a gas phase from what is clearly a liquid phase, but it has a great weakness of being dependent on the method of identifying the minimum, and therefore not having an unambiguous transition line. The position being slightly protocol dependent due to the finite and discrete nature of the computer simulations. The radial distribution functions found in the computer simulations is calculated from binning the particles - thus the more bins the better the resolution, but the poorer the statistics in each bin and the more noise. To get more robust result an algorithm to filter out noise must be used, but nonetheless some ambiguity about the exact position of the transition line will persist. Even if the transition line is somewhat ill-defined the definition serves it purpose: gas behavior is in gas phase, and liquid behavior in the liquid phase.

4.6.2   Structure in the gas: $g(r) = \exp(-\beta u(r))$

In an ideal gas the particles are point particles that only interacts by hard collisions. Thus there is nothing to create deviations from a uniform distribution on average on all length scales, and the radial distribution will constant have value one. Increasing the interactions will change the structure: At short distances an exclusion volume due to repulsion between the

particles will arise on average and define a characteristic size of the particles. Some collisions will happen with larger energies than others, so sometimes particles will come closer than other times. The distribution of kinetic energies is a Boltzmann distribution, and therefore must also the instantaneous exclusion volume be, and therefor also the pair correlation function. Thus the radial distribution function for gas systems with potential interactions must be: $g(r) = \exp(-\beta v(r))$, where $\beta = 1/k_B T$.

4.6.3   Theory for gas-phase: predicting R and γ.

In this part predictions for R and γ in the gas phase of the EXP system will be made. The predictions assumes: that the structure of the gas phase to be well described by the gaussian distribution: $g(r) = \exp(-v(r)/k_B T)$ or the probability function $p(r) = \frac{r^2}{K_r} \exp(-v(r)/k_B T)$, where K_r is a normalization constant, that the individual pair energies and forces are statistically independent, and that the average of the potential energy and the virial can be calculated from the single pair interactions. Thus the potential energy is given by $v(r) = \varepsilon \exp(-r/\sigma) = -\exp(-r)$, in the EXP unit system ($\varepsilon = \sigma = 1$), and the virial by $w(r) = -\frac{1}{3} r v'(r)$. Before proceeding some considerations regarding the pair potential function: The domain is $[0, \infty[$ and the range is $]0, 1]$, it is a smooth function, so it can be differentiated: $v'(r) = -v(r)$, and it is a bijective function, so it can be inverted: $r = \ln(\frac{1}{v})$. Noted that the domain of the inverted function can be expanded to $v \in]0, \infty[$. Now the virial can be expressed in v as

$$ w(r) = \frac{1}{3} v \ln(1/v). \tag{4.11} $$

Transforming the probability function $p(r)$ to the probability function in v ($p(v)$) is done by $p(v) = p(r)|\frac{dr}{dv}|$ yielding:

$$ p(v) = \frac{1}{K} \frac{\ln^2(\frac{1}{v}) \exp(-\beta v)}{v}, \ v \in]0, \infty[\tag{4.12} $$

with $K = \int_0^\infty \frac{\ln^2(\frac{1}{v}) \exp(-\beta v)}{v}$ and $\beta = 1/T$. This distribution and normalization constant is ill-posed as it diverges as $v \to 0$ - corresponding to $r \to \infty$. Therefore a large distance cutoff is introduced - or rather an almost zero energy left side cutoff, thus defining the distribution:

$$ p_c(v) = \frac{1}{K_c} \frac{\ln^2(\frac{1}{v}) \exp(-\beta v)}{v}, \ v \in [c, \infty[\tag{4.13} $$

with $k_c = \int_c^\infty \frac{\ln^2(\frac{1}{v})\exp(-\beta v)}{v}$ being the normalization constant. This distribution is well defined, and the mean $\langle v_c \rangle$ can be calculated as:

$$\langle v_c \rangle = \int_c^\infty p_c(v)\, v\, dv \tag{4.14}$$

$$= \frac{1}{K_c} \int_c^\infty \ln^2(\frac{1}{v}) \exp(-\beta v) dv. \tag{4.15}$$

Consider now the mean of the distribution as $c \to 0$: K_c is still diverging, while $\lim_{c\to 0^+} \left(\int_c^\infty \ln^2(\frac{1}{v}) \exp(-\beta v) dv \right) = \mathrm{C}^2 + \frac{\pi^2}{6}$ - where C is Euler's constant defined by $\mathrm{C} \equiv \lim_{n\to\infty} \left(\sum_{p=1}^n \frac{1}{p} - \ln n \right) = 0.577216...$. Thus

$$\lim_{c\to 0^+} (\langle v_c \rangle) = \langle v \rangle = 0. \tag{4.16}$$

We now turn to the Pearson correlation:

$$R = \frac{\langle \Delta U \Delta W \rangle}{\sqrt{\langle (\Delta U)^2 \rangle \langle (\Delta W)^2 \rangle}} \tag{4.17}$$

$$= \frac{\langle UW \rangle - \langle U \rangle \langle W \rangle}{\sqrt{(\langle U^2 \rangle - \langle U \rangle^2)(\langle W^2 \rangle - \langle W \rangle^2)}}. \tag{4.18}$$

With results from above this can be rewritten as:

$$R = \frac{\langle vw \rangle}{\sqrt{\langle v^2 \rangle \langle w^2 \rangle}}, \tag{4.19}$$

since every term containing $\langle v \rangle$ vanishes as $c \to 0$ because $K_c \to \infty$. Let

$$A_n = \int_0^\infty v \ln(1/v) \exp(-\beta v) dv \tag{4.20}$$

then the correlation coefficient can be rewritten in terms of A_n as

$$R = \frac{A_3}{\sqrt{A_2 A_4}} \tag{4.21}$$

since $\langle v^2 \rangle = K A_2$, $\langle vw \rangle = \frac{K}{3} A_3$ and $\langle w^2 \rangle = \frac{K}{9} A_4$, where K is the diverging normalization constant from $\langle v \rangle$. Even if K is diverging, R remains well defined as K does not enter in Eq. (4.21).

The density scaling exponent γ is likewise expressed by the fluctuations in the potential energy and the virial:

$$\gamma = \frac{\langle \Delta U \Delta W \rangle}{\langle (\Delta U)^2 \rangle} \tag{4.22}$$

$$= \frac{\langle UW \rangle - \langle U \rangle \langle W \rangle}{\langle U^2 \rangle - \langle U \rangle^2} \tag{4.23}$$

$$= \frac{\langle vw \rangle}{\langle v^2 \rangle} \tag{4.24}$$

where the last step again explores what was derived above about U, W and $\langle v \rangle$. Rewriting in terms of A_n gives the equation for γ in the gas phase:

$$\gamma = \frac{A_3}{3A_2}.$$ (4.25)

The prediction for density scaling exponent can be seen in Fig. 4.10(a) as a black dashed line.

By evaluating the predictions for the correlation coefficient (Eq. (4.21)) and the prediction for density scaling exponent (Eq. (4.25)) in different temperatures a (R, γ)-plot can be built. In Fig. 4.26(b) this has been done, and the prediction from the gas phase is plotted as a dashed black line. In the figure all simulated non-crystalline state points has been plotted: gas phase state points in red, and liquid state points in blue. Observe that gas phase always represents the the upper bound on γ at a given R, and the lower bound in R at a given γ.

In order to calculate and plot the predictions of Eq. (4.21) and Eq. (4.25), the integrals A_n must be solved. This can be done using computer algebra systems and using Maple one gets:

$$A_2 = \beta^{-2}\left(\ln^2 \beta - 2(1 - \mathrm{C}) \ln \beta + (\pi^2/6 + \mathrm{C}^2 - 2\mathrm{C}) \right),$$ (4.26)

$$A_3 = \beta^{-2}\left(\ln^3 \beta - 3(1 - \mathrm{C}) \ln^2 \beta + (\pi^2/2 + 3\mathrm{C}^2 - 6\mathrm{C}) \ln \beta + k_3 \right),$$ (4.27)

and

$$A_4 = \beta^{-2}\left(\ln^4 \beta - 4(1 - \mathrm{C}) \ln^3 \beta + (\pi^2 + 6\mathrm{C}^2 - 12\mathrm{C}) \ln^2 \beta + h_4 \ln \beta + k_4 \right).$$ (4.28)

Here

$$k_3 = \mathrm{C}^3 - 3\mathrm{C}^2 + (\pi^2/2)\mathrm{C} - \pi^2/2 + 2\zeta(3) = -0.48946$$ (4.29)

in which $\zeta(3) = 1.20206$ is the Riemann zeta function's value at 3 ("Apery's constant"),

$$h_4 = 2\left(2\mathrm{C}^3 - 6\mathrm{C}^2 + \pi^2\mathrm{C} - \pi^2 + 4\zeta(3)\right) = 4k_3 = -1.9578,$$ (4.30)

and

$$k_4 = \mathrm{C}^4 - 4\mathrm{C}^3 + \pi^2\mathrm{C}^2 - 2\pi^2\mathrm{C} + 8\zeta(3)\mathrm{C} - 8\zeta(3) + 3\pi^4/20 = 1.7820.$$ (4.31)

Numerically, the three integrals are given by

$$\beta^2 A_2 = \ln^2 \beta - 0.8456 \ln \beta + 0.8237 , \qquad (4.32)$$

$$\beta^2 A_3 = \ln^3 \beta - 1.268 \ln^2 \beta + 2.471 \ln \beta - 0.4895 , \qquad (4.33)$$

and

$$\beta^2 A_4 = \ln^4 \beta - 1.691 \ln^3 \beta + 4.942 \ln^2 \beta - 1.958 \ln \beta + 1.782 . \qquad (4.34)$$
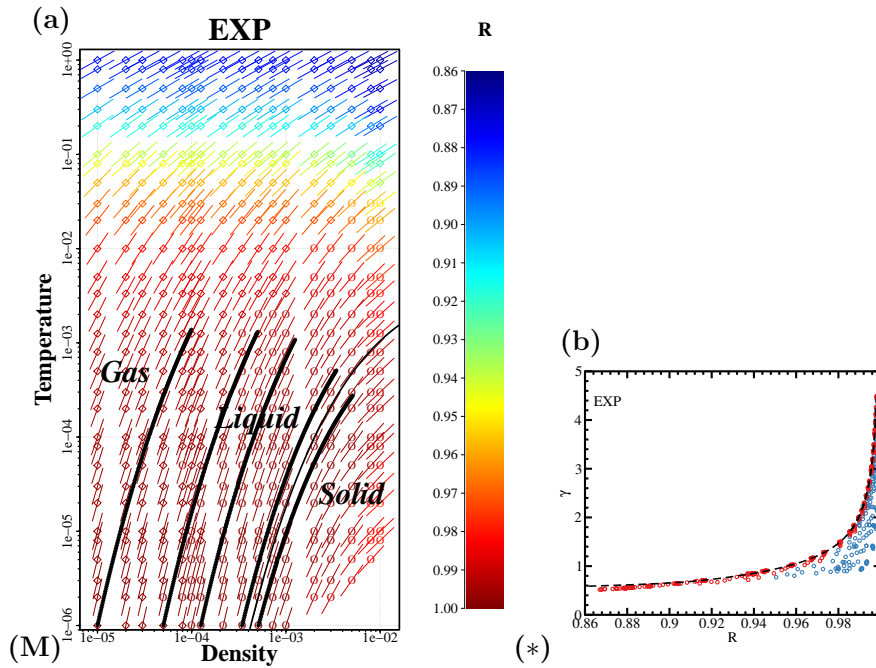
Figure 4.26: (a) The density-temperature thermodynamic phase diagram with line slopes given by the density-scaling exponent and color coding indicating the virial potential-energy correlation coefficient R. The diamonds mark gas-phase state points, the circles mark liquid or solid state points. Because the phase diagram is a log-log plot, the line segments give the slopes of the local isomorphs, compare Eq. (3.14). The black dashed line is the approximate melting-line isomorph (see Section 5.4). (b) Density-scaling exponent γ versus virial potential-energy correlation coefficient R for all state points of (a). The red circles are gas state points, the blue circles are liquid state points. The dashed line is the prediction of the analytical gas-phase theory, which is obtained by combining Eq. (4.25) with the result for R Eq. (4.21). For a given value of R the gas phase has the highest γ, for a given value of γ the gas phase has the lowest R.

Chapter 5

EXP and isomorphs

In this Chapter five isomorphs in the phase diagram of the EXP-potential is traced - two of which not previously reported. The structure and dynamics, as well as the reduced excess isochoric heat capacity, is investigated for isomorph invariance. Different methods for finding the isomorph is compared - including a technique not in the papers: The $h_p(\rho)$-approximate isomorphs.

As explained in Section 3.2 isomorphs are lines in the phase diagram along which a number of structural, dynamic and thermodynamic quantities are invariant in reduced units[52, 55, 60]. The reduced excess entropy is an isomorph invariant, and thus the isomorphs can be identified as iso-reduced-excess-entropy lines (configurational adiabats) in the phase diagram whenever the system has strong correlations. Isomorphs can therefore be traced by tracing the lines of constant $/Sex$, where the density scaling exponent (Eq. (3.14)) gives the slope of the isomorphs at a given state point - thus tracing an isomorph is knowing γ.

In this chapter different techniques to trace an isomorph will be reviewed in regards to the EXP-system. First the original method with short density-temperature jumps based directly on Eq. (3.14) and that γ can be determined from an equilibrium simulation by the fluctuation in the potential energy and the virial (Eq. (3.13)). The direct isomorph check (DIC-isomorphs) based on Eq. (3.1) allowing for larger density-temperature steps[55], and the functional form (h-isomorphs) allowing to generate a functional form of the isomorph from a single state point simulation[60].

5.1 Small step isomorphs

As briefly mentioned above, the small step or short jump method directly uses Eq. (3.13) to determined the density scaling exponent in a given state

point, and then by Eq. (3.14) the slope of the isomorph is known. In experiments often the density scaling exponent is treated as a constant (see for instance Alba-Simionesco et al. [69]), as a constant exponent in the experimental density range makes data collapse well. The slow variations in γ can be exploited in simulations as well, since γ can be assumed constant in some small neighborhood around a given state point. In order to stay inside this small neighborhood, the density change must be on the order of 1%, as the typical values of γ is of order 1-10. Scaling density with $r\% \approx 1\%$, the temperature must be scaled by $\approx \gamma r\%$. The new and the old state point will be on the same configurationel adiabat, an will be isomorphic if the system is strongly correlating in both state points.

The protocol for tracing the isomorphs is: From a NVT-ensemble simulation in the first state point (ρ_0, T_0), γ is determined from the fluctuations of the virial and the potential energy [55]. The next state point can be found as $(\rho_1, T_1) = (\rho_0 + \rho_0 r, T_0 (1 + r)^\gamma)$. A new NVT-ensemble simulation is preformed in the new state point in order to obtain the new density scaling exponent in order to find the next state point. This procedure is slowly mapping the configurational adiabat directly. Hereby the "true" isomorph can determined. Below five such isomorphs will be reported. All isomorphs span a decade in density and approximately 3 decades in temperature, and was traced using 230 evenly spaced state points - thus the density was increased by $10^{1/230} - 1 \approx 1.0062\%$ in each step. Different step sizes ($\approx 5\%$, $\approx 2\%$ and $\approx 1\%$) ware tested, and since the $\approx 1\%$ and $\approx 2\%$ gave similar results the chosen step size seems small enough to give trustworthy results. Likewise system size and cutoff were tested along the dense-liquid isomorph. The system size was chosen to be 1000 and a reduced unit cutoff of four was used in all cases. The initial preparation of the system was an isochoric cooling on a linear ramp from $4 \cdot T_0$ to T_0, where $T_0 = 10^{-6}$ is the offset temperature for all isomorphs. The system was then pre-equilibrated at the offset state point for 10^7 time steps. This pre-equilibrated configuration was used in every state point, where it was equilibrated in 10^7 time steps, before data was collected in 10^7 time steps.

The initial density of the different isomorphs was chosen to investigate the different phases and structures. Most emphasize was on the fluid phase. Only one solid state isomorph ($\rho = 5.12 \cdot 10^{-4}$) was traced. Moreover, the solid state isomorph suffered form being recrystallized from melt, resulting in some quantities being very sample sensitive. This includes especially the dynamical quantities, as motion on a longer length scale than the nearest neighbour distance is due to defects in crystal. A quantity known to be highly sensitive on initial configuration and round-off errors during the simulation run[28]. The fluid state isomorphs cover the gas ($\rho = 10^{-5}$), the gas-liquid transition ($\rho = 5 \cdot 10^{-5}$), the dilute-liquid ($\rho = 1.25 \cdot 10^{-4}$) and the dense-liquid ($\rho = 3.43 \cdot 10^{-4}$).

In Fig. 5.1 all five isomorphs is plotted, as well as the freezing line.

In the following structure probed by the radial distribution function $(g(\tilde{r}))$, and the relative change hereof along the isomorphs, dynamics probed by the reduced mean-square displacement, and the reduced diffusion constant $(\tilde{D})$, and thermodynamics in form of the reduced isochoric excess heat capacity $(\tilde{c}_V^{\text{ex}})$ will be reported. The correlation and density scaling exponent variation is also reported.

The structure and the relative deviation hereof, along the five isomorphs are seen in Fig. 5.2 - 5.4. The relative change in structure is the difference between the radial distribution function in the state point, and the radial distribution function in the staring state point, normalized by the one in the starting state point.

In Fig. 5.2(1a-b) the gas isomorph with very little structure, and in Fig. (2a-b) the gas-liquid isomorph is. Along both isomorphs the structure changes gradually as the departure from zero becomes less and less steep. This is consistent with decrease in the density scale parameter as seen in Fig. 5.19 as discussed in Section 4.4.

Figure 5.3(1-2a) gives the structure of the liquid isomorphs. Both has a clear minimum after the first peak, but there is considerably more structure in the dense-liquid. The deviations in Fig. 5.3(1-2b) confirms again that the main deviation is in the first peak, even if there is also small deviations after the first peak they gradually diminishes. The structure of the crystal isomorph in Fig. 5.4 shows only small relative deviations in the first peak due to the height of the peak. The crystal structure is developing throughout the isomorph even if the same configuration is used in each state point. This indicates that the system is not in equilibrium, and an ease of structural relaxation along the isomorph.

In Fig. 5.5(a-e) the reduced mean-square displacements along the isomorphs shows very good collapse in all the fluid isomorphs. The crystal is rather invariant considering it is crystallized from the melt. The structure of the crystal becomes more and more well-defined as density and temperature is increased (see Fig. 5.1). An possible explanation is that the crystal becomes better and better equilibrated in the same number of time steps. As the reduced diffusion coefficient is estimated from the diffusive part of the mean-square displacements, the uncontrolled crystallizations will have a great impact as is seen in Fig. 5.5(f): While all the fluid isomorphs have invariant reduced diffusion constants, the crystal is rather noisy.

In Fig. 5.6(a) the reduced excess isochoric heat capacity along the isomorphs is plotted - a quantity thought to be isomorphic invariant in the first formulations of the isomorph theory - is seen to increase with density on the reduced excess entropy lines. The same can be observed from Fig. 4.23. The increase is steepest in the gas, while the crystal is almost constant around the 3/2-value of the perfect harmonic crystal. The gas phase isomorphic density dependence of the reduced excess entropy isochoric heat capacity is predicted in the following. The prediction is plotted in Fig. 5.6(a) as a black

dotted straight line with slope 1/3. The isomorph prediction is based on
the same assumptions as the derivation of the expressions for the reduced
diffusion coefficient and the correlation and density scaling exponent: the
physics is controlled by single pair interactions, and an effective particle size
can be obtained from equating the pair potential to $k_B T$ ($r_0 = -\ln(T)$).
Furthermore it is assumed that the density scaling exponent can be approx-
imate by Eq. (4.4), where n is determined by the evaluating the logarithmic
derivative - corresponding to n_0 in Eq. (4.3). An assumption also made in
Stillinger [61] for the dilute gaussian core model and to be justified for the
EXP system in Sec. 5.3.

The heat capacity can be determined from $dQ = CdT$ and $dS = dQ/T$,
where $dS = \left(\frac{\partial S}{\partial T}\right)_V dT + \left(\frac{\partial S}{\partial V}\right)_T dV$. By combining, and evaluating at con-
stant density (and volume) the isochoric heat capacity can be expressed as
$C_V = \left(\frac{\partial S}{\partial \ln T}\right)_\rho$ or in the excess:

$$C_V{}^{\text{ex}} = \left(\frac{\partial S_{\text{ex}}}{\partial \ln T}\right)_\rho \tag{5.1}$$

The density scaling exponent expresses the slopes of the isomorphs by Eq. (3.14),
and as mentioned can be estimated from Eq. (4.4) evaluated at an effective
particle size:

$$\gamma = \left(\frac{\partial \ln(T)}{\partial \ln(\rho)}\right)_{S_{\text{ex}}} \cong \frac{n_0(r_0)}{3} \tag{5.2}$$
$$= \frac{-\ln(T)}{3}$$

solving the first order homogeneous differential equation along an isomorph
gives $\ln(T) = A\rho^{-1/3}$ where A is an constant of integration for the specific
isomorph. Generalizing to all isomorphs in gas phase A becomes a function
of the excess entropy: $A(S_{\text{ex}})$. Taking the derivative with respect to excess
entropy gives $\left(\frac{\partial \ln(T)}{\partial S_{\text{ex}}}\right)_\rho = A'(S_{\text{ex}})\rho^{-1/3}$. Comparing to Eq. (5.1) to get:

$$C_V{}^{\text{ex}} \propto \rho^{1/3} \text{ (for constant } S_{\text{ex}}). \tag{5.3}$$

In Fig. 5.7 the density scaling exponent and the correlation along the five
isomorphs can be seen. While the correlation remain high along all the
isomorphs, the density scaling exponent is decreasing as density increases.
Note that the shape of the density dependence is similar to the dashed line
of Fig. 4.9(a). Also note that the density scaling exponent varies between
almost four, to become less than two for a number of state points; corre-
sponding to the exponent of the approximate inverse power law decreasing
from almost 12 to less than six. Thus from a system with a face centered
cubic crystal structure, to some very soft system with a body center cubic

crystal structure .

In the following sections different methods to approximate the isomorphs will be used. They all allow for larger density changes and thus fewer simulations. It is interesting to compare the different methods i order to determine how well the give the same results as the small step isomorph.
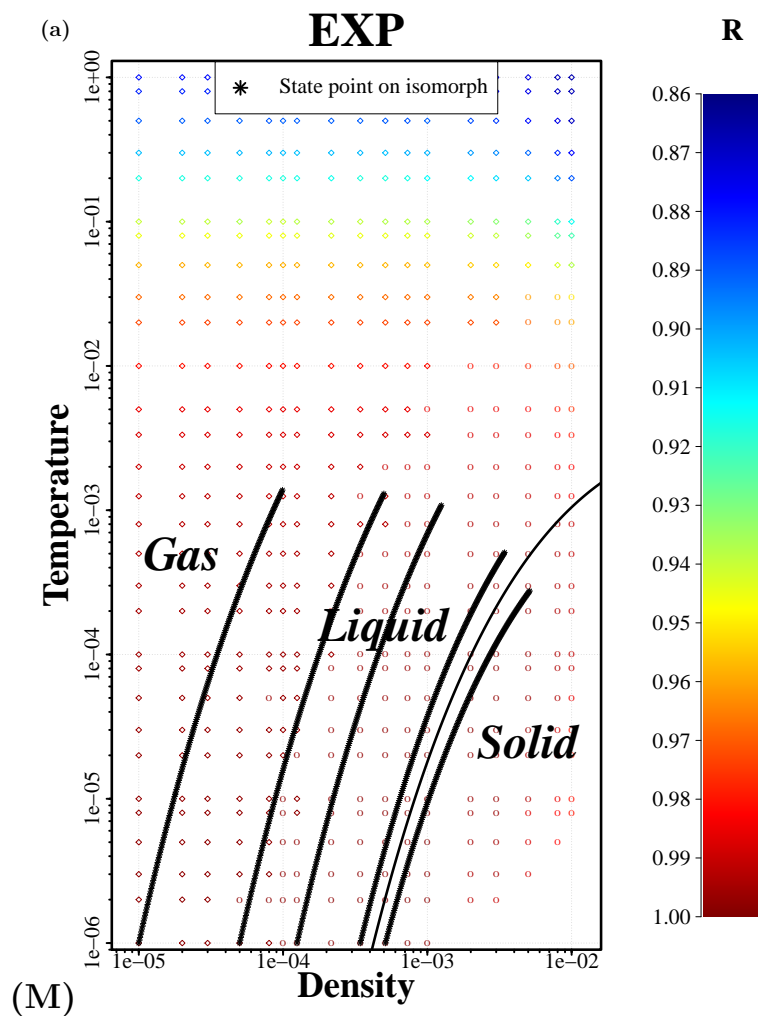
Figure 5.1: The five small step isomorphs marked by black stars merging into lines. Each isomorph span a decade in density and is traced in 230 steps - changing density approximately 1% for each step. The starting temperature is $T = 10^{-6}$ for all isomorphs, while the starting densities was chosen to explore the different structures of the system: the gas ($\rho = 10^{-5}$), the gas-liquid transition ($\rho = 5/cdot10^{-5}$), the dilute-liquid ($\rho = 1.25 \cdot 10^{-4}$), the dense-liquid ($\rho = 3.43 \cdot 10^{-4}$), and the crystal ($\rho = 5.12 \cdot 10^{-4}$). The circles indicate condensed phase: liquid and crystal, while diamonds indicate gas phase. The color coding gives the correlation.
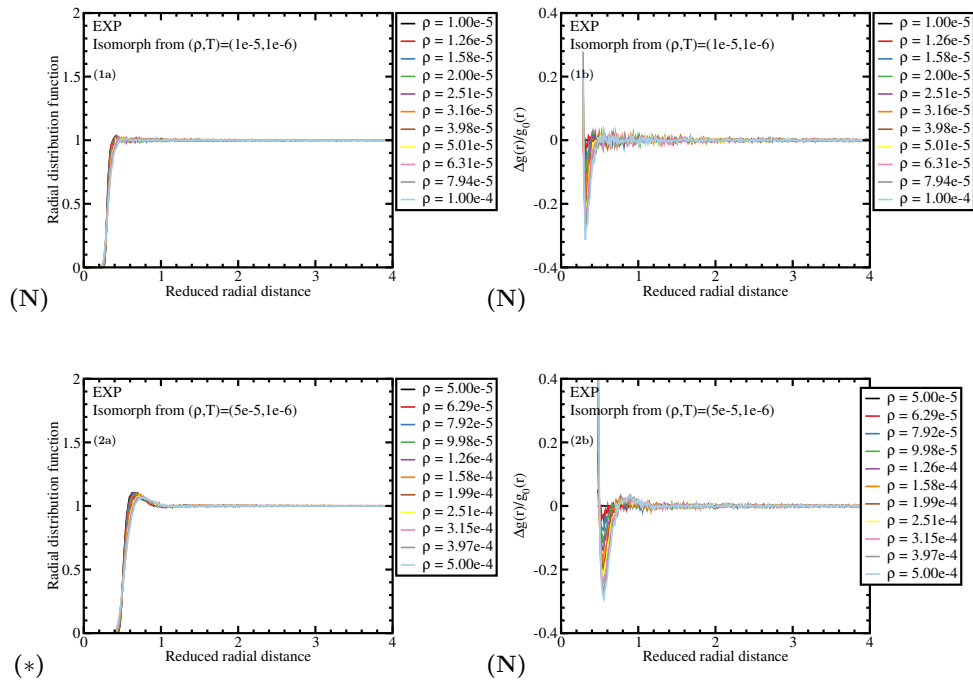
Figure 5.2: Structure of the initial state point and 10 evenly spaced state points along the gas and gas-liquid isomorph. *(a)* gives the radial distribution function with reduced distance along the isomorphs. *(b)* gives the change in structure along the isomorphs, quantified by the relative change in the radial distribution function compared to initial state point. The deviation increases steadily along isomorph.
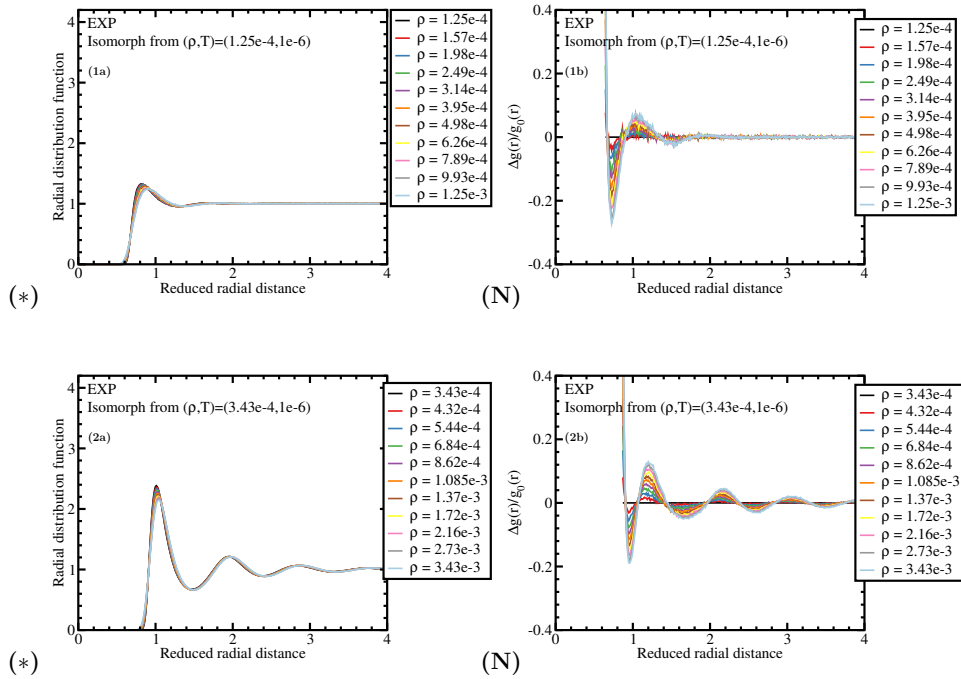
Figure 5.3: Structure of the initial state point and 10 evenly spaced state points along the liquid isomorphs. *(a)* gives the radial distribution function with reduced distance along the isomorphs. *(b)* gives the change in structure along the isomorphs, quantified by the relative change in the radial distribution function compared to initial state point. The deviation in each state point compared to the initial one, peaks on the first peak, and decreases with distance. Along the isomorph the deviation increases steadily.
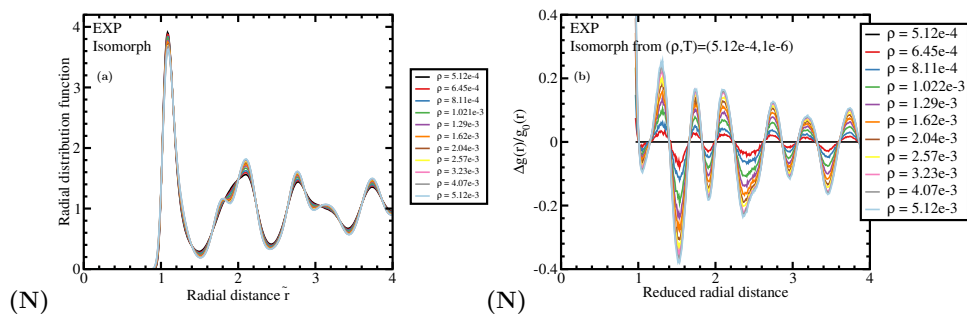
Figure 5.4: Structure of the initial state point and 10 evenly spaced state points along the crystal isomorph. *(a)* gives the radial distribution function with reduced distance along the isomorphs. The structure is seen to increase as the peaks narrow. This is reflecting a more order crystal in the higher density, higher temperature state points. *(b)* gives the change in structure along the isomorphs, quantified by the relative change in the radial distribution function compared to initial state point. The small deviation on the first peak is related to the manitude of the peak.
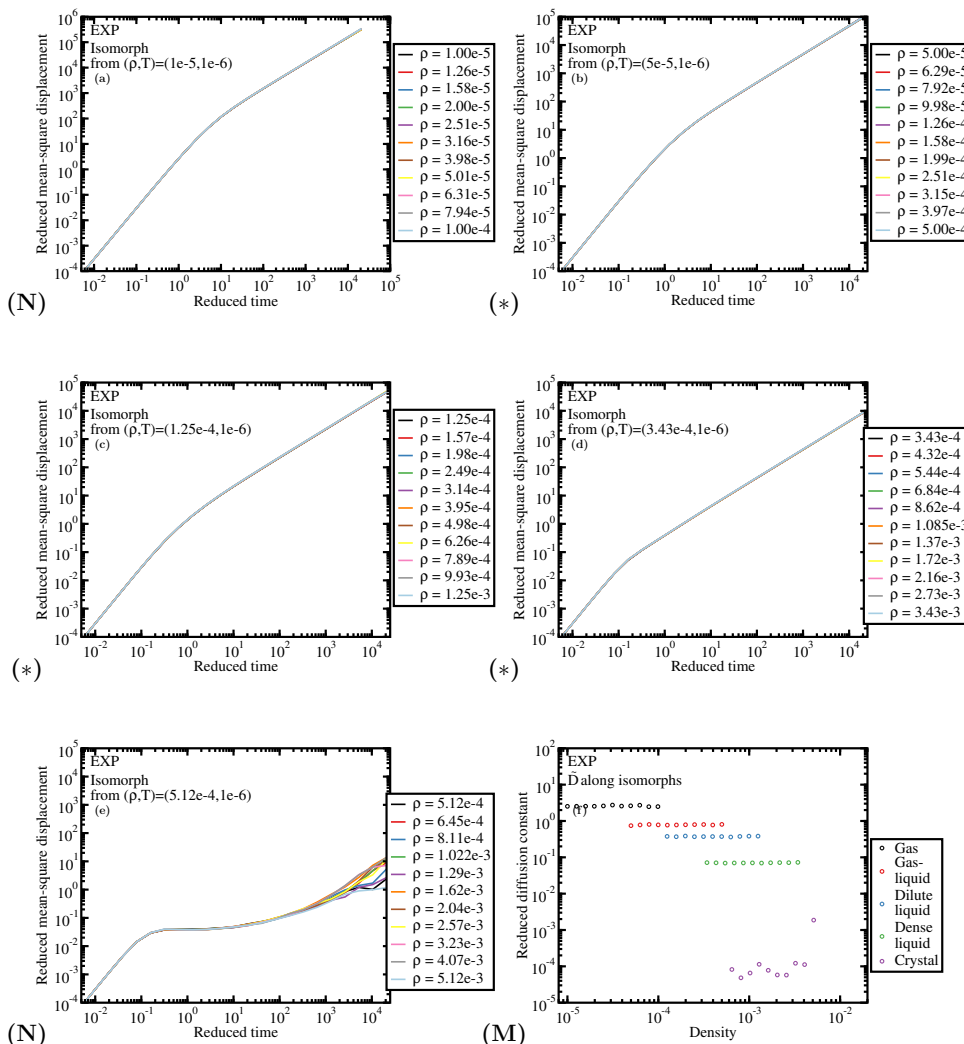
Figure 5.5: *(a-e)* The reduced mean-square displacement of the initial state point and 10 evenly spaced state points along each of the five isomorphs. In all the four fluid isomorphs (a-d) good collapse is observed. The mean-square displacement of the crystal (e) in the long time scales is due to defects in the non-perfect crystals. Isomorph invariance in the crystal cannot be confimed, nor can it be ruled out.

(f) The reduced diffusion constant determined from the diffusive part of the mean-square displacement, along the five isomorphs. The four fluid isomorphs show a high degreee of invariance, also reflected in the collaps of the mean-spuare displacements in (a-d), but again the results from the isomorph in crystal phase is noisy and due to defect diffusion
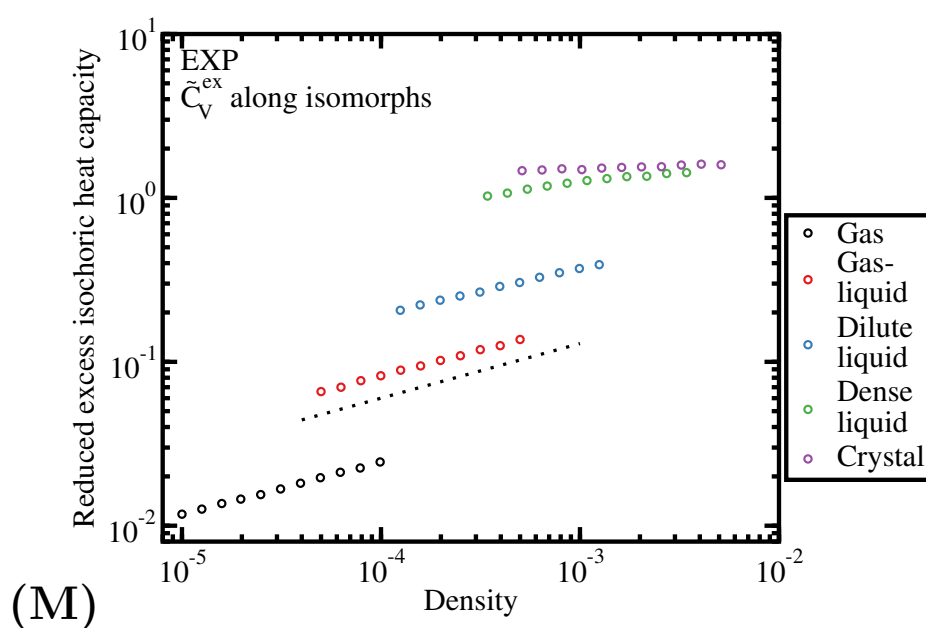
Figure 5.6: Reduced excess isochoric specific heat capacity ($\tilde{c}_V^{\mathrm{ex}}$) along the five isomorphs. Along all the fluid isomorphs $\tilde{c}_V^{\mathrm{ex}}$ is increasing. Most so along the gas-phase isomorphs, where the increase is proportionel to $\rho^{1/3}$ as indicated by the black dashed line. The crystal is almost constant around the perfect-harmonic crystal value of $3/2$. In the orignal (2009) version of the isomorph theory $\tilde{c}_V^{\mathrm{ex}}$ was an isomorph invariant[55], while in the (2014) version this was no longer the case[57].
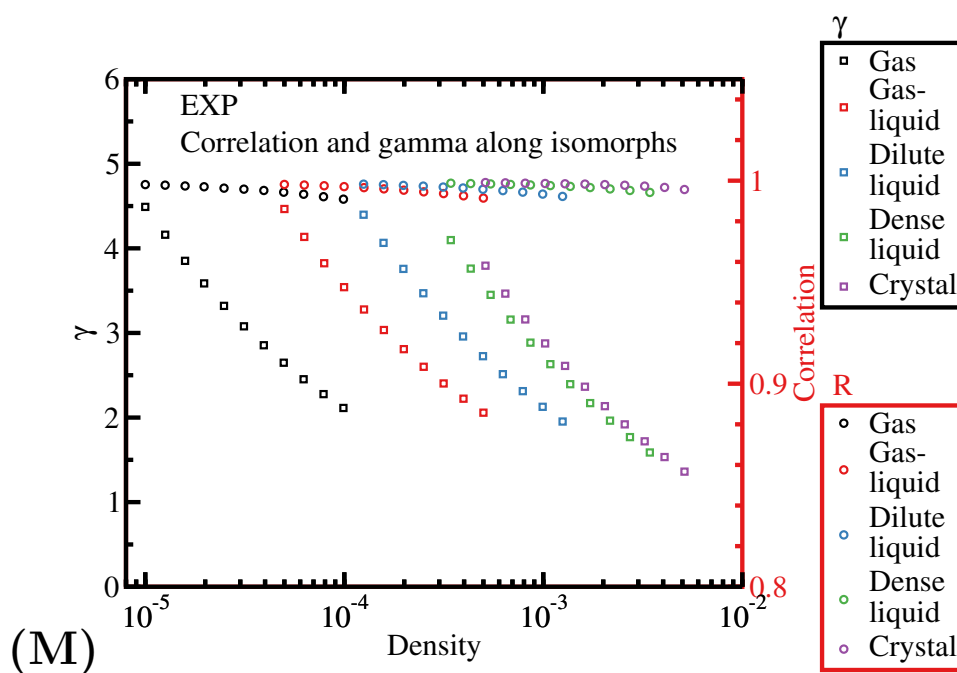
Figure 5.7: Correlation and density scaling exponent along the five iso-
morphs. The correlation remains high high along all the isomorphs. The
density scaling exponent varies between almost 1.5 and 4.5 - decreasing as
density increases. Note that the shape of the density dependence is similar
to the dashed line of Fig. 4.9(a).

5.2   Direct isomorph check

In this section the same five starting state points as in Section 5.1 will be used to trace out approximate isomorphs by the The Direct Isomorph Check[55]. Two different strategies will be used: a successive (step-by-step) strategy (termed DIC) where the result from the previous state point is used to find next, and a "single-state point" strategy (termed SSDIC) where all jumps is made from the starting state point. As indicated the method allows for much larger density jump than the small step method. As in the case of the small step method the isomorph is traced out starting with a simulation in the starting state point (ρ_1, T_1). From here a number of configurations is stored and rescaled to the target density (ρ_2). The task is then to determine the temperature (T_2) of the new state point so the two points are on the same isomorph. Two points on an isomorph fulfils the isomorph condition - thus having the same reduced unit configuration $(\tilde{\mathbf{R}})$ and the same excess entropy $(S_{\mathrm{ex}}(\tilde{\mathbf{R}}))$. The potential energy of the two state points is by 3.6:

$$U_1 = U(\rho_1, S_{\mathrm{ex}}(\tilde{\mathbf{R}}))$$
$$U_2 = U(\rho_2, S_{\mathrm{ex}}(\tilde{\mathbf{R}}))$$

These quantities fluctuate with $\mathbf{R}_1$ during the simulation, while the densities are fixed. By the chain rule:

$$\Delta U_1 = \left(\frac{\partial U(\rho_1, S_{\mathrm{ex}}(\tilde{\mathbf{R}}))}{\partial S_{\mathrm{ex}}(\tilde{\mathbf{R}})} \right)_{\rho_1} \left(\frac{\partial S_{\mathrm{ex}}(\tilde{\mathbf{R}})}{\partial \tilde{\mathbf{R}}} \right) \tag{5.4}$$

$$\Delta U_2 = \left(\frac{\partial U(\rho_2, S_{\mathrm{ex}}(\tilde{\mathbf{R}}))}{\partial S_{\mathrm{ex}}(\tilde{\mathbf{R}})} \right)_{\rho_2} \left(\frac{\partial S_{\mathrm{ex}}(\tilde{\mathbf{R}})}{\partial \tilde{\mathbf{R}}} \right) \tag{5.5}$$

Using $(\partial U/\partial S_{\mathrm{ex}})_\rho = T$ and taking the ratios of gives[26]:

$$\frac{\Delta U_2}{\Delta U_1} = \frac{T_2}{T_1} \,. \tag{5.6}$$

By Eq. (5.6) the new temperature T_2 can be estimated by linear regression analysis of $U(\mathbf{R}_1)$ versus $U(\mathbf{R}_2)$. Hence it is possible to determine the temperature jump required to stay on the isomorph when density is changed. It is important that the potential energies of the unscaled and scaled configurations is highly correlated. In Fig. 4.6 examples of scatter of potential energies of the unscaled and scaled configurations is seen.

   In this section a comparison between DIC-isomorphs generated from successive jumps and DIC-isomorphs generated by all jumps being made from a single state point. The latter ultimately making a jump increasing density ten fold, while all jumps in the former is of order 26% - thus covering the total density increase of factor ten in ten jumps. The UU-correlations remains

higher than 0.9 for all jumps, except for the two longest jumps in both the
gas-liquid and the dilute liquid, and the three longest jumps in the gas along
the SSDIC-approximate isomorphs. Along the DIC-approximate isomorphs
all jumps have a UU-correlation higher than 0.998. The relative deviation
in temperatures between state points traced by the direct isomorph check
and the isomorphs traced by the small step method can be seen in Fig. 5.8.
In (a) is the comparison from the DIC-approximate isomorphs, where the
deviation of most state points is within 1 %. Only state points along the
gas and crystal approximate isomorphs deviates more. The more dilute the
system the more does the direct isomorph check methods overestimate the
temperatures - and even more so he longer the jumps used. In the other
direction, as the system densifies the overestimation becomes underestima-
tions - in the crystal DIC-approximate isomorph by upto approximately 2%.
Here the longer jumps of the SSDIC seems to work better.   The struc-
ture and the relative change hereof along the DIC- and SSDIC-approximate
isomorphs is seen in Figs. 5.9 to 5.13. There is little difference between the
two strategies, and the more the radial distribution function differs from
one, the more signal also in the deviations. Only in the crystal is there a
somewhat clear difference, where the larger deviations is found along the
SSDIC-approximate isomorph. Comparing the differences along the small
step isomorphs (Figs. 5.2 to 5.4) and the (SS)DIC-approximate isomorphs
mainly shows a difference in the crystal case. Comparing the structures
along the crystal (approximate) isomorphs shows that while the general
structure is more or less the same, the substructures differs quite some even
if the starting configuration was the exact same.   In Figs. 5.14 and 5.15 very
good collapse of the dynamics probed by the reduced mean-square displace-
ment along the fluid isomorphs is observed, while in the crystal (Fig. 5.16)
has some deviations at the long time scales. Comparing to the reduced
mean-square displacement of the small step isomorph (Fig. 5.5(e)) the col-
lapse appears to be somewhat better.

The reduced diffusion coefficient confirms the observations from the
mean-square displacement: Good collapse along the fluid approximate iso-
morphs, but some randomness in along the crystal one. Furthermore very
good agreement with the small step isomorphs is observed in the fluid. In
Fig. 5.18 the reduced excess isochoric specific heat along the approximate
isomorphs is seen to very similar to the ones obtained by the small step
method. The correlation and density scaling exponent along the DIC- and
SSDIC-approximate isomorphs is plotted in Fig. 5.19 together with the re-
sults from the small step isomorphs (marked by + and ×). Good agree-
ment across the different methods is observed, except for the density scaling
exponent along the SSDIC-approximate gas isomorph. Here a systematic
deviation towards an underestimation can be observed.

(M)

(M)
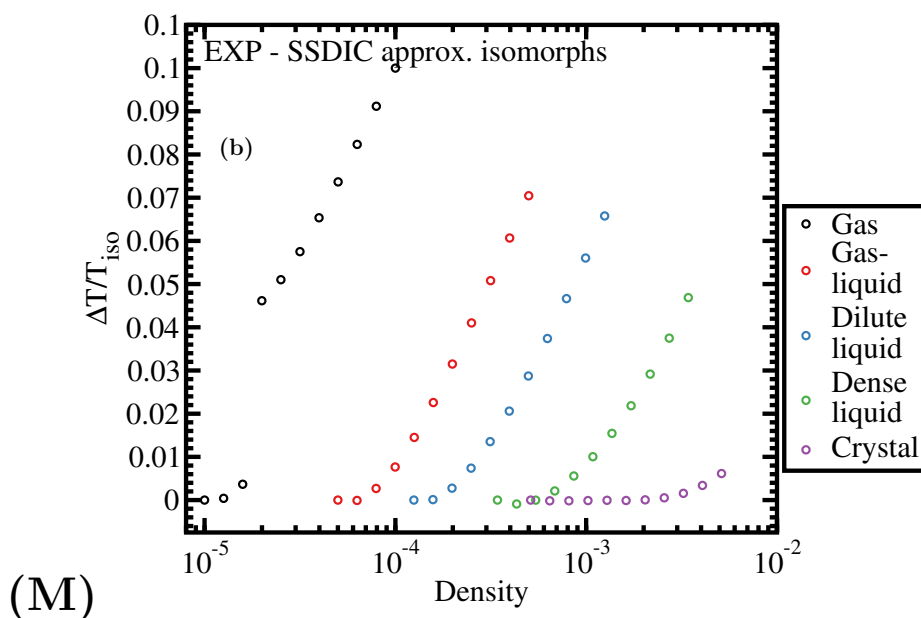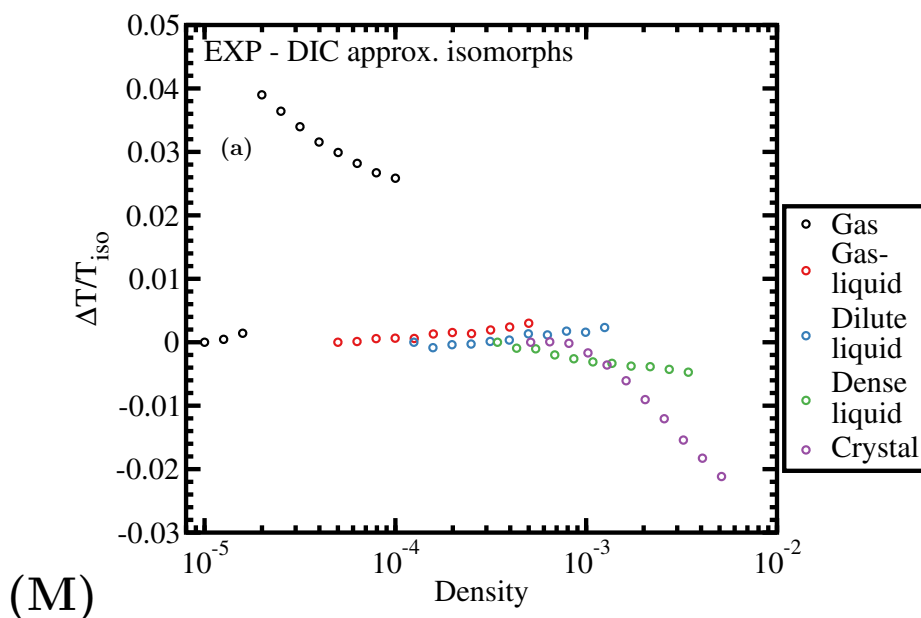
Figure 5.8: The relative deviation in temperatures between state points traced by the direct isomorph check and the isomorphs traced by the small step method. *(a)* The DIC-approximate method overestimates the temperature in the gas phase isomorphs, but as the system densifies the overshot becomes an underestimation along the dense-liquid and the crystal. All deviations are within a few procent. *(b)* The SSDIC-approximate method systematically overestimate the temperature more and more as the jumps becomes longer, and the more dilute the system is, the larger is the overshot.
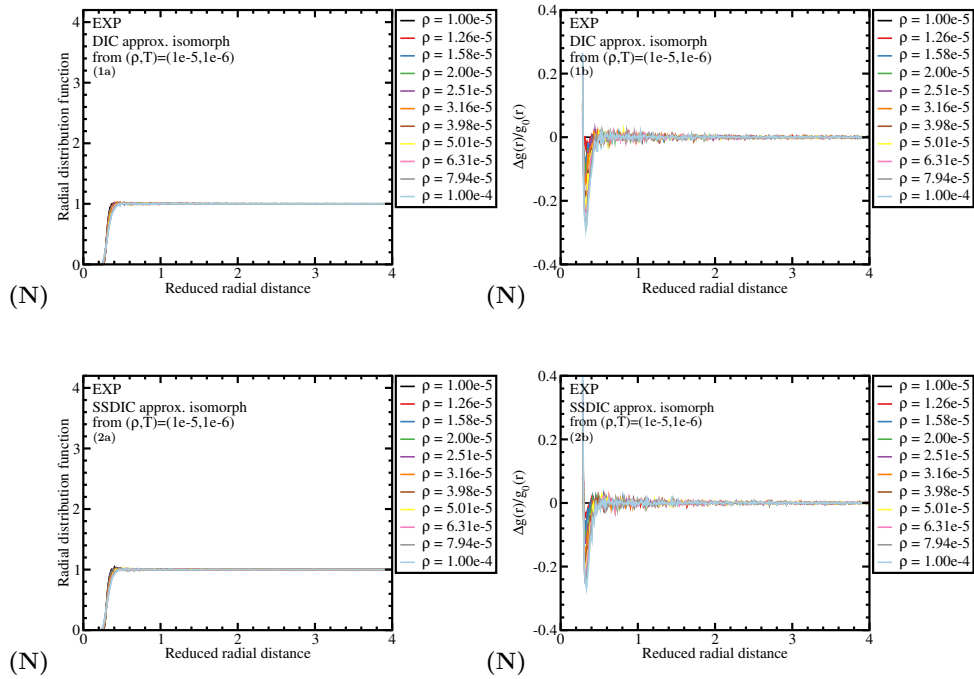
Figure 5.9: Structure of the initial state point and 10 evenly spaced state points along (1) the gas DIC-approximate isomorph and (2) the gas SSDIC-approximate isomorph. Both behaves very similar. *(a)* gives the radial distribution function with reduced distance along the isomorphs. *(b)* gives the change in structure along the isomorphs, quantified by the relative change in the radial distribution function compared to initial state point.
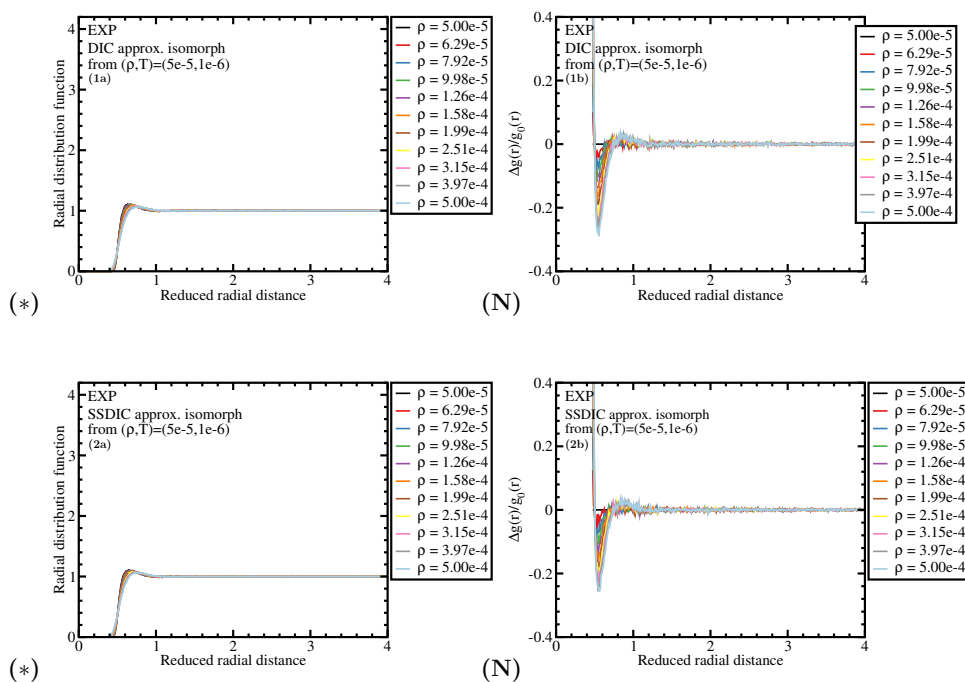
Figure 5.10: Structure of the initial state point and 10 evenly spaced state points along (1) the gas-liquid DIC-approximate isomorph and (2) the gas-liquid SSDIC-approximate isomorph. Both behaves very similar. *(a)* gives the radial distribution function with reduced distance along the isomorphs. *(b)* gives the change in structure along the isomorphs, quantified by the relative change in the radial distribution function compared to initial state point.
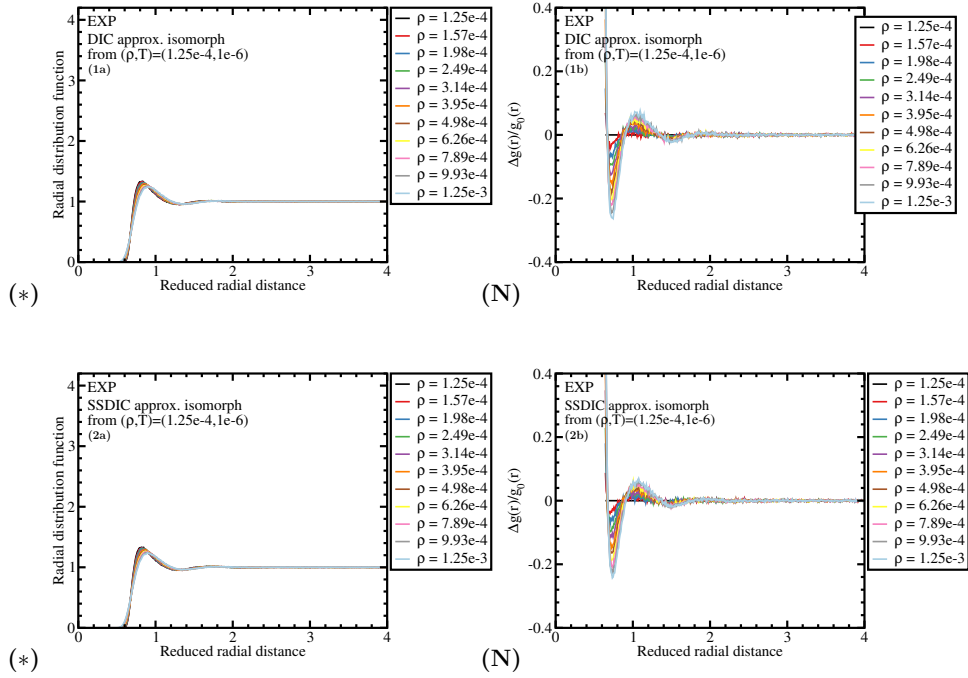
Figure 5.11: Structure of the initial state point and 10 evenly spaced state points along (1) the dilute liquid DIC-approximate isomorph and (2) the dilute liquid SSDIC-approximate isomorph. Both behaves very similar. *(a)* gives the radial distribution function with reduced distance along the isomorphs. *(b)* gives the change in structure along the isomorphs, quantified by the relative change in the radial distribution function compared to initial state point. The deviation in each state point compared to the initial one, have to peaks: one around the peak maximum of radial distribution, and one approximately halfway between the peak and the first minimum. Along the isomorph the deviation increases steadily for both methods.
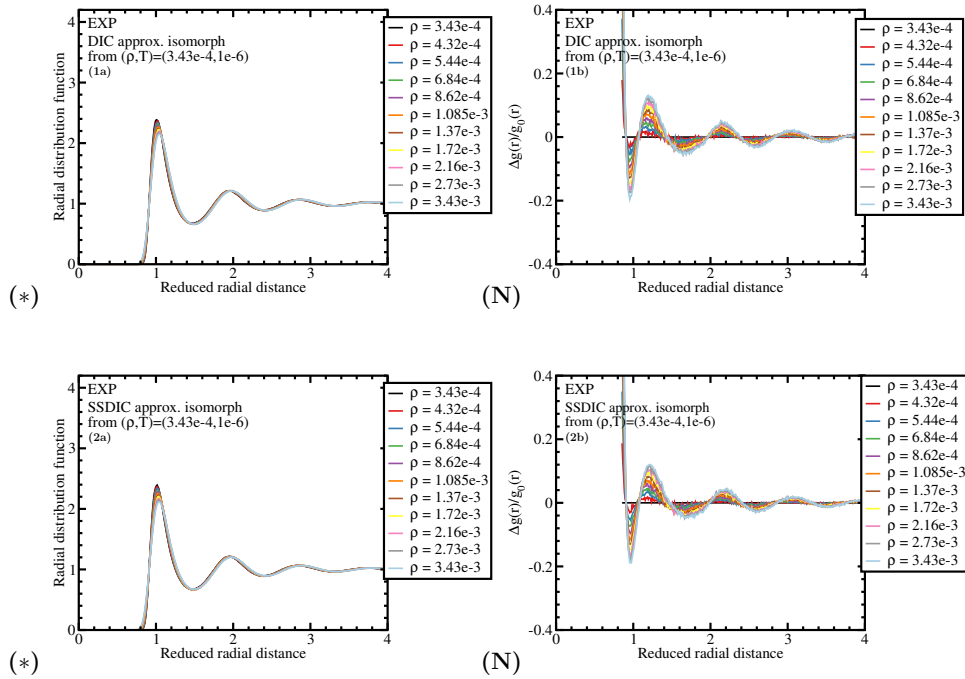
Figure 5.12: Structure of the initial state point and 10 evenly spaced state points along (1) the dense liquid DIC-approximate isomorph and (2) the dense liquid SSDIC-approximate isomorph. Both behaves very similar. *(a)* gives the radial distribution function with reduced distance along the isomorphs. *(b)* gives the change in structure along the isomorphs, quantified by the relative change in the radial distribution function compared to initial state point. Much same as in Fig. 5.11, just with increased deviation at longer distances due to more structure in systems.
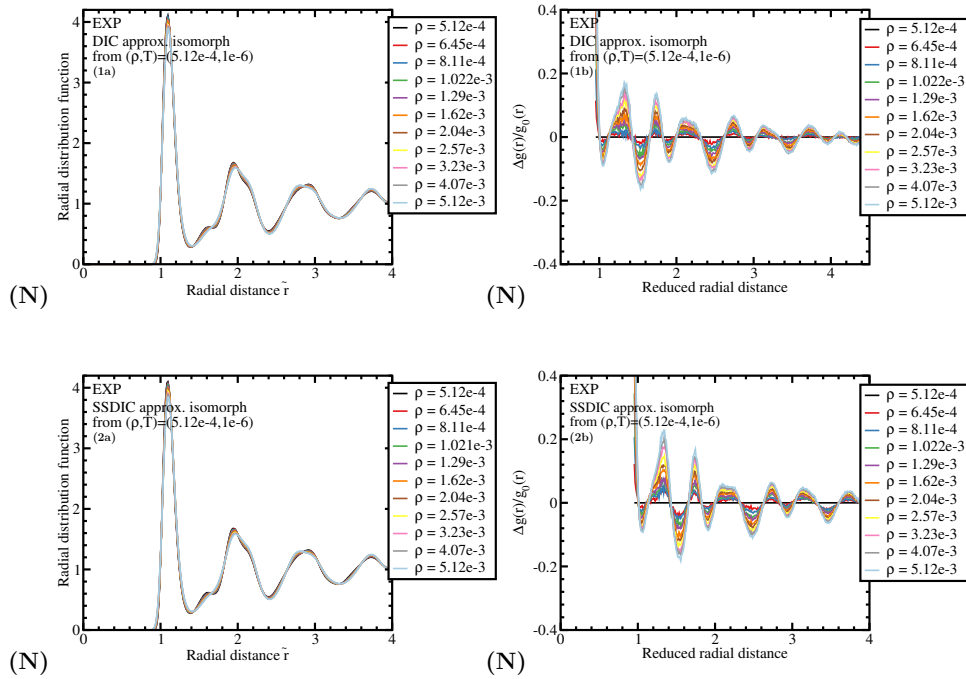
Figure 5.13: Structure of the initial state point and 10 evenly spaced state points along (1) the crystal DIC-approximate isomorph and (2) the crystal SSDIC-approximate isomorph. Both behaves very similar even if the deviations along the SSDIC-approximate isomorph is a little bit bigger. *(a)* gives the radial distribution function with reduced distance along the isomorphs. *(b)* gives the change in structure along the isomorphs, quantified by the relative change in the radial distribution function compared to initial state point.
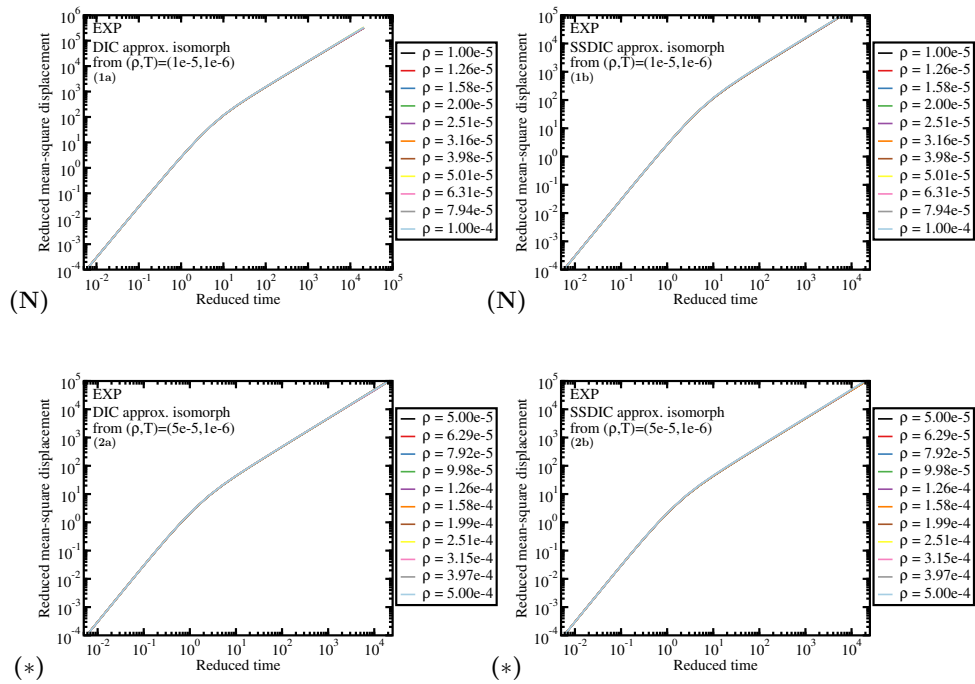
Figure 5.14: The reduced mean-square displacement of states point along *(1)* the gas and *(2)* the gas-liquid,along the *(a)* DIC- and *(b)* SSDIC-approximate isomorphs. A very good collapse is observed in all cases.
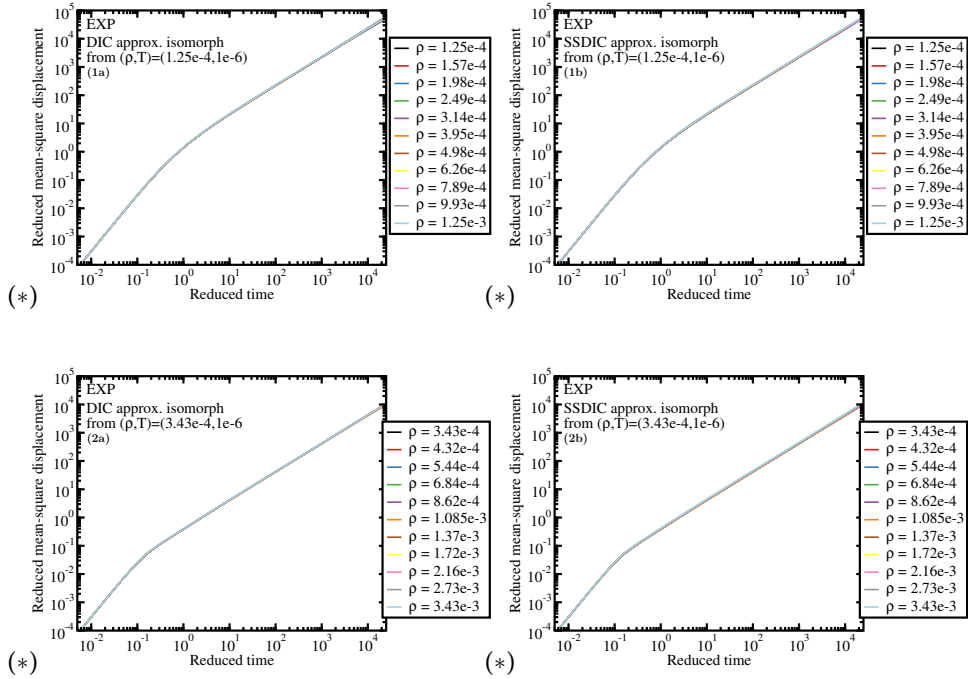
Figure 5.15: The reduced mean-square displacement of states point along the dilute- and dense liquid DIC- and SSDIC-approximate isomorphs. A very good collapse is observed in all cases.
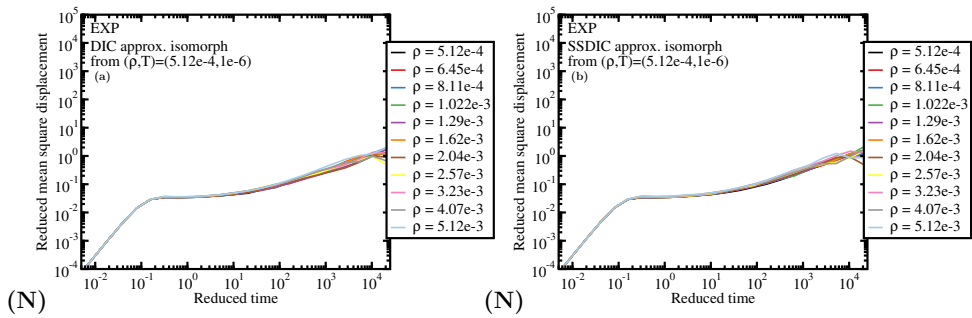
Figure 5.16: The reduced mean-square displacement of states point along the crystal DIC- and SSDIC-approximate isomorphs. The diffusive motion at long time scales is due to defects in the non-perfect crystals. Isomorph invariance in the crystal seems likely.
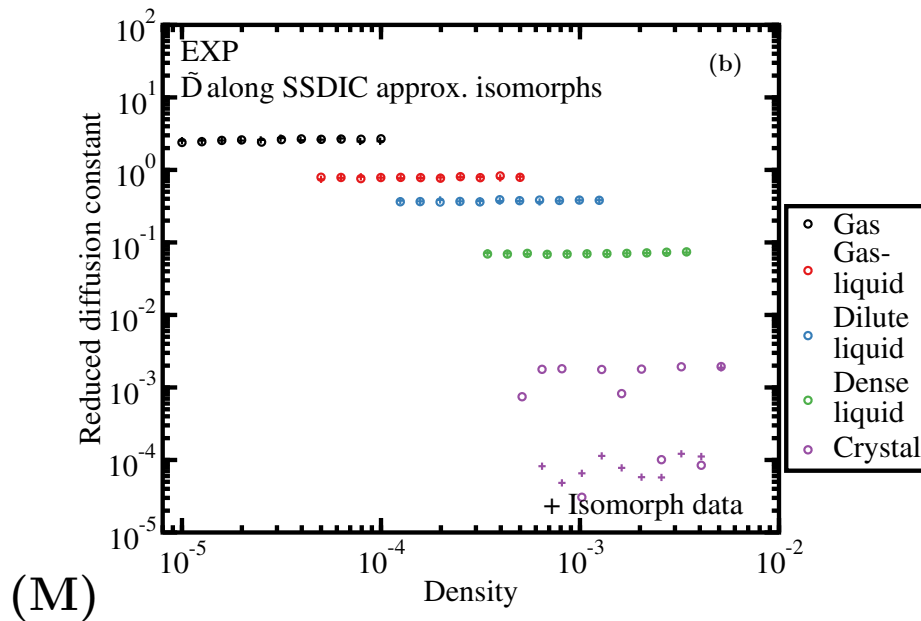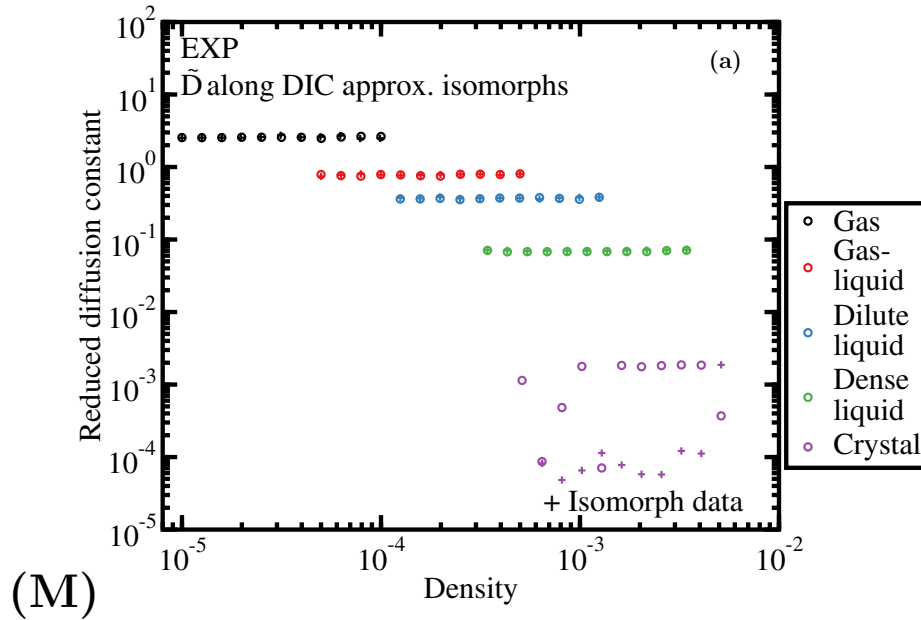
Figure 5.17: The reduced diffusion coefficient estimated from the diffusive part of the reduced mean-square displacement is marked by open circles. Crosses mark the results from the small step isomorphs (Fig. 5.5(f)). *(a)* along the DIC-approximate isomorphs. *(b)* along the SSDIC-approximate isomorphs. Good collaps is seen along all fluide isomorphs. The estimation of the diffusion in the crystal suffers from the crystal being formed from the melt.
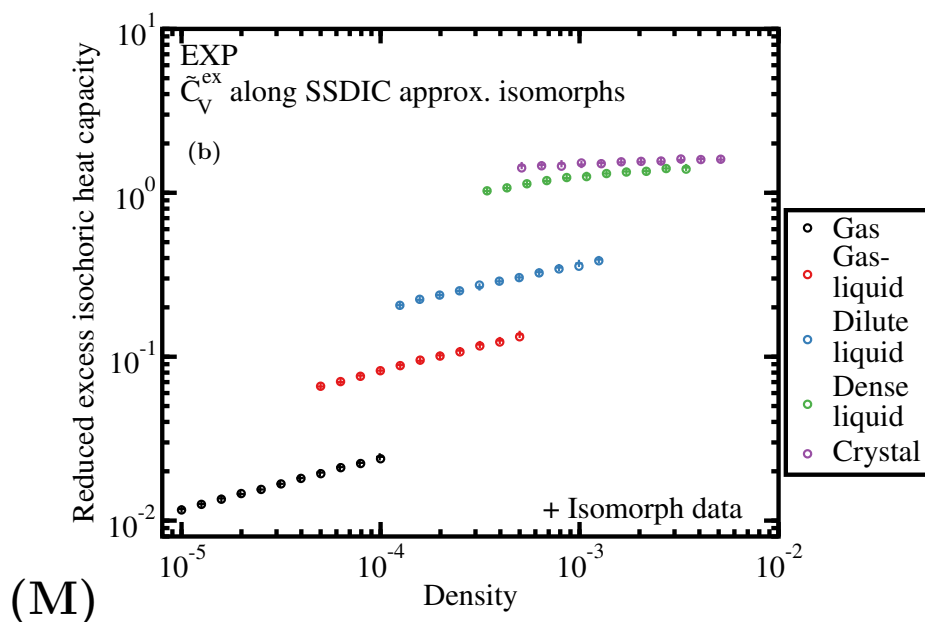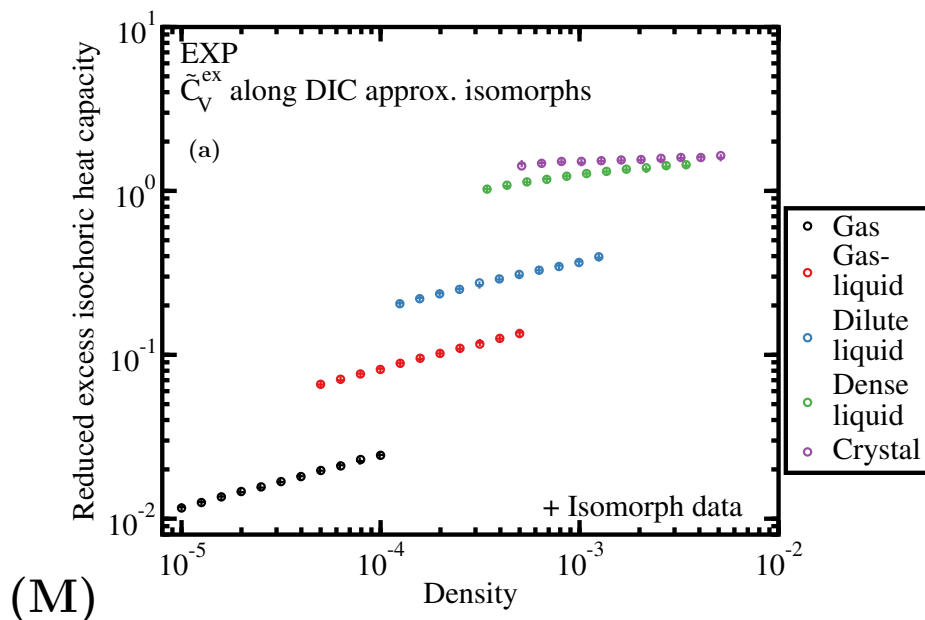
Figure 5.18: The reduced excess isochoric specific heat capacity along the
(a) DIC- and *(b)* SSDIC-approximate isomorphs is marked by open circles.
Crosses mark the results from the small step isomorphs (Fig. 5.6). Very
good agreement is seen along both approximate methods.
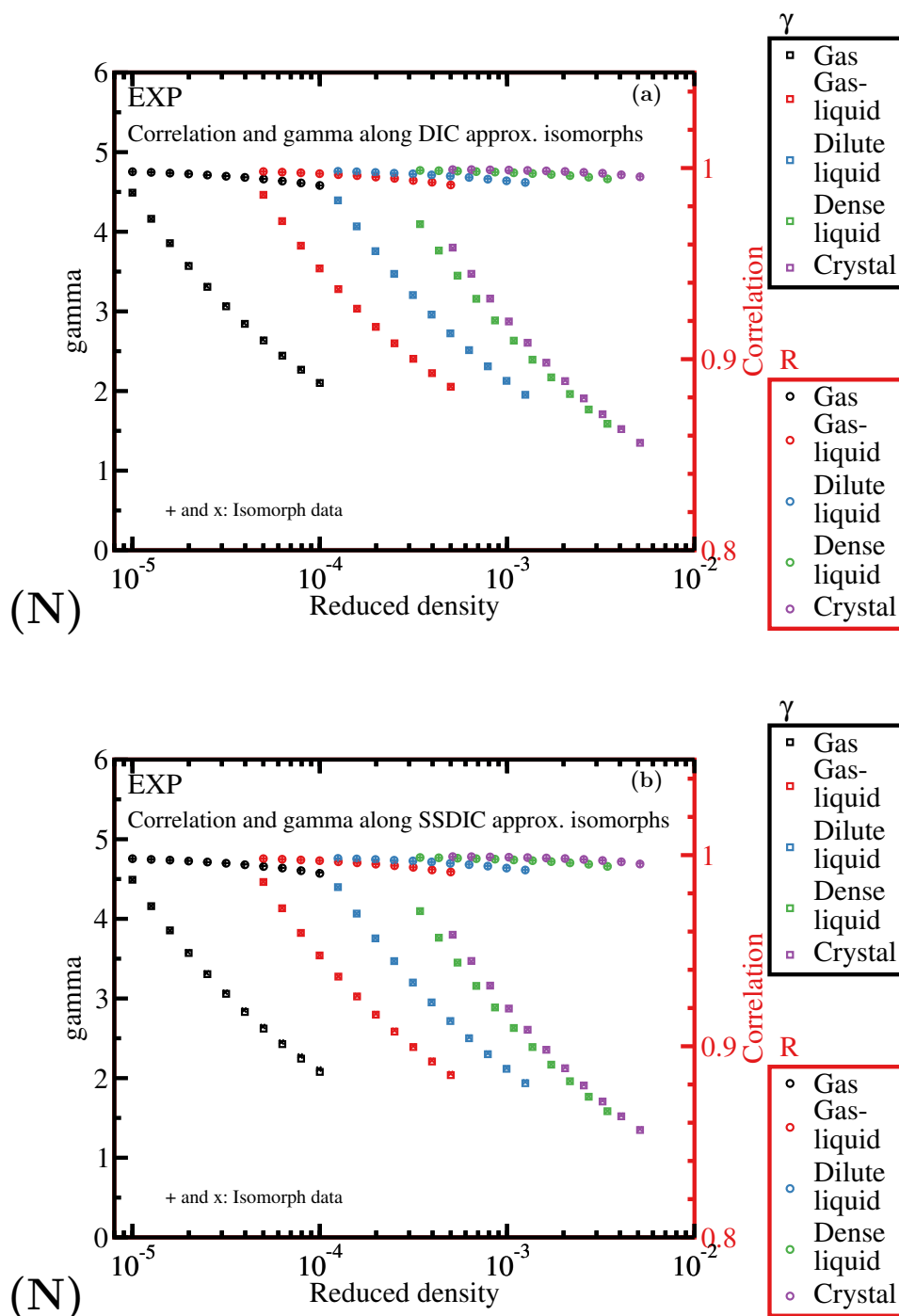
Figure 5.19: Correlation and density scaling exponent along the *(a)* DIC- and *(b)* SSDIC-approximate isomorphs. The results from the small step isomorphs is marked by + and ×. Good agreement is observed - only for the density scaling exponent along the SSDIC-approximate gas isomorph can a systematical deviation be observed: The approximate method gives a smaller value.

5.3 $h_p(\rho)$-approximated isomorphs

This section is new compared to Bacher et al. [26, 27] and the figures herein are all new.

This section deals with with analytically approximated isomorphs generated by what is termed $h_p(\rho)$ approximations. This method is based on the idea that an approximate inverse power law (IPL) exponent can be used to estimate the density-scaling exponent γ. It is argued below that the optimal p varies with the state point in question: $p \sim 2$ in the condensed liquid phase, consistent with the findings based on the eIPL approximation of Section 4.3, whereas $p \sim 0$ in the gas phase consistent with the dominance of pair collisions there.

The background of the $h_p(\rho)$ approximations is the following. In the original (2009) isomorph theory $C_V{}^{\mathrm{ex}}$ is an isomorph invariant [55], i.e., throughout the phase diagram $C_V{}^{\mathrm{ex}}$ depends only on S_{ex}. Integrating the identity $(\partial S_{\mathrm{ex}}/\partial \ln T)_\rho = C_V{}^{\mathrm{ex}}(S_{\mathrm{ex}})$ leads [70] to an equation of state of the form (in which $s = S_{\mathrm{ex}}/N$ is the excess entropy per particle)

$$T \;=\; f(s)\, h(\rho)\,. \tag{5.7}$$

Substituting this into Eq. (3.14) one finds

$$\gamma \;=\; \frac{d\ln h(\rho)}{d\ln \rho}\,. \tag{5.8}$$

Equation (5.8) implies that γ depends only on the density. For the EXP system this is only a good approximation at high densities and low temperatures (compare Fig. 4.8). One therefore needs to generalize Eq. (5.8) to allow for more general $h(\rho)$ functions, i.e., ones that also depend on S_{ex}. This was also the conclusion from the numerical study of Lennard-Jones type systems of Bøhling et al. [60] that developed the following method for calculating $h(\rho)$ from the pair potential.

Recalling the definition of the effective p and r-dependent IPL exponent for a general pair potential $v(r)$ (Eq. (4.3)), one may ask which function $h_p(\rho)$ this corresponds to in Eq. (5.8). The answer is (in which Λ is an isomorph-invariant number to be determined)

$$h_p(\rho) \;\equiv\; r^p\, v^{(p)}(r)\Big|_{r=\Lambda\rho^{-1/3}}\,. \tag{5.9}$$

To show this, first note that $r = \Lambda\rho^{-1/3}$ implies $d\ln\rho = -3\, d\ln r$. Assume that Eq. (5.7) can be generalized into $T = f(s)\, h_p(\rho, S_{\mathrm{ex}})$ and Eq. (3.14) to $\gamma \equiv (\partial \ln h_p(\rho, S_{\mathrm{ex}})/\partial \ln \rho)_{S_{\mathrm{ex}}}$. Since n_p can be expressed as $\left.\frac{-\partial \ln(r^p v^{(p)}(r))}{\partial \ln r}\right|_{r=\Lambda\rho^{-1/3}}$ one get

$$\gamma \;=\; \left.\frac{n_p(r)}{3}\right|_{r=\Lambda\rho^{-1/3}}\,. \tag{5.10}$$

The $h_p(\rho)$ approximations are based on assuming that $T = h_p(\rho, S_{\text{ex}})$, i.e., that the temperature is given by the following equation of state in which B is constant along each isomorph:

$$T = B \rho^{-p/3} \exp\left[-\Lambda \rho^{-1/3}\right] . \tag{5.11}$$

The corresponding expression for the density-scaling exponent is

$$\gamma_p = \frac{-p + \Lambda \rho^{-1/3}}{3} . \tag{5.12}$$

For a given state point, and choice of p, by combining Eqs. (5.11) and (5.12), and making a simulation to determine γ, the two unknowns B and Λ can be determined. Knowing these Eq. (5.11) gives the functional form of the $h_p(\rho)$-approximate isomorph. This has been done for different values of p using the starting state points of the small step isomorphs. Along the approximate isomorphs in ten evenly spaced in $\log(\rho)$ state points, simulations has been carried out to check the isomorph invariance. In the following results along the $h_p(\rho)$-approximate isomorph for $p \in \{0, 1, 2\}$ will be compared. Afterwards a method for predicting the optimal p-value will be discussed.

In Fig. 5.20(a-c) the relative deviation in temperatures between state points predicted by the $h_p(\rho)$-approximate isomorphs and the isomorphs traced by the small step method is plotted. Figure 5.20(d) shows the $h_p(\rho)$-approximate isomorphs for $p \in \{0, 1, 2\}$, compared to each of the five small step isomorphs. As p increases the deviations changes from overestimating the temperature to underestimating it. This is in agreement with Eq. (5.12). The $p = 0$ is in (a) seen to predict the isomorph well in the gas phase, but as the system densifies (b) and (c) shows that higher p-values is better, with $p = 2$ being best in case of the crystal and the dense liquid. These findings is also seen in (d).
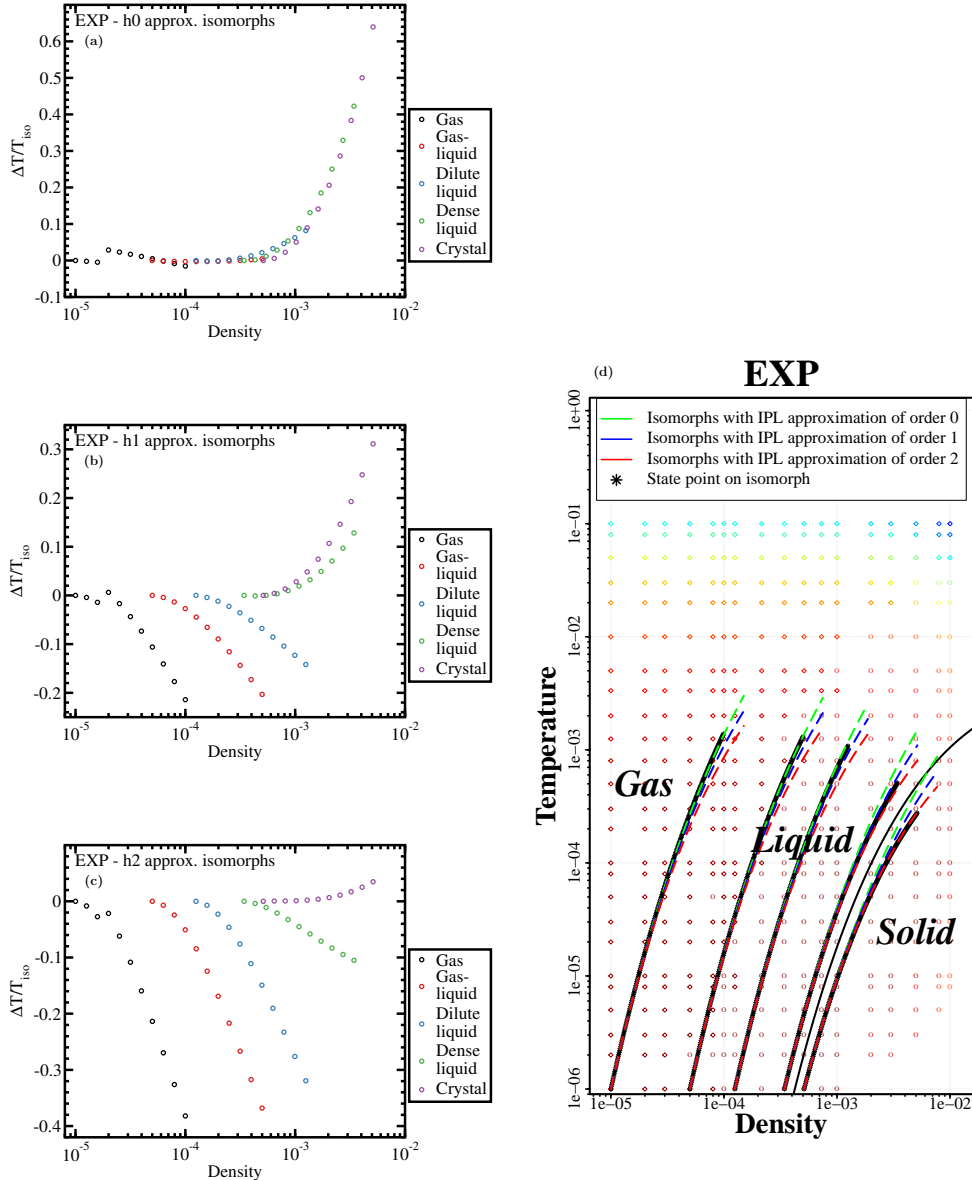
Figure 5.20: In (a-c) the relative deviation in temperatures between state points predicted by the $h_p(\rho)$-approximate isomorphs and the isomorphs traced by the small step method. *(a)* The $h_0(\rho)$-approximate isomorphs predictions for the temperature agrees well with the isomorphs as long as the system remains in the gas phase and in the transition region. In liquid and in the crystal deviations gets higher than 1%, and in the crystal even higher than 6%. All deviations is an overshot of temperature. *(b)* The $h_1(\rho)$-approximate isomorphs predictions for the temperature changes from being too low, to too high as the system densifies. *(c)* The $h_2(\rho)$-approximate isomorphs predictions for the temperature is seen to work best for the dense systems. *(d)* $h_p(\rho)$-approximate isomorphs for $p = 0, 1, 2$ (colored dashed lines) and the "true" isomorph traced by the small step method (black lines), plotted in the phase diagram of the EXP system. A crossover from $p \cong 0$ to $p \cong 2$ is seen when increasing the denseness of the system. The colors indicate the R values.

The isomorph invariance of the structure can be seen in Figs. 5.21 to 5.25, and the deviations matched well with the predictions from Fig. 5.20.

The dynamics in form of the reduced mean-square displacement and the reduced diffusion constant along the $h_p(\rho)$-approximated isomorphs can be seen in Figs. 5.26 to 5.28. Again, the $h_0(\rho)$-approximated isomorph works best for the gas, gas-liquid and dilute-liquid isomorphs whereas $p = 2$ works best for the dense liquid isomorph. Fig. 5.28(2) compares results for the diffusion constant along $h_p(\rho)$-approximated isomorphs for $p = 0$ (a), $p = 1$ (b), and $p = 2$ (c). The open symbols give result for the approximate isomorphs, the crosses the exact isomorph results. We see that $p = 0$ works best for the gas and gas-like isomorphs, whereas $p = 2$ works best for the dense liquid isomorph. The results for the dynamics of the crystal is noisy, so conclusions is hard to make.

Figure 5.29 compares results for the isochoric specific heat along $h_p(\rho)$-approximated isomorphs for $p = 0$ (a), $p = 1$ (b), and $p = 2$ (c). The open symbols give result for the approximate isomorphs, the crosses the exact isomorph results. We see that $p = 0$ works best for the gas and gas-like isomorphs, whereas $p \in \{1, 2\}$ works best for the dense liquid and crystal isomorphs.

In 5.30 the correlation and density scaling exponent along the $h_p(\rho)$-approximate isomorphs for $p = 0$ (a), $p = 1$ (b), and $p = 2$ (c). Comparing to the results from the small step isomorphs (marked by $+$ and $\times$), good agreement is observed between the gas, gas-liquid and dilute liquid $h_0(\rho)$-approximate isomorphs, while the dense liquid and crystal is well approximated by the $h_2(\rho)$-approximate isomorphs.
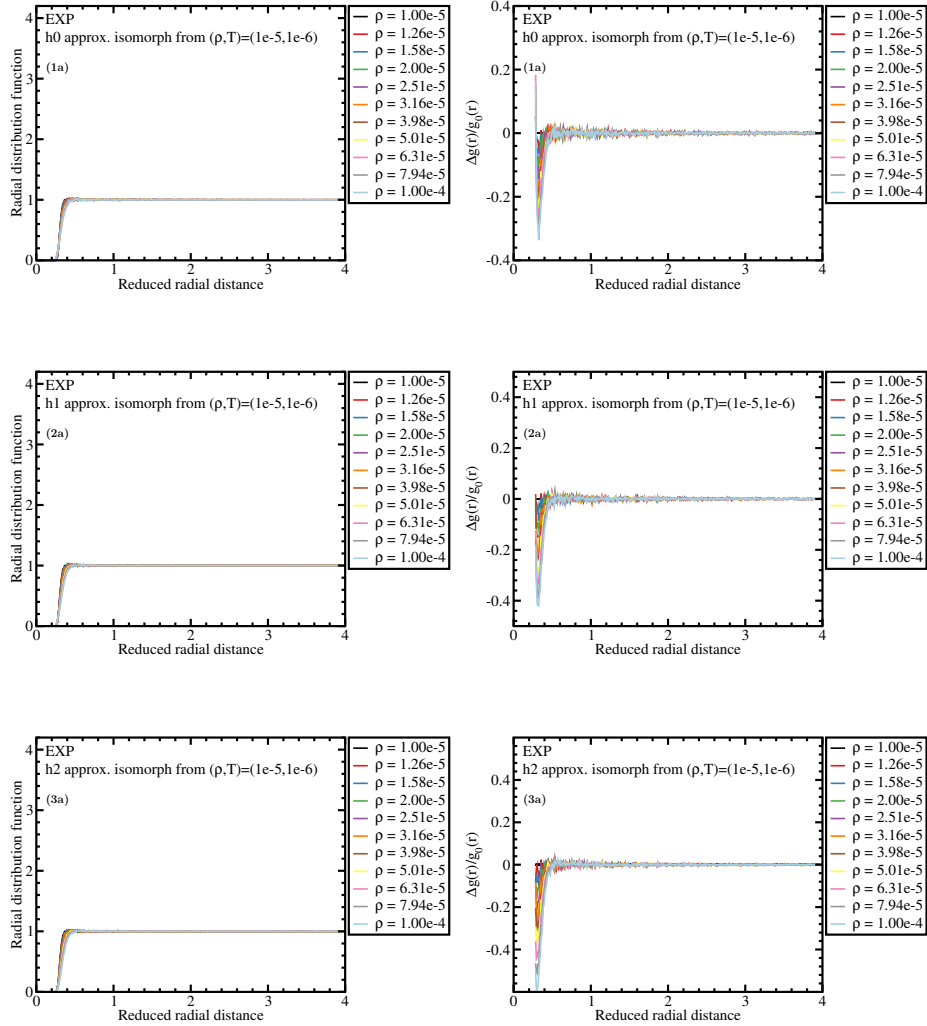
Figure 5.21: Structure of the initial state point and 10 evenly spaced state points along (1) the gas $h_0(\rho)$-approximate isomorph, (2) the gas $h_1(\rho)$-approximate isomorph, and (3) the gas $h_2(\rho)$-approximate isomorph. (a) gives the radial distribution function with reduced distance along the isomorphs. (b) gives the change in structure along the isomorphs, quantified by the relative change in the radial distribution function compared to initial state point. The deviations is increasing with p inline with the expectation from Fig. 5.20.
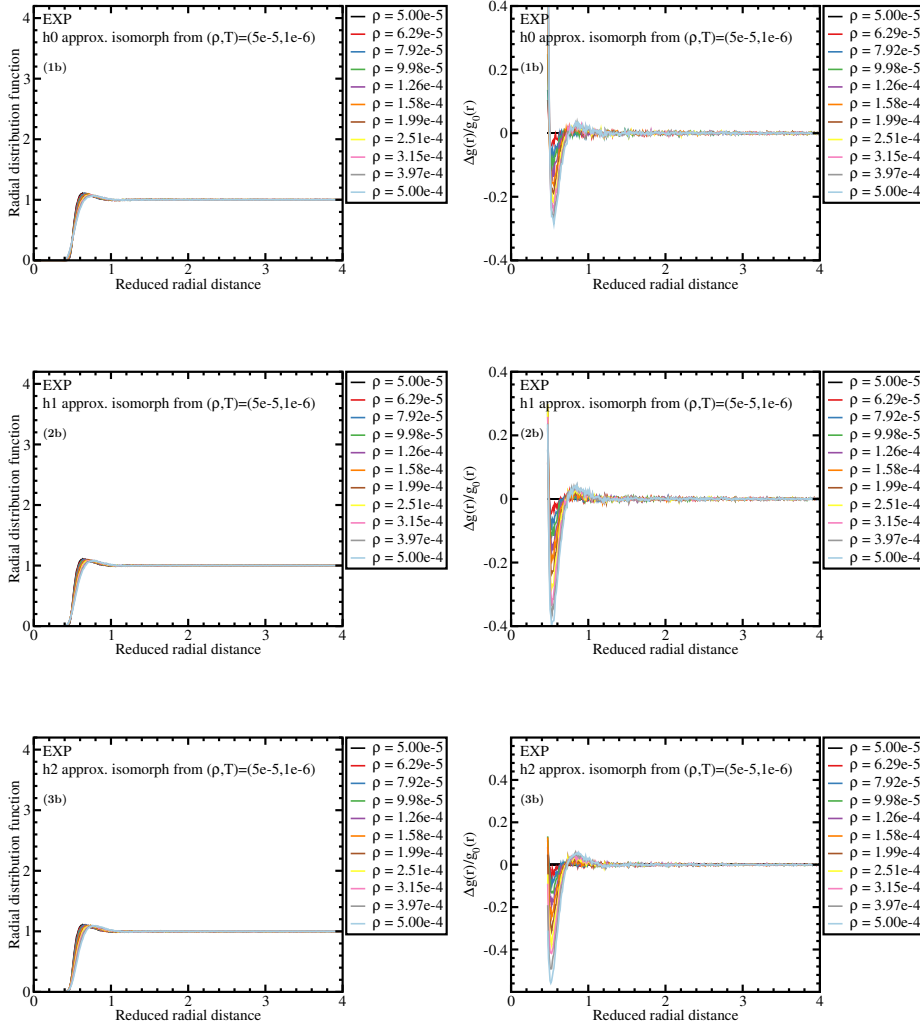
Figure 5.22: Structure of the initial state point and 10 evenly spaced state points along (1) the gas-liquid $h_0(\rho)$-approximate isomorph, (2) the gas-liquid $h_1(\rho)$-approximate isomorph, and (3) the gas-liquid $h_2(\rho)$-approximate isomorph. *(a)* gives the radial distribution function with reduced distance along the isomorphs. *(b)* gives the change in structure along the isomorphs, quantified by the relative change in the radial distribution function compared to initial state point. The deviations is increasing with p inline with the expectation from Fig. 5.20.
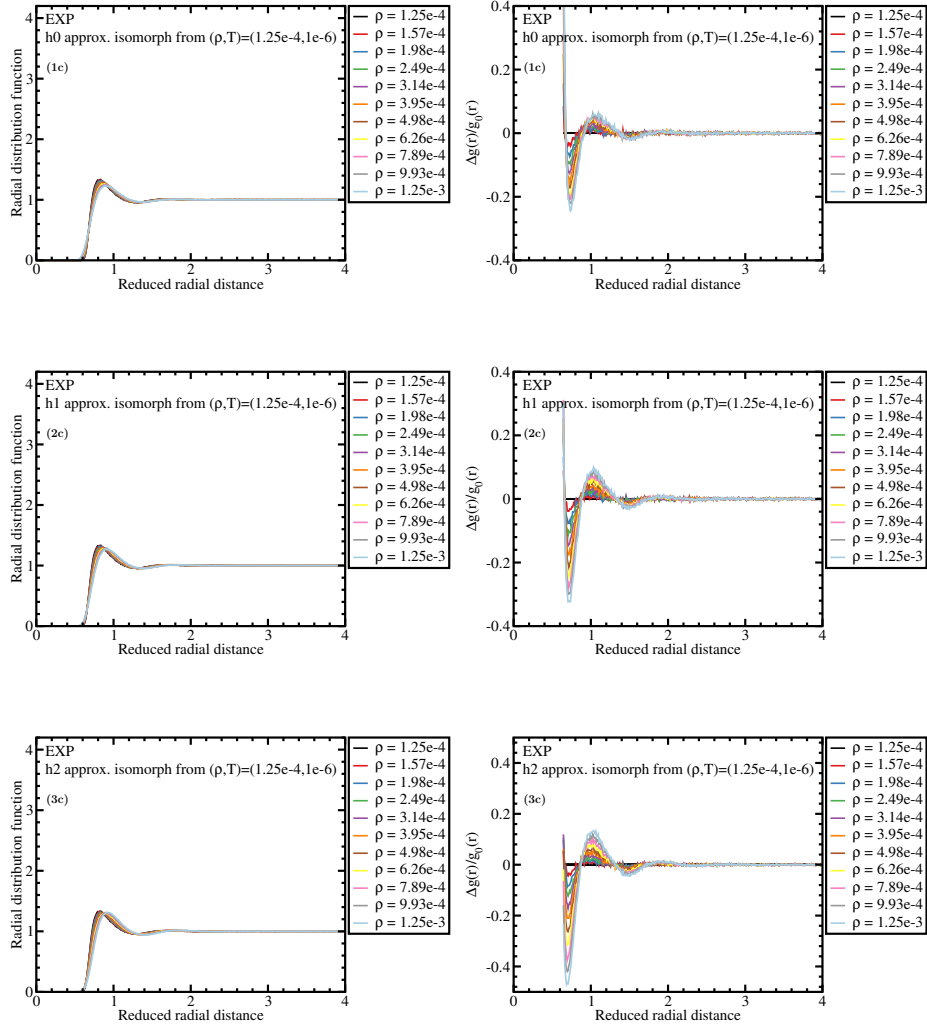
Figure 5.23: Structure of the initial state point and 10 evenly spaced state points along (1) the dilute liquid $h_0(\rho)$-approximate isomorph, (2) the dilute liquid $h_1(\rho)$-approximate isomorph, and (3) the dilute liquid $h_2(\rho)$-approximate isomorph. *(a)* gives the radial distribution function with reduced distance along the isomorphs. *(b)* gives the change in structure along the isomorphs, quantified by the relative change in the radial distribution function compared to initial state point. The deviations is increasing with p inline with the expectation from Fig. 5.20.
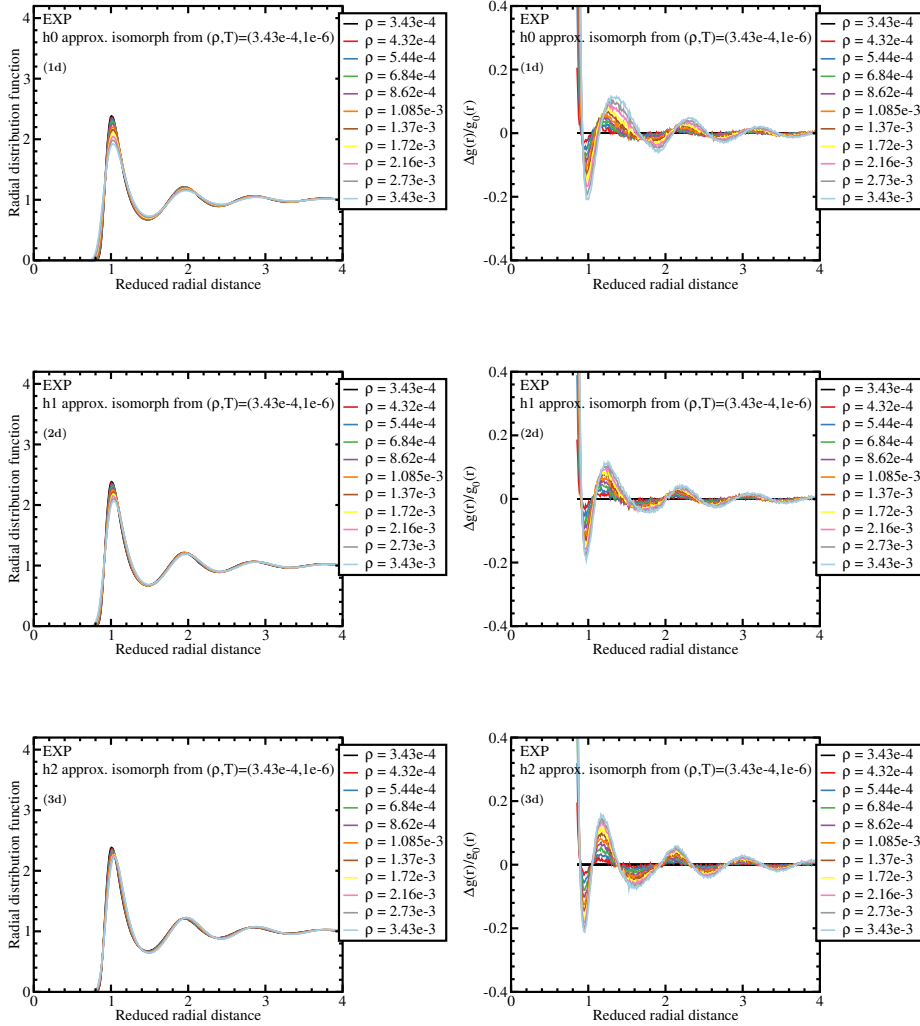
Figure 5.24: Structure of the initial state point and 10 evenly spaced state points along (1) the dense liquid $h_0(\rho)$-approximate isomorph, (2) the dense liquid $h_1(\rho)$-approximate isomorph, and (3) the dense liquid $h_2(\rho)$-approximate isomorph. *(a)* gives the radial distribution function with reduced distance along the isomorphs. *(b)* gives the change in structure along the isomorphs, quantified by the relative change in the radial distribution function compared to initial state point. The deviations is largest for $p = 0$, but quite similar for the other two.
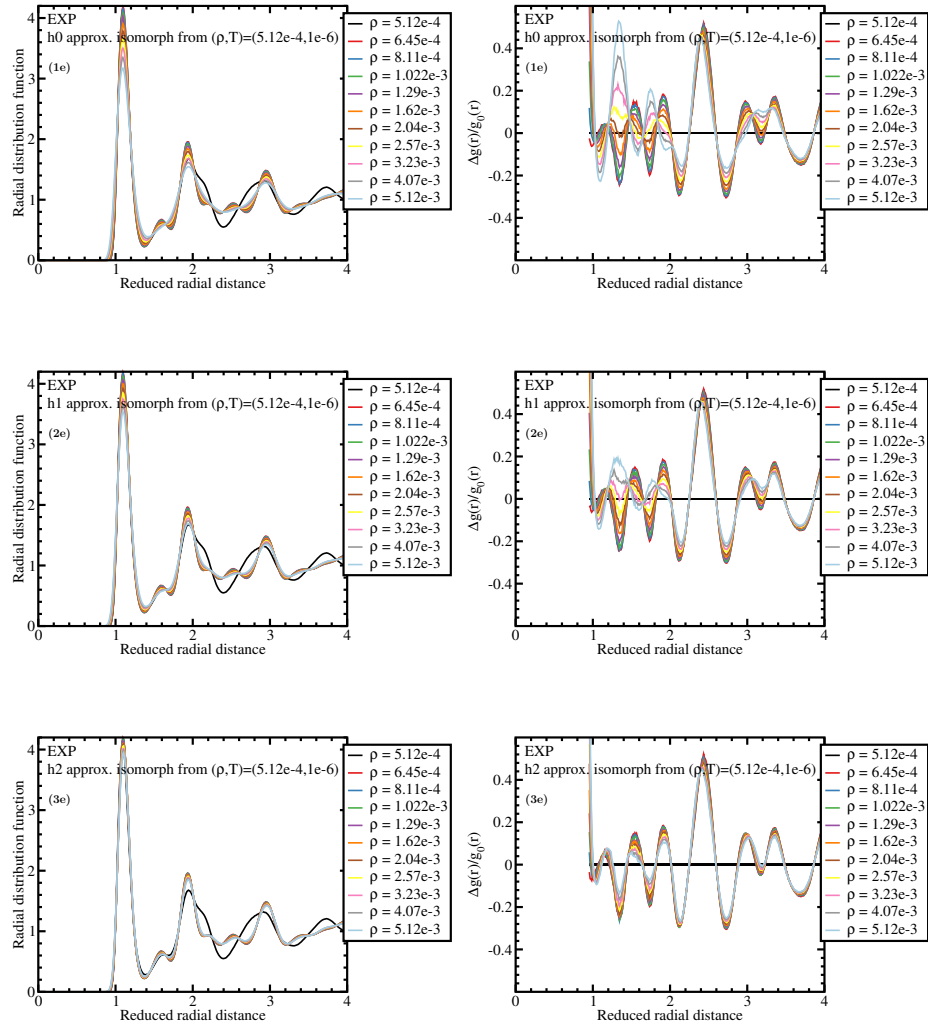
Figure 5.25: Structure of the initial state point and 10 evenly spaced state points along (1) the crystal $h_0(\rho)$-approximate isomorph, (2) the crystal $h_1(\rho)$-approximate isomorph, and (3) the crystal $h_2(\rho)$-approximate isomorph. *(a)* gives the radial distribution function with reduced distance along the isomorphs. *(b)* gives the change in structure along the isomorphs, quantified by the relative change in the radial distribution function compared to initial state point. The collapse with the initial state point is poor in all cases, but with $p = 2$ the collapse of the rest of the state points is quite good.
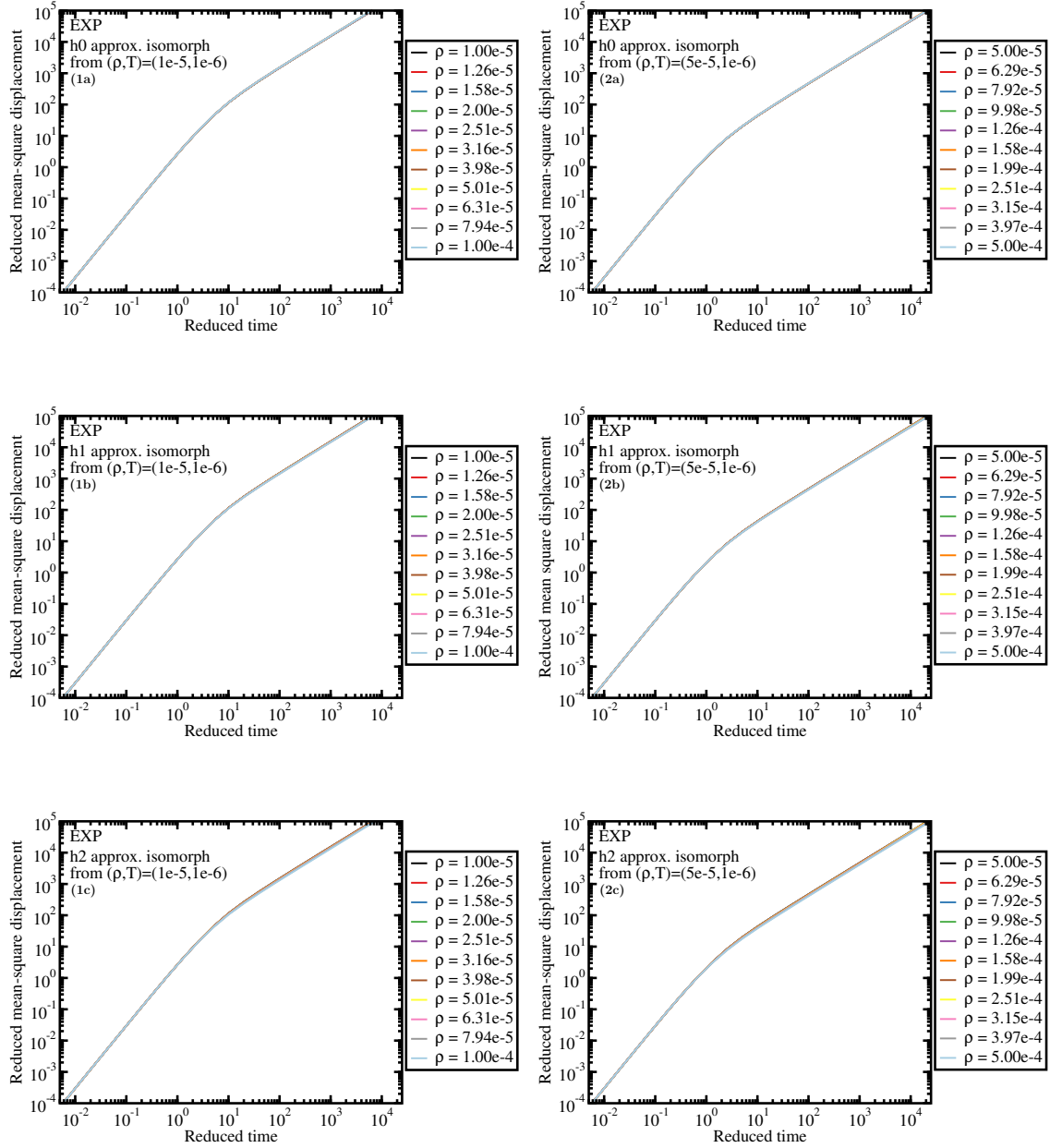
Figure 5.26: The reduced mean-square displacement of states point along the gas and gas-liquid $h_p(\rho)$-approximate isomorphs for $p = 0$ (a), $p = 1$ (b), and $p = 2$ (c). The best collapse is observed along the $h_0(\rho)$-approximate isomorphs.
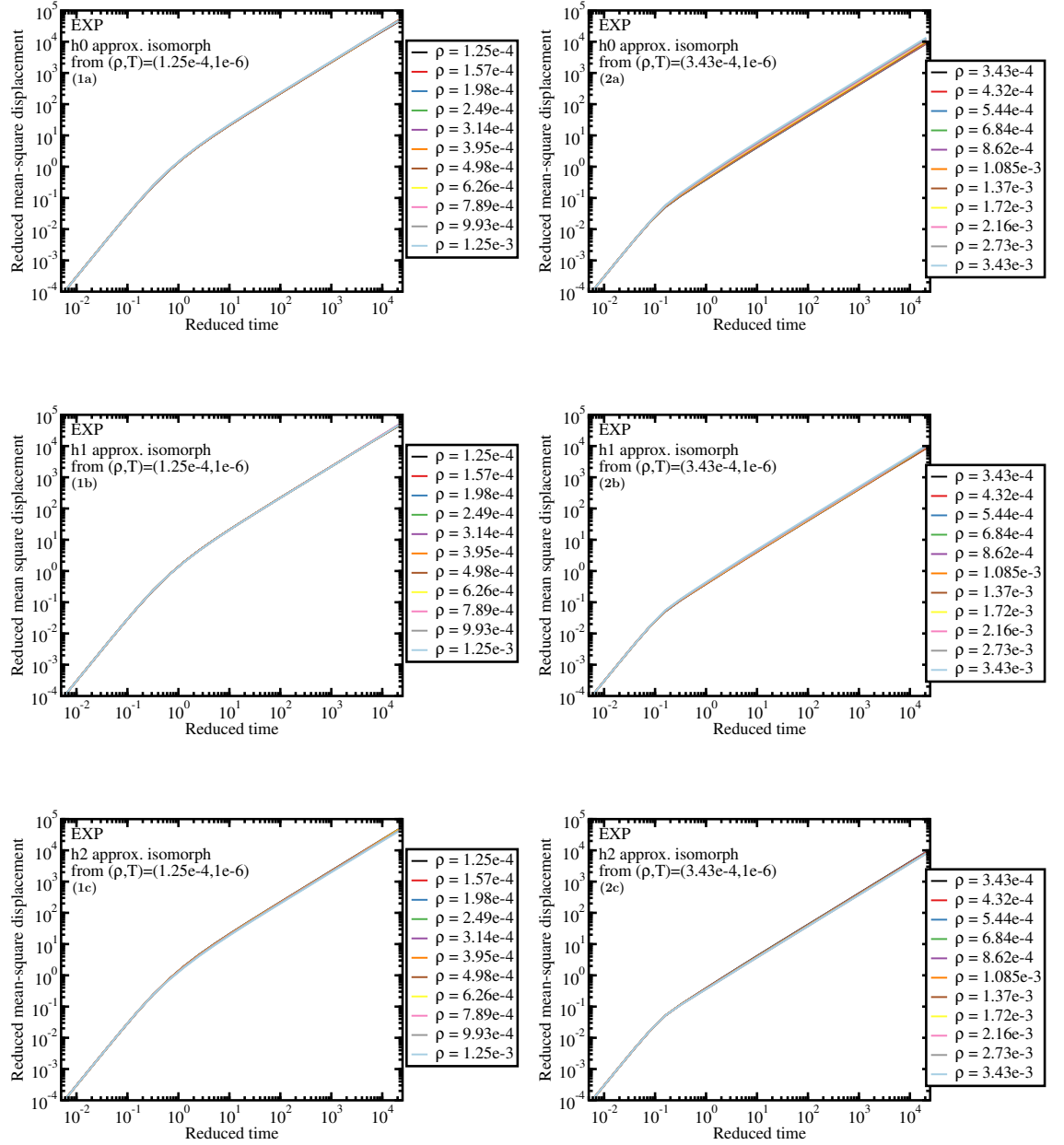
Figure 5.27: The reduced mean-square displacement of states point along the dilute- and dense-liquid $h_p(\rho)$-approximate isomorphs for $p = 0$ (a), $p = 1$ (b), and $p = 2$ (c). The best collapse is observed along the $h_0(\rho)$-approximate isomorph for the dilute liquid (1), while the better collaps of the dense-liquid (2) is along the $h_1(\rho)$-approximate isomorph.
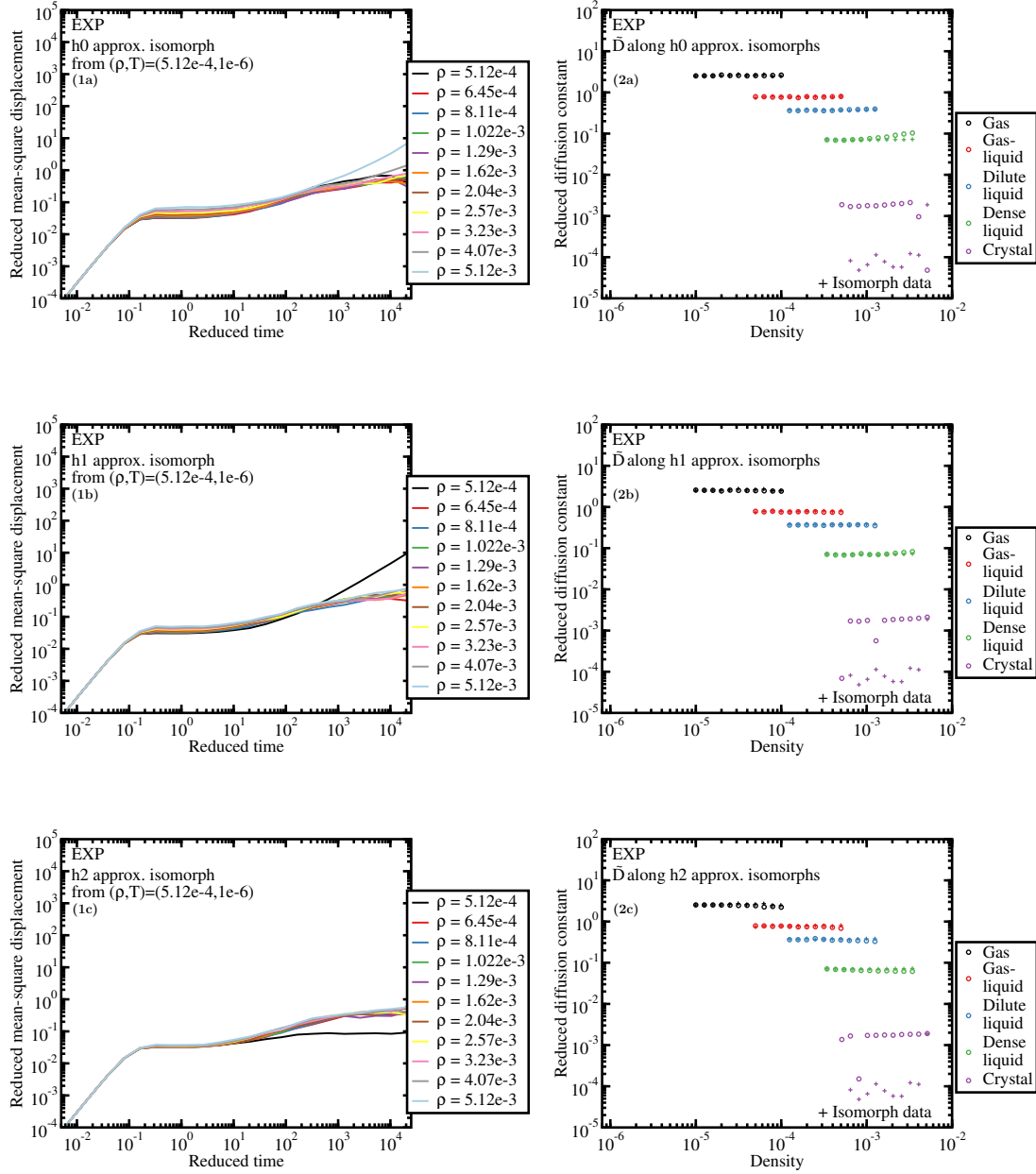
Figure 5.28: *(1)* The reduced mean-square displacement of states point along the crystal $h_p(\rho)$-approximate isomorphs for $p = 0$ (a), $p = 1$ (b), and $p = 2$ (c). The best collapse is observed along the $h_2(\rho)$-approximate isomorph, where except from noise only the first state point is notably different from the rest.

(2) The reduced diffusion constant determined from the diffusive part of the mean-square displacement along all the $h_p(\rho)$-approximate isomorphs for $p = 0$ (a), $p = 1$ (b), and $p = 2$ (c).
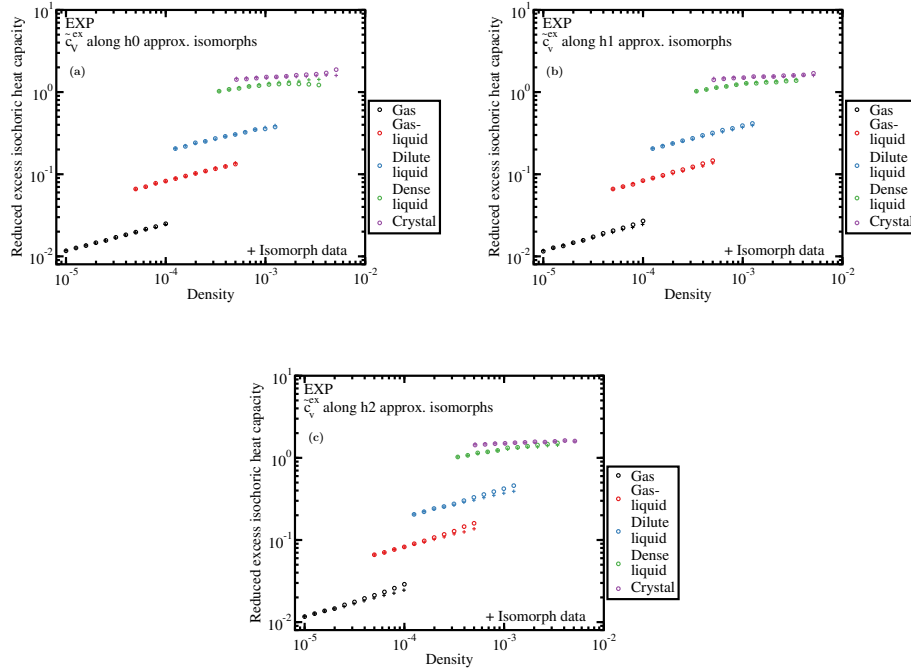
Figure 5.29: The reduced excess isochoric specific heat capacity along the $h_p(\rho)$–approximate isomorphs for $p = 0$ (a), $p = 1$ (b), and $p = 2$ (c), is marked by open circles. Crosses mark the results from the small step isomorphs (Fig. 5.6).Good agreement is observed between the gas, gas-liquid and dilute liquid $h_0(\rho)$-approximate isomorphs, while the dense liquid and crystal is well approximated by the $h_p(\rho)$-approximate isomorphs with $p \in \{1, 2\}$.
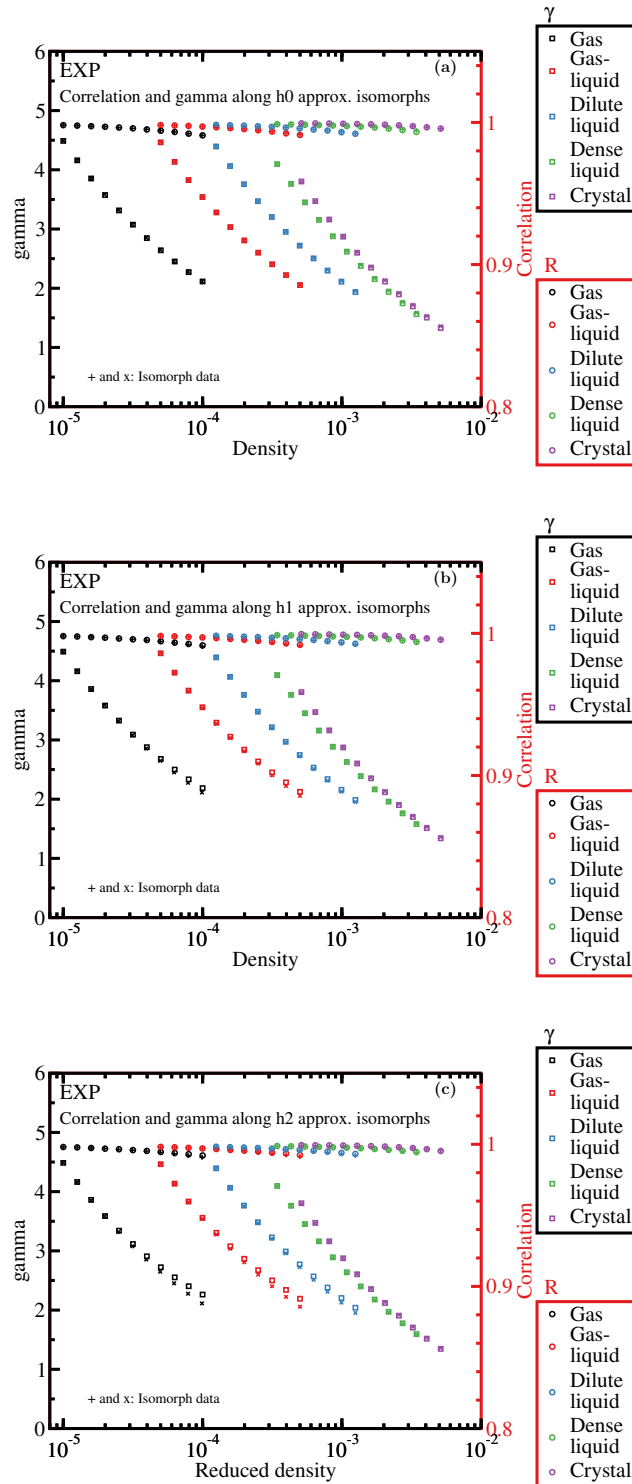
Figure 5.30: Correlation and density scaling exponent along the $h_p(\rho)$-approximate isomorphs for $p = 0$ (a), $p = 1$ (b), and $p = 2$ (c). The results from the small step isomorphs is marked by $+$ and $\times$. Good agreement is observed between the gas, gas-liquid and dilute liquid $h_0(\rho)$-approximate isomorphs, while the dense liquid and crystal is well approximated by the $h_2(\rho)$-approximate isomorphs.

So far in it clear that different values of p should be used in different parts of phase space, and it has been concluded the the more dilute the system is, the lower the value of p. Furthermore it has been found here that also for the EXP system does p of order two work the best. This was also observed in 4.9(a) where the density dependence of the density scaling exponent matched the $h_2(\rho)$ evaluated at $\Lambda = 1.075$. In what follows predictions for the optimal value of p will be made.

In order to identify the best-fit value of p throughout the phase diagram we reason as follows. The above was derived assuming that Λ is an isomorph invariant. In order to capture the gas phase of the EXP system we will, however, allow for a more general variation of Λ. The need for this comes from the fact that the relevant interaction distance r_0 in the gas phase is that of two-particle nearest encounters that independent of density are determined by the condition $v_{\text{EXP}}(r_0) = T$, i.e., $r_0 = \ln(1/T)$. In the dilute gas phase r_0 is much smaller than the average interparticle spacing $\rho^{-1/3}$, in contrast to what is the case for the dense-liquid phase in which $r_0 \sim \rho^{-1/3}$.

The optimal p value is identified by determining Λ from $\ln(1/T) = r_0 = \Lambda \rho^{-1/3}$, i.e.,

$$\Lambda = \ln(1/T)\, \rho^{1/3}\,. \tag{5.13}$$

As the system densifies, Λ increases and becomes unphysical as the individual particle becomes surround by other particles in a nearest neighbor shell. This is also where the physics controlling the system switches from single pair interactions to collective interaction of many simultaneous interactions. In order to capture the change in physics of the system the Λ of Eq. (5.13) is used whenever it gives a Λ below 1.075, corresponding to the gas and dilute liquid phases where the collision approximation makes sense. In the dense liquid phase Λ is fixed to the value 1.075, which was determined by requiring the best fit to the density-scaling exponent results, compare Fig. 4.9. The exact value of Λ changes the values of the expected best value of p but the overall picture is maintained.

With the above convention for determining Λ at each state point, the optimal value of p was determined by identifying $\gamma = \gamma_p$ in Eq. (5.12). This results in

$$p_{\text{opt}} = -3\gamma + \Lambda \rho^{-1/3}\,. \tag{5.14}$$

Note that this expression allows for non-integer values of p_{opt}.

The optimal values p_{opt} are shown in Fig. 5.31. A comparison with the isomorphs reveals that p_{opt} is roughly isomorph invariant, which is gratifying given that the physics is invariant to a good approximation along the isomorphs. The gas phase has p_{opt} values around zero, and p_{opt} increases continuously towards values around two that are reached close to solid-liquid

coexistence. Since $p_{\mathrm{opt}} = 0$ corresponds to approximating the pair poten-
tial in question by an IPL pair potential determined by requiring correct
slope at the interaction distance r_0, this confirms that two-particle colli-
sions dominate the gas phase. In contrast, in the condensed liquid phase
the nearest-neighbor-shell picture of interactions justifying the eIPL approx-
imation works best ($p_{\mathrm{opt}} \cong 2$).
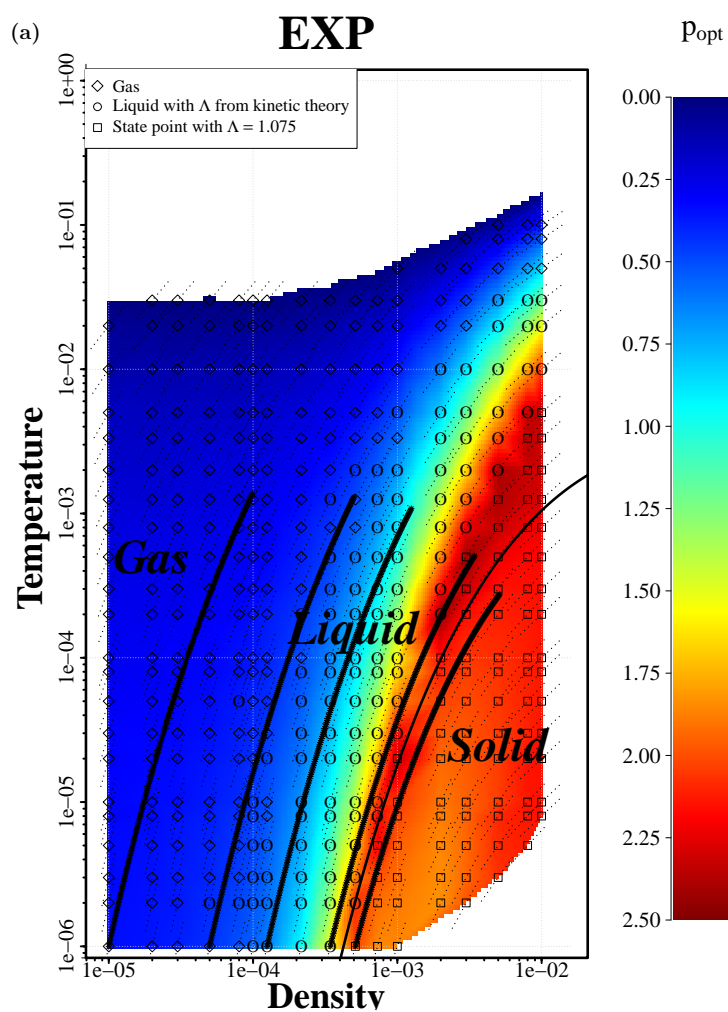
Figure 5.31: Optimal p values calculated from Eq. (5.14) with $\Lambda = \rho^{1/3}\ln(1/T)$ capped at $\Lambda = 1.075$. The p values are close to zero in the gas phase and increase with density through the liquid to end up close to two as liquid-solid coexistence is approached. Note that the optimal p value is roughly isomorph invariant.

5.4 Melting and freezing line

The melting and freezing line as drawn in the phase diagrams of the EXP system (e.g. Fig. 4.1) is a $h_2(\rho)$-approximate isomorph generated from the state point $(\rho, T) = (2.02 \cdot 10^{-3}, 10^{-4})$ with $\Lambda = 1.045$. The state point and Λ-value has chosen to match known state points on the melting line as determined by interface pinning[71]. The interface pinning is a method to determine the melting line by calculating the Gibbs free energy of a system consisting of half crystal and half liquid separated by two interfaces. The simulations is thermostated and barostated along the axis perpendicular to the interfaces between liquid and solid and a bias field is applied to keep the system from completely melting or freezing. The bias field is applied by adding a spring like term to the potential energy of the form $\frac{\kappa}{2}(Q(\mathbf{R}) - a)^2$, where a is the "anchor point" and κ the spring constant. Q is an order parameter to determine the size of the crystal (and/or liquid). The difference in chemical potential between the two phases can be determined from the force of this bias field, and if the difference is zero, then the state point in question is on the coexistence curve. If it differs, then either temperature or pressure must be adjusted. The method is well described in Pedersen [71] and the algorithm summarized in section D.

In this work the interface pinning was used to determine the coexistens between liquid and crystal for the following temperatures: $T \in \{1e-4, 2e-4, 5e-4, 1e-3\}$. At each temperature the coexistens between liquid and both the bcc- and fcc-crystal was found - marked by triangles pointing up (bcc) and down (fcc) in 5.32. As the interface pinning gives the coexistence point in pressure-temperature, both the density of the liquid and the crystal is known, and therefore also the width of the coexistence region - a width on order of a few percent. While there is indications that the bcc crystal is formed at a lower density than the fcc crystal at high temperature, and that as temperature is lowered the two crystal forms have almost the same coexistence region, the data is insufficient to make conclusions on the preferred crystal structure at a given temperature.

The simulations was done in LAMMPS[47], achieving the EXP pair potential by setting the constants on IPL terms of the Born-Meyer-Higgins potential[1] to zero. The time step size was 0.005 and the thermostat relaxation time 0.4, while the barostat relaxation time was 0.8. Reduced unit cutoffs of 2.5 and 4 was used. The number of particles in the simulations to determine the coexistence between liquid and bcc crystal was 2560, while 5120 particles was used in the fcc case. The precision in the determined coexistence points is mainly suffering from the choice of order parameter, and therefore throughout testing of the simulation choices has not been car-

---

[1]The implementation in Lammps[47] has the following form: $v(r) = Ae^{(\sigma - r)/\rho} - C/r^6 + D/r^8$. Therefore the EXP potential can be simulated by letting $\sigma = C = D = 0$.

ried out. The data is believed to be trustworthy within the precision of the log-log phase diagram.

All together only an approximate position of the freezing and melting line is known. A careful determination is needed in order to know the exact position hereof - such a determination could follow the ideas of Pedersen et al. [72], and might reveal that so some state point near the marked line would be on the opposite side. Judging from the values of the reduced diffusion (Fig. 4.12) the following points might change "phase": $(\rho, T) = (5.12e-04, 2e-06)$, $(\rho, T) = (7.29e-04, 5e-05)$, $(\rho, T) = (2e-03, 1e-04)$ and $(\rho, T) = (5e-03, 5e-04)$.
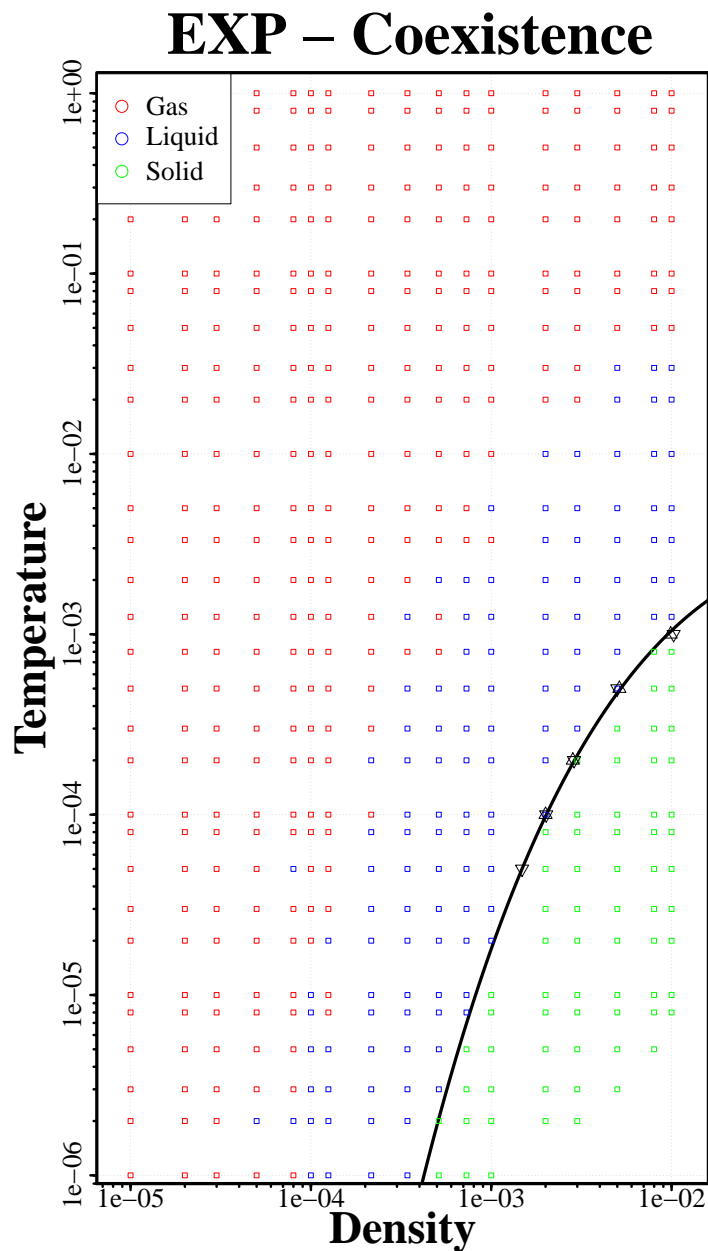
Figure 5.32: Phase diagram of simulated state point and there phases color coded. Along the melting and freezing line is the results from interface pinning marked with triangles. The triangles pointing up mark the liquid-crystal coexistence for the bcc crystal, while the triangles pointing down marks the liquid-crystal coexistence of the fcc crystal.

Chapter 6

Quasi-universality

Definition of Quasi-universality

In [25] it was argued that if a system can be written as a sum of exponential functions taken from the strongly correlating part of the phase diagram, then the system has the same structure and dynamics as the EXP system - it inherits the hidden scale invariance. The arguments in [25] is based on the first version of the isomorph theory, but can be generalized with a line of arguments is based on the NVU dynamics[40–42] and the finding of [73] combined with second version of the isomorph theory as presented in [57]. It is the same line of arguments as found in [26].

First consider the EXP system $v_{EXP} = \varepsilon e^{-r/\sigma}$ in a region where it fulfills the isomorph condition (Eq. (3.1)), then writing 3.6 explicitly for the EXP system:

$$U_{EXP}(\mathbf{R}) = U(\rho, S_{\text{ex}}^{EXP}(\tilde{\mathbf{R}})) \,. \tag{6.1}$$

Since ε has the unit of energy, the potential energy can be written as ε multiplied by a dimensionless function Φ_{EXP} of the two dimensionless variables ($\tilde{S}_{\text{ex}} = S_{\text{ex}}/k_B$): $\rho\sigma^3$ and $\tilde{S}_{\text{ex}}^{\text{EXP}}\left(\tilde{\mathbf{R}}\right)$ exists so

$$U_{EXP}(\mathbf{R}, \varepsilon, \sigma) = \varepsilon\Phi_{EXP}(\rho\sigma^3, \tilde{S}_{\text{ex}}^{EXP}(\tilde{\mathbf{R}})) \,. \tag{6.2}$$

Consider now a system that conforms with the isomorph condition: The potential energy can be written as $U(\mathbf{R}) = U(\rho, S_{\text{ex}}(\tilde{\mathbf{R}}))$, and has NVU dynamics on the constant-potential-energy hyper-surface Ω with $U(\mathbf{R})$ constant. Assume that the system can be expressed as a sum of EXP:

$$v(r) = \sum_{i=1}^{n} \varepsilon_i \exp(-\frac{r}{\sigma}) \tag{6.3}$$

in a state point (ρ, U), then the potential energy can be written as

$$U(\mathbf{R}) = \sum_{i=1}^{n} \varepsilon_i \Phi_{EXP}(\rho\sigma^3, \tilde{S}_{\text{ex}}^{EXP}(\tilde{\mathbf{R}})) \,. \tag{6.4}$$

Because this is constant on Ω and the temperature is positive ($T > 0$):

$$\left(\frac{\partial U(\mathbf{R})}{\partial S_{\text{ex}}} \right)_\rho > 0$$

$$\Leftrightarrow \sum_{i=1}^n \left(\frac{\partial U_i(\mathbf{R})}{\partial S_{\text{ex}}} \right)_\rho > 0$$

$$\Leftrightarrow \sum_{i=1}^n \left(\frac{\varepsilon_i \partial \Phi_{EXP}(\rho\sigma_i^3, \tilde{S}_{\text{ex}}^{EXP}(\tilde{\mathbf{R}}))}{\partial S_{\text{ex}}} \right)_\rho > 0$$

then also $\tilde{S}_{\text{ex}}^{EXP}(\tilde{\mathbf{R}})$ is constant, and then also $U^{EXP}(\mathbf{R})$ is constant - meaning that the constant-potential-energy hyper-surface of each of the terms in potential of the system in question is equal to that of the EXP system: $\Omega = \Omega^{EXP}$.

It follows that the *NVU* dynamics of the system must be identical to the *NVU* dynamic of the EXP system. For the system to be quasi-universal the different EXP pair potential terms of Eq. (6.3) must correspond to a strongly correlating state point in the EXP system. A condition also arrived at in [25]: the prefactores must be large in order to sample from the low temperature, strong correlating part of the phase diagram (see Fig. 4.7).

In the above equations and statement it was concluded that if the system in question can be written as a finite sum over EXP terms, and the prefactors of these terms is large, so corresponding EXP system conforms the hidden scale invariance, then the system is it self conforming to the hidden scale invariance. The derivation should be thought of more as sketch or a dream than a solid conclusion. This has to do with the isomorph theory not being exact, and that a difference of two EXP terms with large prefactors can more or less cancel and result in an effective EXP potential not conforming the hidden scale invariance. The conditions and the conclusions must therefore be somewhat relaxed.

Approximating the Lennard-Jones system by the EXP system

The Lennard-Jones system $v(r) = 4\varepsilon \left(\left(\frac{r}{\sigma}\right)^{12} - \left(\frac{r}{\sigma}\right)^6 \right)$ is well known to be quasi-universal in a large part of its phase diagram[25]. It therefore is possible to find an approximate EXP system for a given LJ state point. As a consequence of the quasi universality there is multiple ways to identify the approximate EXP system. In this work the reduced diffusion coefficient was chosen as a proxy for the dynamics of the system, as it is a single number representing the invariant dynamics. Thus for each LJ state point an EXP system with same reduced diffusion coefficient was located, and the structure probed by the radial distribution function was compared. Thus choosing an EXP system matching the dynamic, it is shown that also the structure matches which is a sign of the quasi-universality: similar structure

$\Leftrightarrow$ similar dynamics, or in the understanding of the EXP system: choosing state points with matching dynamics is choosing state points with the same constant-excess-entropy surface, the same dimensionless constant potential energy surface, and therefore also the same structure.

In this part approximate EXP systems will be found for four such LJ state points: One at $(\rho, T) = (0.029, 199.6)$ - a dilute hot gas, one at $(\rho, T) = (1.09, 482.17)$ - a dense, but hot gas, one in $(\rho, T) = (1.09, 10.17)$ - a liquid,and one in $(\rho, T) = (1.09, 2.17)$ - a condensed-phase liquid close to the freezing line. The reduced diffusion of the four LJ state points is given in same order: $\tilde{D} = 4.81$, $\tilde{D} = 0.379$, $\tilde{D} = 0.1068$, and $\tilde{D} = 0.0266$. For each state point two or three EXP systems (or state points) with the same reduced diffusion coefficient (within 1%) was found. Since the reduced dynamics and diffusion coefficient is an isomorph invariant, there is an isomorph in the EXP system with the same reduced diffusion coefficient to choose from when approximating the LJ state point. Each of these system will have almost the same structure as shown in chapter 5. The main difference between the structure along the isomorphs is on the first peak. This difference is well known also from other systems and can be explained by the changing γ along the isomorph (see section 4.4). In Fig. 6.1 the black line is all cases the radial distribution function of the LJ system. In (a) is the low density gas with very little structure and three EXP systems with different γ-values all lower than the 4.290 of the LJ system.. The numerical order of the γ-values is red, green, and blue. This order is re-found in the plot; the higher the γ-value, the better the collapse of the structure. In (b) and (c) only two EXP state point is included, but reveals the same picture: a good match in both system, but choosing the one with γ-value closest to the one of the LJ system gives the better collapse. In (d) is again three EXP system and a almost perfect collapse when the γ-values are matching.
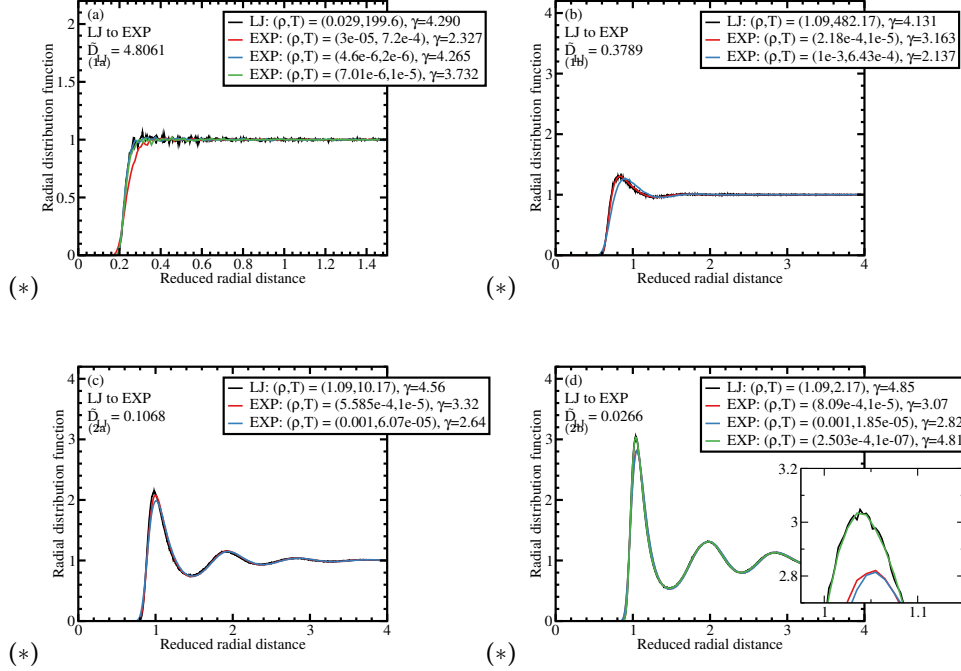
Figure 6.1: Quasiuniversality illustrated by comparing radial distribution functions (RDF) at four state points for the Lennard-Jones (LJ) system (black curves) to those of EXP systems with the same reduced diffusion constant (within 1%, colored curves). EXP state points are specified by density, temperature, and density-scaling exponent γ. (a) LJ state point $(\rho, T) = (0.029, 199.6)$, a typical high-temperature gas state point at which $\tilde{D} = 4.8061$. γ is here 4.29, which is not far from the value 4 predicted from the repulsive r^{-12} term of the LJ pair potential [53]. The red, blue and green curves are RDF predictions for different EXP systems with the same reduced diffusion constant. (b) LJ state point $(\rho, T) = (1.09, 482.17)$, a moderate-density, high-temperature gas state point at which $\tilde{D} = 0.3789$. The red EXP system fits better than the blue one. Deviations are centered around the first peak, with largest deviations for the EXP state point with density-scaling exponent γ most different from its LJ value (blue). (c) LJ state point $(\rho, T) = (1.09, 10.17)$ at which $\tilde{D} = 0.1068$. There are slight deviations around the first peak; again these are smallest for the EXP system with γ closest to that of the LJ system. (d) LJ state point $(\rho, T) = (1.09, 2.17)$, a condensed-phase liquid state point close to the melting line at which $\tilde{D} = 0.0266$. The green curve, which fits best, represents an EXP system that has virtually the same γ as the LJ system. The inset provides a blow up of the first peak.

Chapter 7

Outlook

Exploration of a new potential is both an awarding task, but also frustration. The more one gets to know about the EXP-potential, the more it seems there is to know. Always with a feeling of just getting started, just realize how much data has been collected and analysed, and how much time is spend in the process. Looking ahead there is many promising direction to take:

- Precisely establishment of the melting and freezing lines by following the ideas of Pedersen et al. [72],

- Comparison with the Gaussian core model: A dilute phase well approximated by effective IPL exponent determined from $p < 2$ [2, 61] and possibly a re-entrant melting. The thermodynamic phase diagram may even look somewhat like that of the Gaussian core model as seen in e.g Prestipino et al. [74].

- The crystal phase is still largely unexplored, so far only small indication from the values of the density scaling exponent in the crystal phase, and the interface pinning results, points to the existence of both a fcc phase and a bcc phase.

- Frustrating the system by introducing polydispersity to prevent crystallization so the glassy state can be explored.

- A further exploration of the consequences of the properties gas phase.

The EXP potential seems to be applicable in many different settings, and will hopefully aid to the understanding of the properties of matter.

State points

The state points simulated involve the following densities: $1.00 \cdot 10^{-5}$; $2.00 \cdot 10^{-5}$; $3.00 \cdot 10^{-5}$; $5.00 \cdot 10^{-5}$; $8.00 \cdot 10^{-5}$; $1.00 \cdot 10^{-4}$; $1.25 \cdot 10^{-4}$; $2.16 \cdot 10^{-4}$; $3.43 \cdot 10^{-4}$; $5.12 \cdot 10^{-4}$; $7.29 \cdot 10^{-4}$; $1.00 \cdot 10^{-3}$; $2.00 \cdot 10^{-3}$; $3.00 \cdot 10^{-3}$; $5.00 \cdot 10^{-3}$; $8.00 \cdot 10^{-3}$; $1.00 \cdot 10^{-2}$; and the following temperatures: $1.00 \cdot 10^{-6}$; $2.00 \cdot 10^{-6}$; $3.00 \cdot 10^{-6}$; $5.00 \cdot 10^{-6}$; $8.00 \cdot 10^{-6}$; $1.00 \cdot 10^{-5}$; $2.00 \cdot 10^{-5}$; $3.00 \cdot 10^{-5}$; $5.00 \cdot 10^{-5}$; $8.00 \cdot 10^{-5}$; $1.00 \cdot 10^{-4}$; $2.00 \cdot 10^{-4}$; $3.00 \cdot 10^{-4}$; $5.00 \cdot 10^{-4}$; $8.00 \cdot 10^{-4}$; $1.25 \cdot 10^{-3}$; $2.00 \cdot 10^{-3}$; $3.33 \cdot 10^{-3}$; $5.00 \cdot 10^{-3}$; $1.00 \cdot 10^{-2}$; $2.00 \cdot 10^{-2}$; $3.00 \cdot 10^{-2}$; $5.00 \cdot 10^{-2}$; $8.00 \cdot 10^{-2}$; $1.00 \cdot 10^{-1}$; $2.00 \cdot 10^{-1}$; $3.00 \cdot 10^{-1}$; $5.00 \cdot 10^{-1}$; $8.00 \cdot 10^{-1}$; 1.

ρ	T
.0000000000000008e-05	1e-06
1.2589254117941712e-05	2.7095668783251287e-06
1.5848931924611212e-05	6.8239548210735882e-06
1.9753869206662062e-05	1.5492599637880406e-05
2.4868647925525196e-05	3.4334247617407183e-05
3.1307772830406045e-05	7.1780397570085801e-05
3.941415080287726e-05	0.00014216821477153701
4.9619476030029706e-05	0.0002679483540835922
6.2467219294116e-05	0.0004822678538733984
7.86415697734816e-05	0.00083171327714667419
9.90038706112203e-05	0.0013786657578480732

Table 1: State points along the gas isomorph. Only every 23.th state point is listed.

ρ	T
5e-05	1e-06
6.294627058971e-05	2.692989175158e-06
7.924465962306e-05	6.7383335513502e-06
9.976311574844e-05	1.5751918759493e-05
0.00012559432157548	3.4566878978528e-05
0.0001581138830084	7.155417135224e-05
0.00019905358527675	0.00014031943870256
0.00025059361681364	0.00026169191060377
0.0003154786722401	0.0004658593922203
0.00039716411736215	0.0007942537944996
0.0005	0.001300924689954

Table 2: State points along the gas-liquid isomorph. Only every 23.th state point is listed.

ρ	T
0.000125	1e-06
0.00015736567647427	2.65210617041e-06
0.00019811164905764	6.5325191529899e-06
0.00024940778937111	1.5023595744774e-05
0.0003139858039387	3.242014238958e-05
0.0003952847075211	6.595380043868e-05
0.000497633963192	0.0001269628749625
0.000626484042034	0.00023221573271542
0.0007886966806003	0.0004048971578912
0.000992910293405	0.0006753946093764
0.00125	0.001080808024819

Table 3: State points along the dilute-liquid isomorph. Only every 23.th state point is listed.

ρ	T
0.000343	1e-06
0.00043181141624540	2.474458000714e-06
0.0005436183650142	5.682478983985e-06
0.0006843749740343	1.2174220189705e-05
0.0008615770460078	2.443853999220e-05
0.0010846612374378	4.6169668024723e-05
0.0013655075949985	8.241288621435e-05
0.0017190722113416	0.00013949692378350
0.0021641836915671	0.00022469324251984
0.0027245458451043	0.00034552950257571
0.00343	0.0005088528948930

Table 4: State points along the dense-liquid isomorph. Only every 23.th state point is listed.

ρ	T
0.0005120000000000003	1e-06
0.0006445698108386145	2.3096933029639338e-06
0.0008114653145400926	4.9589854320478404e-06
0.0010215743052640709	9.9474651836696029e-06
0.0012860858529329135	1.8729509766277452e-05
0.0016190861620062238	3.3248605609761359e-05
0.0020383087132339285	5.5859607015867518e-05
0.0025660786361716647	8.9152850498520192e-05
0.003230501603738634	0.00013563418211581633
0.004066960561788389	0.00019735201807200161
0.005120000000000096	0.00027552235257826492

Table 5: State points along the crystal isomorph. Only every 23.th state point is listed.

Reprints of articles

Explaining why simple liquids are quasi-universal

Andreas K. Bacher[1], Thomas B. Schrøder[1] & Jeppe C. Dyre[1]

It has been known for a long time that many simple liquids have surprisingly similar structure as quantified, for example, by the radial distribution function. A much more recent realization is that the dynamics are also very similar for a number of systems with quite different pair potentials. Systems with such non-trivial similarities are generally referred to as 'quasi-universal'. From the fact that the exponentially repulsive pair potential has strong virial potential-energy correlations in the low-temperature part of its thermodynamic phase diagram, we here show that a liquid is quasi-universal if its pair potential can be written approximately as a sum of exponential terms with numerically large prefactors. Based on evidence from the literature we moreover conjecture the converse, that is, that quasi-universality only applies for systems with this property.

[1] DNRF Center 'Glass and Time', IMFUFA, Department of Sciences, Roskilde University, Postbox 260, DK-4000 Roskilde, Denmark. Correspondence and requests for materials should be addressed to J.C.D. (email: dyre@ruc.dk).

A cornerstone of liquid-state theory is the fact that the hard-sphere (HS) model gives an excellent representation of simple liquids. This was discussed in 1959 by Bernal[1], and the first liquid-state computer simulations at the same time by Alder and Wainwright[2] likewise studied the HS system. Following this the HS model has been the fundament of liquid-state theory, in particular since the 1970s when perturbation theory matured into its present form[3–5]. The HS model is usually invoked to explain the fact that many simple liquids have very similar structure. This cannot explain, however, the more recent observation of dynamic quasi-universality[6–14] or why some mathematically simple pair potentials violate quasi-universality[15–19].

An early hint of dynamic quasi-universality was provided by Rosenfeld[6] who showed that the diffusion constant is an almost universal function of the excess entropy (the entropy minus that of an ideal gas at the same temperature and density). This finding did not attract a great deal of attention at the time, but the last decade has seen renewed interest in excess-entropy scaling[7,8] and, more generally, in the striking similarities of the structure and dynamics of many simple model liquids[9–14]. Thus Heyes and Branka[9,11,20–23] and others have documented that inverse power-law (IPL) systems with different exponents have similar structure and dynamics, Medina-Noyola and co-workers[10,13,14] have established that quasi-universality extends to the dynamics for Newtonian as well as Brownian equations of motion, Scopigno and co-workers[21] have documented HS-like dynamics in liquid gallium studied by quasi-elastic neutron scattering, and Liu and co-workers[12] have suggested a mapping of a soft-sphere system's dynamics to that of the HS system.

Further examples of similarities between apparently quite different systems, identified throughout the years but still largely unexplained, include: the Young–Andersen[24] approximate scaling principle according to which two systems that have the same radial distribution function—even at different thermodynamic state points—also have the same dynamics; the fact that different systems have similar order-parameter maps in the sense of Debenedetti and co-workers[8,25], that is, when the relevant orientational order parameter is plotted against the translational one, almost identical curves result; the Lindemann and other melting rules[26,27]; freezing rules like Andrade's finding[28] that freezing initiates when the reduced viscosity upon cooling reaches a certain value or the Hansen–Verlet[29,30] rule that a liquid freezes when the maximum structure factor reaches 2.85.

In the literature the term 'quasi-universality' refers to the general observation that different simple systems have very similar physics as regards structure and dynamics, but before proceeding we need to define the term precisely. To do this, recall first the definition of so-called reduced quantities. These are quantities made dimensionless by dividing by the appropriate combination of the following three units: the length unit is $\rho^{-1/3}$ where ρ is the number density, the energy unit is $k_B T$ where T is the temperature, and the time unit is $\rho^{-1/3}\sqrt{m/k_B T}$ for Newtonian dynamics where m is the particle mass (for Brownian dynamics a different time unit is used[31,32]). Henceforth, reduced quantities are denoted by a tilde, for instance the reduced pair distance is defined by $\tilde{r} \equiv \rho^{1/3} r$.

By quasi-universality we shall mean the property of many simple model liquids that knowledge of a single quantity characterizing the structure or dynamics in reduced units is enough to determine all other reduced-unit structural and dynamic quantities to a good approximation. Note that a special case of this is Rosenfeld's observation that the excess entropy over k_B, a structural quantity, determines the reduced diffusion constant. Likewise, the Young–Andersen[33] approximate scaling principle is a consequence of quasi-universality as defined here—

as these authors expressed it '... certain dynamical properties are very insensitive to large changes in the interatomic potential that leave the pair correlation function largely unchanged'.

It is straightforward to show that if quasi-universality applies, the other points mentioned above also follow. The fundamental questions are: which systems are quasi-universal? what causes quasi-universality? The conventional explanation of quasi-universality starts from the fact that the HS system provides an excellent reference system for structure calculations[6,10,12–14,34]. Approximate theories of liquid dynamic properties like renormalized kinetic theory or mode-coupling theory in its simplest version predict that the dynamics is uniquely determined by the static structure factor, that is, that structure determines dynamics. This reasoning led to the search for and discovery of dynamic quasi-universality back in 2003 (refs 10,24).

The dynamics of the HS system consists of constant-velocity free-particle motion interrupted by infinitely fast collisions, which is quite different from the continuous motion described by Newton's laws for smooth potentials. Thus it is far from physically obvious why the HS explanation of quasi-universal structure extends to the dynamics. Moreover, while the HS explanation does account for the finding that, for example, the Gaussian-core model[15,35,36] violates quasi-universality—a model without harsh repulsions except at low temperatures—it cannot explain why some strongly repulsive or hard-core pair-potential systems violate quasi-universality. Examples of such systems are the Lennard–Jones (LJ) Gaussian model[17] and the Jagla model[37]. Finally, the one-component plasma (OCP) model is well-known to be quasi-universal[6], but it is not intuitively clear when and why the gently varying Coulomb force can be well-approximated by the harsh HS interaction.

In this paper we do not use the HS reference system. In a continuation of recent works[38–40] we take a different approach to quasi-universality by showing that any pair potential, which can be approximated by a sum of exponential terms with numerically large prefactors, is quasi-universal. This introduces the 'EXP quasi-universality class' of pair potentials. Based on the available evidence from the literature we moreover conjecture the converse, that is, that all quasi-universal systems are in the EXP quasi-universality class.

Results

The exponentially repulsive pair potential. We study below the monatomic system described by the purely repulsive 'EXP' pair potential

$$v_{\text{EXP}}(r, \varepsilon, \sigma) = \varepsilon\, e^{-r/\sigma}. \tag{1}$$

This was discussed already by Born and Meyer[41] and by Buckingham[42] in the context of a pair potential with an exponentially repulsive term plus an r^{-6} attractive term; note also that the well-known Morse pair potential is a difference of two exponentials[43]. The EXP pair potential may be justified physically as reflecting the overlap of electron wavefunctions in conjunction with the fact that bound-state wavefunctions decay exponentially in space[41]. Although the EXP pair potential since 1932 has been used occasionally in computer simulations and for interpretation of experiments[40,44–48], it never became a standard pair potential like the LJ and Yukawa pair potentials[29,49]. Given the mathematical simplicity of the EXP function this may seem surprising, but a likely explanation is that no system in nature is believed to be well-described by this purely repulsive pair potential. The present paper suggests that it may nevertheless be a good idea to regard the EXP pair potential as the fundamental building block of the physics of simple liquids, much like the exponential function in the Fourier and Laplace transform theories of pure mathematics.
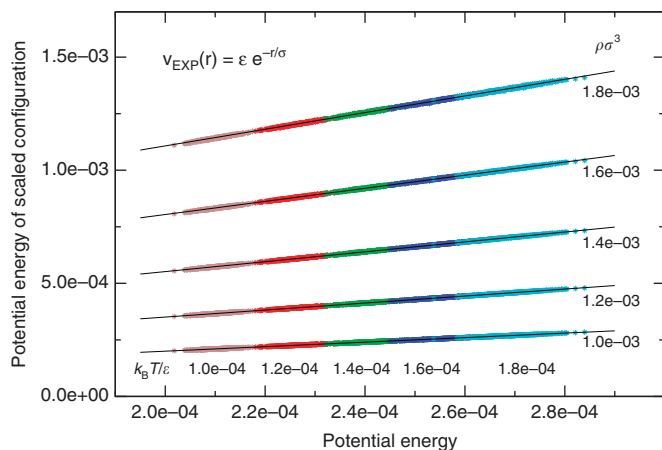
Figure 1 | Scatter plots of potential energies per particle of the EXP system. At the state point with density $\rho\sigma^3 = 1.0 \times 10^{-3}$ and temperature $k_BT/\varepsilon = 1.0 \times 10^{-4}$ several configurations were selected from an equilibrium simulation and scaled uniformly to four higher densities (the light brown points); the same was done for four other temperatures at this density. The figure shows that there are very strong correlations between scaled and unscaled potential energies, with a scaling factor that only depends on the two densities involved. The lines are best fits to the green data points, that is, those generated from simulations at temperature $k_BT/\varepsilon = 1.4 \times 10^{-4}$. This figure validates the hidden-scale-invariance property of the EXP pair-potential system as expressed below in equation (4).

Our simulations focused on the low-temperature part of the thermodynamic phase diagram, that is, where

$$k_BT \ll \varepsilon. \qquad (2)$$

The potential energy as a function of all the particle coordinates $\mathbf{R} \equiv (\mathbf{r}_1,...,\mathbf{r}_N)$ is denoted by $U_{EXP}(\mathbf{R})$. Figure 1 shows scatter plots of $U_{EXP}(\mathbf{R})$ for several configurations $\mathbf{R}$ plotted versus the potential energies of the same configurations scaled uniformly to a different density, that is, $U_{EXP}(\mathbf{R})$ plotted versus $U_{EXP}(\lambda\mathbf{R})$ in which λ^3 is the ratio of the two densities in question. The figure was constructed by simulating five temperatures at the density $\rho\sigma^3 = 1.0 \times 10^{-3}$ (lower line, different colours); at each of these five state points, configurations were selected and scaled to four higher densities. We see that there are very strong correlations between the potential energies of scaled and unscaled configurations.

As shown elsewhere strong correlations between scaled and unscaled potential energies are characteristic for systems that have strong correlations between their virial and potential energy thermal equilibrium fluctuations at the relevant state points[31]. Systems with this property include not only 'atomic' pair-potential systems like the IPL, Yukawa, and LJ systems and so on, but also a number of rigid molecular model systems and even the flexible LJ chain model[50,51]. Such systems were previously referred to as 'strongly correlating', but are now called Roskilde-simple or just Roskilde systems[52–57], which avoids confusion with strongly correlated quantum systems.

The strength of the virial potential-energy correlations of the EXP system is reported in Fig. 2a for a large number of state points. If virial and potential energy are denoted by W and U, respectively, and sharp brackets denote canonical constant-volume (NVT) averages, the colour coding of the figure gives the Pearson correlation coefficient R defined[58] by

$$R = \frac{\langle \Delta W \Delta U \rangle}{\sqrt{\langle (\Delta U)^2 \rangle \langle (\Delta W)^2 \rangle}}. \qquad (3)$$
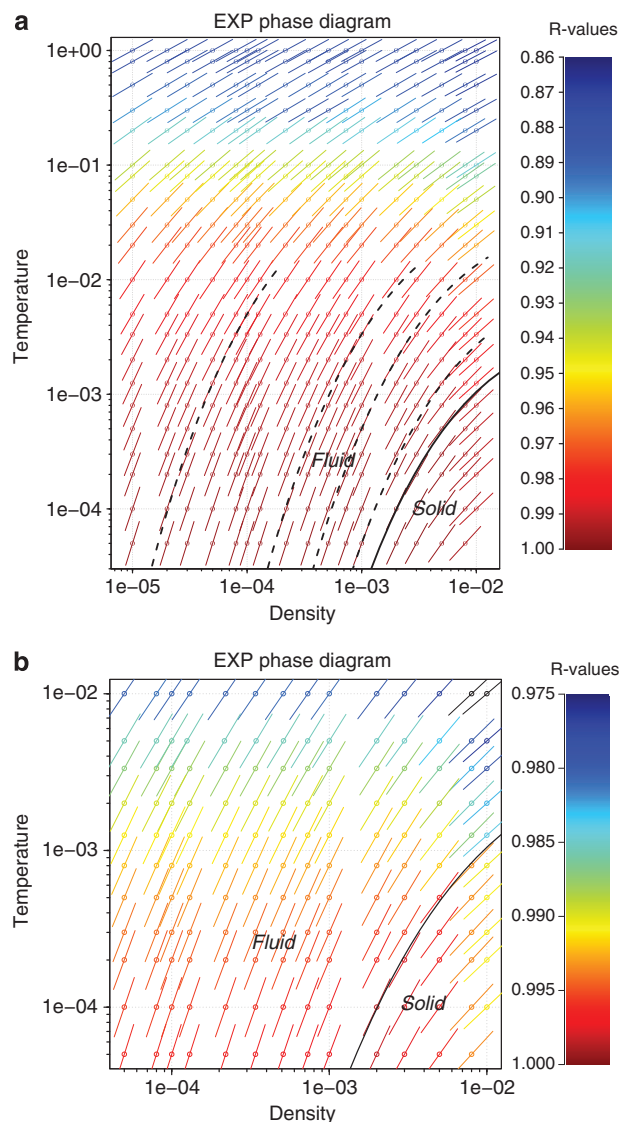
Figure 2 | Thermodynamic phase diagram of the EXP system. Density and temperature are both given in the unit system defined by pair-potential parameters (equation (1)). (**a**) gives an overview of the phase diagram and (**b**) zooms in on its low-temperature part; in both cases the colours indicate the value of the virial potential-energy correlation coefficient R defined in equation (3). The slope of each line segment is that of the isomorph through the state point in question, the curve along which structure and dynamics are (approximately) invariant in reduced units. The full curves mark the melting isomorph; this curve's width in **a** is approximately that of the coexistence region. The dashed curves mark a few other isomorphs.

A pragmatic definition is that a given system is Roskilde simple at the state point in question if $R > 0.9$ (ref. 58). This is the case for the EXP system whenever $k_BT/\varepsilon < 0.1$.

Figure 2b zooms in on the low-temperature part of the phase diagram where the EXP system has particularly strong virial potential-energy correlations. In both figures the line segments have slope γ, the slope of the so-called isomorph through the state point in question that is calculated from the expression $\gamma = \langle \Delta W \Delta U \rangle / \langle (\Delta U)^2 \rangle$ (ref. 31). An isomorph is a curve in the phase diagram along which structure and dynamics to a good approximation are invariant in reduced units[31,59]. A system has isomorphs if and only if the system has strong virial potential-
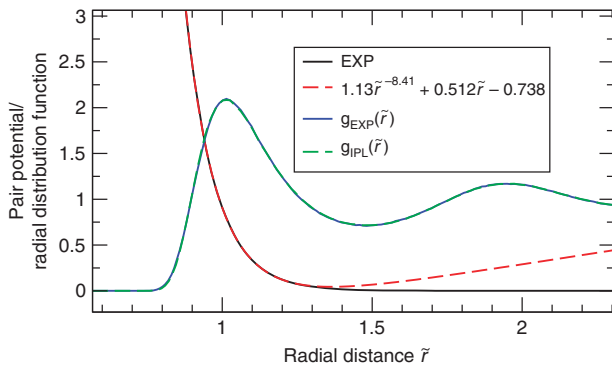
Figure 3 | Illustration of how the EXP pair potential may be fitted by an eIPL pair potential[58]. The eIPL pair potential (ref. 58) a sum of an inverse power-law (IPL) term and a linear term (red-dashed curve); $\tilde{r} \equiv r\rho^{1/3}$ is the reduced pair distance and the pair potential is given in units of $k_B T$. The eIPL function was fitted to the EXP function over the range of radial distances for which the radial distribution function (RDF) at the state point defined by $\rho\sigma^3 = 1.0 \times 10^{-3}$ and $k_B T/\varepsilon = 5.0 \times 10^{-5}$ is larger than unity. The blue and green curves are the RDFs at this state point of the EXP pair potential and the IPL pair potential, respectively. The EXP and IPL pair potentials' diffusion constants differ by $<1\%$ at this state point (data not shown).

energy correlations at the relevant state points[31]. The existence of isomorphs implies that the phase diagram becomes effectively one-dimensional for many physical properties; ref. 57 gives a recent review of the isomorph theory with a focus on its validation in computer simulations and experiments. The curves in Fig. 2a are examples of isomorphs of which the full curve is the melting isomorph.[31] Isomorphs of the EXP system were studied briefly in ref. 40.

Before proceeding we address the question why the EXP pair potential has strong virial potential-energy correlations. Our explanation refers to IPL pair potentials, which by Euler's theorem for homogeneous functions have 100% virial potential-energy correlations (recall that the microscopic virial is defined generally by $W(\mathbf{R}) = (-1/3)\mathbf{R} \cdot \nabla U(\mathbf{R})$ (ref. 5)). Figure 3 refers to the state point $\rho\sigma^3 = 1.0 \times 10^{-3}$, $k_B T/\varepsilon = 5.0 \times 10^{-5}$. The figure shows that the EXP pair potential (black curve) may be fitted very well over the entire first coordination shell by an extended IPL ('eIPL') function, which is defined as an IPL term plus a linear term (the red-dashed line). As shown in ref. 58 the linear term contributes little to neither the virial nor the potential-energy constant-volume fluctuations because the sum of nearest-neighbour distances is almost constant. This is because if one particle is moved, some nearest-neighbour distances decrease and others increase, resulting in almost no change in the sum of the nearest-neighbour distances (this argument is exact in one dimension). As a consequence, the WU fluctuations are dominated by the IPL term and thus strongly correlating. This explains why the EXP pair potential has very strong WU correlations. To confirm the equivalence between the EXP pair potential and the IPL pair potential ($1.13\tilde{r}^{-8.41}$), we performed a simulation with the IPL pair potential at the same state point. As predicted[58,60] there is good agreement between the two systems' structure (blue and green curves) and dynamics (not shown), confirming that the linear term of the eIPL pair potential fitting the EXP pair potential, $0.512\tilde{r} - 0.738$, is not important for the physics.

Derivation of quasi-universality. We proceed to show that the strong virial potential-energy correlation property of the EXP system implies quasi-universality for a large class of monatomic

systems. As shown recently[39], any Roskilde-simple system, that is, with strong virial potential-energy correlations and isomorphs, is characterized by 'hidden-scale-invariance' in the sense that two functions of density exist, $h(\rho)$ and $g(\rho)$, such that the potential-energy function $U(\mathbf{R})$ can be expressed as follows

$$U(\mathbf{R}) \cong h(\rho)\tilde{\Phi}(\tilde{\mathbf{R}}) + g(\rho). \tag{4}$$

Here $\tilde{\Phi}(\tilde{\mathbf{R}})$ is a dimensionless, state-point-independent function of the reduced dimensionless configuration vector $\tilde{\mathbf{R}} \equiv \rho^{1/3}\mathbf{R}$. In particular, equation (4) implies the strong correlations between the potential energies of scaled and unscaled configurations documented in Fig. 1: consider two configurations $\mathbf{R}_1$ and $\mathbf{R}_2$ at density ρ_1 and ρ_2, respectively, with the same reduced coordinates, that is, obeying $\rho_1^{1/3}\mathbf{R}_1 = \rho_2^{1/3}\mathbf{R}_2$. By elimination of $\tilde{\Phi}(\tilde{\mathbf{R}})$ in equation (4) we get $U(\mathbf{R}_2) \cong (h(\rho_2)/h(\rho_1))U(\mathbf{R}_1) + g(\rho_2) - g(\rho_1)h(\rho_2)/h(\rho_1)$. Thus any two configurations with the same reduced coordinates have potential energies that are approximately linear functions of each other with constants that only depend on the two densities in question, see Fig. 1.

According to equation (4) a change of density implies that the potential-energy landscape to a good approximation undergoes a linear, affine transformation. Moreover, equation (4) implies invariant structure and dynamics in reduced units along the curves defined by constant $h(\rho)/k_B T$, the equation identifying the isomorphs[31,39,57]: along any curve defined by $h(\rho)/k_B T = C$ the reduced force $\tilde{\mathbf{F}} \equiv -\tilde{\nabla}U(\mathbf{R})/k_B T$ is given by $\tilde{\mathbf{F}} = -C\,\tilde{\nabla}\tilde{\Phi}(\tilde{\mathbf{R}})$, which implies that $\tilde{\mathbf{F}}$ is a certain function of the reduced coordinates, that is, $\tilde{\mathbf{F}} = \tilde{\mathbf{F}}(\tilde{\mathbf{R}})$. Since Newton's second law in reduced coordinates is $d^2\tilde{\mathbf{R}}/d\tilde{t}^2 = \tilde{\mathbf{F}}$ (the reduced mass is unity), it follows that the particles move in the same way at different isomorphic state points—except for the trivial linear uniform scalings of space and time involved in transforming back to real units.

Since the EXP pair potential has strong virial potential-energy correlations, equation (4) implies that functions $h_{EXP}(\rho)$, $g_{EXP}(\rho)$ and $\tilde{\Phi}_{EXP}(\tilde{\mathbf{R}})$ exist such that

$$U_{EXP}(\mathbf{R}) \cong h_{EXP}(\rho)\tilde{\Phi}_{EXP}(\tilde{\mathbf{R}}) + g_{EXP}(\rho). \tag{5}$$

The functions $h_{EXP}(\rho)$ and $g_{EXP}(\rho)$ in equation (5) both have dimension energy. They can therefore be written as $h_{EXP}(\rho) = \varepsilon\tilde{h}_{EXP}(\rho\sigma^3)$ and $g_{EXP}(\rho) = \varepsilon\tilde{g}_{EXP}(\rho\sigma^3)$ in which $\tilde{h}_{EXP}$ and $\tilde{g}_{EXP}$ are dimensionless functions that only depend on the dimensionless density $\rho\sigma^3$.

Consider now a pair potential $\upsilon(r)$ that can be expressed as follows

$$\upsilon(r) = \int_0^\infty f(\sigma)e^{-r/\sigma}d\sigma. \tag{6}$$

The system's potential energy is the sum of the individual pair-potential contributions with the same weights as in equation (6). Therefore, if $U(\mathbf{R})$ is the potential energy and we define $h(\rho) \equiv \int_0^\infty f(\sigma)\tilde{h}_{EXP}(\rho\sigma^3)d\sigma$ and $g(\rho) \equiv \int_0^\infty f(\sigma)\tilde{g}_{EXP}(\rho\sigma^3)d\sigma$, it follows from equation (5) that

$$U(\mathbf{R}) \cong h(\rho)\tilde{\Phi}_{EXP}(\tilde{\mathbf{R}}) + g(\rho). \tag{7}$$

Because the reduced-unit physics is encoded in the function $\tilde{\Phi}_{EXP}(\tilde{\mathbf{R}})$ via Newton's equation $d^2\tilde{\mathbf{R}}/d\tilde{t}^2 = -C\,\tilde{\nabla}\tilde{\Phi}_{EXP}(\tilde{\mathbf{R}})$ where $C = h(\rho)/k_B T$ identifes the isomorph through the state point in question, equation (7) implies identical structure and dynamics to a good approximation for systems obeying equation (6). This argument would be exact if the EXP pair potential had 100% virial potential-energy correlations. This is not the case, though, and the approximation equation (7) is only useful when it primarily involves EXP functions from the low-

temperature part of the phase diagram where strong virial potential-energy correlations and thus equation (4) apply.

We have shown that a pair potential $\upsilon(r)$ is quasi-universal if it can be written as a sum of low-temperature EXP pair potentials. To translate this into an operational criterion, note the following. If the integral in equation (6) is discretized into a finite sum and expressed in terms of the reduced pair potential $\tilde{\upsilon} \equiv \upsilon/k_B T$ regarded as a function of the reduced pair distance $(\tilde{r} \equiv \rho^{1/3} r)$, the condition for quasi-universality is that

$$\tilde{\upsilon}(\tilde{r}) \cong \sum_j \Lambda_j e^{-u_j \tilde{r}}, \; |\Lambda_j| \gg 1. \tag{8}$$

It is understood that the 'wavevectors' u_j are not so closely spaced that large positive and negative neighbouring terms may almost cancel one another. Several points should be noted: (1) Equation (8) is state-point dependent because the function $\tilde{\upsilon}(\tilde{r})$ varies with state point; (2) a continuous integral of EXP functions does not automatically obey equation (8)—it is necessary that the integral can be approximated by a finite sum of EXP terms, each with a numerically large prefactor; (3) a sum or product of two pair potentials obeying equation (8) with all $\Lambda_j > 0$ gives a function that also obeys this equation.

Important examples. Consider first the IPL pair potential $\upsilon_n(r) \equiv \varepsilon(r/\sigma)^{-n}$. In terms of the reduced radius $\tilde{r}$, the reduced IPL pair potential is given by $\tilde{\upsilon}_n(\tilde{r}) \equiv \upsilon_n(r)/k_B T = \Gamma_n \tilde{r}^{-n}$ in which $\Gamma_n \equiv (\rho \sigma^3)^{n/3} \varepsilon / k_B T$. The mathematical identity $\int_0^\infty x^{n-1} \exp(-x) dx = (n-1)!$ implies that $\tilde{\upsilon}_n(\tilde{r}) = [\Gamma_n / (n-1)!] \int_0^\infty u^{n-1} \exp(-u\tilde{r}) du$. Discretizing the integral leads to $\tilde{\upsilon}_n(\tilde{r}) \cong [\Gamma_n / (n-1)!] \Delta u \sum_{j=0}^\infty ((j+1/2)\Delta u)^{n-1} \exp(-(j+1/2)\Delta u \tilde{r})$. Writing $((j+1/2)\Delta u)^{n-1} = \exp[(n-1) \ln((j+1/2)\Delta u)]$, by differentiation with respect to j it is easy to see that the dominant contributions to the sum come from the terms with $(n-1)/(j+1/2) \simeq \Delta u \tilde{r}$. Thus for typical nearest-neighbour distances $(\tilde{r} \simeq 1)$ the terms with $(j+1/2)\Delta u \simeq n-1$ are the most important ones. For these values of j the prefactor of the exponential in the above sum is roughly $\Gamma_n \Delta u (n-1)^{n-1} / (n-1)!$. The largest realistic discretization step Δu is in order of unity, so we conclude that for values of n larger than three or four equation (8) is obeyed unless Γ_n is very small, a condition that applies for the state points that have typically been studied[9,20–23]. The case of a Coulomb repulsive system ($n = 1$) is discussed in the next section.

As a consequence of the above, at most state points the potential energy of the IPL system, $U_n(\mathbf{R})$, can be written as

$$U_n(\mathbf{R}) \cong h_n(\rho) \tilde{\Phi}_{EXP}(\tilde{\mathbf{R}}) + g_n(\rho). \tag{9}$$

Since $U_n(\mathbf{R}) \propto \rho^{n/3}$ for the density variation induced by a uniform scaling of a configuration $\mathbf{R}$, that is, keeping $\tilde{\mathbf{R}}$ constant, one has $h_n(\rho) \propto \rho^{n/3}$ and $g_n(\rho) \propto \rho^{n/3}$. This means that two numbers α_n and β_n exist such that $U_n(\mathbf{R}) \cong \varepsilon [\alpha_n (\rho \sigma^3)^{n/3} \tilde{\Phi}_{EXP}(\tilde{\mathbf{R}}) + \beta_n (\rho \sigma^3)^{n/3}]$. For a general pair potential of the form $\upsilon(r) = \varepsilon \sum_n \upsilon_n (r/\sigma)^{-n}$, by a linear combination of equation (9) we arrive at equation (7) in which $h(\rho) = \varepsilon \sum_n \upsilon_n \alpha_n (\rho \sigma^3)^{n/3}$ and $g(\rho) = \varepsilon \sum_n \upsilon_n \beta_n (\rho \sigma^3)^{n/3}$.

A well-known case is the LJ pair potential $\upsilon_{LJ}(r) = 4\varepsilon[(r/\sigma)^{-12} - (r/\sigma)^{-6}]$. Consider the LJ liquid state point given by $\rho \sigma^3 = 1$, $k_B T = 2\varepsilon$. In terms of the above-defined reduced IPL functions, it is easy to see that this is of the form equation (8), implying quasi-universality of the LJ liquid at this state point.

An application of the EXP theory of quasi-universality is the intriguing 'additivity of melting temperatures'[61] according to which if two systems have melting temperatures that as functions of density are denoted by $T_{m,1}(\rho)$ and $T_{m,2}(\rho)$, the melting temperature of the system with the sum potential energy is

$T_{m,1}(\rho) + T_{m,2}(\rho)$. This property follows from quasi-universality because the dynamics of all three systems are controlled by the same function $\tilde{\Phi}_{EXP}(\tilde{\mathbf{R}})$. For the EXP system melting initiates when this function's average upon heating reaches a certain value, and the same must apply for all quasi-universal systems. In particular, since for an IPL system one has $T_m(\rho) \propto \rho^{n/3}$ (ref. 62), the melting temperature of the LJ system varies with density according to the expression $T_m(\rho) = A\rho^4 - B\rho^2$ (refs 61,63).

Discussion

Denominating the systems that obey equation (8) collectively as the EXP quasi-universality class, we have shown that all systems in this class are quasi-universal in the sense of this paper: if a single reduced-unit structural or dynamic quantity is known, all other reduced-unit structural or dynamic quantities are known to a good approximation. This is because these are all encoded in the function $\tilde{\Phi}_{EXP}(\tilde{\mathbf{R}})$, and any reduced-unit quantity characterizing structure or dynamics identifies the constant $C = h(\rho)/k_B T$ of the reduced-unit version of Newton's second law $d^2\tilde{\mathbf{R}}/d\tilde{t}^2 = -C\tilde{\nabla}\tilde{\Phi}_{EXP}(\tilde{\mathbf{R}})$.

The obvious question is whether all quasi-universal systems are in the EXP quasi-universality class. We cannot prove this, but conjecture it is the case based on the available evidence in the literature for the following systems:

The Jagla pair potential is a HS potential plus a finite-width potential well defined by two terms that are linear in r (ref. 37). This pair potential is not in the EXP quasi-universality class—it cannot be approximated as a sum of exponentials because its Laplace transform only has a pole at zero. Indeed, the Jagla pair potential reproduces water's anomalous density maximum and has a liquid–liquid critical point[19], properties which are both inconsistent with quasi-universality.

The Gaussian core model (GCM) is a Gaussian centred at $r = 0$. For this system there is a re-entrant body-centered cubic phase above the triple point[15] and the transport coefficients have a non-monotonous density dependence at constant temperature[18]. These observations both contradict quasi-universality. Consistent with the above conjecture, a representation of the form $\exp(-r^2/2\sigma^2) = \int_0^\infty \phi(u) e^{-ur} du$ does not exist because the Laplace transform of a Gaussian has no poles; thus the GCM system is not in the EXP quasi-universality class. At low temperatures and low densities, the GCM pair potential can be approximated well by an exponential, however, and in this part of the phase diagram the GCM system is indeed quasi-universal[11,15].

The LJ Gaussian (LJG) model is a pair potential that is arrived at by adding a negative, displaced Gaussian to the LJ pair potential[17]. Like the GCM it cannot be written as a sum of exponentials. The LJG system has thermodynamic and dynamic anomalies[16] and 'a surprising variety of crystals'[17], both of which are observations that violate quasi-universality.

The OCP is the common name for the single-charge Coulomb system. The Coulomb potential is too long ranged for a thermodynamic limit to exist for the free energy per particle unless a uniform charge-compensating background is introduced[5,49]. Nevertheless, any finite OCP system is well-defined and amenable to computer simulation—in fact the OCP system was an important example in Rosenfeld's original paper on excess-entropy scaling[6]. The OCP system is the $n = 1$ case of the above discussed IPL pair potential; it is quasi-universal in the dense fluid case, that is, whenever $\Gamma_1 \gg 1$ (writing $\tilde{\upsilon}_1 \equiv \Gamma_1/\tilde{r}$). Violations of quasi-universality are indeed known to gradually appear when Γ_1 goes below 50 (ref. 64).

The Yukawa pair potential is given by the expression $\upsilon(r) = \varepsilon(\sigma/r)\exp(-r/\sigma)$. Since $\upsilon(r)/\varepsilon = \int_0^\infty \exp(-r(u+1)/\sigma) du$ it is

easy to see that this pair potential is in the EXP quasi-universality class whenever $k_B T \ll \varepsilon$. This is consistent with known properties[65].

This paper has argued that one may replace the HS by the EXP system as the generic simple pair-potential system from which quasi-universality is derived. We do not suggest that the HS system's role in liquid-state physics is entirely undeserved, however, because this model is still uniquely simple and mathematically beautiful. Nevertheless, by using the EXP pair potential as the fundamental building block, a number of advantages are obtained. First of all, smoothness is ensured. Second, if the conjecture that all quasi-universal functions are in the EXP quasi-universality class is confirmed, we now have a mathematically precise characterization of all quasi-universal pair potentials (equation (8)). Third, the present explanation of quasi-universality gives a natural explanation of dynamic quasi-universality. Finally, the role of the HS pair potential in liquid-state physics is clarified: quasi-universality is not *caused* by a given system's similarity to the HS system—rather, quasi-universality *implies* similarity between the properties of many systems and those of the HS system simply because the latter is in the EXP quasi-universality class by being the $n \to \infty$ limit of an IPL system. Note that while this paper focused on quasi-universality for liquid models, the crystalline phases of these models are likewise quasi-universal, for instance by having quasi-universal radial distribution functions, phonon spectra and vacancy jump dynamics[66].

In continuing work it will be interesting to investigate the consequences of the EXP approach for the fact that quasi-universality appears to apply beyond the framework of thermal equilibrium, for example, for the jamming transition in which the HS model is presently used as the generic model[67]. It is an open question whether replacing the HS model by the EXP model in thermodynamic perturbation theory would have advantages[5]. Another open question is to which extent mixtures are quasi-universal[68]. Finally, recent results from the works of Truskett and co-workers[11] show that classical Rosenfeld excess-entropy scaling may be modified into more general excess-entropy scalings, and it would be interesting to investigate whether the present approach can somehow be extended to account for this.

Method

Simulation system. A system of $N = 1,000$ particles interacting via the EXP pair potential was simulated using standard Nose–Hoover NVT simulations with a time step of 0.0025 and thermostat relaxation time of 0.2 (LJ units). A shifted-forces cut-off at $r = 2\rho^{-1/3}$ was used for densities below 1.0×10^{-3}, at larger densities the cut-off was $4\rho^{-1/3}$. At each state point the simulations involved 10,000,000 time steps after equilibration. For temperatures below 2.0×10^{-3}, the simulations were initiated from a state of 2,000 particles placed in a body-centred cubic crystal structure. The melting isomorph was determined by the interface pinning method[69]—the NPT simulations involved here were made using LAMMPS[70] (http://lammps.sandia.gov) with shifted-potential cut-offs ranging from $2.5\,\rho^{-1/3}$ to $4.0\,\rho^{-1/3}$ for a system of 2,560 particles; the time step was 0.005 and the relaxation time was 0.4 for the thermostat and 0.8 for the barostat.

References

1. Bernal, J. D. A geometrical approach to the structure of liquids. *Nature* **183,** 141–147 (1959).
2. Alder, B. J. & Wainwright, T. E. Phase transition for a hard sphere system. *J. Chem. Phys.* **27,** 1208–1209 (1957).
3. Weeks, J. D., Chandler, D. & Andersen, H. C. Role of repulsive forces in determining the equilibrium structure of simple liquids. *J. Chem. Phys.* **54,** 5237–5247 (1971).
4. Barker, J. A. & Henderson, D. What is "liquid"? Understanding the states of matter. *Rev. Mod. Phys.* **48,** 587–671 (1976).
5. Hansen, J.-P. & McDonald, I. R. *Theory of Simple Liquids: With Applications to Soft Matter,* 4th edn (Academic, 2013).
6. Rosenfeld, Y. Relation between the transport coefficients and the internal entropy of simple systems. *Phys. Rev. A* **15,** 2545–2549 (1977).
7. Krekelberg, W. P., Mittal, J., Ganesan, V. & Truskett, T. M. How short-range attractions impact the structural order, self-diffusivity, and viscosity of a fluid. *J. Chem. Phys.* **127,** 044502 (2007).
8. Chakraborty, S. N. & Chakravarty, C. Entropy, local order, and the freezing transition in Morse liquids. *Phys. Rev. E* **76,** 011201 (2007).
9. Branka, A. C. & Heyes, D. M. Pair correlation function of soft-sphere fluids. *J. Chem. Phys.* **134,** 064115 (2011).
10. de J. Guevara-Rodríguez, F. & Medina-Noyola, M. Dynamic equivalence between soft- and hard-core Brownian fluids. *Phys. Rev. E* **68,** 011405 (2003).
11. Pond, M. J., Errington, J. R. & Truskett, T. M. Generalizing Rosenfeld's excess-entropy scaling to predict long-time diffusivity in dense fluids of brownian particles: from hard to ultrasoft interactions. *J. Chem. Phys.* **134,** 081101 (2011).
12. Schmiedeberg, M., Haxton, T. K., Nagel, S. R. & Liu, A. J. Mapping the glassy dynamics of soft spheres onto hard-sphere behavior. *Europhys. Lett.* **96,** 36010 (2011).
13. Lopez-Flores, L. *et al.* Dynamic equivalence between atomic and colloidal liquids. *Europhys. Lett.* **99,** 46001 (2012).
14. Lopez-Flores, L., Ruiz-Estrada, H., Chavez-Paez, M. & Medina-Noyola, M. Dynamic equivalences in the hard-sphere dynamic universality class. *Phys. Rev. E* **88,** 042301 (2013).
15. Prestipino, S., Saija, F. & Giaquinta, P. V. Phase diagram of softly repulsive systems: the Gaussian and inverse-power-law potentials. *J. Chem. Phys.* **123,** 144110 (2005).
16. Barros de Oliveira, A., Netz, P. A., Colla, T. & Barbosa, M. C. Thermodynamic and dynamic anomalies for a three-dimensional isotropic core-softened potential. *J. Chem. Phys.* **124,** 084505 (2006).
17. Engel, M. & Trebin, H.-R. Self-assembly of monatomic complex crystals and quasicrystals with a double-well interaction potential. *Phys. Rev. Lett.* **98,** 225505 (2007).
18. Krekelberg, W. P. *et al.* Generalized Rosenfeld scalings for tracer diffusivities in not-so-simple fluids: mixtures and soft particles. *Phys. Rev. E* **80,** 061205 (2009).
19. Gallo, P. & Sciortino, F. Ising universality class for the liquid-liquid critical point of a one component fluid: A finite-size scaling test. *Phys. Rev. Lett.* **109,** 177801 (2012).
20. Heyes, D. M. & Branka, A. C. The influence of potential softness on the transport coefficients of simple fluids. *J. Chem. Phys.* **122,** 234504 (2005).
21. Scopigno, T. *et al.* Hard-sphere-like dynamics in a non-hard-sphere liquid. *Phys. Rev. Lett.* **94,** 155301 (2005).
22. Branka, A. C. & Heyes, D. M. Thermodynamic properties of inverse power fluids. *Phys. Rev. E* **74,** 031202 (2006).
23. Heyes, D. M. & Branka, A. C. Self-diffusion coefficients and shear viscosity of inverse power fluids: from hard- to soft-spheres. *Phys. Chem. Chem. Phys.* **10,** 4036–4044 (2008).
24. Young, T. & Andersen, H. C. A scaling principle for the dynamics of density fluctuations in atomic liquids. *J. Chem. Phys.* **118,** 3447–3450 (2003).
25. Truskett, T. M., Torquato, S. & Debenedetti, P. G. Towards a quantification of disorder in materials: distinguishing equilibrium and glassy sphere packings. *Phys. Rev. E* **62,** 993–1001 (2000).
26. Ubbelohde, A. R. *Melting and Crystal Structure* (Clarendon, 1965).
27. Khrapak, S. A., Chaudhuri, M. & Morfill, G. E. Communication: universality of the melting curves for a wide range of interaction potentials. *J. Chem. Phys.* **134,** 241101 (2011).
28. Andrade, E. N. C. A theory of the viscosity of liquids—Part I. *Phil. Mag.* **17,** 497–511 (1934).
29. Hansen, J.-P. & Verlet, L. Phase transitions of the Lennard-Jones system. *Phys. Rev.* **184,** 151–161 (1969).
30. Baus, M. The modern theory of crystallization and the Hansen-Verlet rule. *Mol. Phys.* **50,** 543–565 (1983).
31. Gnan, N., Schrøder, T. B., Pedersen, U. R., Bailey, N. P. & Dyre, J. C. Pressure-energy correlations in liquids. IV. "isomorphs" in liquid phase diagrams. *J. Chem. Phys.* **131,** 234504 (2009).
32. Pond, M. J., Errington, J. R. & Truskett, T. M. Mapping between long-time molecular and Brownian dynamics. *Soft Matter* **7,** 9859–9862 (2011).
33. Young, T. & Andersen, H. C. Tests of an approximate scaling principle for dynamics of classical fluids. *J. Phys. Chem. B* **109,** 2985–2994 (2005).
34. Rosenfeld, Y. A quasi-universal scaling law for atomic transport in simple fluids. *J. Phys. Condens. Matter* **11,** 5415–5427 (1999).
35. Stillinger, F. H. Phase transitions in the Gaussian core system. *J. Chem. Phys.* **65,** 3968–3974 (1976).
36. Zachary, C. E., Stillinger, F. H. & Torquato, S. Gaussian core model phase diagram and pair correlations in high euclidean dimensions. *J. Chem. Phys.* **128,** 224505 (2008).
37. Yan, Z., Buldyrev, S. V., Giovambattista, N., Debenedetti, P. G. & Stanley, H. E. Family of tunable spherically symmetric potentials that span the range from hard spheres to waterlike behavior. *Phys. Rev. E* **73,** 051204 (2006).

38. Dyre, J. C. *NVU* perspective on simple liquids' quasiuniversality. *Phys. Rev. E* **87,** 022106 (2013).

39. Dyre, J. C. Isomorphs, hidden scale invariance, and quasiuniversality. *Phys. Rev. E* **88,** 042139 (2013).

40. Bacher, A. K. & Dyre, J. C. The mother of all pair potentials. *Colloid Polym. Sci.* **292,** 1971–1975 (2014).

41. Born, M. & Meyer, J. E. Zur Gittertheorie der Ionenkristalle. *Z. Phys.* **75,** 1–18 (1932).

42. Buckingham, R. A. The classical equation of state of gaseous helium, neon and argon. *Proc. R. Soc. Lond. A* **168,** 264–283 (1938).

43. Girifalco, L. A. & Weizer, V. G. Application of the Morse potential function to cubic metals. *Phys. Rev.* **114,** 687–690 (1959).

44. Buckingham, R. A. & Corner, J. Tables of second virial and low-pressure Joule-Thompson coefficients for intermolecular potentials with exponential repulsion. *Proc. R. Soc. A* **189,** 118–129 (1947).

45. Mason, E. A. & Rice, W. E. The intermolecular potentials for some simple nonpolar molecules. *J. Chem. Phys.* **22,** 843–851 (1954).

46. Abrahamson, A. A. Born-Mayer-type interatomic potential for neutral ground-state atoms with $Z = 2$ to $Z = 105$. *Phys. Rev.* **178,** 76–79 (1969).

47. Gupta, N. P. Interpretation of phonon dispersion in solid argon and neon. *J. Solid State Chem.* **5,** 477–480 (1972).

48. Toda, A. *Nonlinear Waves and Solitons* (Kluwer, 1983).

49. Hansen, J.-P., McDonald, I. R. & Pollock, E. L. Statistical mechanics of dense ionized matter. III. Dynamical properties of the classical one-component plasma. *Phys. Rev. A* **11,** 1025–1039 (1975).

50. Ingebrigtsen, T. S., Schrøder, T. B. & Dyre, J. C. Isomorphs in model molecular liquids. *J. Phys. Chem. B* **116,** 1018–1034 (2012).

51. Veldhorst, A. A., Dyre, J. C. & Schrøder, T. B. Scaling of the dynamics of flexible Lennard-Jones chains. *J. Chem. Phys.* **141,** 054904 (2014).

52. Malins, A., Eggers, J. & Royall, C. P. Investigating isomorphs with the topological cluster classification. *J. Chem. Phys.* **139,** 234505 (2013).

53. Prasad, S. & Chakravarty, C. Onset of simple liquid behaviour in modified water models. *J. Chem. Phys.* **140,** 164501 (2014).

54. Flenner, E., Staley, H. & Szamel, G. Universal features of dynamic heterogeneity in supercooled liquids. *Phys. Rev. Lett.* **112,** 097801 (2014).

55. Henao, A., Pothoczki, S., Canales, M., Guardia, E. & Pardo, L. C. Competing structures within the first shell of liquid C_2Cl_6: a molecular dynamics study. *J. Mol. Liq.* **190,** 121–125 (2014).

56. Pieprzyk, S., Heyes, D. M. & Branka, A. C. Thermodynamic properties and entropy scaling law for diffusivity in soft spheres. *Phys. Rev. E* **90,** 012106 (2014).

57. Dyre, J. C. Hidden scale invariance in condensed matter. *J. Phys. Chem. B* **118,** 10007–10024 (2014).

58. Bailey, N. P., Pedersen, U. R., Gnan, N., Schrøder, T. B. & Dyre, J. C. Pressure-energy correlations in liquids. II. analysis and consequences. *J. Chem. Phys.* **129,** 184508 (2008).

59. Ingebrigtsen, T. S., Schrøder, T. B. & Dyre, J. C. What is a simple liquid? *Phys. Rev. X* **2,** 011011 (2012).

60. Pedersen, U. R., Schrøder, T. B. & Dyre, J. C. Repulsive reference potential reproducing the dynamics of a liquid with attractions. *Phys. Rev. Lett.* **105,** 157801 (2010).

61. Rosenfeld, Y. Universality of melting and freezing indicators and additivity of melting curves. *Mol. Phys.* **32,** 963–977 (1976).

62. Stishov, S. M. The thermodynamics of melting of simple substances. *Sov. Phys. Usp.* **17,** 625–643 (1975).

63. Khrapak, S. A. & Morfill, G. E. Accurate freezing and melting equations for the Lennard-Jones system. *J. Chem. Phys.* **134,** 094108 (2011).

64. Daligault, J. Liquid-state properties of a one-component plasma. *Phys. Rev. Lett.* **96,** 065003 (2006).

65. Rosenfeld, Y. Quasi-universal melting-temperature scaling of transport coefficients in Yukawa systems. *J. Phys. Condens. Matter* **13,** L39–L43 (2001).

66. Albrechtsen, D. E., Olsen, A. E., Pedersen, U. R., Schrøder, T. B. & Dyre, J. C. Isomorph invariance of the struccture and dynamics of classical crystals. *Phys. Rev. B* **90,** 094106 (2014).

67. Lerner, E., Düring, G. & Wyart, M. Toward a microscopic description of flow near the jamming threshold. *Europhys. Lett.* **99,** 58003 (2012).

68. Lerner, E., Bailey, N. P. & Dyre, J. C. Density scaling and quasiuniversality of flow-event statistics for athermal plastic flows. *Phys. Rev. E.:* Preprint at http://arxiv.org/pdf/1405.0156.pdf (2014).

69. Pedersen, U. R. Direct calculation of the solid-liquid Gibbs free energy difference in a single equilibrium simulation. *J. Chem. Phys.* **139,** 104102 (2013).

70. Plimpton, S. Fast parallel algorithms for short-range molecular dynamics. *J. Comp. Phys.* **117,** 1–19 (1995).

Acknowledgements

Author contributions

A.K.B. and T.B.S. performed the simulations and carried out the data analysis; J.C.D. conceived the project and wrote the paper.

Additional information

Competing financial interests: The authors declare no competing financial interests.

Reprints and permission information is available online at http://npg.nature.com/reprintsandpermissions/

How to cite this article: Bacher, A. K. *et al.* Explaining why simple liquids are quasi-universal. *Nat. Commun.* 5:5424 doi: 10.1038/ncomms6424 (2014).

The EXP pair-potential system. I. Fluid phase isotherms, isochores, and quasiuniversality

Andreas Kvist Bacher,[a] Thomas B. Schrøder, and Jeppe C. Dyre[b]
Glass and Time, IMFUFA, Department of Science and Environment, Roskilde University,
P.O. Box 260, DK-4000 Roskilde, Denmark

It was recently shown that the exponentially repulsive EXP pair potential defines a system of particles in terms of which simple liquids' quasiuniversality may be explained [A. K. Bacher *et al.*, Nat. Commun. **5**, 5424 (2014); J. C. Dyre, J. Phys.: Condens. Matter **28**, 323001 (2016)]. This paper and its companion [A. K. Bacher *et al.*, J. Chem. Phys. **149**, 114502 (2018)] present a detailed simulation study of the EXP system. Here we study how structure monitored by the radial distribution function and dynamics monitored by the mean-square displacement as a function of time evolve along the system's isotherms and isochores. The focus is on the gas and liquid phases, which are distinguished pragmatically by the absence or presence of a minimum in the radial distribution function above its first maximum. A constant-potential-energy (*NVU*)-based proof of quasiuniversality is presented, and quasiuniversality is illustrated by showing that the structure of the Lennard-Jones system at four state points is well approximated by those of EXP pair-potential systems with the same reduced diffusion constant. Paper II studies the EXP system's isomorphs, focusing also on the gas and liquid phases. © *2018 Author(s).*
All article content, except where otherwise noted, is licensed under a Creative Commons Attribution (CC BY) license (http://creativecommons.org/licenses/by/4.0/). https://doi.org/10.1063/1.5043546

I. INTRODUCTION

For more than half a century, the term "simple liquid" has implied a system of point particles interacting via pair-wise additive forces.[1–8] The paradigmatic simple liquid is the hard-sphere (HS) system of identical spheres that do not interact unless they touch each other, at which point the potential energy jumps to infinity.[8–14] The HS system embodies a physical picture going back to van der Waals' seminal thesis from 1873[15] according to which the harshly repulsive forces between a liquid's atoms or molecules determine the structure. This idea is the basis of the present understanding of liquids as elucidated, e.g., in the classical monograph by Hansen and McDonald from 1976,[8] and in the classical reviews by Widom from 1967[11] and by Chandler, Weeks, and Andersen from 1983.[14] The HS picture has had many successes, for instance leading to very useful perturbation theories of the liquid state.[8,16–22]

van der Waals' fundamental insight was that liquids' properties to a large extent derive from the repulsive forces.[15] The weaker and longer-ranged attractive forces play little role for the structure and dynamics; they mainly serve to reduce energy and pressure by providing a virtually constant negative cohesive energy. It has been found from computer simulations, however, that some pair-potential systems are not simple in any reasonable understandings of the term, whereas, on the other hand, a number of *molecular* liquids[23] and even polymer-like

systems[24] have simple and regular behavior. A liquid like water exhibits non-simple behavior by having, e.g., a diffusion constant that increases upon isothermal compression, by melting instead of freezing upon compression, etc.[25] Pair-potential systems with such anomalous behavior include the Gaussian-core model,[26,27] the Lennard-Jones Gaussian model,[28] and the Jagla model.[25] At high and moderate temperatures, the Gaussian-core model is not steeply repulsive, which may explain its anomalies, but the other two systems are complex despite their strongly repulsive forces. Thus pair-wise additive forces between point particles are neither necessary nor sufficient for a liquid to be "simple," and a different definition of simplicity is called for.

An alternative definition of liquid simplicity is provided by the isomorph theory according to which simple behavior is found whenever the system in question to a good approximation exhibits "hidden scale invariance" ("hidden" because this property is rarely obvious from the mathematical expression for the potential energy).[7,29–31] This defines the class of Roskilde (R)-simple systems that include the standard Lennard-Jones (LJ) model, a class which was first identified by characteristic strong correlations between the virial and potential-energy thermal fluctuations in the canonical (*NVT*) ensemble.[32–34]

R-simple systems have isomorphs,[29] which are lines in the thermodynamic phase diagram along which structure and dynamics in reduced units (see below) are invariant to a good approximation. These invariances reflect the fact that state points on the same isomorph have approximately the same canonical probabilities for configurations that scale uniformly into one another.[29] Isomorph-theory predictions have been

a)ankvba@gmail.com
b)dyre@ruc.dk

validated in computer simulations of LJ type systems,[29,35,36] simple molecular models,[23] crystals,[37] nano-confined liquids,[38] non-linear shear flows,[39] zero-temperature plastic flows of glasses,[40] polymer-like flexible molecules,[24,41] metals studied by *ab initio* density functional theory computer simulations,[42] plasmas,[43] and other liquids.[31,44] Experimental confirmations of the isomorph theory were presented in Refs. 45–50. The numerical and experimental confirmations notwithstanding, it is important to emphasize that the isomorph theory is rarely exact, that it usually works only in the liquid and solid parts of the thermodynamic phase diagram [the exponential (EXP) system is an interesting exception to this], and that the theory does not apply for systems with strong directional bonding (hydrogen-bonding or covalently bonded systems).

The basic characteristic of an R-simple system is that, because of its isomorphs, the thermodynamic phase diagram is effectively one-dimensional in regard to structure and dynamics.[29,31] R-simple systems have this property in common with the HS system for which the packing fraction determines the physics throughout the phase diagram.[8]

In 2014, it was shown[51] that the isomorph theory is a consequence of the following scale-invariance property in which $\mathbf{R} = (\mathbf{r}_1, \ldots, \mathbf{r}_N)$ is the vector of all particle coordinates, $U(\mathbf{R})$ is the potential-energy function, and λ is a uniform scaling parameter,

$$U(\mathbf{R}_a) < U(\mathbf{R}_b) \implies U(\lambda \mathbf{R}_a) < U(\lambda \mathbf{R}_b). \tag{1}$$

Thus if the potential energy of some configuration $\mathbf{R}_a$ is lower than that of another configuration $\mathbf{R}_b$, both of the same density, this property is maintained after a uniform scaling of the configurations. Strong virial potential-energy correlations,[32] as well as the approximate invariance along isomorphs of Boltzmann probabilities of uniformly scaled configurations that originally defined isomorphs,[29] are consequences of Eq. (1).[51]

The scale-invariance property Eq. (1) is only obeyed rigorously for the unrealistic case of a system with an Euler-homogeneous potential-energy function plus a constant. For realistic R-simple systems, Eq. (1) applies to a good approximation, i.e., for modest density variations of most of its physically relevant configurations. This is, nevertheless, enough to ensure approximate invariance of the structure and dynamics along the isomorphs.[51] Incidentally, these curves in the phase diagram are virtually parallel to the freezing and melting lines,[29,44] a fact that explains several well-known phenomenological melting-line characterizations, e.g., the Lindemann melting criterion's pressure independence.[29,52,53]

The invariance of the structure and dynamics along isomorphs relates to "reduced" quantities.[29,31,51] These are quantities that have been made dimensionless by scaling with the *length*

$$l_0 \equiv \rho^{-1/3} \tag{2}$$

defined from the particle density $\rho \equiv N/V$ in which N is the number of particles and V is the sample volume, the *energy*

$$e_0 \equiv k_B T \tag{3}$$

in which T is the temperature, and the *time*

$$t_0 \equiv \rho^{-1/3} \sqrt{\frac{m}{k_B T}} \tag{4}$$

in which m is the average particle mass. Note that these units vary with the state point in question.

Reduced units are used throughout the present paper and Paper II.[79] Two notable exceptions to this are density and temperature, which are both constant in reduced units. Therefore, in order to specify a state point, the density is reported in units of the EXP pair potential length parameter σ of Eq. (5) below, i.e., in units of $1/\sigma^3$, and temperature is reported in units of the potential's energy parameter over the Boltzmann constant, ε/k_B. We refer to this as the "EXP unit system."

Although the HS system provides a good reference for understanding simple liquids, it has some challenges.[44] For instance, while simple liquids' quasiuniversal *structure* may be understood from the harsh interparticle repulsions modeled by a HS system, it is much less obvious how to explain simple liquids' quasiuniversal *dynamics* by reference to the HS system. After all, the HS system's particles evolve in time according to Newton's first law following straight lines in space, interrupted by infinitely fast collisions. This is quite different from what happens in a real liquid where each particle interacts continuously and strongly with ten or more nearest neighbors. Also, the HS reference system cannot explain the above-mentioned fact that some systems with strong interparticle repulsions do not belong to the quasi-universal class of "simple" systems.[31] Finally, the HS system is unphysical becasuse of its discontinuous potential-energy function, implying, in particular, that the time-averaged potential energy is zero at all state points.

It would be nice to have a generic analytic pair-potential system in terms of which simple liquids' quasiuniversality may be explained, thus defining the "mother of all pair-potential systems." By means of the isomorph theory, it was recently suggested[31,44] that this role may be played by the exponentially repulsive EXP pair potential defined by (in which ε is a characteristic energy and σ a characteristic length)

$$v_{\text{EXP}}(r) = \varepsilon \, e^{-r/\sigma}. \tag{5}$$

References 31 and 44 showed that any system with a pair potential, which may be written as a sum of spatially decaying exponentials of the form given in Eq. (5) with numerically large prefactors relative to $k_B T$, to a good approximation obeys the same equation of motion as the EXP system itself. This explains the quasiuniversality of tradiional simple liquids like the LJ system, inverse power-law systems, Yukawa pair-potential system, etc., as well as exceptions to quasiuniversality that cannot be written in this way.[31,44]

Despite its mathematical simplicity and the fact that the exponential function in mathematics is central, e.g., for defining the Fourier and Laplace transforms, the EXP pair-potential system has been studied little on its own right. In the literature, an EXP term typically appears added to an r^{-6} attractive term[54,55] or multiplied by a $1/r$ term as in the Yukawa pair potential.[56,57] Born and Meyer in 1932 used an exponentially repulsive term in a pair potential and justified this from the fact that electronic bound-state wavefunctions decay

exponentially in space.[54] Kac and co-workers used a HS pair potential minus a long-ranged EXP term for rigorously deriving the van der Waals equation of state in one dimension.[58] Recently, by reference to the EXP pair potential Maimbourg and Kurchan showed that the isomorph theory for pairpotential systems with strong repulsions is exact in infinite dimensions.[59] The EXP pair potential was also used recently by Kooij and Lerner in a study of unjamming in models with analytic pair potentials.[60]

The reason that the pure EXP pair-potential system has not been studied very much may be that this system has been regarded as unrealistic by being purely repulsive. However, even the purely repulsive inverse power law pair-potential systems have been studied much more than the EXP system.[61–67] In view of this, the present paper and Paper II[79] undertake an investigation of the EXP pair-potential system by presenting results from extensive computer simulations.

Figure 1 shows the phase diagram of the EXP system indicating the state points studied. Like for any purely repulsive system there are only two thermodynamically distinct phases: a solid phase at low temperatures and high densities

EXP
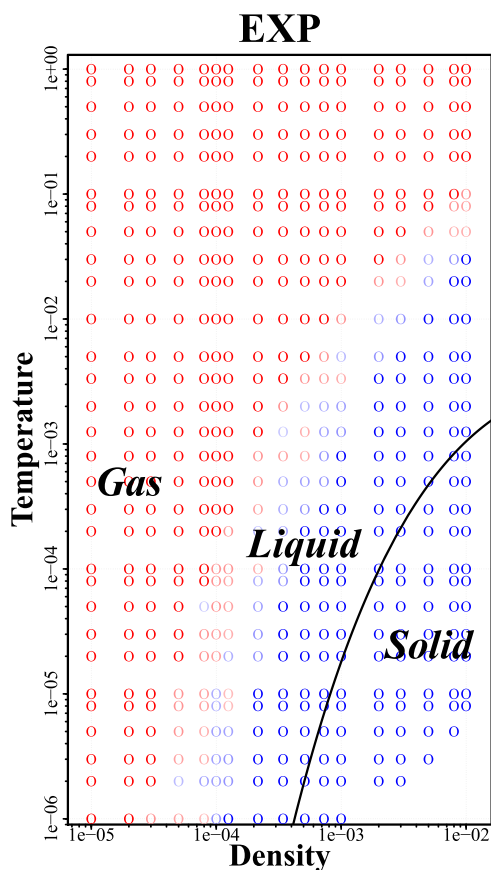
FIG. 1.   Log-log density-temperature phase diagram of the EXP system showing the state points investigated. Gas-phase state points are given in red and condensed-phase (liquid and solid) state points in blue. Because the EXP pair potential is purely repulsive, there is no gas-liquid phase transition and no gas-liquid coexistence region; the gas and liquid phases merge continuously. Liquid state points are distinguished pragmatically from those of the gas phase by having minima in their pair-distribution functions above the nearest-neighbor peak; the light colored state points indicate the transition region between gas and liquid. The solid-liquid coexistence region is covered by the black line (determined as the approximate melting-line isomorph).

and a "fluid" phase; there is no gas-liquid phase transition since this requires attractive forces. We have chosen, nevertheless, to pragmatically distinguish typical "gas" state points from typical "liquid" state points, but it is important to recall throughout the paper that these phases merge continuously into one another, just as in a real system above its critical temperature. To distinguish the gas and liquid phases, we used the following criterion: if the radial distribution has a clear minimum above its first maximum, the state point is liquid; if not, it is a gas-phase state point. The large region of in-between states is indicated in Fig. 1 by the use of light colors. This is where the so-called Frenkel line is located.[80]

In Sec. II, we briefly discuss technicalities relating to computer simulations of the EXP system. Section III shows that the EXP system obeys Eq. (1) to a good approximation by demonstrating that one of its consequences—strong virial potential-energy correlations at constant density[34,68]—applies in a large part of the thermodynamic phase diagram. Section IV gives results for how pressure, virial, and potential energy vary throughout the system's phase diagram. In Sec. V, we report simulations of the structure and dynamics along isotherms, while Sec. VI gives the same information along isochores. Even though the EXP system has no liquid-gas phase transition, its structure and dynamics look pretty much like those of other simple liquids. Section VII rationalizes this by giving a new proof of simple liquids' quasiuniversality in terms of the EXP pair-potential system. This section also presents numerical results for four state points, showing that the physics of the LJ system is fitted well by that of EXP systems with the same reduced diffusion constant. Finally, Sec. VIII provides a brief summary.

II. SIMULATIONS DETAILS

The simulations were performed on graphics cards using the RUMD open-source software.[69] All simulations were carried out using the unit system in which temperature and density are both unity; varying the state point is achieved by changing the parameters ε and σ of the EXP pair potential.

The time step $\Delta t = 0.0025$ was used in most of the phase diagram, except for state points with $T = 10^{-6}$ and $\rho > 2 \cdot 10^{-4}$ for which $\Delta t = 0.002$. Temperature was controlled by a Nose-Hoover thermostat with characteristic time 0.2. For most state points [compare Fig. 2(a)], an initial configuration of 1000 particles in a simple cubic lattice was generated with thermal velocities. An initial configuration of 2000 particles in a body-centered cubic lattice was used for state points with $1.5 \cdot 10^{-6} < T < 1.5 \cdot 10^{-3}$ and $\rho > 1.5 \cdot 10^{-3}$, compare Fig. 2(a). The system was equilibrated by 10 000 000 time steps at the desired state point—ensuring a mean-square displacement (MSD) of at least 1000 at all fluid state points. Data collection was carried out over at least 10 000 000 subsequent time steps.

A shifted-force cutoff was used to allow for a shorter cutoff distance than the standard shifted-potenial cutoff.[70,71] The cut-off was 2σ when $\rho < 1.5 \cdot 10^{-3}$ except for the lowesttemperature state points, else at 4σ, compare Fig. 2(b). RUMD uses single precision as standard. A customized version with double precision was used to validate selected simulations,
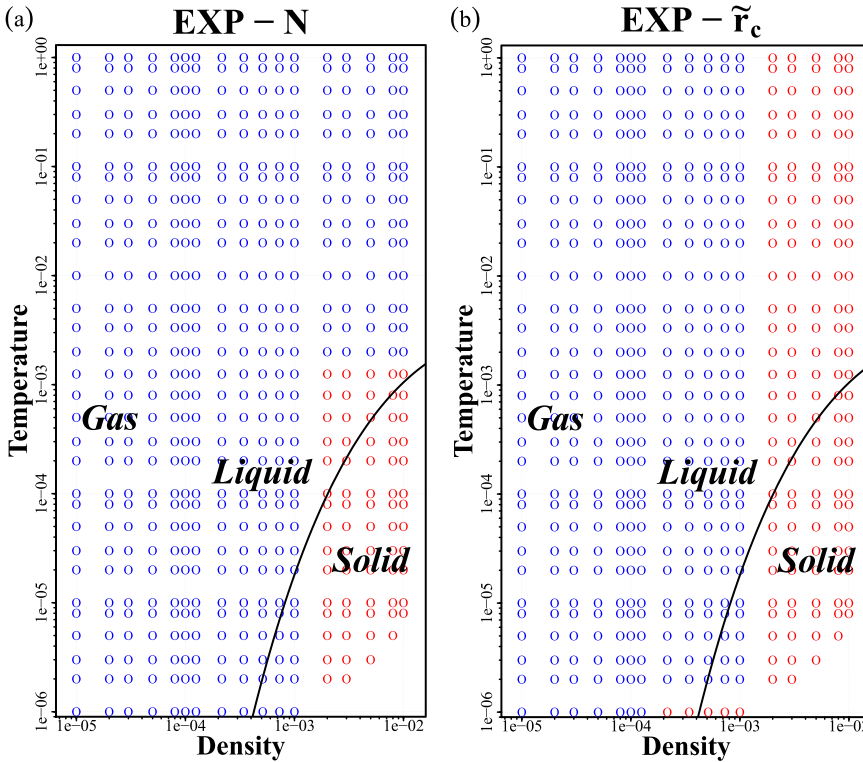
FIG. 2. (a) Number of particles N simulated at different state points where blue indicates 1000 particles and red 2000 particles. (b) Shifted-force cutoff r_c in reduced units ($\tilde{r}_c \equiv r_c \rho^{1/3}$) where blue indicates $\tilde{r}_c = 2$ and red $\tilde{r}_c = 4$.

concluding that single precision works well in the reported part of the phase diagram. Only in the low-temperature, high-density part, i.e., deep into the crystalline phase, did the use of single precision present a problem. These state points have been left out.

The focus of the present paper and Paper II[79] is on the gas and liquid phases. Results are occasionally reported also for the solid (crystalline) phase, but these may be less reliable by deriving from simulations initiated from lattices that in some cases during the simulation reorganized into different crystal structures. This led to crystals with many defects, i.e., solids that are not in proper thermodynamic equilibrium.

III. STRONG VIRIAL POTENTIAL-ENERGY CORRELATIONS

This section studies how well the EXP system's constant-density thermal-equilibrium virial fluctuations correlate with its potential-energy fluctuations. Strong correlations are a consequence of Eq. (1)[51] and have been demonstrated in NVT computer simulations of many model liquids,[32,34] including the molecular ones.[72] Recall that the microscopic virial $W(\mathbf{R})$ is defined as $W(\mathbf{R}) = \partial U(\mathbf{R})/\partial \ln \rho$ in which the density change induces a uniform scaling of $\mathbf{R}$. The virial, which is an extensive quantity of dimension energy, provides the modification of the ideal-gas law caused by particle interactions,

$$pV = Nk_BT + W \tag{6}$$

in which $W = \langle W(\mathbf{R}) \rangle$ where the sharp brackets denote a thermal average.

The microscopic virial is calculated by summing over all particles as follows: $W(\mathbf{R}) = \sum_{i<j} \mathbf{r}_{ij} \cdot \mathbf{F}_{ij}/3$, where $\mathbf{r}_{ij}$ is the vector from particle i to particle j and $\mathbf{F}_{ij}$ is the force

with which particle i acts on particle j.[8,70] Figure 3 shows results from simulations of the EXP system's equilibrium fluctuations at a liquid state point. The black stars give the potential energy and the red circles give the virial. From both quantities the mean has been subtracted, after which they were normalized to unit variance. There is a very strong correlation. The EXP pair potential has the unique property that the pair force is proportional to the pair potential energy. Thus, if interactions corresponding to a narrow range of pair distances dominate the potential energy as well as the virial, one expects strong correlations between these two quantities.

The Pearson correlation coefficient R quantifying correlations is defined by

$$R \equiv \frac{\langle \Delta U \Delta W \rangle}{\sqrt{\langle (\Delta U)^2 \rangle \langle (\Delta W)^2 \rangle}} \tag{7}$$
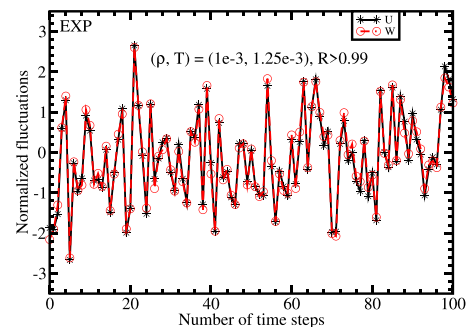
FIG. 3. Normalized equilibrium fluctuations of potential energy (black) and virial (red) at the state point $(\rho, T) = (10^{-3}, 1.25 \cdot 10^{-3})$. The correlations are strong ($R = 0.9916$), showing that the EXP pair potential system is R-simple at this state point.
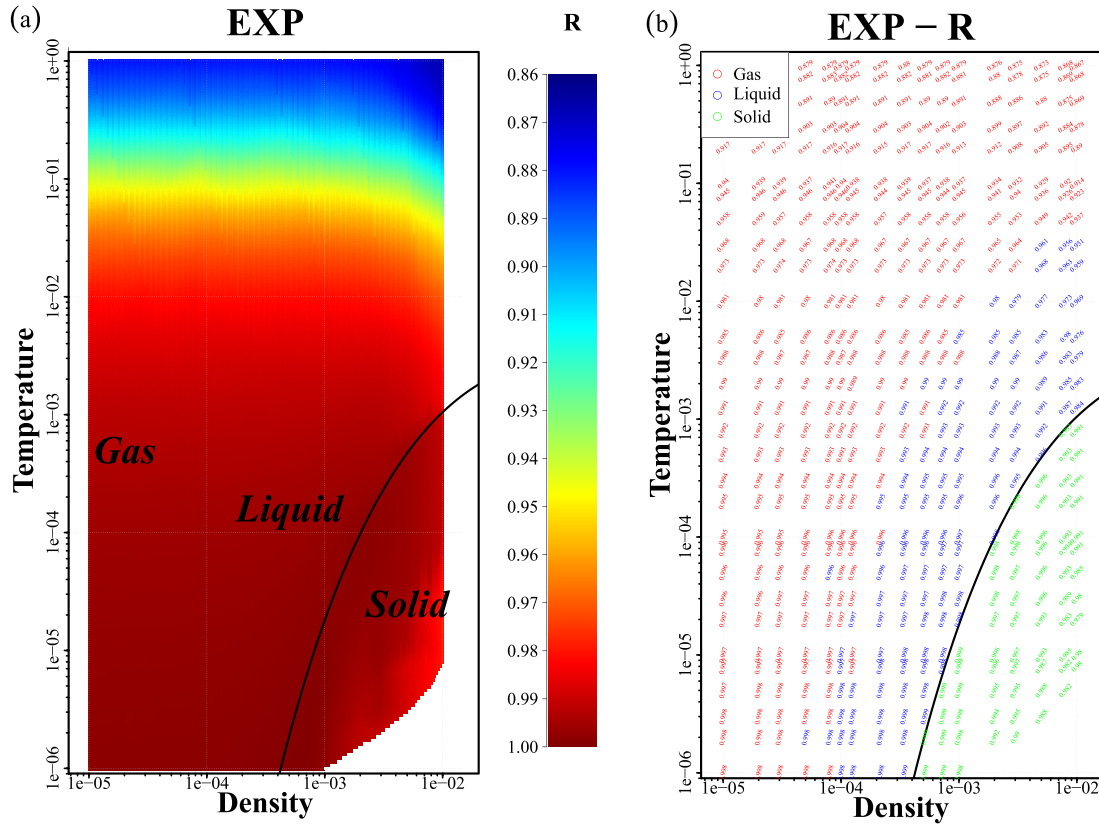
FIG. 4. (a) Phase diagram of the EXP system giving the virial potential-energy correlation coefficient R [Eq. (7)] in color coding. The EXP system is R-simple in the low-temperature part of the phase diagram. The correlation coefficient depends predominantly on the temperature, which is the prediction of the analytical theory for R in the gas phase (Appendix A). The black line covers the solid-liquid coexistence region. (b) Numerical values of R at different state points (visible upon magnification) at the densities and temperatures listed in Appendix B. At each state point, the value of R is written with a slope marking the direction of the isomorph through the state point in question (see Paper II[79]). Red indicates gas, blue liquid, and green solid phase state points.

in which Δ denotes the quantity in question minus its state-point average. A system is defined to be R-simple or strongly correlating whenever $R > 0.9$,[34] which provides a pragmatic though somewhat arbitrary criterion. The state point studied in Fig. 3 has better than 99% correlation. This is quite strong compared to, for instance, the LJ system that has $R \sim 95\%$ for liquid state points close to the triple point.

We evaluated R for the EXP system at several state points. Figure 4(a) shows the thermodynamic phase diagram colored after the value of R, while (b) gives numerical values of R throughout the phase diagram as tiny numbers written into the figure. Interestingly, R is fairly independent of the density. The virial potential-energy correlation coefficient is close to unity at low temperatures (Paper II[79] proposes that $R \to 1$ as $T \to 0$ if the limit is taken along an isomorph). Note that $R \cong 1$ applies at low temperatures for all phases, which may be interpreted as reflecting an effective inverse-power law behavior of the EXP system at low temperatures, independent of the density. In particular, it is notable that the low-temperature gas phase exhibits strong correlations, which may be contrasted to the LJ system for which this does not apply due to the attractive pair forces.[34,68]

At small densities, the EXP system is a gas in which individual pair interactions (collisions) dominate the physics. In this limit, it is possible to calculate R analytically assuming that the particle collisions are random and uncorrelated. The

derivation, which is given in Appendix A, results in

$$R = \frac{A_3}{\sqrt{A_2 A_4}} \tag{8}$$

in which (with $\beta \equiv \varepsilon/k_B T$)

$$A_n = \int_0^\infty v \, \ln^n(1/v) \, e^{-\beta v} dv. \tag{9}$$

Table I compares the theory's predictions to numerical results for R, which at each temperature have been averaged over the simulated gas-phase state points.

TABLE I. Predictions of the analytical theory for the virial potential-energy correlation coefficient R at low densities where the system is in the gas phase (Appendix A). The simulation results are averages over all gas state points at the given temperature (compare Fig. 1).

Temperature	R from theory	R from gas-phase simulations
$1.00 \cdot 10^{-1}$	0.9396	0.9348
$1.00 \cdot 10^{-2}$	0.9808	0.9807
$1.25 \cdot 10^{-3}$	0.9911	0.9912
$1.00 \cdot 10^{-4}$	0.9955	0.9955
$1.00 \cdot 10^{-5}$	0.9972	0.9972
$1.00 \cdot 10^{-6}$	0.9981	0.9981

IV. THERMODYNAMICS

A visual representation of the EXP system's equation of state (pVT relation) is provided in Fig. 5 showing how the average reduced pressure $\langle \tilde{p} \rangle \equiv \langle p \rangle/(\rho k_B T)$ and the average reduced virial per particle $\langle \tilde{W} \rangle/N$ vary throughout the phase diagram. Both quantities are colored after the value of their

logarithm. The reduced pressure is close to unity in the gas phase ($\tilde{p} = 1$ corresponds to the ideal gas equation), but it grows and becomes much larger than unity as the liquid and solid phases are approached. Comparing Figs. 5(a) and 5(b) reveals that the virial per particle in the gas phase is much lower than the pressure, whereas in the solid and liquid phases the pressure is dominated by the virial. For reference, (c)
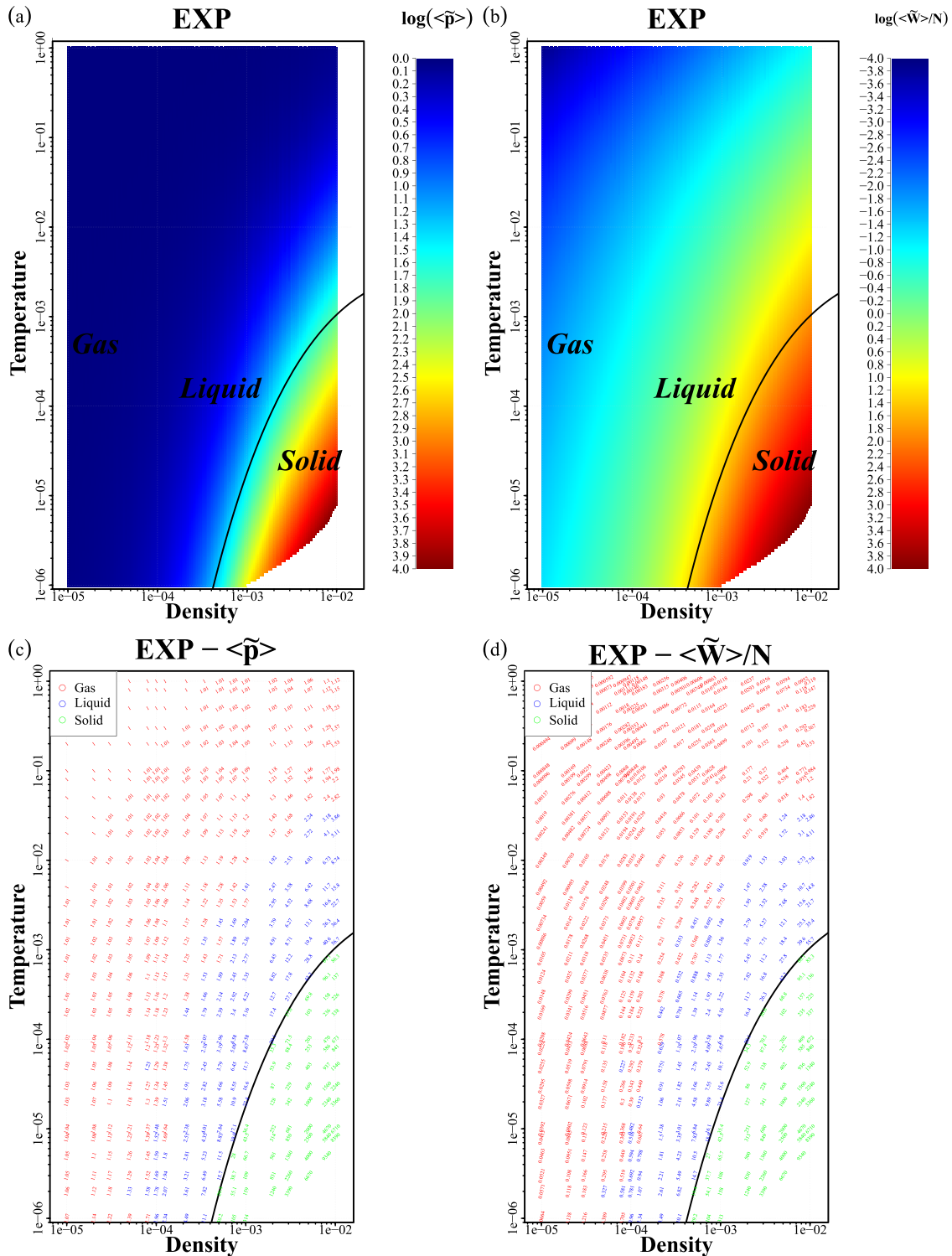
FIG. 5. (a) Variation of the logarithm of the average reduced pressure $\langle \tilde{p} \rangle$. (b) Logarithm of the average reduced virial per particle $\langle \tilde{W} \rangle/N$. (c) and (d) give the numerical values (visible upon magnification) at the densities and temperatures listed in Appendix B. The numerical values are written with a slope marking the direction of the isomorph through the state point in question; red indicates gas, blue liquid, and green solid phase state points.
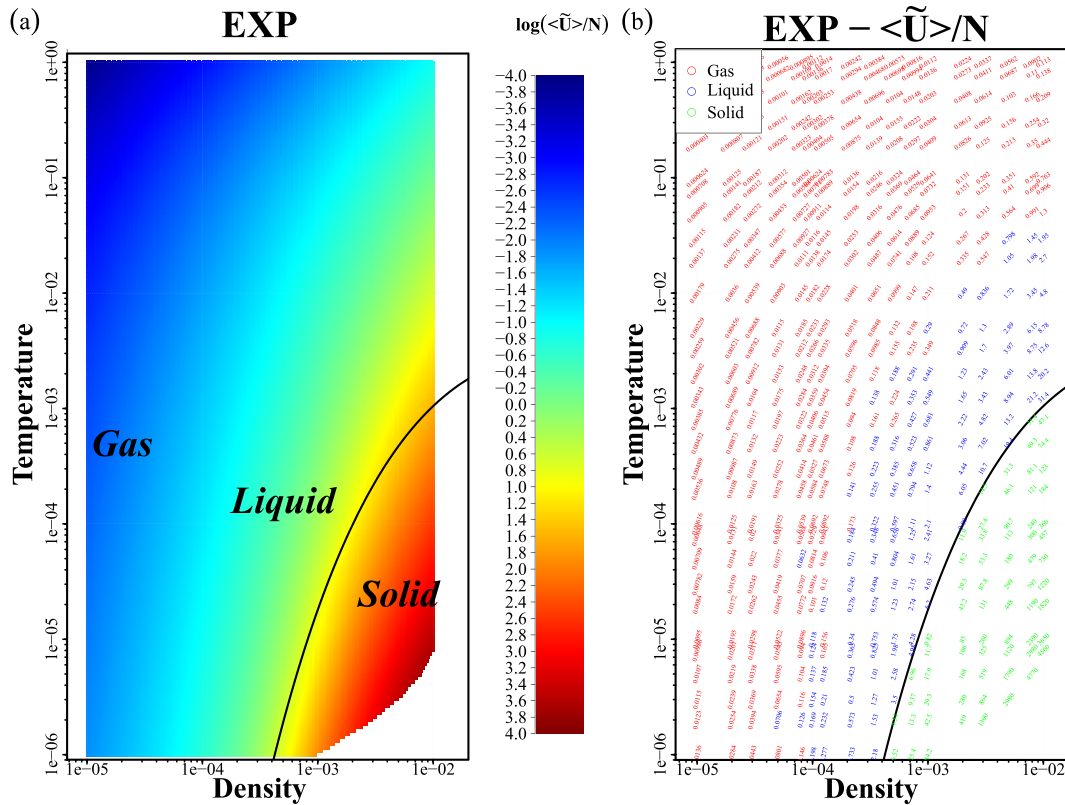
FIG. 6. (a) Variation of the logarithm of the reduced potential energy throughout the phase diagram. (b) gives the numerical values of $\bar{U}$ at different state points (visible upon magnification) at the densities and temperatures listed in Appendix B. At each state point, the numerical value is written with a slope marking the direction of the isomorph through the state point in question; red indicates gas, blue liquid, and green solid phase state points.

and (d) report the numerical values of average pressure and virial.

The variation of the reduced average potential energy per particle is shown in Fig. 6(a). The gas phase is characterized by a much lower potential energy than the kinetic energy, implying $\langle \tilde{U} \rangle / N \ll 1$. In the solid phase, the opposite behavior is seen; here the potential energy dominates.

V. STRUCTURE, DYNAMICS, AND SPECIFIC HEAT ALONG ISOTHERMS

This section investigates the EXP system's properties along selected isotherms; Sec. VI does the same along isochores. Both sections cover temperatures between 10^{-6} and 1 and densities between 10^{-5} and 10^{-2}, with a focus on the gas and liquid phases (compare Fig. 1).

Figure 7 shows how the radial distribution function (RDF) $g(r)$ develops with density at four temperatures: $T = 1$, $T = 10^{-2}$, $T = 10^{-4}$, and $T = 10^{-6}$. Recall that the RDF gives the probability to find two particles the distance r from each other relative to that of an ideal gas at the same density. When comparing $g(r)$ at different state points, it is convenient to use reduced units, $\tilde{r} \equiv \rho^{1/3} r$.

At the highest temperature $T = 1$, there is little structure; here the system is a gas at all densities investigated. At close distances, the RDF falls below unity, reflecting the interparticle repulsion. Because of the reduced units used, at low densities this happens for $\tilde{r} \ll 1$. (b) shows $T = 10^{-2}$ data; some structure

now appears at the highest densities. (c) shows the data for $T = 10^{-4}$. The range of densities studied here comprise a few solid state points, revealed as spikes in the RDFs that are present also at large distances (dashed lines). (d) gives RDFs for $T = 10^{-6}$ at which a similar pattern appears. For all four temperatures, the low-density state points have little structure because they are all in the gas phase.

Figure 8 shows the reduced mean-square displacement (MSD) $\langle \Delta r^2(t) \rangle$ as a function of time evaluated along the same four isotherms. The MSD is converted into reduced units by multiplying by $\rho^{2/3}$ while time is multiplied by $\rho^{1/3} \sqrt{k_B T/m}$, which is the inverse of the time for a free particle of kinetic energy $k_B T$ to move a typical nearest-neighbor distance. (a) gives the $T = 1$ results for the same range of densities as in Fig. 7. At short times corresponding to ballistic motion, the reduced MSD equals $3\tilde{t}^2$ since $\langle \Delta \tilde{r}^2(t) \rangle = \rho^{2/3} \langle \mathbf{v}^2 \rangle t^2 = \rho^{2/3} 3(k_B T/m) t^2 = 3\tilde{t}^2$. At long times, the MSD varies in proportion to $\tilde{t}$, which is the well-known diffusive motion. The lower density is, the later does the transition to diffusive motion take place. This is because for gas-like states, the mean free path l is much larger than the average nearest-neighbor distance[73,74] (see below). At lower temperature (b), the transition moves closer to $\tilde{t} \sim 1$ as density increases. In (c) and (d) reporting results for the two lowest temperatures, we observe at high densities a solid phase MSD (dashed lines, not equilibrated).

Figure 9(a) shows the reduced diffusion constant $\tilde{D}$ derived from long-time MSD data via $\langle \Delta r^2(t) \rangle = 6Dt$ along
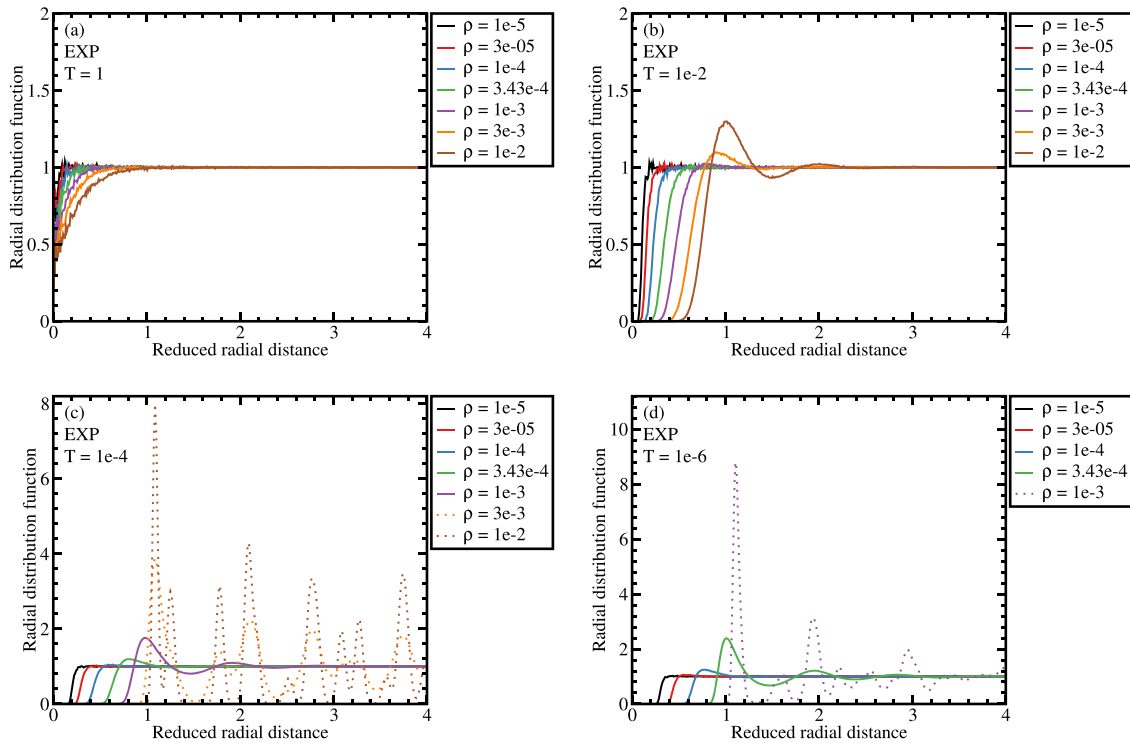
FIG. 7. Structure along isotherms probed by the radial distribution function (RDF) as a function of the reduced pair distance $\tilde{r} \equiv \rho^{1/3} r$ at the following temperatures: (a) $T = 1$, (b) $T = 10^{-2}$, (c) $T = 10^{-4}$, and (d) $T = 10^{-6}$. The RDFs of state points in the gas and liquid phases (Fig. 1) are indicated by full lines and solid-phase RDFs by dotted lines. Panel (a) corresponds to the average kinetic energy per particle comparable to the pair potential energy at zero separation. In this case, the system is gas-like over the entire density range investigated. (b) Liquid-like structure is observed at the highest densities. (c) and (d) With increasing density, the system transforms from gas to liquid to solid behavior.
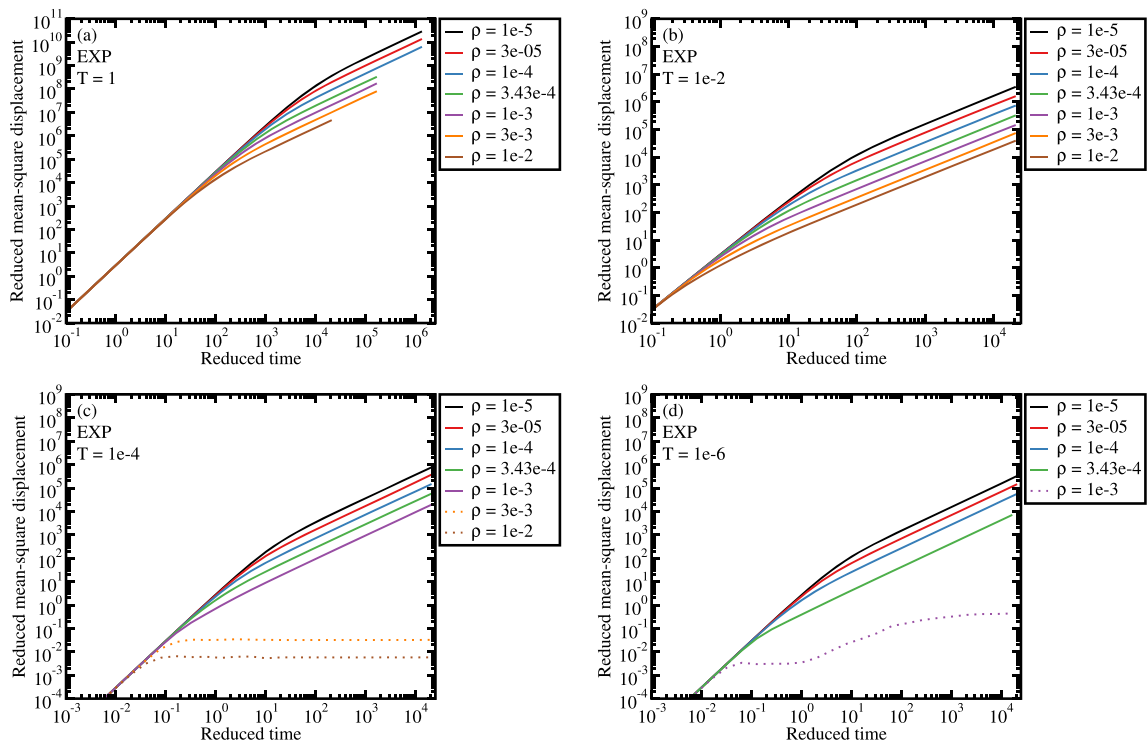
FIG. 8. Reduced-unit mean-square displacement (MSD) for selected state points along the four isotherms $T = 1$, $T = 10^{-2}$, $T = 10^{-4}$, and $T = 10^{-6}$. Gas and liquid phase state points are indicated by full lines and solid state points by dotted lines. At short times, the MSD in all cases follows the ballistic prediction $3\tilde{t}^2$ (see the text), and at long times it follows the diffusion equation prediction $\propto \tilde{t}$. Not surprisingly, the solid phase does not reach the long-time diffusive limit.
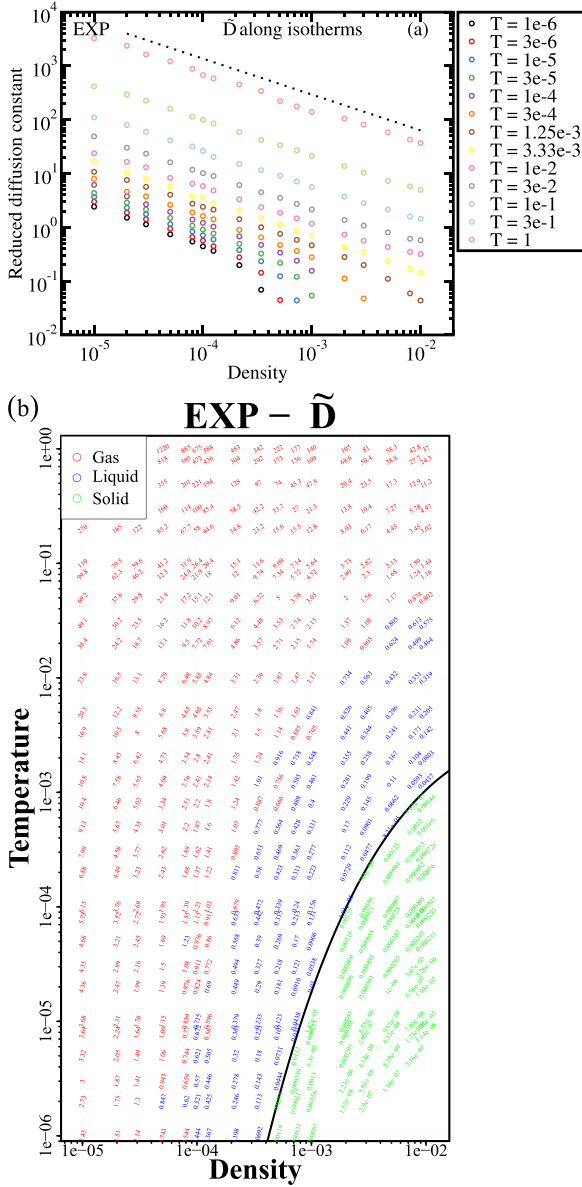
FIG. 9. Reduced diffusion constants determined from the long-time limit of the MSD. (a) shows results for isotherms as a function of the density. At all temperatures, the reduced diffusion constant decreases as density increases; at high temperatures one finds $\tilde{D} \propto \rho^{-2/3}$ as predicted by kinetic theory [Eq. (10), slope indicated by the dashed line]. (b) gives the numerical values of the reduced diffusion constants (visible upon magnification) at the same state points as those of Fig. 4 (Appendix B). Red are gas, blue liquid, and green solid phase state points. At each state point, the value of the reduced diffusion coefficient is written with a slope marking the direction of the isomorph through the state point in question.

several isotherms in the gas and liquid phases. At fixed temperature, $\tilde{D}$ decreases when density increases; as the gas phase transforms smoothly into the liquid phase, the mean-free path is reduced and approaches the average interparticle distance. More accurately, as we now proceed to show, in the gas phase $\tilde{D} \propto \rho^{-2/3}$ at fixed temperature [dashed line in Fig. 9(a)].

According to kinetic theory,[73,74] the diffusion constant in the gas phase is proportional to lv in which l is the mean free path and v the thermal velocity. Since v is basically l_0/t_0, compare Eqs. (2) and (4), this implies
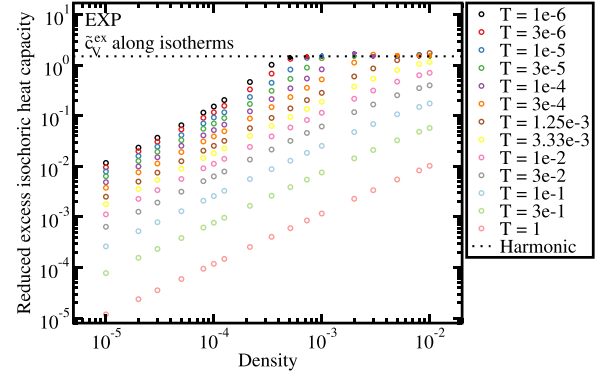
FIG. 10. Reduced isochoric excess heat capacity per particle along isotherms. Gas and liquid state points are given as open symbols; stars represent crystal state points. The dashed line is the prediction for a harmonic crystal, $\tilde{c}_V^{ex} = 3/2$.

$\tilde{D} \equiv D/(l_0^2/t_0) \propto l/l_0 = l\rho^{1/3}$. Gas-phase kinetic theory moreover predicts that l is given by $\rho l r_0^2 \sim 1$ where r_0 is the effective hard-sphere radius that may be estimated from $v_{EXP}(-r_0) = k_B T$, implying $r_0 = \ln(1/T) = -\ln T$ in the EXP unit system. Thus one expects the reduced diffusion constant in the gas phase to be given by $\tilde{D} \propto l\rho^{1/3} \propto \rho^{-2/3}/r_0^2 = \rho^{-2/3}/\ln^2(T)$. The Enskog kinetic theory determines the constant of proportionality,[73,74] resulting in

$$\tilde{D} = \frac{3}{8\sqrt{\pi}} \frac{\rho^{-2/3}}{\ln^2(T)} = 0.212 \frac{\rho^{-2/3}}{\ln^2(T)}. \quad (10)$$

This expression is validated below in Fig. 13. The hard-sphere approximation is expected to work best at low densities and low temperatures, which is consistent with the findings of Fig. 9(a).

Figure 10 gives the reduced excess isochoric specific heat per particle $\tilde{c}_V^{ex}$, i.e., c_V/k_B subtracted the 3/2 ideal-gas per-particle contribution. This quantity is calculated from the system's potential-energy fluctuations in NVT simulations via the canonical-ensemble expression $\tilde{c}_V^{ex} = \langle(\Delta U)^2\rangle/k_B T^2 N$.[29,70] The lowest temperatures have the largest $\tilde{c}_V^{ex}$, reflecting stronger interactions than at higher temperatures, which are more gas like. There is a transition to a virtually constant $\tilde{c}_V^{ex} \cong 3/2$ at high densities at which the system is in the crystalline state.

VI. STRUCTURE, DYNAMICS, AND SPECIFIC HEAT ALONG ISOCHORES

Next we study how the above quantities vary along the lines of constant volume, reporting results for the densities 10^{-5}, 10^{-4}, 10^{-3}, and 10^{-2}.

Figure 11 shows the reduced RDFs along these four isochores. At the lowest density (a), there is little structure. Here the system is a gas at all temperatures, compare Fig. 1. As density is increased, structure begins to appear at the lowest temperatures, and for the two highest densities, we recognize the crystalline phase (dashed lines).

Figure 12 shows the reduced MSD along the same isochores. At high temperatures, the system is a dilute gas and the transition to diffusive behavior takes place much above $\tilde{t} \sim 1$; compare Fig. 8.
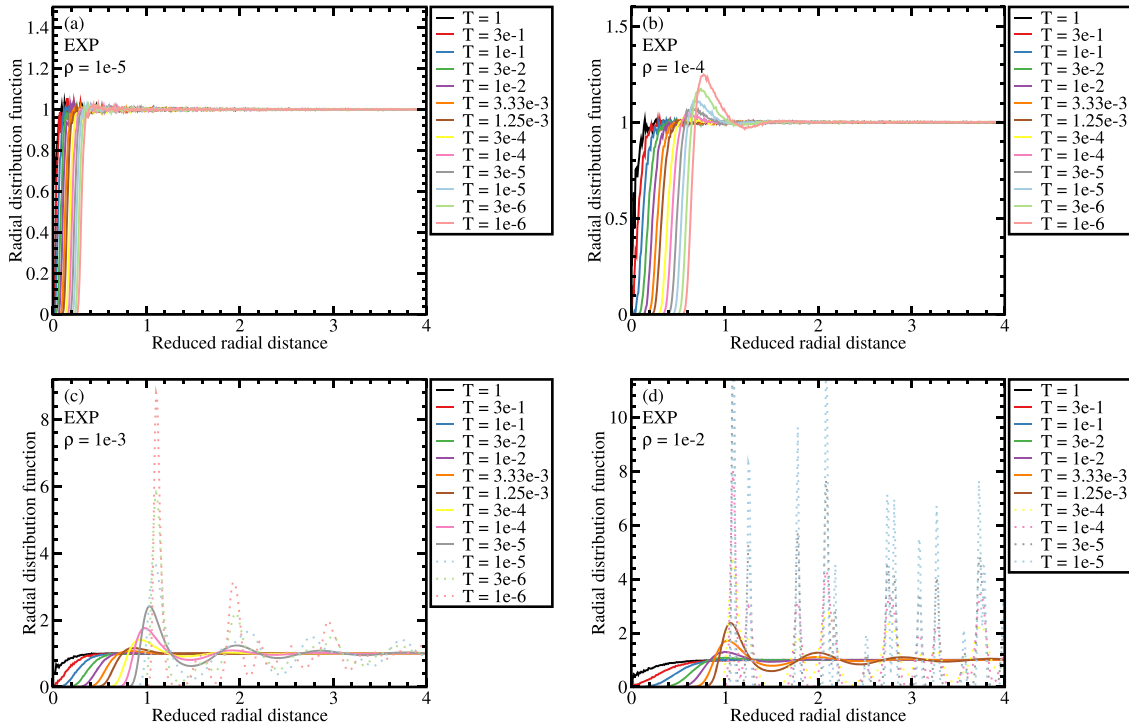
FIG. 11. Radial distribution functions along the following isochores: (a) $\rho = 10^{-5}$, (b) $\rho = 10^{-4}$, (c) $\rho = 10^{-3}$, (d) $\rho = 10^{-2}$. State points in the gas and liquid phases (compare Fig. 1) are indicated by full lines, solid-phase state points by dotted lines. At the lowest densities little structure is present and the system is a gas even at the lowest temperatures studied. At higher densities liquid-like structure appears at the lowest temperatures, and for $\rho = 10^{-3}$ and $\rho = 10^{-2}$ crystal structure is observed at the lowest temperatures.

Figure 13(a) shows how the reduced diffusion constant varies with temperature along the seven isochores. For a given temperature, the reduced diffusion constant is largest at low densities. The increase with temperature reflects the effective particle size decreasing; compare kinetic theory (Sec. V). The Enskog prediction Eq. (10) for $\rho = 10^{-4}$ is shown as the dashed line in Fig. 13(a). Figure 13(b) plots $\rho^{2/3}\tilde{D}$ versus $1/\ln^2(T)$ in order to test Eq. (10), which is expected to apply
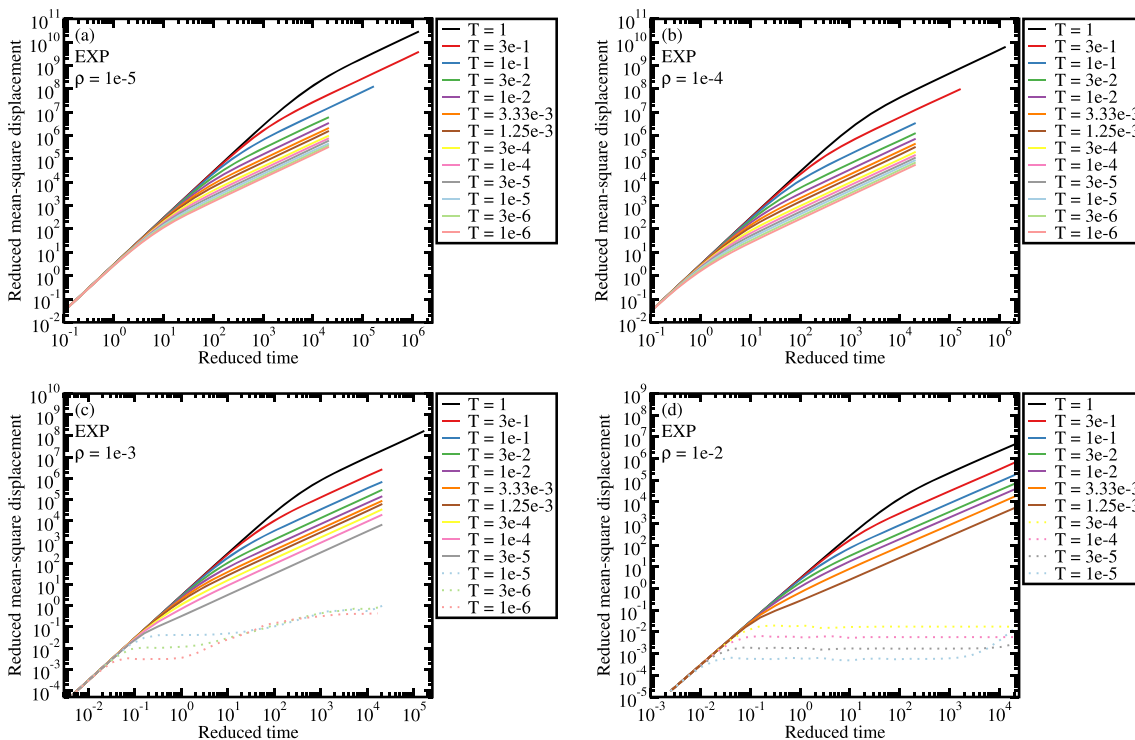
FIG. 12. Reduced MSD along four isochores: (a) $\rho = 10^{-5}$, (b) $\rho = 10^{-4}$, (c) $\rho = 10^{-3}$, and (d) $\rho = 10^{-2}$. Gas and liquid phase state points are indicated by full lines and solid-phase state points by dotted lines.
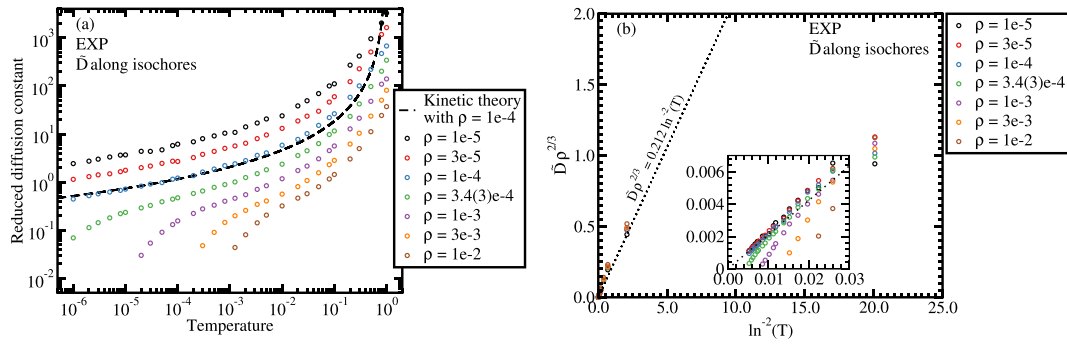
FIG. 13. (a) Gas and liquid phase reduced diffusion constants along seven isochores. The dashed line is the Enskog kinetic-theory prediction for $\rho = 10^{-4}$, Eq. (10). The inflection at low temperatures and high densities is where the condensed liquid phase is approached, signaling strong deviations from the gas-phase prediction. Panel (b) investigates Eq. (10) more closely by plotting $\rho^{2/3}\tilde{D}$ versus $1/\ln^2(T)$. The dotted line is the Enskog prediction, which works well at low densities. The inset focuses on the data close to the origin.

asymptotically as the density goes to zero. This is the case to a good approximation.

Finally, Fig. 14 shows how the excess isochoric heat capacity $\tilde{c}_V^{\text{ex}}$ varies with temperature along seven isochores. At low temperatures and high densities, the reduced heat capacity is high and constant, close to the 3/2 per particle harmonic contribution expected in the solid phase. For other state points, the excess heat capacity is considerably lower.

VII. QUASIUNIVERSALITY

As mentioned in Sec. I, the EXP pair potential is central in a recent proof of simple liquids' quasiuniversality,[44] a review of which is given in Ref. 31. The idea is that—to a good approximation—any pair-potential system for which $v(r)$ is a sum of exponential functions corresponding to the strongly correlating part of the phase diagram (Fig. 4), i.e., with coefficients that are much larger than $k_B T$, has the same structure and dynamics as the EXP system itself. This section presents a constant-potential-energy (NVU)-based proof of quasiuniversality, combining arguments from Refs. 51 and 75. After this, as an example it is shown how the LJ system's structure at four state points may be approximated by those of EXP pair-potential systems with the same reduced diffusion constant.
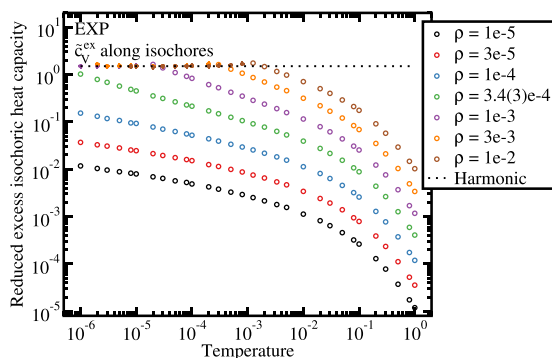
FIG. 14. Reduced isochoric excess heat capacity per particle $\tilde{c}_V^{\text{ex}}$ along seven isochores. Gas and liquid phase state points are represented by open symbols and stars correspond to solid-phase state points. The dashed line is the prediction of a harmonic crystal ($\tilde{c}_V^{\text{ex}} = 3/2$).

A. *NVU* proof of simple liquids' quasiuniversality

NVU dynamics is molecular dynamics based on conservation of the potential energy.[76–78] The idea is the following. The 3N-dimensional configuration space of the particle coordinates **R**—usually implemented assuming periodic boundary conditions, i.e., on a high-dimensional torus—has (3N-1)-dimensional hypersurfaces of constant potential energy. *NVU* dynamics is defined as motion at constant velocity on these hypersurfaces along geodesic curves, i.e., curves of minimum length (locally). A geodesic curve is a generalized straight line, so *NVU* dynamics may be regarded as realizing Newton's first law in the curved high-dimensional space defined by the relevant constant-potential-energy hypersurface. Geodesic dynamics also appears in the general theory of relativity, but there just in four dimensions. Despite the fact that the potential and kinetic energies are both conserved in *NVU* dynamics, it has been shown analytically as well as numerically that *NVU* dynamics in the thermodynamic limit leads to the same structure and dynamics as ordinary Newtonian *NVE* or *NVT* dynamics.[76,77]

Quasiuniversality of systems with a pair-potential function that is a sum of EXP pair potentials from the strongly correlating part of the EXP phase diagram (Fig. 4) is based on the following fact: For different pair-potential parameters ε and σ, the EXP system's family of reduced-unit constant-potential-energy hypersurfaces are identical. We show this below, followed by a proof that systems with a pair potential that is a linear combination of two or more EXP terms have the same constant-potential-energy hypersurfaces as the EXP system itself and, consequently, have the same *NVU* trajectories. This implies identical reduced-unit structure and dynamics.

For any system at density ρ, one defines the microscopic excess-entropy function by $S_{\text{ex}}(\mathbf{R}) \equiv S_{\text{ex}}(\rho, U)|_{U=U(\mathbf{R})}$ in which $S_{\text{ex}}(\rho, U)$ is the thermodynamic excess entropy as a function of density and average potential energy.[51] In other words, $S_{\text{ex}}(\mathbf{R})$ is the thermodynamic excess entropy of the state point with density ρ corresponding to **R** and average potential energy $U(\mathbf{R})$. By inversion, one has $U(\mathbf{R}) = U(\rho, S_{\text{ex}}(\mathbf{R}))$ in which $U(\rho, S_{\text{ex}})$ is the average potential energy at the state point with density ρ and excess entropy S_{ex}. From the configuration-space microcanonical ensemble

expression for the excess entropy, it is straightforward to show that the hidden-scale-invariance condition Eq. (1) implies $S_{ex}(\lambda\mathbf{R}) = S_{ex}(\mathbf{R})$, i.e., a uniform scaling of a configuration does not change its excess entropy.[51] This scale invariance means that the microscopic excess entropy is a function of the configuration's reduced coordinate vector $\tilde{\mathbf{R}} \equiv \rho^{1/3}\mathbf{R}$,[51] implying that

$$U(\mathbf{R}) = U(\rho, S_{ex}(\tilde{\mathbf{R}})). \qquad (11)$$

Having in mind that the EXP system's potential-energy function $U_{EXP}(\mathbf{R})$ depends on ε and σ, Eq. (11) implies that a dimensionless function Φ_{EXP} of two variables exists such that ($\tilde{S}_{ex} \equiv S_{ex}/k_B$)

$$U_{EXP}(\mathbf{R}, \varepsilon, \sigma) = \varepsilon\, \Phi_{EXP}\left(\rho\sigma^3, \tilde{S}_{ex}^{EXP}(\tilde{\mathbf{R}})\right). \qquad (12)$$

The appearances of ε in front and of σ^3 multiplied by the density are dictated by dimensional analysis. A consequence of Eq. (12) is that different EXP systems have the same family of reduced-coordinate constant-potential-energy hypersurfaces, all of which are given by $\tilde{S}_{ex}^{EXP}(\tilde{\mathbf{R}}) = \text{Const}$. The constant defines the relevant isomorph.

Consider now the system defined by the pair potential $v(r) = \varepsilon_1 \exp(-r/\sigma_1) + \varepsilon_2 \exp(-r/\sigma_2)$ and let us focus on one particular configuration $\mathbf{R}$. Since it defines all pair distances, this system's potential-energy function is given by adding the

two EXP system's potential energies,

$$U(\mathbf{R}) = \varepsilon_1\, \Phi_{EXP}\left(\rho\sigma_1^3, \tilde{S}_{ex}^{EXP}(\tilde{\mathbf{R}})\right)$$
$$+ \varepsilon_2\, \Phi_{EXP}\left(\rho\sigma_2^3, \tilde{S}_{ex}^{EXP}(\tilde{\mathbf{R}})\right). \qquad (13)$$

Assuming positive temperature, i.e., that

$$\varepsilon_1(\partial\Phi_{EXP}(\rho\sigma_1^3, S_{ex})/\partial S_{ex})_\rho$$
$$+ \varepsilon_2(\partial\Phi_{EXP}(\rho\sigma_2^3, S_{ex})/\partial S_{ex})_\rho > 0, \qquad (14)$$

the potential energy $U(\mathbf{R})$ of Eq. (13) can be constant only if $\tilde{S}_{ex}^{EXP}(\tilde{\mathbf{R}})$ is constant. Via Eq. (12), this implies that $U_{EXP}(\mathbf{R}, \varepsilon, \sigma)$ is constant. Thus the constant-potential-energy hypersurfaces for the function $U(\mathbf{R})$ of Eq. (13) are identical to the EXP system's constant-potential-energy hypersurfaces. The *NVU* dynamics of the sum of two EXP systems is consequently identical to that of the EXP system, implying identical structure and dynamics.

The above generalizes to pair-potential systems of arbitrary linear combinations of EXP terms, and EXP pair-potential terms may also be subtracted. Basically, the only requirement is that each EXP pair-potential term refers to the strongly correlating part of the EXP system's phase diagram, i.e., that the energy parameter obeys $\varepsilon \gg k_B T$.[31] This requirement, which ensures that Eq. (12) applies for each term, translates into requiring that the reduced-unit pair potential
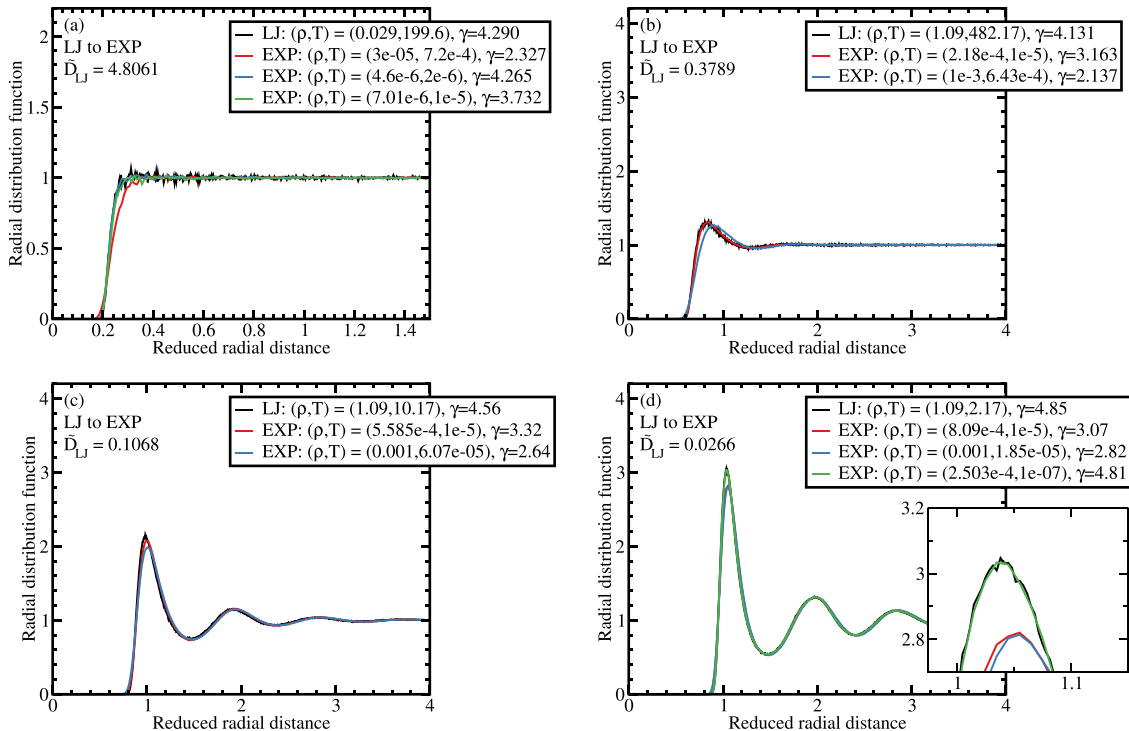
FIG. 15. Quasiuniversality illustrated by comparing radial distribution functions (RDF) at four state points for the Lennard-Jones (LJ) system (black curves) to those of EXP systems with the same reduced diffusion constant within 1% (colored curves). EXP state points are specified by density, temperature, and density-scaling exponent γ. (a) LJ state point $(\rho, T) = (0.029, 199.6)$, a typical high-temperature gas state point at which $\tilde{D} = 4.8061$. γ here is 4.29, which is not far from the value 4 predicted from the repulsive r^{-12} term of the LJ pair potential.[68] The red, blue, and green curves are RDF predictions for different EXP systems with the same reduced diffusion constant. (b) LJ state point $(\rho, T) = (1.09, 482.17)$, a moderate-density, high-temperature gas state point at which $\tilde{D} = 0.3789$. The red EXP system fits better than the blue one. Deviations are centered around the first peak, with the largest deviations for the EXP state point with density-scaling exponent γ most different from its LJ value (blue). (c) LJ state point $(\rho, T) = (1.09, 10.17)$ at which $\tilde{D} = 0.1068$. There are slight deviations around the first peak, which are smallest for the EXP system with γ closest to that of the LJ system. (d) LJ state point $(\rho, T) = (1.09, 2.17)$, a condensed-phase liquid state point close to the melting line at which $\tilde{D} = 0.0266$. The green curve, which fits best, represents an EXP system that has virtually the same γ as the LJ system. The inset provides a blow up of the first peak.

in question is a sum of EXP terms with numerically large prefactors.[31]

B. Example: The EXP system approximates the Lennard-Jones system

The LJ system ($v(r) = 4\varepsilon[(r/\sigma)^{-12} - (r/\sigma)^{-6}]$) is in the EXP quasiuniversality class.[8,44] As a demonstration of quasiuniversality, we consider four state points of the LJ system typical for the high-temperature gas, the high-temperature liquid, and the liquid close to the melting line. At each state point, the reduced diffusion constant $\tilde{D}$ was evaluated. According to quasiuniversality, $\tilde{D}$ determines the reduced structure. For each of the four reduced LJ diffusion constants, we identified two or three EXP systems (equivalently: EXP state points) with the same $\tilde{D}$ and calculated the RDF in order to compare to those of the LJ system.

The results are shown in Fig. 15, which gives LJ system RDFs as black curves and those of EXP systems with same reduced diffusion constant as colored curves. The fits are generally good. Deviations are center around the first peak. These reflect the following breakdown of quasiuniversality: At small interparticle separation the RDF is dominated by the pair potential via the asymptotic behavior $g(r) \sim \exp(-v(r)/k_BT)$ for $r \to 0$.[8] The quantity $v(r)/k_BT$ is not isomorph invariant, however, implying that the way in which $g(r)$ approaches zero at short distances violates quasiuniversality. If one assumes that the number of particles in the first coordination shell *is* quasiuniversal, there must be a compensating non-quasiuniversal height of the first peak of the RDF. For the EXP system, the larger the density-scaling exponent becomes along an isomorph (see Paper II[79]), the higher is the peak because the more rapidly does $g(r)$ go to zero at short distances. This explains the slight deviations from quasiuniversality observed in Fig. 15. If one wishes from the reduced diffusion constant to identify an EXP system with almost identical RDF also around the first peak, an EXP system should be sought with both the correct reduced diffusion constant and the correct density-scaling exponent. This is illustrated in Fig. 15(d), compare the inset.

VIII. CONCLUDING REMARKS

We have presented an investigation of the EXP pair-potential system's structure and dynamics over a large part of its low-temperature, low-density thermodynamic phase diagram, focusing on gas and liquid state points. At temperatures higher than those studied here the EXP system changes character because particles there may overlap and pass through one another. As for other systems with no attractive forces, the EXP system has a solid and a fluid phase, but no liquid-gas phase transition. We find gas-like behavior in a large part of the studied phase diagram as revealed by a virtual absence of structure probed by the RDF. When varying density or temperature, we find, not surprisingly, that the EXP fluid has more structure the closer it is to the melting transition. For both the structure and the dynamics, one finds the same trends whether density or temperature is lowered. This reflects the existence of isomorphs, which are lines in the thermodynamic phase

diagram along which the reduced-unit physics is invariant[29,51] (Paper II[79]).

The motivation for studying the EXP pair-potential system is the recent suggestion that the EXP potential may be regarded as "the mother of all pair potentials" in the sense that any pair potential of an R-simple single-component pair-potential system may be well approximated by a sum of EXP pair potentials with coefficients that in reduced units are numerically much larger than unity.[31,44] Because the EXP system is R-simple, isomorph theory implies that any such linear combination has virtually the same structure and dynamics as the pristine EXP system;[31] compare Sec. VII. This is our explanation of the quasiuniversality reported for the majority of simple liquids, which is traditionally explained by reference to the hard-sphere system.

The present paper focused on the gas and liquid phases. This is also the focus of Paper II studying the EXP system's isomorphs.[79]

APPENDIX A: ANALYTICAL THEORY FOR THE VIRIAL POTENTIAL-ENERGY CORRELATION COEFFICIENT IN THE GAS PHASE

For mathematical simplicity, we use below the EXP unit system in which $\varepsilon = \sigma = 1$; moreover we put $k_B = 1$. The EXP pair potential is given by

$$v(r) = e^{-r}. \tag{A1}$$

The inverse temperature is denoted by β, i.e., $\beta \equiv 1/T$.

When the density is sufficiently low, the individual pair energies and forces are statistically independent and one can calculate the averages in R [Eq. (7)] by reference to single particle pairs. This is the same simplification that was recently used to prove that the isomorph theory is exact in infinite dimensions for all pair-potential systems with strong repulsions.[81] For a pair at distance r, the virial is given by $w = (-1/3)rv'(r)$, i.e.,

$$w = \frac{1}{3}\ln(1/v)v. \tag{A2}$$

In terms of v and w, Eq. (7) becomes

$$R = \frac{\langle vw \rangle - \langle v \rangle \langle w \rangle}{\sqrt{(\langle v^2 \rangle - \langle v \rangle^2)(\langle w^2 \rangle - \langle w \rangle^2)}}. \tag{A3}$$

The gas-phase physics is determined by the two-particle Boltzmann canonical probability, $p(r) \propto r^2 \exp(-\beta v(r))$. The pair-potential energy $v = \exp(-r)$ varies between zero and one, but when the temperature is low, little error arises from allowing v to be any positive number. The probability of finding the pair potential energy v is given by $p(v) = p(r)|dr/dv|$. Since $r = \ln(1/v)$, one has $p(v) \propto \ln^2(1/v) \exp(-\beta v)|dr/dv|$ or

$$p(v) \propto \frac{\ln^2(1/v)\exp(-\beta v)}{v} \quad (0 < v < \infty). \quad \text{(A4)}$$

This distribution is not normalizable in the $v \to 0$ limit, reflecting the infinitely many particle pairs found far from each other. Introducing a lower v cut-off, the normalization constant thus diverges as the cutoff goes to zero. This means that in expressions like $\langle \Delta v \Delta w \rangle = \langle vw \rangle - \langle v \rangle \langle w \rangle$ the latter product disappears as the v cutoff goes to zero, so Eq. (A3) simplifies into

$$R = \frac{\langle vw \rangle}{\sqrt{\langle v^2 \rangle \langle w^2 \rangle}}. \quad \text{(A5)}$$

If one defines

$$A_n = \int_0^\infty v\,\ln^n(1/v)\,e^{-\beta v} dv \quad \text{(A6)}$$

and K is the normalization constant of $p(v)$ with a cutoff, one has $\langle v^2 \rangle = KA_2$, $\langle vw \rangle = KA_3/3$, and $\langle w^2 \rangle = KA_4/9$, but K does not enter into the final expression,

$$R = \frac{A_3}{\sqrt{A_2 A_4}}. \quad \text{(A7)}$$

Using Maple, one gets

$$A_2 = \beta^{-2}\Big(\ln^2 \beta - 2(1-C)\ln \beta + (\pi^2/6 + C^2 - 2C)\Big), \quad \text{(A8)}$$

$$A_3 = \beta^{-2}\big(\ln^3 \beta - 3(1-C)\ln^2 \beta \\ + (\pi^2/2 + 3C^2 - 6C)\ln \beta + k_3 \big), \quad \text{(A9)}$$

and

$$A_4 = \beta^{-2}\Big(\ln^4 \beta - 4(1-C)\ln^3 \beta + (\pi^2 + 6C^2 - 12C)\ln^2 \beta \\ + h_4 \ln \beta + k_4 \Big). \quad \text{(A10)}$$

Here

$$C \equiv \lim_{n \to \infty}\left(\sum_{p=1}^n \frac{1}{p} - \ln n \right) = 0.577\,216\ldots \quad \text{(A11)}$$

is Euler's constant (in his original notation, this number is sometimes denoted by γ),

$$k_3 = C^3 - 3C^2 + (\pi^2/2)C - \pi^2/2 + 2\zeta(3) = -0.489\,46 \quad \text{(A12)}$$

in which $\zeta(3) = 1.202\,06$ is the Riemann zeta function's value at 3 ("Apery's constant"),

$$h_4 = 2\big(2C^3 - 6C^2 + \pi^2 C - \pi^2 + 4\zeta(3)\big) = 4k_3 = -1.9578, \quad \text{(A13)}$$

and

$$k_4 = C^4 - 4C^3 + \pi^2 C^2 - 2\pi^2 C + 8\zeta(3)C - 8\zeta(3) + 3\pi^4/20 \\ = 1.7820. \quad \text{(A14)}$$

Numerically, the three integrals are given by

$$\beta^2 A_2 = \ln^2 \beta - 0.8456 \ln \beta + 0.8237, \quad \text{(A15)}$$

$$\beta^2 A_3 = \ln^3 \beta - 1.268 \ln^2 \beta + 2.471 \ln \beta - 0.4895, \quad \text{(A16)}$$

and

$$\beta^2 A_4 = \ln^4 \beta - 1.691 \ln^3 \beta + 4.942 \ln^2 \beta \\ - 1.958 \ln \beta + 1.782. \quad \text{(A17)}$$

APPENDIX B: SIMULATED STATE POINTS

The state points simulated involve the following densities $1.00 \cdot 10^{-5}$; $2.00 \cdot 10^{-5}$; $3.00 \cdot 10^{-5}$; $5.00 \cdot 10^{-5}$; $8.00 \cdot 10^{-5}$; $1.00 \cdot 10^{-4}$; $1.25 \cdot 10^{-4}$; $2.16 \cdot 10^{-4}$; $3.43 \cdot 10^{-4}$; $5.12 \cdot 10^{-4}$; $7.29 \cdot 10^{-4}$; $1.00 \cdot 10^{-3}$; $2.00 \cdot 10^{-3}$; $3.00 \cdot 10^{-3}$; $5.00 \cdot 10^{-3}$; $8.00 \cdot 10^{-3}$; $1.00 \cdot 10^{-2}$ and the following temperatures: $1.00 \cdot 10^{-6}$; $2.00 \cdot 10^{-6}$; $3.00 \cdot 10^{-6}$; $5.00 \cdot 10^{-6}$; $8.00 \cdot 10^{-6}$; $1.00 \cdot 10^{-5}$; $2.00 \cdot 10^{-5}$; $3.00 \cdot 10^{-5}$; $5.00 \cdot 10^{-5}$; $8.00 \cdot 10^{-5}$; $1.00 \cdot 10^{-4}$; $2.00 \cdot 10^{-4}$; $3.00 \cdot 10^{-4}$; $5.00 \cdot 10^{-4}$; $8.00 \cdot 10^{-4}$; $1.25 \cdot 10^{-3}$; $2.00 \cdot 10^{-3}$; $3.33 \cdot 10^{-3}$; $5.00 \cdot 10^{-3}$; $1.00 \cdot 10^{-2}$; $2.00 \cdot 10^{-2}$; $3.00 \cdot 10^{-2}$; $5.00 \cdot 10^{-2}$; $8.00 \cdot 10^{-2}$; $1.00 \cdot 10^{-1}$; $2.00 \cdot 10^{-1}$; $3.00 \cdot 10^{-1}$; $5.00 \cdot 10^{-1}$; $8.00 \cdot 10^{-1}$; 1.

[1] I. Z. Fisher, *Statistical Theory of Liquids* (University of Chicago, Chicago, 1964).

[2] S. A. Rice and P. Gray, *The Statistical Mechanics of Simple Liquids* (Interscience, New York, 1965).

[3] H. N. V. Temperley, J. S. Rowlinson, and G. S. Rushbrooke, *Physics of Simple Liquids* (Wiley, New York, 1968).

[4] S. M. Stishov, "The thermodynamics of melting of simple substances," Sov. Phys. Usp. **17**, 625–643 (1975).

[5] M. Baus and J.-P. Hansen, "Statistical mechanics of simple Coulomb systems," Phys. Rep. **59**, 1 (1980).

[6] J.-L. Barrat and J.-P. Hansen, *Basic Concepts for Simple and Complex Liquids* (Cambridge University Press, 2003).

[7] T. S. Ingebrigtsen, T. B. Schrøder, and J. C. Dyre, "What is a simple liquid?," Phys. Rev. X **2**, 011011 (2012).

[8] J.-P. Hansen and I. R. McDonald, *Theory of Simple Liquids: With Applications to Soft Matter*, 4th ed. (Academic, New York, 2013).

[9] J. O. Hirschfelder, C. F. Curtiss, and R. B. Bird, *Molecular Theory of Gases and Liquids* (John Wiley & Sons, New York, 1954).

[10] J. D. Bernal, "The Bakerian lecture, 1962. The structure of liquids," Proc. R. Soc. London, Ser. A **280**, 299–322 (1964).

[11] B. Widom, "Intermolecular forces and the nature of the liquid state," Science **157**, 375–382 (1967).

[12] J. S. Rowlinson, "Legacy of van der Waals," Nature **244**, 414–417 (1973).

[13] J. A. Barker and D. Henderson, "What is 'liquid'? Understanding the states of matter," Rev. Mod. Phys. **48**, 587–671 (1976).

[14] D. Chandler, J. D. Weeks, and H. C. Andersen, "van der Waals picture of liquids, solids, and phase transformations," Science **220**, 787–794 (1983).

[15] J. D. van der Waals, *Over de Continuiteit van den Gas- en Vloeistoftoestand* (Dissertation, University of Leiden, 1873).

[16] J. D. Weeks, D. Chandler, and H. C. Andersen, "Role of repulsive forces in determining the equilibrium structure of simple liquids," J. Chem. Phys. **54**, 5237–5247 (1971).

[17] Y. Rosenfeld, "Variational soft-sphere perturbation theory and conditions for a Gruneisen equation of state for dense fluids," Phys. Rev. A **28**, 3063–3069 (1983).

[18] H. S. Kang, S. C. Lee, T. Ree, and F. H. Ree, "A perturbation theory of classical equilibrium fluids," J. Chem. Phys. **82**, 414–423 (1985).

[19] K. K. Mon, "Hard sphere perturbation theory for thermodynamics of soft-sphere model liquid," J. Chem. Phys. **115**, 4766–4769 (2001).

[20] D. Ben-Amotz and G. Stell, "Reformulaton of Weeks-Chandler-Andersen perturbation theory directly in terms of a hard-sphere reference system," J. Phys. Chem. B **108**, 6877–6882 (2004).

[21] S. Zhou and J. R. Solana, "Progress in the perturbation approach in fluid and fluid-related theories," Chem. Rev. **109**, 2829–2958 (2009).

[22] N. E. Dubinin, N. A. Vatolin, and V. V. Filippov, "Thermodynamic perturbation theory in studies of metal melts," Russ. Chem. Rev. **83**, 987–1002 (2014).

[23] T. S. Ingebrigtsen, T. B. Schrøder, and J. C. Dyre, "Isomorphs in model molecular liquids," J. Phys. Chem. B **116**, 1018–1034 (2012).

[24] A. A. Veldhorst, J. C. Dyre, and T. B. Schrøder, "Scaling of the dynamics of flexible Lennard-Jones chains," J. Chem. Phys. **141**, 054904 (2014).

[25] E. A. Jagla, "Core-softened potentials and the anomalous properties of water," J. Chem. Phys. **111**, 8980–8986 (1999).

[26] F. H. Stillinger, "Phase transitions in the Gaussian core system," J. Chem. Phys. **65**, 3968–3974 (1976).

[27]M. J. Pond, W. P. Krekelberg, V. K. Shen, J. R. Errington, and T. M. Truskett, "Composition and concentration anomalies for structure and dynamics of Gaussian-core mixtures," J. Chem. Phys. **131**, 161101 (2009).

[28]V. V. Hoang and T. Odagaki, "Glasses of simple liquids with double-well interaction potential," Physica B **403**, 3910–3915 (2008).

[29]N. Gnan, T. B. Schrøder, U. R. Pedersen, N. P. Bailey, and J. C. Dyre, "Pressure-Energy correlations in liquids. IV. 'Isomorphs' in liquid phase diagrams," J. Chem. Phys. **131**, 234504 (2009).

[30]J. C. Dyre, "Hidden scale invariance in condensed matter," J. Phys. Chem. B **118**, 10007–10024 (2014).

[31]J. C. Dyre, "Simple liquids' quasiuniversality and the hard-sphere paradigm," J. Phys.: Condens. Matter **28**, 323001 (2016).

[32]U. R. Pedersen, N. P. Bailey, T. B. Schrøder, and J. C. Dyre, "Strong pressure-energy correlations in van der Waals liquids," Phys. Rev. Lett. **100**, 015701 (2008).

[33]U. R. Pedersen, T. Christensen, T. B. Schrøder, and J. C. Dyre, "Feasibility of a single-parameter description of equilibrium viscous liquid dynamics," Phys. Rev. E **77**, 011201 (2008).

[34]N. P. Bailey, U. R. Pedersen, N. Gnan, T. B. Schrøder, and J. C. Dyre, "Pressure-energy correlations in liquids. I. Results from computer simulations," J. Chem. Phys. **129**, 184507 (2008).

[35]T. B. Schrøder, N. Gnan, U. R. Pedersen, N. P. Bailey, and J. C. Dyre, "Pressure-energy correlations in liquids. V. Isomorphs in generalized Lennard-Jones systems," J. Chem. Phys. **134**, 164505 (2011).

[36]L. Costigliola, T. B. Schrøder, and J. C. Dyre, "Communication: Studies of the Lennard-Jones fluid in 2, 3, and 4 dimensions highlight the need for a liquid-state 1/d expansion," J. Chem. Phys. **144**, 231101 (2016).

[37]D. E. Albrechtsen, A. E. Olsen, U. R. Pedersen, T. B. Schrøder, and J. C. Dyre, "Isomorph invariance of the structure and dynamics of classical crystals," Phys. Rev. B **90**, 094106 (2014).

[38]T. S. Ingebrigtsen, J. R Errington, T. M. Truskett, and J. C. Dyre, "Predicting how nanoconfinement changes the relaxation time of a supercooled liquid," Phys. Rev. Lett. **111**, 235901 (2013).

[39]L. Separdar, N. P. Bailey, T. B. Schrøder, S. Davatolhagh, and J. C. Dyre, "Isomorph invariance of Couette shear flows simulated by the SLLOD equations of motion," J. Chem. Phys. **138**, 154505 (2013).

[40]E. Lerner, N. P. Bailey, and J. C. Dyre, "Density scaling and quasiuniversality of flow-event statistics for athermal plastic flows," Phys. Rev. E **90**, 052304 (2014).

[41]A. A. Veldhorst, J. C. Dyre, and T. B. Schrøder, "Scaling of the dynamics of flexible Lennard-Jones chains: Effects of harmonic bonds," J. Chem. Phys. **143**, 194503 (2015).

[42]F. Hummel, G. Kresse, J. C. Dyre, and U. R. Pedersen, "Hidden scale invariance of metals," Phys. Rev. B **92**, 174116 (2015).

[43]A. A. Veldhorst, T. B Schrøder, and J. C. Dyre, "Invariants in the Yukawa system's thermodynamic phase diagram," Phys. Plasmas **22**, 073705 (2015).

[44]A. K. Bacher, T. B. Schrøder, and J. C. Dyre, "Explaining why simple liquids are quasi-universal," Nat. Commun. **5**, 5424 (2014).

[45]A. I. Nielsen, S. Pawlus, M. Paluch, and J. C. Dyre, "Pressure dependence of the dielectric loss minimum slope for ten molecular liquids," Philos. Mag. **88**, 4101–4108 (2008).

[46]D. Gundermann, U. R. Pedersen, T. Hecksher, N. P. Bailey, B. Jakobsen, T. Christensen, N. B. Olsen, T. B. Schrøder, D. Fragiadakis, R. Casalini, C. M. Roland, J. C. Dyre, and K. Niss, "Predicting the density–scaling exponent of a glass–forming liquid from Prigogine–Defay ratio measurements," Nat. Phys. **7**, 816–821 (2011).

[47]L. A. Roed, D. Gundermann, J. C. Dyre, and K. Niss, "Communication: Two measures of isochronal superposition," J. Chem. Phys. **139**, 101101 (2013).

[48]W. Xiao, J. Tofteskov, T. V. Christensen, J. C. Dyre, and K. Niss, "Isomorph theory prediction for the dielectric loss variation along an isochrone," J. Non-Cryst. Solids **407**, 190–195 (2015).

[49]K. Niss, "Mapping isobaric aging onto the equilibrium phase diagram," Phys. Rev. Lett. **119**, 115703 (2017).

[50]H. W. Hansen, A. Sanz, K. Adrjanowicz, B. Frick, and K. Niss, "Evidence of a one-dimensional thermodynamic phase diagram for simple glass-formers," Nat. Commun. **9**, 518 (2018).

[51]T. B. Schrøder and J. C. Dyre, "Simplicity of condensed matter at its core: Generic definition of a Roskilde-simple system," J. Chem. Phys. **141**, 204502 (2014).

[52]L. Costigliola, T. B. Schrøder, and J. C. Dyre, "Freezing and melting line invariants of the Lennard-Jones system," Phys. Chem. Chem. Phys. **18**, 14678–14690 (2016).

[53]U. R. Pedersen, L. Costigliola, N. P. Bailey, T. B Schrøder, and J. C. Dyre, "Thermodynamics of freezing and melting," Nat. Commun. **7**, 12386 (2016).

[54]M. Born and J. E. Meyer, "Zur Gittertheorie der Ionenkristalle," Z. Phys. **75**, 1–18 (1932).

[55]R. A. Buckingham, "The classical equation of state of gaseous helium, neon and argon," Proc. R. Soc. London A **168**, 264–283 (1938).

[56]H. Yukawa, "On the interaction of elementary particles," Proc. Phys.-Math. Soc. Jpn. **17**, 48–57 (1935).

[57]J. S. Rowlinson, "The Yukawa potential," Physica A **156**, 15–34 (1989).

[58]M. Kac, G. E. Uhlenbeck, and P. C. Hemmer, "On the van der Waals theory of the vapor-liquid equilibrium. I. Discussion of a one-dimensional model," J. Math. Phys. **4**, 216–228 (1963).

[59]T. Maimbourg and J. Kurchan, "Approximate scale invariance in particle systems: A large-dimensional justification," Europhys. Lett. **114**, 60002 (2016).

[60]S. Kooij and E. Lerner, "Unjamming in models with analytic pairwise potentials," Phys. Rev. E **95**, 062141 (2017).

[61]Y. Hiwatari, H. Matsuda, T. Ogawa, N. Ogita, and A. Ueda, "Molecular dynamics studies on the soft-core model," Prog. Theor. Phys. **52**, 1105–1123 (1974).

[62]D. M. Heyes and A. C. Branka, "Physical properties of soft repulsive particle fluids," Phys. Chem. Chem. Phys. **9**, 5570–5575 (2007).

[63]D. M. Heyes and A. C. Branka, "Self-diffusion coefficients and shear viscosity of inverse power fluids: From hard- to soft-spheres," Phys. Chem. Chem. Phys. **10**, 4036–4044 (2008).

[64]E. Lange, J. B. Caballero, A. M. Puertas, and M. Fuchs, "Comparison of structure and transport properties of concentrated hard and soft sphere fluids," J. Chem. Phys. **130**, 174903 (2009).

[65]A. C. Branka and D. M. Heyes, "Pair correlation function of soft-sphere fluids," J. Chem. Phys. **134**, 064115 (2011).

[66]S. Pieprzyk, D. M. Heyes, and A. C. Branka, "Thermodynamic properties and entropy scaling law for diffusivity in soft spheres," Phys. Rev. E **90**, 012106 (2014).

[67]Y. Ding and J. Mittal, "Equilibrium and nonequilibrium dynamics of soft sphere fluids," Soft Matter **11**, 5274–5281 (2015).

[68]N. P. Bailey, U. R. Pedersen, N. Gnan, T. B. Schrøder, and J. C. Dyre, "Pressure-energy correlations in liquids. II. Analysis and consequences," J. Chem. Phys. **129**, 184508 (2008).

[69]N. P. Bailey, T. S. Ingebrigtsen, J. S. Hansen, A. A. Veldhorst, L. Bøhling, C. A. Lemarchand, A. E. Olsen, A. K. Bacher, L. Costigliola, U. R. Pedersen, H. Larsen, J. C. Dyre, and T. B. Schrøder, "RUMD: A general purpose molecular dynamics package optimized to utilize GPU hardware down to a few thousand particles," Scipost Phys. **3**, 038 (2017).

[70]M. P. Allen and D. J. Tildesley, *Computer Simulation of Liquids* (Oxford Science Publications, 1987).

[71]S. Toxvaerd and J. C. Dyre, "Communication: Shifted forces in molecular dynamics," J. Chem. Phys. **134**, 081102 (2011).

[72]T. B. Schrøder, U. R. Pedersen, N. P. Bailey, S. Toxvaerd, and J. C. Dyre, "Hidden scale invariance in molecular van der Waals liquids: A simulation study," Phys. Rev. E **80**, 041502 (2009).

[73]S. Chapman and T. G. Cowling, *The Mathematical Theory of Non-Uniform Gases: An Account of the Kinetic Theory of Viscosity, Thermal Conduction and Diffusion in Gases* (Cambridge University Press, 1970).

[74]W. Kauzmann, *The Kinetic Theory of Gases* (Benjamin, New York, 1966).

[75]J. C. Dyre, "*NVU* perspective on simple liquids' quasiuniversality," Phys. Rev. E **87**, 022106 (2013).

[76]T. S. Ingebrigtsen, S. Toxvaerd, O. J. Heilmann, T. B. Schrøder, and J. C. Dyre, "*NVU* dynamics. I. Geodesic motion on the constant-potential-energy hypersurface," J. Chem. Phys. **135**, 104101 (2011).

[77]T. S. Ingebrigtsen, S. Toxvaerd, T. B. Schrøder, and J. C. Dyre, "*NVU* dynamics. II. Comparing to four other dynamics," J. Chem. Phys. **135**, 104102 (2011).

[78]T. S. Ingebrigtsen and J. C. Dyre, "*NVU* dynamics. III. Simulating molecules," J. Chem. Phys. **137**, 244101 (2012).

[79]A. K. Bacher, T. B. Schrøder, and J. C. Dyre, "The EXP pair-potential system. II. Fluid phase isomorphs," J. Chem. Phys. **149**, 114502 (2018).

[80]V. V. Brazhkin, Yu. D. Fomin, A. G. Lyapin, V. N. Ryzhov, and K. Trachenko, "Two liquid states of matter: A dynamic line on a phase diagram," Phys. Rev. E **85**, 031203 (2012).

[81]T. Maimbourg and J. Kurchan, "Approximate scale invariance in particle systems: A large-dimensional justification," Europhys. Lett. **114**, 60002 (2016).

The EXP pair-potential system. II. Fluid phase isomorphs

Andreas Kvist Bacher,[a] Thomas B. Schrøder, and Jeppe C. Dyre[b]
Glass and Time, IMFUFA, Department of Science and Environment, Roskilde University,
P.O. Box 260, DK-4000 Roskilde, Denmark

This paper continues the investigation of the exponentially repulsive EXP pair-potential system of Paper I [A. K. Bacher *et al.*, J. Chem. Phys. **149**, 114501 (2018)] with a focus on isomorphs in the low-temperature gas and liquid phases. As expected from the EXP system's strong virial potential-energy correlations, the reduced-unit structure and dynamics are isomorph invariant to a good approximation. Three methods for generating isomorphs are compared: the small-step method that is exact in the limit of small density changes and two versions of the direct-isomorph-check method that allows for much larger density changes. Results from the latter two approximate methods are compared to those of the small-step method for each of the three isomorphs generated by 230 one percent density changes, covering one decade of density variation. Both approximate methods work well. © *2018 Author(s).*
All article content, except where otherwise noted, is licensed under a Creative Commons Attribution
(CC BY) license (http://creativecommons.org/licenses/by/4.0/). https://doi.org/10.1063/1.5043548

I. INTRODUCTION

This paper and its companion (Paper I, Ref. 1) present an investigation of the exponential (EXP) pair-potential system consisting of identical particles interacting via the purely repulsive pair potential,

$$v_{\text{EXP}}(r) = \varepsilon\, e^{-r/\sigma}. \tag{1}$$

Both papers focus on the region of the thermodynamic phase diagram where temperature is so low that the finite value $v_{\text{EXP}}(0)$ plays little role for the physics, i.e., where $k_B T \ll \varepsilon$. The focus is, moreover, on the low-density gas and liquid phases, i.e., where $\rho\sigma^3 \ll 1$. While the densities considered are low in relation to the σ parameter of Eq. (1), it should be emphasized that at low temperature the densities are not, in fact, low relative to the effective hard-sphere (HS) radius but typical for studies of simple systems.

The EXP pair potential has not been studied much on its own right, in fact even less than other purely repulsive pair potentials like the family of inverse-power law pair potentials.[2–9] In most cases, an exponential function appears as a term in mathematically more involved potentials, for instance, (1) giving the repulsive part of the Born-Meyer pair potential from 1932[10] or in embedded-atom models of metals,[11,12] (2) multiplied by a Coulomb term to give the Yukawa (screened Coulomb) potential,[13,14] or (3) giving the attractive long-ranged part in a model that rigorously obeys the van der Waals equation of state in one dimension.[15]

As shown below (Fig. 1), to a good approximation the EXP system conforms to the following "hidden-scale invariance" condition for uniform scaling of same-density configurations $\mathbf{R}_a$ and $\mathbf{R}_b$[16] [$\mathbf{R}$ is the vector of all particle coordinates and

$U(\mathbf{R})$ is the system's potential-energy function],

$$U(\mathbf{R}_a) < U(\mathbf{R}_b) \;\Rightarrow\; U(\lambda\mathbf{R}_a) < U(\lambda\mathbf{R}_b). \tag{2}$$

Here $\lambda > 0$ is a scaling parameter. Equation (2) expresses that if the potential energy of configuration $\mathbf{R}_a$ is lower than that of configuration $\mathbf{R}_b$, this applies also after a uniform scaling of both configurations. For most systems, including the EXP system, Eq. (2) is approximate and not obvious from the mathematical expression for the potential energy, hence the term "hidden scale invariance."[17,18]

Paper I[1] demonstrated one of the consequences of Eq. (2) for the EXP pair potential, namely, strong virial potential-energy correlations in the constant-volume thermal-equilibrium fluctuations. The EXP pair-potential system has stronger such correlations than, e.g., the Lennard-Jones (LJ) system.[19,20] In fact, the EXP system's virial potential-energy Pearson correlation coefficient R is larger than 99% in a large part of its phase diagram (see Paper I[1] and Ref. 21). A system is termed "R-simple" if it has better than 90% correlation.

The fact that the EXP pair-potential system obeys Eq. (2) to a good approximation implies that it has isomorphs, which are curves in the phase diagram along which the structure and dynamics are approximately invariant in proper units.[16,22] Isomorphs are defined as curves of constant excess entropy; they are the system's configurational adiabats. While all systems have configurational adiabats, only R-simple systems, i.e., those obeying the hidden-scale-invariance condition Eq. (2) to a good approximation, have invariant physics along their configurational adiabats.[16,22–25]

A derivation of simple liquids' quasiuniversality based on the EXP pair potential was given in Refs. 21 and 25; an alternative proof utilizing constant-potential-energy (*NVU*) dynamics[26] was presented in Paper I.[1] Both proofs are based on the fact that under certain conditions a sum of two EXP pair

---

a)ankvba@gmail.com
b)dyre@ruc.dk
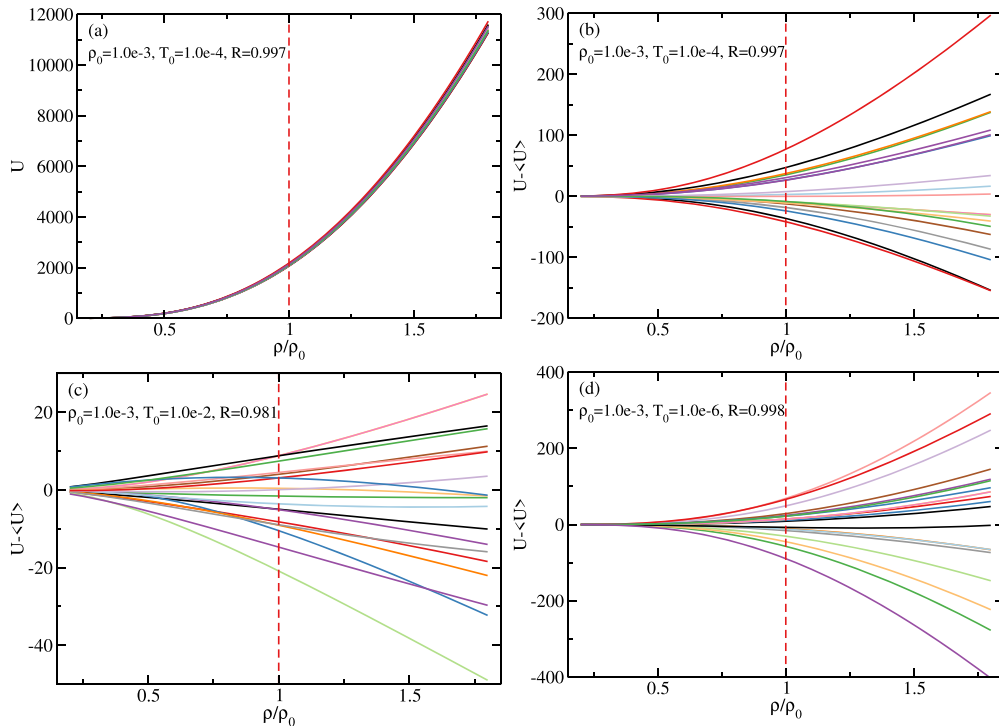
FIG. 1. Investigating Eq. (2) for the EXP pair-potential system. R is the virial potential-energy correlation coefficient. (a) Potential energies of 20 statistically independent configurations from an equilibrium simulation of a system with 1000 particles at density 10^{-3} and temperature 10^{-4} (red dashed line), scaled uniformly to different densities and plotted as a function of density. (b) The same data with the average potential energy subtracted at each density, making it easier to investigate the implication of Eq. (2) that no crossings should take place. This is seen to apply to a good approximation. (c) The same as in (b) for configurations selected from a simulation at density 10^{-3} and temperature 10^{-2}. There are here more crossings, meaning that Eq. (2) is less accurately obeyed, consistent with the lower R. (d) The same as in (b) for configurations from simulations at density 10^{-3} and temperature 10^{-6}; here, $R = 99.8\%$ and Eq. (2) is very well obeyed.

potentials describes a system, which has virtually the same physics as that of a single EXP pair-potential system. Thus, quasiuniversality applies for any system with a pair potential that to a good approximation may be written as a sum of EXP terms with numerically large prefactors in reduced units (see below).[21] The EXP pair-potential system is thereby central for understanding the physics of simple liquids.[38] This justifies a closer investigation of the properties of the EXP system itself.

The isomorph theory is based on the use of reduced units,[2,22,23,27] which are different from those usually applied for presenting simulation data using the potential-energy function's characteristic energy and length. Instead reduced units utilize *macroscopic* parameters that vary with the thermodynamic state point. Consider a state point of temperature T and density $\rho = N/V$ (N is the number of particles and V is the system volume). If the average particle mass is m, reduced units make quantities dimensionless by scaling with the length $l_0 = \rho^{-1/3}$, the energy $e_0 = k_B T$, and the time $t_0 = \rho^{-1/3}\sqrt{m/k_B T}$.[22,24,25] Reduced quantities are denoted by a tilde, for instance, $\tilde{\mathbf{R}} \equiv \mathbf{R}/l_0 = \rho^{1/3}\mathbf{R}$ is the reduced configuration vector. We can now make precise the statement that the isomorphs of an R-simple system are lines of virtually identical physic; this refers to the system's reduced-unit structure and dynamics.

Besides demonstrating approximate isomorph invariance of the EXP system's structure and dynamics, the present paper discusses methods for generating the system's isomorphs in computer simulations. Before doing this, we show in Sec. II examples of the system's hidden scale invariance, and Sec. III presents results for the density-scaling exponent's variation throughout the thermodynamic phase diagram (the isomorph slope in the log-log density-temperature phase diagram). Sections IV and V report results from computer simulations along isomorphs traced out in different ways. Section IV presents the "small-step" method which, in the limit of infinitely small density changes, rigorously identifies the configurational adiabats; Sec. V discusses two versions of the so-called direct-isomorph-check (DIC) method, both allowing for much larger density changes. Finally, Sec. VI gives a brief discussion.

II. THE EXP SYSTEM'S HIDDEN SCALE INVARIANCE

The excess entropy S_{ex} of a thermodynamic state point is defined as the entropy minus that of an ideal gas at the same density and temperature[28] (note that $S_{ex} < 0$ since no system is more disordered than an ideal gas). S_{ex} is the non-trivial part of a system's entropy, the contribution deriving from interactions. In general, excess thermodynamic quantities are calculated by leaving out the momentum degrees of freedom in the partition function;[28] excess quantities obey all standard thermodynamic relations like $T = (\partial U/\partial S_{ex})_\rho$, etc.

If one defines the microscopic excess entropy function $S_{ex}(\mathbf{R})$ as the thermodynamic equilibrium excess entropy of the state point with the density ρ of the configuration $\mathbf{R}$ and with the average potential energy equal to $U(\mathbf{R})$, it

is straightforward to show that the hidden-scale-invariance condition Eq. (2) implies a scale-invariant entropy function, i.e., $S_{ex}(\mathbf{R}) = S_{ex}(\lambda \mathbf{R})$ in which λ is a scaling parameter.[16] This means that $S_{ex}(\mathbf{R})$ depends only on the configuration's reduced coordinates, $\tilde{\mathbf{R}} = \rho^{1/3}\mathbf{R}$. Inserting this into the identity $U(\mathbf{R}) = U(\rho, S_{ex}(\mathbf{R}))$ that defines $S_{ex}(\mathbf{R})$ where $U(\rho, S_{ex})$ is the thermodynamic average potential energy as a function of density and excess entropy, one arrives[16] at

$$U(\mathbf{R}) = U(\rho, S_{ex}(\tilde{\mathbf{R}})). \tag{3}$$

This is the basic identity characterizing an R-simple system from which the isomorph invariance of structure and dynamics follows.[16] Note that these invariances do not imply that all excess thermodynamics is isomorph invariant since there is also a density dependence in Eq. (3). For instance, the Helmholtz and Gibbs free energies are not isomorph invariant. A recent paper that used the isomorph theory for predicting how a number of quantities vary along the melting line gives an example of how the Gibbs free energy variation along a LJ system isomorph may be calculated.[29]

Physically, the hidden-scale-invariance condition Eq. (2) states that if configurations at some density are ordered according to their potential energy, this ordering is maintained if the configurations are scaled uniformly to a different density. It is important to note that Eq. (2)—and thus Eq. (3) and the entire isomorph theory—is approximate except for systems with an Euler-homogeneous potential-energy function (plus a constant).

A consequence of Eq. (3) is that an R-simple system has strong correlations between its constant-density thermal-equilibrium fluctuations of virial and potential energy. This property was documented for the EXP system in Ref. 21 and in Paper I,[1] and previously for many other systems, including molecular and polymeric systems.[19,20,30,31] Recall that the microscopic virial $W(\mathbf{R})$ is defined from the change of potential energy upon a uniform scaling of all particle coordinates, i.e., $W(\mathbf{R}) \equiv (\partial U(\mathbf{R})/\partial \ln \rho)_{\tilde{\mathbf{R}}}$ since a uniform scaling leaves $\tilde{\mathbf{R}}$ unchanged. Substituting Eq. (3) into this expression, one finds

$$W(\mathbf{R}) = \left.\frac{\partial U(\rho, S_{ex})}{\partial \ln \rho}\right|_{S_{ex}=S_{ex}(\tilde{\mathbf{R}})}. \tag{4}$$

In other words, $W(\mathbf{R}) = W(\rho, S_{ex}(\tilde{\mathbf{R}}))$, in which the function $W(\rho, S_{ex})$ is the thermodynamic virial, the average of the microscopic virial at the state point with density ρ and excess entropy S_{ex}. In conjunction with Eq. (3), the identity $W(\mathbf{R}) = W(\rho, S_{ex}(\tilde{\mathbf{R}}))$ implies perfect correlation between the virial and the potential energy at a fixed density in the sense that one of these two quantities uniquely determines the other. This one-to-one relation between W and U is predicted to apply whether or not configurations are selected from an equilibrium simulation, for instance, also during aging.[32]

We proceed to demonstrate numerically that the EXP pair-potential system obeys the hidden-scale-invariance condition Eq. (2) to a good approximation. While most quantities below are reported in reduced units, density and temperature are by definition constant in reduced units. This makes it impossible to specify a state point using reduced units for

density and temperature, so numerical values of the density are reported below in units of $1/\sigma^3$ and numerical temperatures in units of ε/k_B. This is referred to as the "EXP unit system" (Paper I[1]).

Figures 1(a) and 1(b) show results from an equilibrium simulation at density 10^{-3} and temperature 10^{-4}, a liquid state point close to the melting line (simulation details are provided in Paper I[1]). From the simulations, we selected 20 statistically independent configurations (separated by $5 \cdot 10^5$ time steps). Each configuration was scaled uniformly to a different density ρ in the range $0.25 \cdot 10^{-3} < \rho < 1.75 \cdot 10^{-3}$, i.e., a factor of seven density variation is involved. Figure 1(a) plots the potential energies of the scaled configurations as a function of their density. Note that no new simulations were performed to generate this figure, we merely scaled the 20 configurations uniformly and then evaluated their potential energies. Not surprisingly, for all configurations, the potential energy increases strongly with increasing density. While they visually follow each other closely in Fig. 1(a), the figure does not allow for checking Eq. (2). To do this, Fig. 1(b) plots the same data by subtracting at each density the average potential energy of the 20 scaled configurations, making it possible to use a much smaller unit on the potential-energy axis. There are only few crossings of the curves. This confirms that the EXP system obeys Eq. (2) to a good approximation, i.e., it is R-simple in this region of the thermodynamic phase diagram.

Figure 1(c) shows a plot like (b) at the same density but at the higher temperature 10^{-2}. Here crossings are more common, implying that Eq. (2) is less accurately obeyed. This is consistent with the finding of Paper I[1] that the virial potential-energy correlation coefficient decreases if temperature is increased. Moving in the opposite direction, Fig. 1(d) shows data for temperature 10^{-6} where the pattern is similar to that of (b), but with even fewer crossings. In summary, Eq. (2) works well at low temperatures but breaks down gradually as higher temperatures are approached.

The absence of crossings upon a uniform scaling of all particle coordinates is not trivial. Hidden scale invariance is exact only for inverse power-law pair potentials, but it applies to a good approximation for many pair-potential systems, e.g., LJ type systems.[16] By contrast, there are many crossings, e.g., for the Lennard-Jones Gaussian pair potential for a density change of merely 20%.[16]

III. THE DENSITY-SCALING EXPONENT

At any state point in the thermodynamic phase diagram, one defines the so-called density-scaling exponent γ[22] by

$$\gamma \equiv \left(\frac{\partial \ln T}{\partial \ln \rho}\right)_{S_{ex}}. \tag{5}$$

For an R-simple system, since isomorphs are curves of constant S_{ex},[22] γ gives the slope of the isomorph through the state point in the log-log density-temperature phase diagram. If γ were constant, according to the isomorph theory there would be invariance of the reduced-unit structure and dynamics along the phase diagram's lines of constant ρ^γ/T. This is the origin of the name "density-scaling exponent." Before isomorph

theory was developed, density scaling was demonstrated experimentally for many glass-forming liquids.[33]

By means of standard thermodynamic fluctuation theory, γ may be calculated from the canonical-ensemble constant-density (NVT) equilibrium virial and potential-energy fluctuations,[22]

$$\gamma = \frac{\langle \Delta U \Delta W \rangle}{\langle (\Delta U)^2 \rangle}. \tag{6}$$

This identity makes it straightforward to determine γ in simulations. Figure 2 shows results for the density-scaling exponent with (a) giving γ's density variation along isotherms and (b) giving γ's temperature variation along isochores. In the figure, we mark three phases: gas, liquid, and solid, although the EXP system like any purely repulsive system has no liquid-gas phase transition and merely a single fluid phase. There is a large transition region between typical gas and typical liquid states; the least dense isomorph studied below is located

in this region. The data in Fig. 2 reveal two regimes: At high densities and low temperatures (liquid and solid phases), γ is mainly density dependent; at low densities (gas phase), γ is mainly temperature dependent.

It is possible to construct approximate analytical theories for the two limiting behaviors. Consider first the high-density case corresponding to the liquid and solid phases, both of which are characterized by strong interactions between a given particle and its several nearest neighbors. To explain the strong virial potential-energy correlations of the LJ pair-potential liquid, Ref. 34 developed an approach based on the "extended inverse power-law" (eIPL) approximation that works as follows. At typical liquid or solid densities, within the first coordination shell, the LJ pair potential is very well approximated[34] by the eIPL pair potential

$$v_{\text{eIPL}}(r) = Ar^{-n} + B + Cr. \tag{7}$$
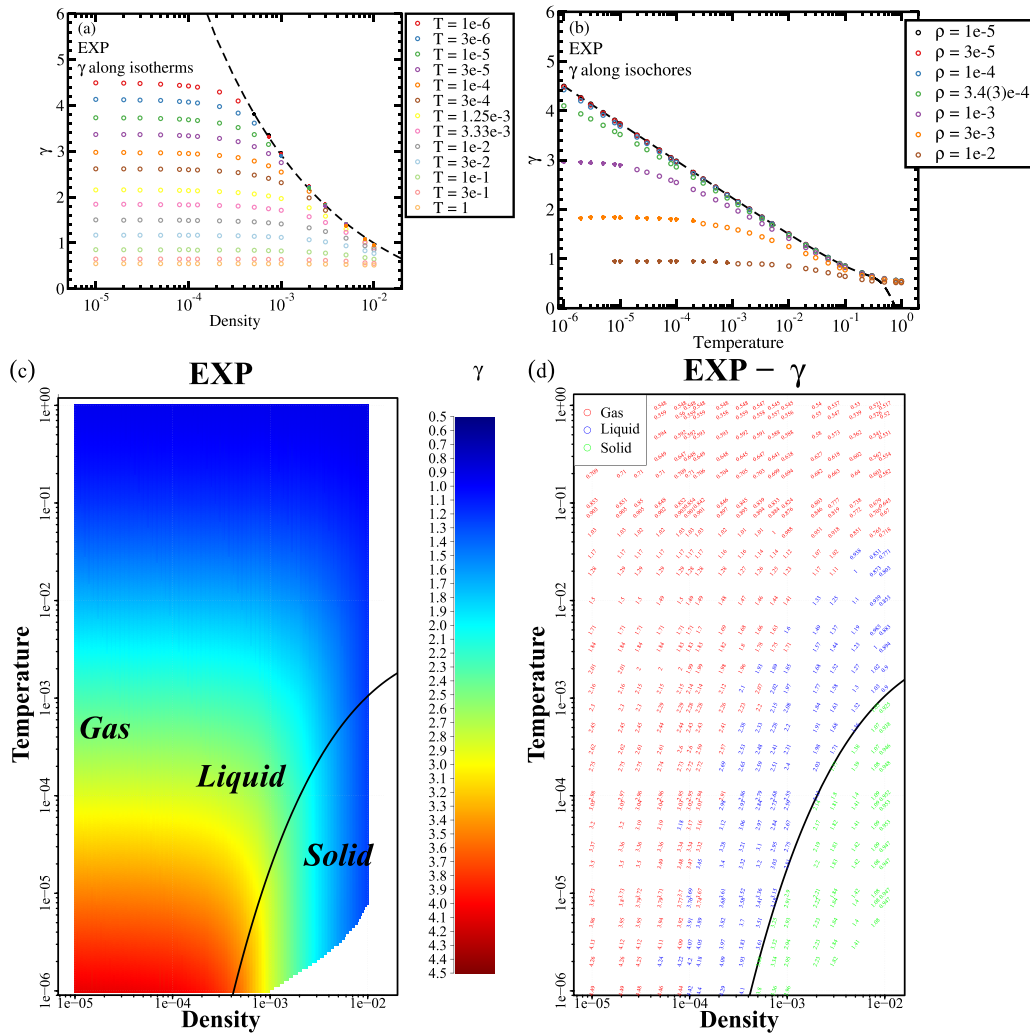
FIG. 2. Density and temperature variation of the density-scaling exponent γ [Eq. (5)]. (a) shows γ along isotherms. At low densities, γ is mainly temperature dependent. The dashed line gives the prediction of the eIPL approximation Eq. (11)[34] with $\Lambda = 1.075$, which describes the condensed liquid phase well. (b) shows γ along isochores. The dashed line is here the prediction of the analytical theory for the gas phase, Eq. (15), in which γ depends only on the temperature. (c) shows γ in a continuous color plot, visualizing the fact that γ at low densities is mainly temperature dependent, whereas it at high densities and low temperatures, i.e., in the liquid and solid phases, is mainly density dependent. (d) reports the numerical values of γ (visible upon magnification) written into the phase diagram at the densities and temperatures listed in Appendix B of Paper I.[1] At each state point, γ is written with a slope marking the direction of the isomorph through the state point in question; red indicates gas, blue indicates liquid, and green indicates solid phase state points.

If one imagines a particle being displaced within its nearest-neighbor cage, some distances increase and some decrease, but the sum of all nearest-neighbor distances remains almost unchanged. This means that the $B + Cr$ term is almost constant, so the eIPL pair potential may effectively be replaced by $v_{\text{eIPL}}(r) \cong Ar^{-n} + D$. When added over all particle pairs, this implies that the hidden-scale-invariance condition Eq. (2) applies to a good approximation.

The above explains the strong virial potential-energy correlations found for the LJ and similar pair-potential systems.[20,35,36] It also suggests a means for approximately calculating the density-scaling exponent γ. Note first that

$$\gamma = n/3 \qquad (8)$$

for the IPL system $v(r) = Ar^{-n} + D$; this follows from Eq. (6) and the definition of the pair virial $w(r) \equiv (-1/3)rv'(r)$.[34] How to identify the effective IPL exponent n at a given state point? For the eIPL pair potential, one has $v'_{\text{eIPL}}(r) = -nAr^{-(n+1)} + C$, $v''_{\text{eIPL}}(r) = n(n+1)Ar^{-(n+2)}$, and $v'''_{\text{eIPL}}(r) = -n(n+1)(n+2)Ar^{-(n+3)}$. This implies $n = -2 - rv'''_{\text{eIPL}}(r)/v''_{\text{eIPL}}(r)$. Thus n is given by $n = n_2(r)$ if one for any pair potential $v(r)$ defines the r-dependent effective IPL exponent $n_p(r)$[34] by [$v^{(p)}(r)$ is the pth derivative of $v(r)$]

$$n_p(r) \equiv -p - r\frac{v^{(p+1)}(r)}{v^{(p)}(r)}. \qquad (9)$$

Realistic values of n are arrived at by using for r a typical nearest-neighbor distance. In the EXP unit system, this means putting

$$r/\sigma = \Lambda\,\rho^{-1/3}, \qquad (10)$$

in which $\Lambda \cong 1$ is a numerical constant. Using this value of r for the EXP pair potential leads for $p = 2$, via Eqs. (8)–(10), to the following estimate of the density-scaling exponent in the EXP system's condensed liquid and solid phases:

$$\gamma(\rho) \cong \frac{-2 + \Lambda\rho^{-1/3}}{3}. \qquad (11)$$

This prediction is shown as the black dashed line in Fig. 2(a), in which $\Lambda = 1.075$ was determined to get the best fit to data. At high densities, the different isotherms collapse onto the line, a collapse that at low temperatures takes place earlier than at high temperatures.

Next we study the dilute gas limit. Here the system is characterized by much longer typical distances between the particles than the interaction range σ, i.e., $\rho \ll 1$. In this limit, particle interactions predominantly take place via two-particles collisions. As shown in Paper I,[1] it is possible to construct an analytical theory for the correlation coefficient R in the gas phase by assuming that particle collisions are random and uncorrelated. It is likewise possible to calculate γ analytically in the gas phase via Eq. (6) (compare Appendix A of Paper I[1]). The relevant equation is

$$\gamma = \frac{\langle wv \rangle}{\langle v^2 \rangle}, \qquad (12)$$

in which v is the EXP pair potential treated as an independent variable, $w = (-1/3)rv'(r) = \ln(1/v)v/3$ is the pair virial, and

averages are taken over the non-normalizable v-probability distribution $p(v) \propto \ln^2(1/v)\exp(-\beta v)/v$. Equation (12) leads to

$$\gamma = \frac{A_3}{3A_2}, \qquad (13)$$

in which

$$A_n = \int_0^\infty v\,\ln^n(1/v)\,e^{-\beta v}dv. \qquad (14)$$
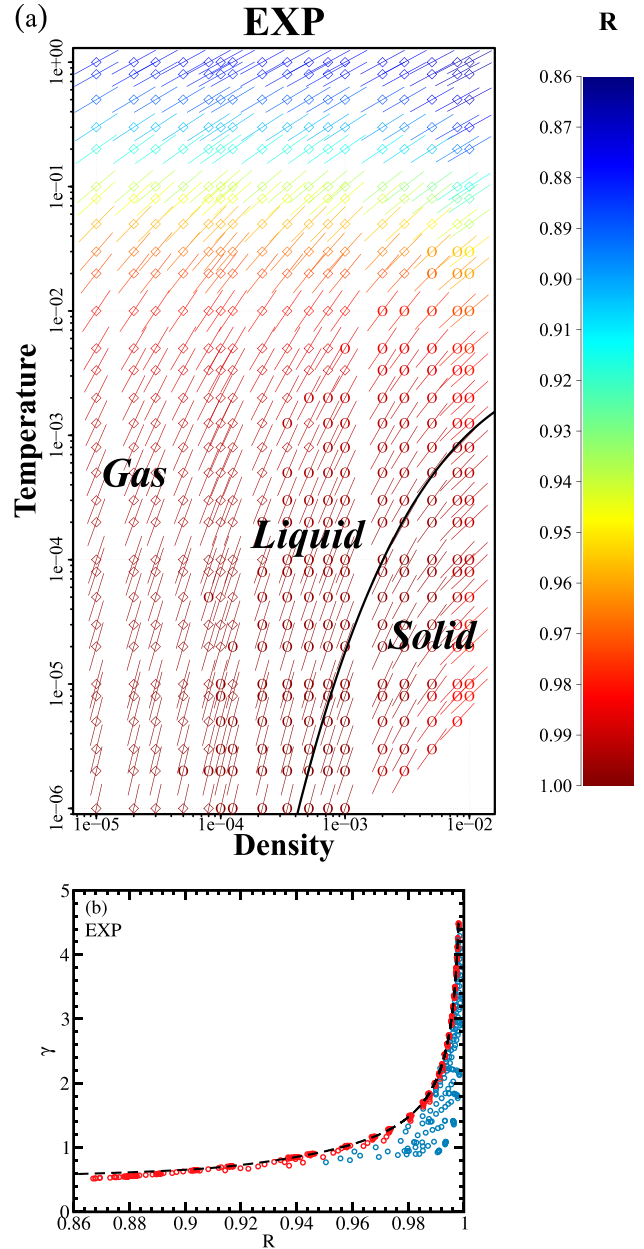
FIG. 3. (a) shows the density-temperature phase diagram with line slopes given by the density-scaling exponent and color coding indicating the virial potential-energy correlation coefficient R. Diamonds mark gas-phase state points and circles mark liquid or solid state points. The line segments give the isomorph slopes, compare Eq. (5). The black dashed line is the approximate melting-line isomorph (covering the entire coexistence region). (b) Density-scaling exponent γ versus the virial potential-energy correlation coefficient R for all state points simulated. Red symbols are gas state points and blue symbols are liquid and solid state points. The dashed line is the prediction of the analytical gas-phase theory, which is obtained by combining Eq. (13) with $R = A_3/\sqrt{A_2 A_4}$ derived in Appendix A of Paper I.[1] For a given value of R, the gas phase has the highest γ; for a given value of γ, the gas phase has the lowest R.

The integrals may be worked out analytically in terms of π, Euler's constant 0.577. . ., and the Riemann zeta function evaluated at 3 (Appendix A of Paper I[1]). Numerically, the result is

$$\gamma = \frac{\ln^3 \beta - 1.268 \ln^2 \beta + 2.471 \ln \beta - 0.4895}{3 \ln^2 \beta - 2.537 \ln \beta + 2.471} . \quad (15)$$

At low temperatures ($\beta \gg 1$), the dominant term is $\gamma \cong \ln \beta /3$. This corresponds to the $p = 0$ effective IPL exponent in Eq. (9) evaluated at the distance at which the pair potential equals $k_B T$, the typical distance of nearest approach in a collision. Our numerical data indicate that Eq. (15) becomes exact at low densities, compare Fig. 2(b) that shows Eq. (15) as the black dashed line.

Figure 3(a) summarizes our numerical findings for the virial potential-energy correlation coefficient R and γ in a single phase diagram.[21] The color coding gives R, the line-segment slopes give γ. The line segments mark how the isomorphs run in the phase diagram, basically parallel to the melting line that is itself an approximate isomorph.[21,22] Figure 3(b) plots all values of (R, γ) with the dashed line marking the gas-phase analytical prediction. An important conclusion from this figure is that as $\gamma \to \infty$ one has $R \to 1$. Since large γ corresponds to an effectively very strongly repulsive pair potential on the $k_B T$ energy scale, this means that one expects $R \to 1$ in the hard-sphere limit of the EXP system, which is obtained by following an isomorph to zero temperature.

IV. STRUCTURE, DYNAMICS, AND SPECIFIC HEAT ALONG THREE ISOMORPHS

The "small-step" method for tracing out an isomorph in the phase diagram is based on Eqs. (5) and (6). The present section investigates predicted invariances along three isomorphs, which serve as reference "true" isomorphs in Sec. V dealing with two faster, approximate methods for generating isomorphs.

It is straightforward to calculate in an *NVT* computer simulation the canonical averages on the right-hand side of Eq. (6). Typical values of γ for the EXP system are between 0.5 and 5 (Fig. 2). If, for instance, $\gamma = 3$, upon a 1% density increase, the temperature is to be increased by 3% in order to keep S_{ex} constant [Eq. (6)]. After this change of density and temperature, one recalculates the right-hand side of Eq. (6), and so on. In this way, an isomorph is traced out with a method that is, in principle, exact in the limit of infinitely small density changes. The method is tedious since many steps are needed if 1% density changes are used to generate an isomorph covering a large density variation. The many steps required also mean that, in order to avoid accumulation of errors, each state-point simulation must be long enough to provide accurate data. Initial simulations for 5%, 2%, and 1% density changes from various state points showed that the latter two give virtually indistinguishable results. We concluded that a 1% density change is small enough to be reliable.

Three isomorphs were traced out for systems of 1000 particles using 1% density changes to cover one decade of

density based on 230 simulations, each involving 10^7 time steps (Fig. 4). One isomorph is located in the gas-liquid transition region, a second one is in the dilute liquid phase, and a third one is in the liquid phase near the melting line. Note that in the log-log phase diagram, the isomorphs are virtually parallel to the melting line. This is because in a simplified version of the isomorph theory,[22] the melting line is an isomorph and isomorphs are given by an expression of the form $h(\rho)/T$ = Const.[37] Different isomorphs correspond to different constants, implying that the isomorphs are parallel to one another in the log-log density-temperature phase diagram. A more accurate melting theory is now available,[29] but the corrections to the older understanding of Ref. 22 are small.

In the following, data are presented for each isomorph for the starting state point and ten more state points evenly spaced on the logarithmic density axis (for reference the coordinates of the selected isomorph state points are given in the Appendix). We first investigate the structure along an isomorph in order to see whether it is invariant. Figure 5 shows the structure probed by the reduced radial distribution function (RDF) at eleven state points for each of the three isomorphs. The density change along each isomorph spans one decade; the temperatures span more than two decades. These variations are large compared to the first isomorph-theory simulations covering density
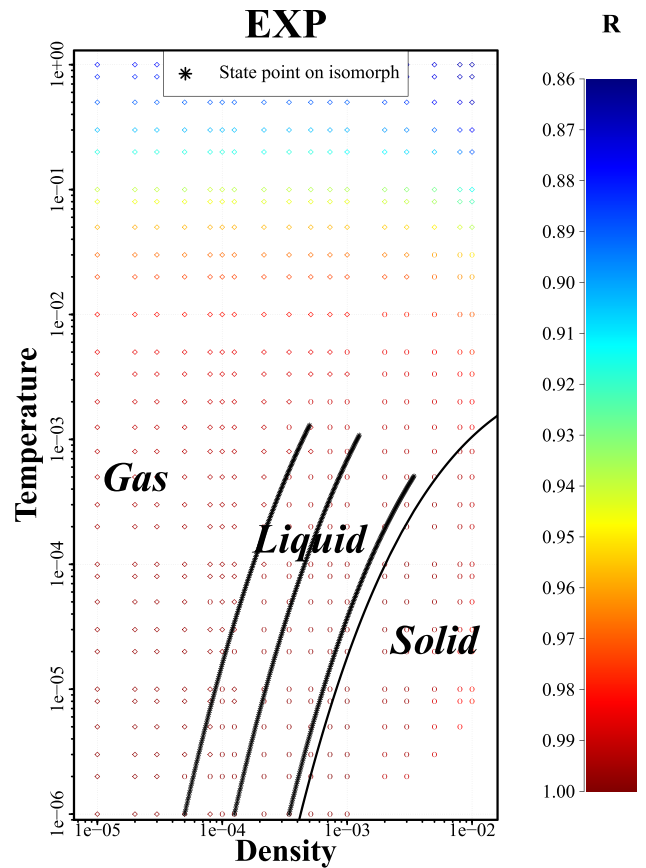
FIG. 4. The three isomorphs studied marked by black crosses merging into lines. The isomorphs were generated by the "small-step method" from 230 simulations, each increasing density by 1% using Eq. (5) in conjunction with Eq. (6) to calculate the corresponding temperature change. The starting temperature for each isomorph was $T = 10^{-6}$; the starting densities were the following: gas-liquid isomorph (left): $5 \cdot 10^{-5}$, dilute-liquid isomorph (middle): $1.25 \cdot 10^{-4}$, and dense-liquid isomorph (right): $3.43 \cdot 10^{-4}$.
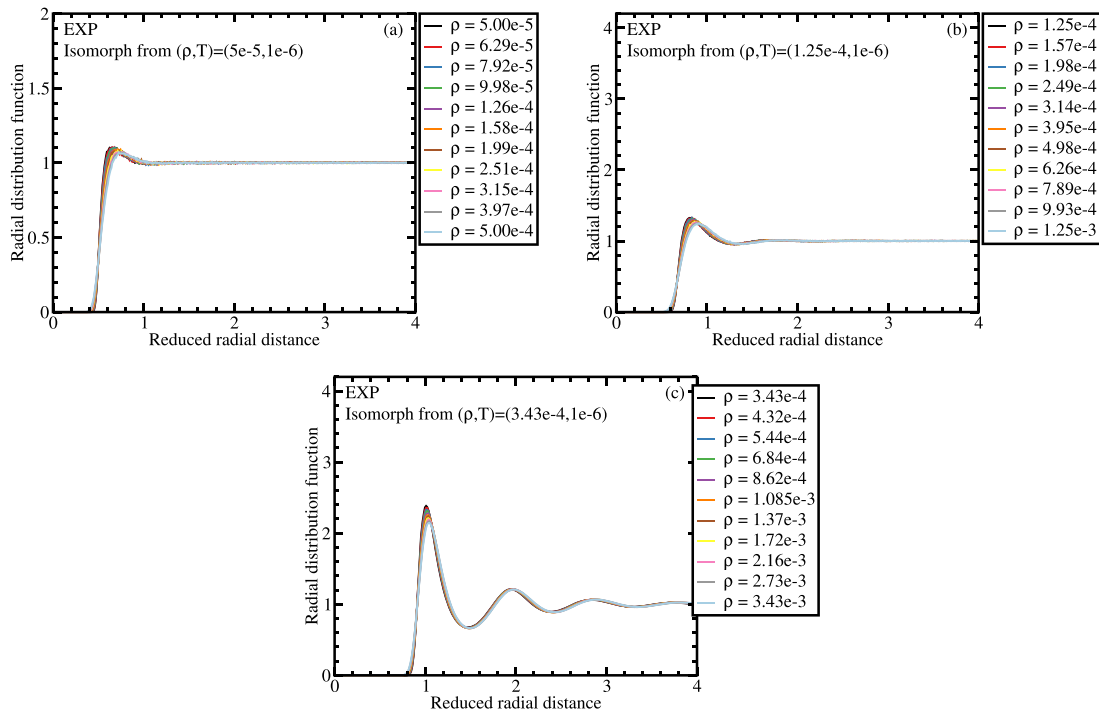
FIG. 5. Structure at selected state points along each of the three isomorphs shown in Fig. 4 probed via the reduced radial distribution function (RDF). (a) Gas-liquid isomorph. This isomorph is located where the system has little structure. (b) Dilute-liquid isomorph. The structure here exhibits more structure and is still approximately invariant. (c) Dense-liquid isomorph. The system here has a typical liquid-like structure that is well maintained along the isomorph.

variations of just a few percent.[22] Nevertheless, deviations from collapse are small; these are mainly observed around the first peak.[22,30]

For each of the three isomorphs, Fig. 6 shows the reduced mean-square displacement (MSD) as a function of

reduced time at the same eleven state points. Good collapse is observed. Figure 7(a) demonstrates that the reduced diffusion constant (derived from the long-time MSD) is invariant along each of the three isomorphs. The more gas-like the isomorph is, the faster the diffusion is (in reduced units).
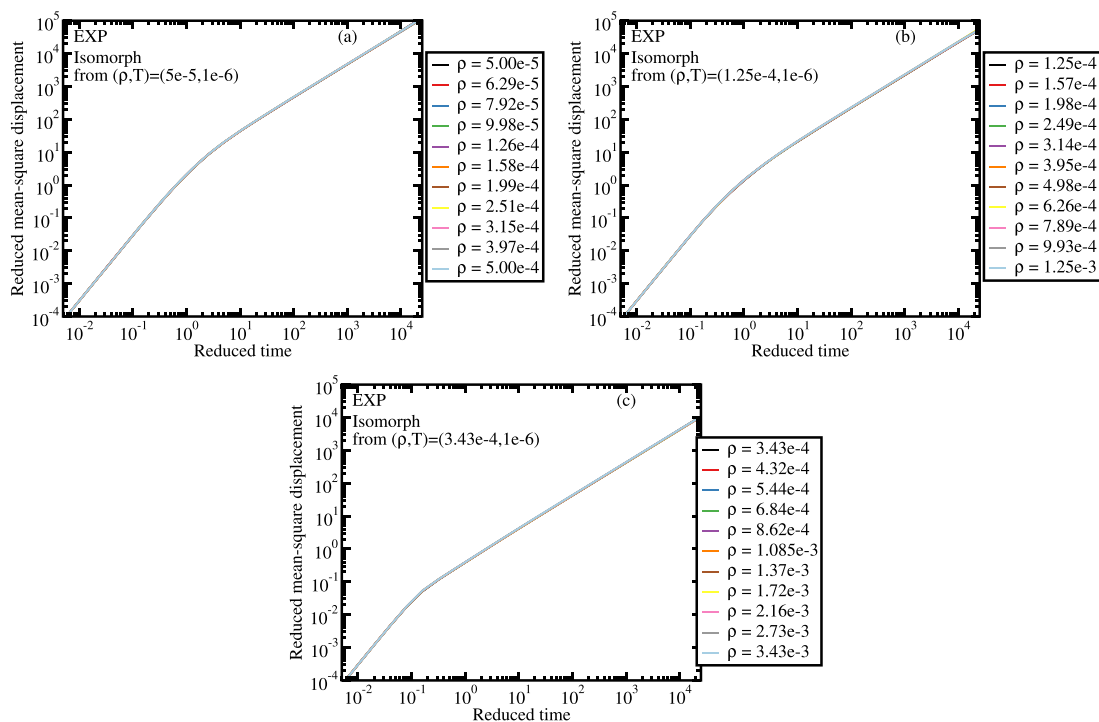
FIG. 6. Reduced mean-square displacement (MSD) at selected state points along each of the three isomorphs plotted as a function of reduced time. At short times, the MSD follows the ballistic prediction $3\tilde{t}^2$ (Paper I[1]); at long times, it follows the diffusion equation prediction $\propto \tilde{t}$. In all cases, there is a good collapse.
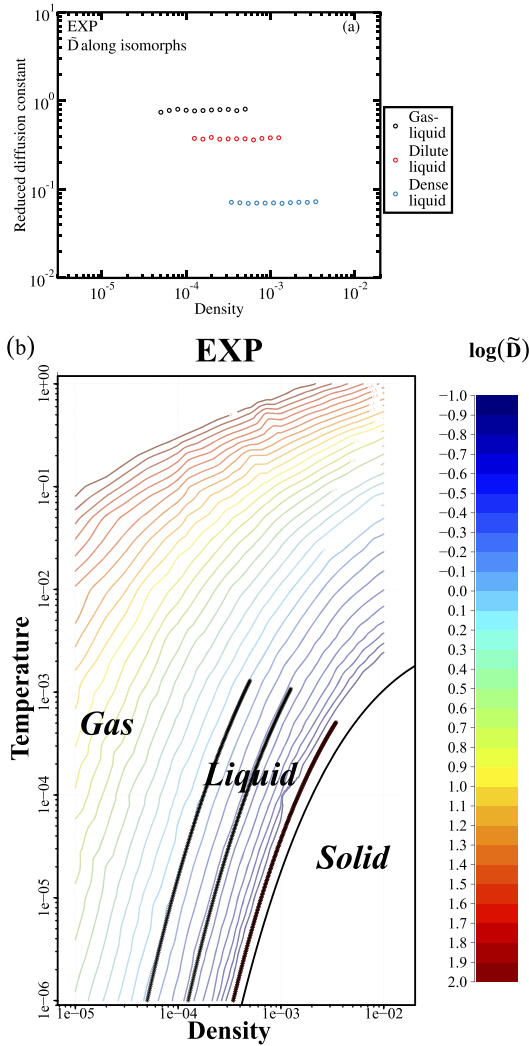
FIG. 7. (a) Reduced diffusion constant $\tilde{D}$ plotted as a function of density along each of the three isomorphs. The diffusion constant varies significantly between the isomorphs, but is virtually constant along each of them. (b) Contour color plot giving the reduced diffusion constant's variation throughout the phase diagram in which lines of constant $\tilde{D}$ are drawn for logarithmically equally distributed values.

FIG. 8. Reduced excess isochoric specific heat per particle plotted as a function of density along each of the three isomorphs. Not surprisingly, the isomorph with least interparticle interactions—the gas-liquid isomorph—has the lowest excess specific heat. A systematic increase with density is observed for all three isomorphs. This is at variance with the original (2009) version of isomorph theory in which the specific heat is an isomorph invariant,[22] but it is consistent with the 2014 version.[16] The dashed line has slope 1/3, which is the prediction for the density variation along gas-phase isomorphs (see the text).
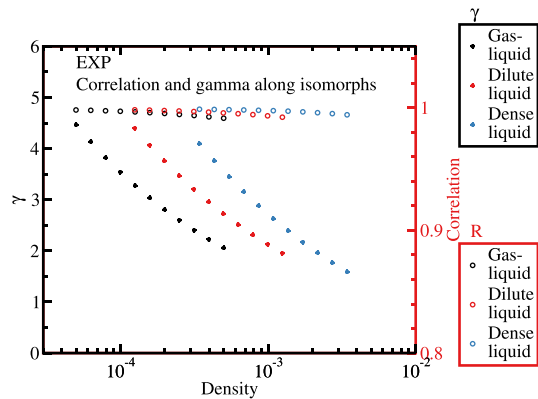
FIG. 9. The density-scaling exponent γ (full circles, left) and the virial potential-energy correlation coefficient R (open circles, right) plotted as a function of density along each of the three isomorphs. Neither γ nor R are predicted to be isomorph invariant. Note that strong correlations are maintained even as γ decreases significantly with increasing density.

Figure 7(b) shows a contour plot of the reduced diffusion constant that again illustrates its isomorph invariance.

Figure 8 gives the reduced excess isochoric specific heat per particle $\tilde{c}_V^{\mathrm{ex}}$ calculated from the fluctuations in potential energy in the *NVT* (canonical) ensemble via the Einstein expression $\tilde{c}_V^{\mathrm{ex}} = \langle (\Delta U)^2 \rangle / N k_B^2 T^2$. The more gas-like the structure is, the lower is the excess specific heat because interactions become infrequent. In the original (2009) version of isomorph theory,[22] the excess specific heat was predicted to be an isomorph invariant. Figure 8 shows that this is not the case; in fact, $\tilde{c}_V^{\mathrm{ex}} \propto \rho^{1/3}$ in the gas phase. This confirms the need for the 2014 revision of the isomorph theory[16] in which it was shown that the originally predicted isomorph invariance of $\tilde{c}_V^{\mathrm{ex}}$ results from a first-order approximation to a simpler and more correct theory, which starts from the hidden-scale-invariance condition Eq. (2).

Along the gas-phase isomorph, the density variation of C_V is determined as follows. At low temperatures, Eq. (15) implies $\gamma = -\ln T/3$. Substituting this into Eq. (5) leads to a simple

first-order differential equation for $\ln T$ as a function of $\ln \rho$. The solution is $\ln T = A(S_{\mathrm{ex}})\rho^{-1/3}$ in which $A(S_{\mathrm{ex}})$ is an integration constant. This implies that $(\partial \ln T/\partial S_{\mathrm{ex}})_\rho = A'(S_{\mathrm{ex}})\rho^{-1/3}$, which via the identity $C_V = (\partial S_{\mathrm{ex}}/\partial \ln T)_\rho$ implies that $C_V \propto \rho^{1/3}$ along the gas-phase isomorphs. The dashed line in Fig. 8 has slope 1/3; it fits well to the density variation of C_V along the gas-liquid isomorph.

Figure 9 shows that the density-scaling exponent γ decreases significantly with increasing density along each isomorph. Note that the EXP system has $R > 0.9$, i.e., is strongly correlating, even with γ values as low as 1.5.

V. DIRECT-ISOMORPH-CHECK APPROXIMATE ISOMORPH

In this section, we use the same three starting state points as above to trace out approximate isomorphs using two versions of the so-called direct isomorph check. This method, which allows for much larger density jumps than 1%, is justified as follows.
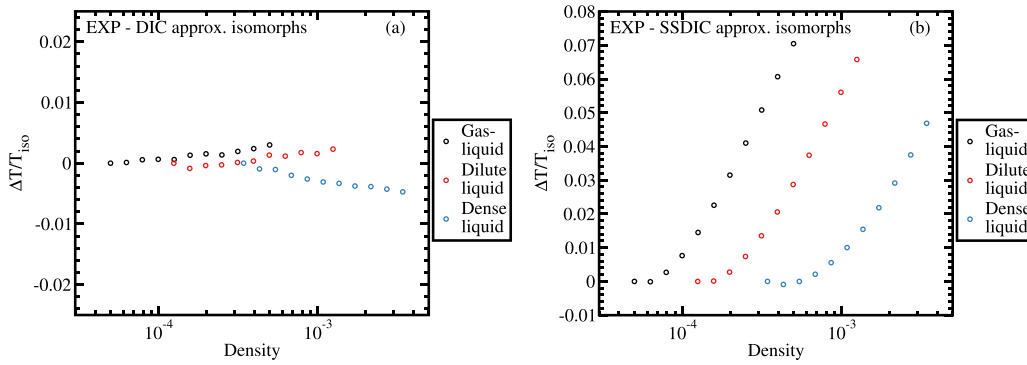
FIG. 10. Relative differences in temperature along three approximate isomorphs generated by the direct isomorph check (DIC) and the single-state-point direct isomorph check (SSDIC) methods, compared to the temperatures of the "exact" isomorphs of Sec. IV. (a) shows results for the DIC method based on ten consecutive density increases, each of 25.9%, covering in all one density decade. (b) shows the results where each of the ten jumps was generated by the SSDIC method, i.e., jumping from the same low-density starting point. Not surprisingly, the latter method is less accurate than the DIC method, in particular for the largest density jumps, but in both cases deviations from the exact isomorph temperatures are small.
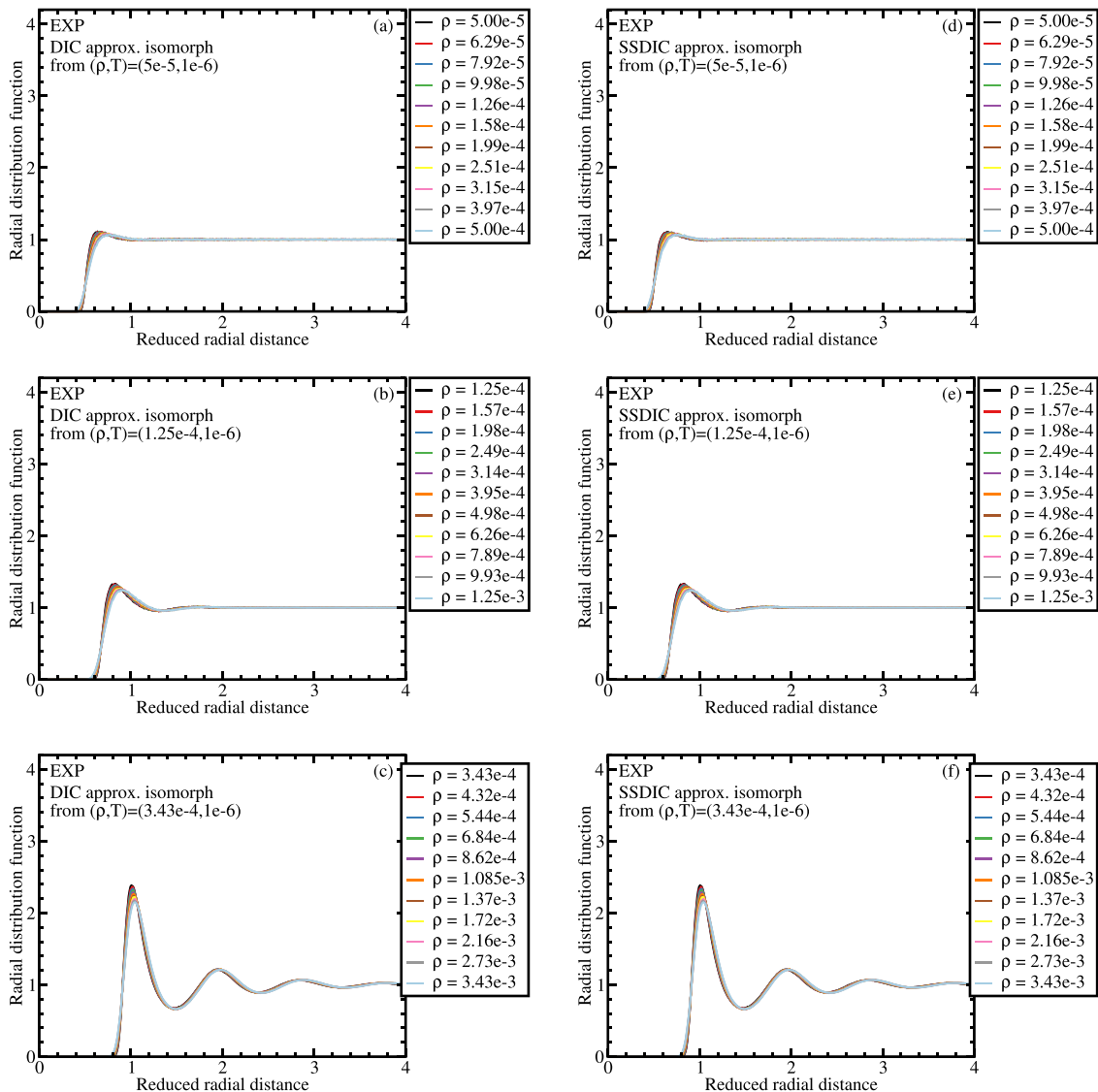
FIG. 11. *Left:* RDFs for selected state points along each of the three approximate isomorphs generated by ten consecutive applications of the DIC method. (a) Gas-liquid isomorph, (b) dilute-liquid isomorph, (c) dense-liquid isomorph. *Right:* Structure for state points along each of the three approximate isomorphs generated by the SSDIC method jumping in each case from the same starting state point (in all cases with starting temperature 10^{-6}). (d) Gas-liquid isomorph, (e) dilute-liquid isomorph, (f) dense-liquid isomorph. The two methods give similar results and compare well to the exact isomorph results of Fig. 5 based on 230 small-step jumps.

Suppose simulations at the state point (ρ_1, T_1) generate a series of configurations. For a different density ρ_2, we wish to determine the temperature T_2 for which the state point (ρ_2, T_2) is on the same isomorph as (ρ_1, T_1). Each of the generated configurations $\mathbf{R}_1$ is scaled uniformly to density ρ_2 via $\mathbf{R}_2 = (\rho_1/\rho_2)^{1/3}\mathbf{R}_1$. We denote the potential energies of $\mathbf{R}_1$ and $\mathbf{R}_2$ by U_1 and U_2, respectively. Because $\mathbf{R}_1$ and $\mathbf{R}_2$ have the same reduced coordinates and $S_{\mathrm{ex}}(\mathbf{R})$ for any R-simple system depends only on the configuration's reduced coordinate,[16] one has $S_{\mathrm{ex}}(\rho_1, U_1) = S_{\mathrm{ex}}(\rho_2, U_2)$. Consequently, Eq. (3) implies

$$U_2 = U(\rho_2, S_{\mathrm{ex}}(\rho_1, U_1)). \tag{16}$$

Since $(\partial U/\partial S_{\mathrm{ex}})_\rho = T$ and ρ_1 and ρ_2 are both fixed, this implies for ratio of the potential-energy variations among different $\mathbf{R}_1$ configurations from the equilibrium simulation, denoted by ΔU_1, to the variation among the scaled configurations' potential energy variation, denoted by ΔU_2, that

$$\frac{\Delta U_2}{\Delta U_1} = \left(\frac{\partial U(\rho_2, S_{\mathrm{ex}}(\rho_1, U_1))}{\partial S_{\mathrm{ex}}}\right)_{\rho_2} \left(\frac{\partial S_{\mathrm{ex}}(\rho_1, U_1)}{\partial U_1}\right)_{\rho_1} = \frac{T_2}{T_1}. \tag{17}$$

In other words, the slope of a U_2 versus U_1 scatter plot is T_2/T_1, which allows for an easy way to determine T_2. This is the direct isomorph check (DIC).[16,22] For it to work properly, it is important that the potential energies of the original and the scaled configurations are well correlated;[22] for the EXP system, we find correlation coefficients above 99.8% when the density is doubled. Even for the largest density jumps—one decade—there is strong correlation between the scaled and the unscaled potential energy, allowing for accurately determining T_2/T_1.

We proceed to compare the approximate isomorphs generated from ten successive DIC jumps to what is termed "single state point DIC" (SSDIC)-generated isomorphs that start from the same density ρ_1. The latter method ultimately increases
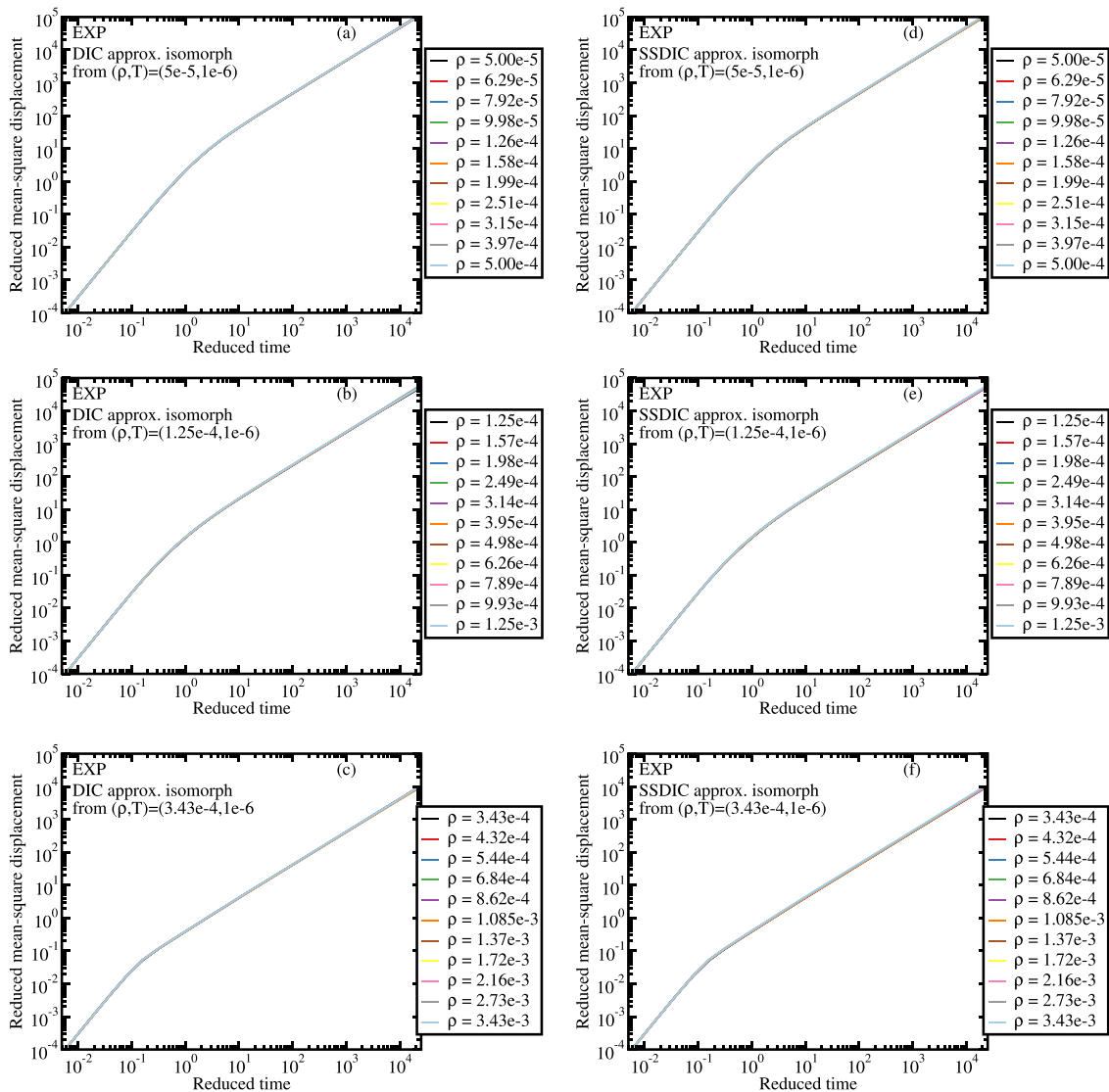
FIG. 12. *Left:* Reduced MSD for selected state points along each of the three approximate isomorphs generated by ten consecutive applications of the DIC method (the same state points as in Fig. 11, left). (a) Gas-liquid isomorph, (b) dilute-liquid isomorph, (c) dense-liquid isomorph. *Right:* Reduced MSD for state points along each of the three approximate isomorphs generated by the SSDIC method jumping in each case from the same starting state point (in all cases with starting temperature 10^{-6}). (d) Gas-liquid isomorph, (e) dilute-liquid isomorph, (f) dense-liquid isomorph. The two methods give similar results and compare well to the exact isomorph results of Fig. 6 based on 230 small-step jumps.
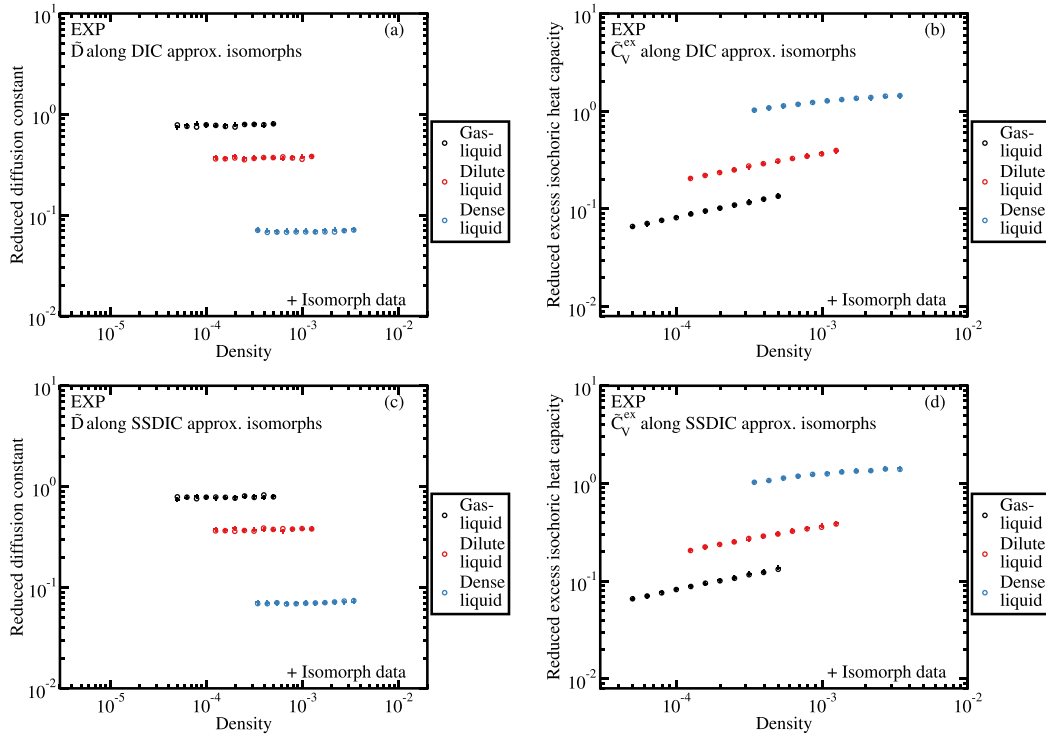
FIG. 13. DIC and SSDIC predicted data (circles) compared to the exact isomorph data (crosses). (a) and (c) (Left) show DIC and SSDIC results for the reduced diffusion constant, which are hard to distinguish from each other and from the exact results of Fig. 7(a). (b) and (d) (Right) show DIC and SSDIC results for the reduced specific heat, which compare well to the exact results of Fig. 8 (crosses).

density by one order of magnitude, whereas the DIC-generated isomorphs cover one decade of densities via ten jumps that are equally spaced on the logarithmic density axis, each increasing density by 25.9%.

Figure 10 shows the relative temperature differences between approximate and "exact" isomorphs as a function of density with (a) giving the DIC method results and (b) the SSDIC method results. As the step size increases, the SSDIC method systematically overshoots the temperature. In this light, it may seem surprising that good collapse is still maintained for the physics (Figs. 11 and 12). This is because the deviations in temperature from the small-step method temperatures obtained in Sec. IV are below 7%, even for temperature changes spanning two decades.

Figure 13 shows the reduced diffusion constant and the reduced specific heats along the DIC- and SSDIC-generated approximate isomorphs, respectively, in both cases showing results close to the those of the exact isomorphs.

VI. DISCUSSION

As shown in Paper I,[1] the EXP system has strong virial potential-energy correlations in the low-temperature part of its phase diagram. The present paper has demonstrated the existence of isomorphs in this part of the phase diagram. Three isomorphs were studied, one in the gas-liquid border area, the second one in the dilute-liquid phase, and the third one in the condensed-liquid phase. Each isomorph covers one decade of density; they were generated by 230 simulations using Eq. (6) in a step-by-step numerical integration of Eq. (5). Two approximate methods were studied for generating isomorphs

numerically, the direct-isomorph-check (DIC) method, and its single-state-point version (SSDIC). Both methods work well.

The virial potential-energy correlation coefficient R is very close to unity at the lowest temperature studied $T = 10^{-6}$, in fact above 99.8% at all densities simulated (Paper I[1]). From this, one may be tempted to conclude that $R \to 1$ for $T \to 0$ at fixed density. We do not think this is the case, though. At any fixed density, the system eventually crystallizes upon cooling. Even though the crystal obeys $R \cong 1$ at low temperatures, there is no reason to expect $R \to 1$ for $T \to 0$ at a fixed density in the crystal. This is because the unlimited range of the EXP pair potential means that in a harmonic approximation there are not just nearest-neighbor springs but also next-nearest neighbor springs, etc., and the different spring constants are not proportional to one another when the density is changed to investigate whether or not Eq. (2) applies rigorously.

We conjecture, however, that $R \to 1$ for $T \to 0$ *along any isomorph*. Here the physics is invariant, and as the temperature is lowered toward zero, the density-scaling exponent γ increases toward infinity because the density decreases (compare Fig. 9). Effectively, the EXP system becomes more and more hard-sphere (HS)-like, and Fig. 3(b) shows that as γ diverges, $R \to 1$ because R is empirically found always to be larger than its gas limit [for which one rigorously has $R \to 1$ as $\rho \to 0$, compare the dashed curve of Fig. 3(b)].

For future work, it would be interesting to undertake a systematic investigation of the crystal phase. Preliminary results indicate that the stable crystal structure is bcc at relatively high temperatures, but is fcc at low temperature (the border is roughly where γ is two).

ACKNOWLEDGMENTS

APPENDIX: STATE POINTS ON THE THREE ISOMORPHS

For reference, we give below the coordinates of selected state points along the three isomorphs determined by the "small-step" method via density changes of 1%. For each isomorph, every 23rd state point is listed (Tables I–III).

TABLE I. Selected state points along the gas-liquid isomorph.

ρ	T
5×10^{-5}	1×10^{-6}
$6.294\,6 \times 10^{-5}$	$2.693\,0 \times 10^{-6}$
$7.924\,5 \times 10^{-5}$	$6.738\,3 \times 10^{-6}$
$9.976\,3 \times 10^{-5}$	$1.575\,2 \times 10^{-5}$
$0.000\,125\,59$	$3.456\,7 \times 10^{-5}$
$0.000\,158\,11$	$7.155\,4 \times 10^{-5}$
$0.000\,199\,05$	$0.000\,140\,32$
$0.000\,250\,59$	$0.000\,261\,69$
$0.000\,315\,48$	$0.000\,465\,86$
$0.000\,397\,16$	$0.000\,794\,25$
5×10^{-4}	$0.001\,300\,9$

TABLE II. Selected state points along the dilute-liquid isomorph.

ρ	T
$0.000\,125\,00$	1×10^{-6}
$0.000\,157\,37$	$2.652\,1 \times 10^{-6}$
$0.000\,198\,11$	$6.532\,5 \times 10^{-6}$
$0.000\,249\,41$	$1.502\,4 \times 10^{-5}$
$0.000\,313\,99$	$3.242\,0 \times 10^{-5}$
$0.000\,395\,28$	$6.595\,4 \times 10^{-5}$
$0.000\,497\,63$	$0.000\,126\,96$
$0.000\,626\,48$	$0.000\,232\,22$
$0.000\,788\,70$	$0.000\,404\,90$
$0.000\,992\,91$	$0.000\,675\,39$
$0.001\,250\,0$	$0.001\,080\,8$

TABLE III. Selected state points along the dense-liquid isomorph.

ρ	T
$0.000\,343\,00$	1×10^{-6}
$0.000\,431\,81$	$2.474\,5 \times 10^{-6}$
$0.000\,543\,62$	$5.682\,5 \times 10^{-6}$
$0.000\,684\,37$	$1.217\,4 \times 10^{-5}$
$0.000\,861\,58$	$2.443\,9 \times 10^{-5}$
$0.001\,084\,7$	$4.617\,0 \times 10^{-5}$
$0.001\,365\,5$	$8.241\,3 \times 10^{-5}$
$0.001\,719\,1$	$0.000\,139\,50$
$0.002\,164\,2$	$0.000\,224\,69$
$0.002\,724\,5$	$0.000\,345\,53$
$0.003\,430\,0$	$0.000\,508\,85$

[1] A. K. Bacher, T. B. Schrøder, and J. C. Dyre, "The EXP pair-potential system. I. Fluid phase isotherms, isochores, and quasiuniversality," J. Chem. Phys. **149**, 114501 (2018).

[2] W. G. Hoover, D. A. Young, and R. Grover, "Statistical mechanics of phase diagrams. I. Inverse power potentials and the close-packed to body-packed cubic transition," J. Chem. Phys. **56**, 2207–2210 (1972).

[3] Y. Hiwatari, H. Matsuda, T. Ogawa, N. Ogita, and A. Ueda, "Molecular dynamics studies on the soft-core model," Prog. Theor. Phys. **52**, 1105–1123 (1974).

[4] D. M. Heyes and A. C. Branka, "Physical properties of soft repulsive particle fluids," Phys. Chem. Chem. Phys. **9**, 5570–5575 (2007).

[5] D. M. Heyes and A. C. Branka, "Self-diffusion coefficients and shear viscosity of inverse power fluids: From hard- to soft-spheres," Phys. Chem. Chem. Phys. **10**, 4036–4044 (2008).

[6] E. Lange, J. B. Caballero, A. M. Puertas, and M. Fuchs, "Comparison of structure and transport properties of concentrated hard and soft sphere fluids," J. Chem. Phys. **130**, 174903 (2009).

[7] A. C. Branka and D. M. Heyes, "Pair correlation function of soft-sphere fluids," J. Chem. Phys. **134**, 064115 (2011).

[8] S. Pieprzyk, D. M. Heyes, and A. C. Branka, "Thermodynamic properties and entropy scaling law for diffusivity in soft spheres," Phys. Rev. E **90**, 012106 (2014).

[9] Y. Ding and J. Mittal, "Equilibrium and nonequilibrium dynamics of soft sphere fluids," Soft Matter **11**, 5274–5281 (2015).

[10] M. Born and J. E. Meyer, "Zur Gittertheorie der Ionenkristalle," Z. Phys. **75**, 1–18 (1932).

[11] S. M. Foiles, M. I. Baskes, and M. S. Daw, "Embedded-atom-method functions for the FCC metals Cu, Ag, Au, Ni, Pd, Pt, and their alloys," Phys. Rev. B **33**, 7983–7991 (1986).

[12] K. N. Lad, N. Jakse, and A. Pasturel, "How closely do many-body potentials describe the structure and dynamics of Cu–Zr glass-forming alloy?," J. Chem. Phys. **146**, 124502 (2017).

[13] H. Yukawa, "On the interaction of elementary particles," Proc. Phys.-Math. Soc. Jpn. **17**, 48–57 (1935).

[14] J. S. Rowlinson, "The Yukawa potential," Physica A **156**, 15–34 (1989).

[15] M. Kac, G. E. Uhlenbeck, and P. C. Hemmer, "On the van der Waals theory of the vapor-liquid equilibrium. I. Discussion of a one-dimensional model," J. Math. Phys. **4**, 216–228 (1963).

[16] T. B. Schrøder and J. C. Dyre, "Simplicity of condensed matter at its core: Generic definition of a Roskilde-simple system," J. Chem. Phys. **141**, 204502 (2014).

[17] T. B. Schrøder, U. R. Pedersen, N. P. Bailey, S. Toxvaerd, and J. C. Dyre, "Hidden scale invariance in molecular van der Waals liquids: A simulation study," Phys. Rev. E **80**, 041502 (2009).

[18] J. C. Dyre, "Hidden scale invariance in condensed matter," J. Phys. Chem. B **118**, 10007–10024 (2014).

[19] U. R. Pedersen, N. P. Bailey, T. B. Schrøder, and J. C. Dyre, "Strong pressure-energy correlations in van der Waals liquids," Phys. Rev. Lett. **100**, 015701 (2008).

[20] N. P. Bailey, U. R. Pedersen, N. Gnan, T. B. Schrøder, and J. C. Dyre, "Pressure-energy correlations in liquids. I. Results from computer simulations," J. Chem. Phys. **129**, 184507 (2008).

[21] A. K. Bacher, T. B. Schrøder, and J. C. Dyre, "Explaining why simple liquids are quasi-universal," Nat. Commun. **5**, 5424 (2014).

[22] N. Gnan, T. B. Schrøder, U. R. Pedersen, N. P. Bailey, and J. C. Dyre, "Pressure-energy correlations in liquids. IV. 'Isomorphs' in liquid phase diagrams," J. Chem. Phys. **131**, 234504 (2009).

[23] Y. Rosenfeld, "Relation between the transport coefficients and the internal entropy of simple systems," Phys. Rev. A **15**, 2545–2549 (1977).

[24] T. S. Ingebrigtsen, T. B. Schrøder, and J. C. Dyre, "What is a simple liquid?," Phys. Rev. X **2**, 011011 (2012).

[25] J. C. Dyre, "Simple liquids' quasiuniversality and the hard-sphere paradigm," J. Phys.: Condens. Matter **28**, 323001 (2016).

[26] T. S. Ingebrigtsen, S. Toxvaerd, O. J. Heilmann, T. B. Schrøder, and J. C. Dyre, "*NVU* dynamics. I. Geodesic motion on the constant-potential-energy hypersurface," J. Chem. Phys. **135**, 104101 (2011).

[27] E. N. C. Andrade, "XLI. A theory of the viscosity of liquids. Part I," London Edinburgh Dublin Philos. Mag. J. Sci. **17**, 497–511 (1934).

[28] J.-P. Hansen and I. R. McDonald, *Theory of Simple Liquids: With Applications to Soft Matter*, 4th ed. (Academic, New York, 2013).

[29] U. R. Pedersen, L. Costigliola, N. P. Bailey, T. B. Schrøder, and J. C. Dyre, "Thermodynamics of freezing and melting," Nat. Commun. **7**, 12386 (2016).

[30] T. S. Ingebrigtsen, T. B. Schrøder, and J. C. Dyre, "Isomorphs in model molecular liquids," J. Phys. Chem. B **116**, 1018–1034 (2012).

[31] A. A. Veldhorst, J. C. Dyre, and T. B. Schrøder, "Scaling of the dynamics of flexible Lennard-Jones chains," J. Chem. Phys. **141**, 054904 (2014).

[32] T. B. Schrøder, N. P. Bailey, U. R. Pedersen, N. Gnan, and J. C. Dyre, "Pressure-energy correlations in liquids. III. Statistical mechanics and thermodynamics of liquids with hidden scale invariance," J. Chem. Phys. **131**, 234503 (2009).

[33] C. M. Roland, S. Hensel-Bielowka, M. Paluch, and R. Casalini, "Super-cooled dynamics of glass-forming liquids and polymers under hydrostatic pressure," Rep. Prog. Phys. **68**, 1405–1478 (2005).

[34] N. P. Bailey, U. R. Pedersen, N. Gnan, T. B. Schrøder, and J. C. Dyre, "Pressure-energy correlations in liquids. II. Analysis and consequences," J. Chem. Phys. **129**, 184508 (2008).

[35] A. A. Veldhorst, T. B. Schrøder, and J. C. Dyre, "Invariants in the Yukawa system's thermodynamic phase diagram," Phys. Plasmas **22**, 073705 (2015).

[36] L. Costigliola, T. B. Schrøder, and J. C. Dyre, "Communication: Studies of the Lennard-Jones fluid in 2, 3, and 4 dimensions highlight the need for a liquid-state 1/d expansion," J. Chem. Phys. **144**, 231101 (2016).

[37] T. S. Ingebrigtsen, L. Bøhling, T. B. Schrøder, and J. C. Dyre, "Thermodynamics of condensed matter with strong pressure-energy correlations," J. Chem. Phys. **136**, 061102 (2012).

[38] T. Maimbourg and J. Kurchan, "Approximate scale invariance in particle systems: A large-dimensional justification," Europhys. Lett. **114**, 60002 (2016).

Bibliography

[1] Frank H Stillinger. *Energy Landscapes, Inherent Structures, and Condensed-Matter Phenomena*. Princeton University Press, 2015. (Cited on p. 2.)

[2] Frank H. Stillinger and Dorothea K. Stillinger. Negative thermal expansion in the gaussian core model. *Physica A: Statistical Mechanics and its Applications*, 244(1):358 – 369, 1997. ISSN 0378-4371. doi: https://doi.org/10.1016/S0378-4371(97)00246-X. URL *http://www.sciencedirect.com/science/article/pii/S037843719700246X*. (Cited on pp. 2 and 119.)

[3] Jayant S. Shah and M.E. Straumanis. Thermal expansion behavior of silicon at low temperatures. *Solid State Communications*, 10 (1):159 – 162, 1972. ISSN 0038-1098. doi: https://doi.org/10.1016/0038-1098(72)90371-7. URL *http://www.sciencedirect.com/science/article/pii/0038109872903717*. (Cited on p. 2.)

[4] J. E. Jones. On the Determination of Molecular Fields. I. From the Variation of the Viscosity of a Gas with Temperature. *Proceedings of the Royal Society of London. Series A*, 106(738):441–462, 1924. doi: 10.1098/rspa.1924.0081. URL *http://rspa.royalsocietypublishing.org/content/106/738/441.short*. (Cited on p. 3.)

[5] J. E. Jones. On the determination of molecular fields. -ii. from the equation of state of a gas. *Proceedings of the Royal Society of London A: Mathematical, Physical and Engineering Sciences*, 106(738):463–477, 1924. ISSN 0950-1207. doi: 10.1098/rspa.1924.0082. URL *http://rspa.royalsocietypublishing.org/content/106/738/463*. (Cited on p. 3.)

[6] Jean-Pierre Hansen and I. R. McDonald. *Theory of Simple Liquids (Fourth Edition)*. Academic Press, fourth edition edition, 2013. ISBN 978-0-12-387032-2. doi: https://doi.org/10.1016/B978-0-12-387032-2.00013-1. URL *http://www.sciencedirect.com/science/article/pii/B9780123870322000131*. (Cited on pp. 3, 7, 10, and 42.)

[7] Trond S. Ingebrigtsen, Thomas B. Schrøder, and Jeppe C. Dyre. What is a Simple Liquid? *PHYSICAL REVIEW X*, 2:011011, 2012.

URL *http://glass.ruc.dk/pdf/articles/2012_PhysRevX_2_011011.pdf*. (Cited on pp. 3, 4, and 17.)

[8] Jeppe C Dyre. Simple liquids' quasiuniversality and the hard-sphere paradigm. *Journal of Physics: Condensed Matter*, 28(32):323001, 2016. URL *http://stacks.iop.org/0953-8984/28/i=32/a=323001*. (Cited on pp. 3, 18, and 36.)

[9] Max Born and Joseph E. Mayer. Zur Gittertheorie der Ionenkristalle. *Zeitschrift für Physik*, 75:1–18, 1931. (Cited on p. 3.)

[10] Adolf A. Abrahamson. Born-Mayer-Type Interatomic Potential for Neutral Ground-State Atoms with $Z = 2$ to $Z = 105$. *Phys. Rev.*, 178:76–79, Feb 1969. doi: 10.1103/PhysRev.178.76. URL *http://link.aps.org/doi/10.1103/PhysRev.178.76*. (Cited on p. 3.)

[11] F. London. Zur theorie und systematik der molekularkräfte. *Zeitschrift für Physik*, 63(3):245–279, Mar 1930. ISSN 0044-3328. doi: 10.1007/BF01421741. URL *https://doi.org/10.1007/BF01421741*. (Cited on p. 3.)

[12] R. A. Buckingham. The Classical Equation of State of Gaseous Helium, Neon and Argon. *Proceedings of the Royal Society of London. Series A. Mathematical and Physical Sciences*, 168(933):264–283, 1938. doi: 10.1098/rspa.1938.0173. URL *http://rspa.royalsocietypublishing.org/content/168/933/264.short*. (Cited on p. 3.)

[13] L. A. Girifalco and V. G. Weizer. Application of the morse potential function to cubic metals. *Phys. Rev.*, 114:687–690, May 1959. doi: 10.1103/PhysRev.114.687. URL *https://link.aps.org/doi/10.1103/PhysRev.114.687*. (Cited on p. 3.)

[14] Hideki Yukawa. On the interaction of elementary particles. i. *Proceedings of the Physico-Mathematical Society of Japan. 3rd Series*, 17:48–57, 1935. doi: 10.11429/ppmsj1919.17.0_48. (Cited on p. 3.)

[15] J.S. Rowlinson. The yukawa potential. *Physica A: Statistical Mechanics and its Applications*, 156(1):15 – 34, 1989. ISSN 0378-4371. doi: https://doi.org/10.1016/0378-4371(89)90108-8. URL *http://www.sciencedirect.com/science/article/pii/0378437189901088*. (Cited on p. 3.)

[16] S. M. Foiles, M. I. Baskes, and M. S. Daw. Embedded-atom-method functions for the fcc metals cu, ag, au, ni, pd, pt, and their alloys. *Phys. Rev. B*, 33:7983–7991, Jun 1986. doi: 10.1103/PhysRevB.33.7983. URL *https://link.aps.org/doi/10.1103/PhysRevB.33.7983*. (Cited on p. 3.)

[17] Stefan Kooij and Edan Lerner. Unjamming in models with analytic pairwise potentials. *Phys. Rev. E*, 95:062141, Jun 2017. doi: 10.1103/PhysRevE.95.062141. URL *https://link.aps.org/doi/10.1103/PhysRevE.95.062141*. (Cited on p. 3.)

[18] D. M. Heyes and A. C. Braṅka. Self-diffusion coefficients and shear viscosity of inverse power fluids: from hard- to soft-spheres. *Phys. Chem. Chem. Phys.*, 10:4036–4044, 2008. doi: 10.1039/B802916D. URL *http://dx.doi.org/10.1039/B802916D*. (Cited on p. 4.)

[19] John D. Weeks, David Chandler, and Hans C. Andersen. Role of repulsive forces in determining the equilibrium structure of simple liquids. *The Journal of Chemical Physics*, 54(12):5237–5247, 1971. doi: 10.1063/1.1674820. URL *https://doi.org/10.1063/1.1674820*. (Cited on p. 4.)

[20] William G. Hoover, David A. Young, and Richard Grover. Statistical mechanics of phase diagrams. i. inverse power potentials and the close-packed to body-centered cubic transition. *The Journal of Chemical Physics*, 56(5):2207–2210, 1972. doi: 10.1063/1.1677521. URL *https://doi.org/10.1063/1.1677521*. (Cited on p. 4.)

[21] D. M. Heyes and A. C. Braṅka. Physical properties of soft repulsive particle fluids. *Phys. Chem. Chem. Phys.*, 9:5570–5575, 2007. doi: 10.1039/B709053F. URL *http://dx.doi.org/10.1039/B709053F*. (Not cited.)

[22] Erik Lange, Jose B. Caballero, Antonio M. Puertas, and Matthias Fuchs. Comparison of structure and transport properties of concentrated hard and soft sphere fluids. *The Journal of Chemical Physics*, 130(17):174903, 2009. doi: 10.1063/1.3124182. URL *https://doi.org/10.1063/1.3124182*. (Cited on p. 4.)

[23] F. de J. Guevara-Rodríguez and Magdaleno Medina-Noyola. Dynamic equivalence between soft- and hard-core brownian fluids. *Phys. Rev. E*, 68:011405, Jul 2003. doi: 10.1103/PhysRevE.68.011405. URL *https://link.aps.org/doi/10.1103/PhysRevE.68.011405*. (Cited on p. 4.)

[24] Dor Ben-Amotz and George Stell. Reformulation of weeks-chandler-andersen perturbation theory directly in terms of a hard-sphere reference system. *The Journal of Physical Chemistry B*, 108(21):6877–6882, 05 2004. doi: 10.1021/jp037810s. URL *https://doi.org/10.1021/jp037810s*. (Cited on p. 4.)

[25] Andreas Kvist Bacher, Thomas B. Schrøder, and Jeppe C. Dyre. Explaining why simple liquids are quasi-universal. *Nature Communications*, 5(5424), 2014. (Cited on pp. 4, 34, 115, and 116.)

[26] Andreas Kvist Bacher, Thomas B. Schrøder, and Jeppe C. Dyre. The exp pair-potential system. i. fluid phase isotherms, isochores, and quasiuniversality. *The Journal of Chemical Physics*, 149(11):114501, 2018. doi: 10.1063/1.5043546. URL *https://doi.org/10.1063/1.5043546*. (Cited on pp. 5, 27, 81, 94, and 115.)

[27] Andreas Kvist Bacher, Thomas B. Schrøder, and Jeppe C. Dyre. The exp pair-potential system. ii. fluid phase isomorphs. *The Journal of Chemical Physics*, 149(11):114502, 2018. doi: 10.1063/1.5043548. URL *https://doi.org/10.1063/1.5043548*. (Cited on pp. 5, 27, and 94.)

[28] Daan Frenkel and B. Smit. *Understanding Molecular Simulation : From Algorithms to Applications*. Academic Press, Amsterdam, NLD, 2001. (Cited on pp. 7, 11, and 70.)

[29] M. P. Allen and D.J. Tildesley. *Computer Simulation of Liquids*. Oxford University Press Inc., 1987. (Cited on p. 8.)

[30] Søren Toxvaerd and Jeppe C. Dyre. Communication: Shifted forces in molecular dynamics. *THE JOURNAL OF CHEMICAL PHYSICS*, 134:081102, 2011. URL *http://glass.ruc.dk/pdf/articles/2011_JChemPhys_134_081102.pdf*. (Cited on pp. 8, 9, and 28.)

[31] Loup Verlet. Computer "Experiments" on Classical Fluids. I. Thermodynamical Properties of Lennard-Jones Molecules. *Phys. Rev.*, 159: 98–103, Jul 1967. doi: 10.1103/PhysRev.159.98. URL *http://link.aps.org/doi/10.1103/PhysRev.159.98*. (Cited on p. 9.)

[32] D. Levesque and L. Verlet. Molecular dynamics and time reversibility. *Journal of Statistical Physics*, 72(3):519–537, Aug 1993. ISSN 1572-9613. doi: 10.1007/BF01048022. URL *https://doi.org/10.1007/BF01048022*. (Cited on p. 9.)

[33] Søren Toxværd, Ole J. Heilmann, and Jeppe C. Dyre. Energy conservation in molecular dynamics simulations of classical systems. *The Journal of Chemical Physics*, 136(22):224106, 2012. doi: 10.1063/1.4726728. URL *https://doi.org/10.1063/1.4726728*. (Cited on p. 10.)

[34] Hans C. Andersen. Molecular dynamics simulations at constant pressure and/or temperature. *The Journal of Chemical Physics*, 72(4): 2384–2393, 1980. doi: 10.1063/1.439486. URL *https://doi.org/10.1063/1.439486*. (Cited on p. 11.)

[35] Shuichi Nosé. A unified formulation of the constant temperature molecular dynamics methods. *THE JOURNAL OF CHEMICAL PHYSICS*, 81(1):511–519, 1984. (Cited on p. 11.)

[36] Shūichi Nosé. A molecular dynamics method for simulations in the canonical ensemble. *Molecular Physics*, 52(2):255–268, 1984. doi: 10.1080/00268978400101201. URL *https://doi.org/10.1080/00268978400101201*. (Cited on p. 11.)

[37] William G. Hoover. Canonical dynamics: Equilibrium phase-space distributions. *PHYSICAL REVIEW A*, 31(3):1695–1697, March 1985. (Cited on p. 11.)

[38] William Graham Hoover and Carol Griswold Hoover. *Time Reversibility, Computer Simulation, Algorithms, Chaos*. WORLD SCIENTIFIC, 2nd edition, 2012. doi: 10.1142/8344. URL *https://www.worldscientific.com/doi/abs/10.1142/8344*. (Cited on p. 12.)

[39] Glenn J. Martyna, Douglas J. Tobias, and Michael L. Klein. Constant pressure molecular dynamics algorithms. *The Journal of Chemical Physics*, 101(5):4177–4189, 1994. doi: 10.1063/1.467468. URL *https://doi.org/10.1063/1.467468*. (Cited on p. 12.)

[40] Trond S. Ingebrigtsen, Søren Toxvaerd, Ole J. Heilmann, Thomas B. Schrøder, and Jeppe C. Dyre. NVU dynamics. I. Geodesic motion on the constant-potential-energy hypersurface. *The Journal of Chemical Physics*, 135(10):104101, 2011. doi: 10.1063/1.3623585. URL *https://doi.org/10.1063/1.3623585*. (Cited on pp. 12 and 115.)

[41] Trond S. Ingebrigtsen, Søren Toxvaerd, Thomas B. Schrøder, and Jeppe C. Dyre. NVU dynamics. II. Comparing to four other dynamics. *The Journal of Chemical Physics*, 135(10):104102, 2011. doi: 10.1063/1.3623586. URL *https://doi.org/10.1063/1.3623586*. (Cited on p. 12.)

[42] Trond S. Ingebrigtsen and Jeppe C. Dyre. NVU dynamics. III. Simulating molecules at constant potential energy. *The Journal of Chemical Physics*, 137(24):244101, 2012. doi: 10.1063/1.4768957. URL *https://doi.org/10.1063/1.4768957*. (Cited on pp. 12 and 115.)

[43] Joshua A. Anderson, Chris D. Lorenz, and A. Travesset. General purpose molecular dynamics simulations fully implemented on graphics processing units. *Journal of Computational Physics*, 227(10):5342 – 5359, 2008. ISSN 0021-9991. doi: https://doi.org/10.1016/j.jcp.2008.01.047. URL *http://www.sciencedirect.com/science/article/pii/S0021999108000818*. (Cited on pp. 12 and 13.)

[44] Nicholas P. Bailey, Trond S. Ingebrigtsen, Jesper Schmidt Hansen, Arno A. Veldhorst, Lasse Bøhling, Claire A. Lemarchand, Andreas E. Olsen, Andreas K. Bacher, Lorenzo Costigliola, Ulf R. Pedersen, Heine Larsen, Jeppe C. Dyre, and Thomas B. Schrøder. RUMD: A general

purpose molecular dynamics package optimized to utilize GPU hardware down to a few thousand particles. *SciPost Phys.*, 3:038, 2017. URL *https://scipost.org/10.21468/SciPostPhys.3.6.038*. (Cited on pp. 13, 14, 27, and 28.)

[45] RUMD, 09 2018. URL *http://rumd.org*. (Cited on p. 13.)

[46] Steve Plimpton. Fast parallel algorithms for short-range molecular dynamics. *Journal of Computational Physics*, 117(1):1 – 19, 1995. ISSN 0021-9991. doi: https://doi.org/10.1006/jcph. 1995.1039. URL *http://www.sciencedirect.com/science/article/pii/ S002199918571039X*. (Cited on p. 14.)

[47] LAMMPS, 09 2018. URL *http://lammps.sandia.gov*. (Cited on pp. 14 and 111.)

[48] Yaakov Rosenfeld. Relation between the transport coefficients and the internal entropy of simple systems. *Phys. Rev. A*, 15:2545–2549, Jun 1977. doi: 10.1103/PhysRevA.15.2545. URL *https://link.aps.org/doi/ 10.1103/PhysRevA.15.2545*. (Cited on pp. 16 and 42.)

[49] Yaakov Rosenfeld. A quasi-universal scaling law for atomic transport in simple fluids. *Journal of Physics: Condensed Matter*, 11(28):5415, 1999. URL *http://stacks.iop.org/0953-8984/11/i=28/a=303*. (Cited on p. 16.)

[50] Ulf R. Pedersen, Tage Christensen, Thomas B. Schrøder, and Jeppe C. Dyre. Feasibility of a single-parameter description of equilibrium viscous liquid dynamics. *Phys. Rev. E*, 77:011201, Jan 2008. doi: 10. 1103/PhysRevE.77.011201. URL *https://link.aps.org/doi/10.1103/ PhysRevE.77.011201*. (Cited on p. 16.)

[51] Ulf R. Pedersen, Günther H. Peters, Thomas B. Schrøder, and Jeppe C. Dyre. Volume-energy correlations in the slow degrees of freedom of computer-simulated phospholipid membranes. *AIP Conference Proceedings*, 982(1):407–409, 2008. doi: 10.1063/1.2897829. URL *https: //aip.scitation.org/doi/abs/10.1063/1.2897829*. (Cited on p. 16.)

[52] Nicholas P. Bailey, Ulf R. Pedersen, Nicoletta Gnan, Thomas B. Schrøder, and Jeppe C. Dyre. Pressure-energy correlations in liquids. I. Results from computer simulations. *Journal of Chemical Physics*, 129: 184507, 2008. URL *http://glass.ruc.dk/pdf/articles/2008_J_Chem_ Phys_129_184507e.pdf*. (Cited on pp. 16, 20, 59, and 69.)

[53] Nicholas P. Bailey, Ulf R. Pedersen, Nicoletta Gnan, Thomas B. Schrøder, and Jeppe C. Dyre. Pressure-energy correlations in liquids. II. Analysis and consequences. *THE JOURNAL OF CHEMICAL*

PHYSICS, 129:184508, 2008. URL *http://glass.ruc.dk/pdf/articles/ 2008_J_Chem_Phys_129_184508.pdf*. (Cited on pp. 16, 36, 37, 38, 40, and 118.)

[54] Thomas B. Schrøder, Nicholas P. Bailey, Ulf R. Pedersen, Nicoletta Gnan, and Jeppe C. Dyre. Pressure-energy correlations in liquids. III. Statistical mechanics and thermodynamics of liquids with hidden scale invariance. *THE JOURNAL OF CHEMICAL PHYSICS*, 131: 234503, 2009. URL *http://glass.ruc.dk/pdf/articles/2009_J_Chem_ Phys_131234503.pdf*. (Cited on p. 16.)

[55] Nicoletta Gnan, Thomas B. Schrøder, Ulf R. Pedersen, Nicholas P. Bailey, and Jeppe C. Dyre. Pressure-energy correlations in liquids. IV. "Isomorphs" in liquid phase diagrams. *THE JOURNAL OF CHEMICAL PHYSICS*, 131:234504, 2009. URL *http://glass.ruc.dk/pdf/articles/ 2009_J_Chem_Phys_131234504.pdf*. (Cited on pp. 16, 20, 59, 69, 70, 79, 81, and 94.)

[56] Thomas B. Schrøder, Nicoletta Gnan, Ulf R. Pedersen, Nicholas P. Bailey, and Jeppe C. Dyre. Pressure-energy correlations in liquids. V. Isomorphs in generalized Lennard-Jones systems. *THE JOURNAL OF CHEMICAL PHYSICS*, 134:164505, 2011. URL *http://glass.ruc.dk/ pdf/articles/2011_JCP_134_164505.pdf*. (Cited on p. 16.)

[57] T. B. Schrøder and J. C. Dyre. Simplicity of condensed matter at its core: Generic definition of a Roskilde-simple system. *Journal of Chemical Physics*, 141(2404502), 2014. (Cited on pp. 17, 18, 30, 33, 59, 79, and 115.)

[58] L.D. Landau and E.M. Lifshitz. *Statistical Physics*. Pergamon, 1958. (Cited on p. 17.)

[59] Spotswood D. Stoddard and Joseph Ford. Numerical experiments on the stochastic behavior of a lennard-jones gas system. *Phys. Rev. A*, 8:1504–1512, Sep 1973. doi: 10.1103/PhysRevA.8.1504. URL *https: //link.aps.org/doi/10.1103/PhysRevA.8.1504*. (Cited on p. 28.)

[60] Lasse Bøhling, Nicholas P. Bailey, Thomas B. Schrøder, and Jeppe C. Dyre. Estimating the density-scaling exponent of a liquid from its pair potential. *Journal of Chemical Physics*, 140(124510), 2014. (Cited on pp. 38, 69, and 94.)

[61] Frank H. Stillinger. Phase transitions in the Gaussian core system. *The Journal of Chemical Physics*, 65(10):3968–3974, 1976. doi: 10.1063/1. 432891. URL *https://doi.org/10.1063/1.432891*. (Cited on pp. 38, 39, 72, and 119.)

[62] Sergey A. Khrapak, Manis Chaudhuri, and Gregor E. Morfill. Communication: Universality of the melting curves for a wide range of interaction potentials. *The Journal of Chemical Physics*, 134(24):241101, 2011. doi: 10.1063/1.3605659. URL *https://doi.org/10.1063/1.3605659*. (Cited on p. 38.)

[63] Alok Samanta, Sk. Musharaf Ali, and Swapan K. Ghosh. New universal scaling laws of diffusion and kolmogorov-sinai entropy in simple liquids. *Phys. Rev. Lett.*, 92:145901, Apr 2004. doi: 10.1103/PhysRevLett. 92.145901. URL *https://link.aps.org/doi/10.1103/PhysRevLett.92. 145901*. (Cited on pp. 38 and 42.)

[64] Chen-Hung Wang, Szu-Hsuan Yu, and Peilong Chen. Universal scaling laws of diffusion in two-dimensional granular liquids. *Phys. Rev. E*, 91:060201, Jun 2015. doi: 10.1103/PhysRevE.91.060201. URL *https://link.aps.org/doi/10.1103/PhysRevE.91.060201*. (Cited on p. 38.)

[65] Mikhail Dzugutov. A universal scaling law for atomic diffusion in condensed matter. *Nature*, 381:137 EP –, 05 1996. URL *http://dx.doi.org/10.1038/381137a0*. (Cited on p. 42.)

[66] M. Dzugutov. addendum: A universal scaling law for atomic diffusion in condensed matter. *Nature*, 411:720 EP –, 06 2001. URL *http://dx.doi.org/10.1038/35079655*. (Cited on p. 42.)

[67] Kunimasa Miyazaki, Goundla Srinivas, and Biman Bagchi. The enskog theory for transport coefficients of simple fluids with continuous potentials. *The Journal of Chemical Physics*, 114(14):6276–6285, 2001. ISSN 0021-9606. (Cited on p. 43.)

[68] J. H. Dymond. Corrected enskog theory and the transport coefficients of liquids. *The Journal of Chemical Physics*, 60(3):969–973, 1974. doi: 10.1063/1.1681175. URL *https://doi.org/10.1063/1.1681175*. (Cited on p. 43.)

[69] C. Alba-Simionesco, A. Cailliaux, A. Alegría, and G. Tarjus. Scaling out the density dependence of the α relaxation in glass-forming polymers. *EPL (Europhysics Letters)*, 68(1):58, 2004. URL *http://stacks.iop.org/0295-5075/68/i=1/a=058*. (Cited on p. 70.)

[70] Trond S. Ingebrigtsen, Lasse Bøhling, Thomas B. Schrøder, and Jeppe C. Dyre. Communication: Thermodynamics of condensed matter with strong pressure-energy correlations. *THE JOURNAL OF CHEMICAL PHYSICS*, 136:061102, 2012. URL *http://glass.ruc.dk/pdf/articles/2012_JChemPhys_136_061102.pdf*. (Cited on p. 94.)

[71] Ulf R. Pedersen. Direct calculation of the solid-liquid Gibbs free energy difference in a single equilibrium simulation. *The Journal of Chemical Physics*, 139(10):104102, 2013. doi: 10.1063/1.4818747. URL *http://scitation.aip.org/content/aip/journal/jcp/139/10/10.1063/1.4818747*. (Cited on p. 111.)

[72] Ulf R. Pedersen, Lorenzo Costigliola, Nicholas P. Bailey, Thomas B. Schrøder, and Jeppe C. Dyre. Thermodynamics of freezing and melting. *Nature Communications*, 7:12386, August 2016. URL *http://dx.doi.org/10.1038/ncomms12386*. (Cited on pp. 112 and 119.)

[73] Jeppe C. Dyre. NVU perspective on simple liquids' quasiuniversality. *arxiv: 1208.1748 [cond-mat.soft]*, 8 August, 2012. URL *http://glass.ruc.dk/pdf/articles/2013_PhysRevE_87_022106.pdf*. (Cited on p. 115.)

[74] Santi Prestipino, Franz Saija, and Paolo V. Giaquinta. Phase diagram of the gaussian-core model. *Phys. Rev. E*, 71:050102, May 2005. doi: 10.1103/PhysRevE.71.050102. URL *https://link.aps.org/doi/10.1103/PhysRevE.71.050102*. (Cited on p. 119.)